Earthquake cycle of the Jalisco-Colima segment of the Mexico subduction zone from modeling of 1993-2020 GPS data

by

Ana Beatriz Cosenza Muralles

A dissertation submitted in partial fulfillment of

the requirements for the degree of

Doctor of Philosophy

(Geophysics)

at the

UNIVERSITY OF WISCONSIN-MADISON

2020

Date of final oral examination: 11/19/2020

The dissertation is approved by the following members of the Final Oral Committee:

Dr. Charles DeMets, Albert and Alice Weeks Professor, Geoscience
Dr. Kurt L. Feigl, Professor, Geoscience
Dr. Basil Tikoff, Professor, Geoscience
Dr. Hiroki Sone, Professor, Geological Engineering

ACKNOWLEDGEMENTS

Before pursuing a doctoral degree at the University of Wisconsin-Madison, I had worn many suits, worked many jobs, and had the fortune of meeting amazing people that led me to great opportunities. I got lucky, despite the not-so-privileged gender or class. From early age, I had people that made me feel I was the smartest person in the room, capable of anything, and the child I was back then believed them. Thank goodness! It built a thick shell of faith in myself, though some might call it plain vanity. In time, as my universe expanded, I was faced with the reality of limitations, and navigating adult life slowly worn that shell out. Nevertheless, it kept my enthusiasm and stubbornness safe for long enough, even after hitting many walls. I watched the hope of ever pursuing doctoral studies fade away with the years and I made my peace with that, or so I thought. Enter Chuck DeMets, I threw my "peace" out the window, tied my loved ones to my heart, packed my bags, and came to Madison, Wisconsin.

I was lucky that my love for science and the humanities was not systematically discouraged. It was even nourished in a world some call "third", where the scent of intellectualism is not necessarily welcomed. At some point, the scientist took over and I became a physicist. Since then, I've been evaluated by five committees at three different public universities in Guatemala, France, and the United States, at various stages of my career. Every single time, the committee members were all men, and so were my mentors. I was so used to it that it took me a long time to realize how important women mentorship is. Nevertheless, I was lucky again that these particular men I came across in my academic journey were nothing but supportive and encouraging. Not once did I feel negatively differentiated for being a woman around them, and I'll be forever thankful for how much they've taught me. These men, who were by my side in different ways and

moments as teachers, advisors, friends, and colleagues, are M.Sc. Edgar Cifuentes, Dr. Mario Arias Salguero, Dr. Louis Pastor, Dr. Richard Vanhoeserlande, Dr. Henri Robain, Dr. Kurt Feigl, Dr. Basil Tikoff, Dr. Hiroki Sone, Dr. Harold Tobin, Dr. Cliff Thurber, and last but in no way least, Dr. Charles (Chuck) DeMets.

Chuck, I don't even know how to begin to thank you. You made this happen. You gave me back a dream I had given up on and made it possible for me to pursue it. These five and a half years were a great experience, and you are the best advisor I could have asked for. Thank you for your very present accompaniment, your constant support, guidance, encouragement, and patience. You made every meeting a learning experience, polishing the work, perfecting the science without losing sight of its limitations. All of it made me grow as a scientist and as a person. Thanks, as well, to Lynn who has always been so welcoming and uplifting. Chuck, you also allowed me to spend some serious time doing work that didn't make it to the dissertation, but will propel my future academic endeavors. While doing that work, you also provided me with the experience of being mentored by a woman for the first time in my life. Thank you for that! So, I also thank Dr. Cécile Lasserre, for stepping up to the task and being an amazing scientist and person to work with. I'm looking forward to the continuation of our work. As I said, I've been incredibly lucky, but I strongly believe women's opportunities shouldn't depend on how lucky they are to come across the right people at the right time. Therefore, I'm committed to paying it forward while I work in academia.

To the members of my Final Examination Committee: Hiroki, I admired your enthusiasm and dedication during the very first time you taught Geodynamics at UW-Madison. You brought that same enthusiastic thoroughness to my evaluation and helped make my work better. Basil, you always shine a light on my blind spots and bring the point of view I hadn't even thought of. I

particularly appreciate the kindness with which you do that. Kurt, my exchanges with you are always enriching. You've gone out of your way to check in on me and keep me moving forward. When in doubt, I would ask the question: How would I justify this to Kurt? And that should tell you something.

I want to mention Dr. Laurel Goodwin, the only female teacher I had during my Ph.D. You have a way to uplift your students like no other, particularly the women. You were instrumental, more than once, to keep impostor syndrome at bay. I've been privileged to meet you and I'd be privileged to be half the teacher that you are.

I want to thank the amazing community of the Department of Geoscience. Students, faculty, and staff made my student experience and my life in Madison great. I specially want to thank several members of the staff. Michelle Szabo and Jane Fox, for keeping all the administrative side of my PhD running smoothly. Ben Abernathy, without your timely assistance and support my work would have been much harder, if not impossible. Neal Lord, I really enjoyed doing the last GPS campaign in Guatemala with you.

I encountered a very unusual geophysics group in our first floor corridor of Weeks Hall, where four professors, Chuck DeMets, Kurt Feigl, Clifford Thurber, and Harold Tobin, had almost exclusively female grad students. It was very refreshing, to say the least. My dear friends, Lesley Parker, Elena Reinisch, Federica Lanza, Sarah Bremmer, and Stephanie Napieralski, thank you for the love, the discussions (academic and otherwise), and the support. My life is richer and more beautiful because of you.

I want to thank my beloved family, who always have supported the pursuit of my goals. You kept me warm from afar and I love you for that. You are my rock and a large part of who I am. You made me feel loved and cherished every step of the way.

Alejandro, my life companion, you get the last thought and the shortest line because no words could ever do justice to what you've been to me these years. All I can say is: you carried me through this. If there weren't already a thousand reasons to love you, I'd love you for that.

ABSTRACT

The Jalisco-Colima segment of the Mexico subduction zone, offshore from western Mexico, accommodates northeastward subduction of the Rivera and Cocos plates beneath the western edge of the North America plate. Several large thrust earthquakes, including the $M_s \sim 8.2$ and $M_s \sim 7.8$ earthquakes in 1932, the 1973 $M_w \sim 7.6$ Colima earthquake, the 1995 $M_w = 8.0$ Colima-Jalisco earthquake, and the 2003 $M_w = 7.5$ Tecomán earthquake have ruptured the entirety of this subduction segment during the last 100 years. Geodetic measurements along the Jalisco-Colima trench segments, which were initiated nearly 25 years ago in order to monitor interseismic strain accumulation and crustal deformation associated with the subduction, recorded the 1995 and 2003 earthquakes on the subduction interface. In this dissertation, I model surface deformation measured by GPS stations in western Mexico to increase our knowledge of the earthquake cycle of the seismically hazardous Jalisco-Colima subduction zone.

The modeling described in my dissertation is divided into two chapters as follows. Chapter 1 focuses on modeling of transient deformation associated with the 1995 Colima-Jalisco and the 2003 Tecomán earthquakes, including their coseismic slips, postseismic afterslips, and the viscoelastic rebound triggered by each earthquake. To this end, I present results from time-dependent inversions of GPS daily site position time series from continuous and campaign stations in western Mexico, which include *a priori* calibrations for the postseismic mantle viscoelastic response triggered by both earthquakes determined for a plausible range of Maxwell times for a linear mantle rheology. The coseismic slip solutions estimated for both earthquakes agree well with results from previous seismic and geodetic studies. The afterslip following both earthquakes appears to have coincided with parts of their respective rupture zones and also extended farther downdip below depths of 15 km. The cumulative energy released by the afterslips of both

earthquakes was of the same order or greater than their corresponding coseismic moment releases, indicating that postseismic afterslip relieves significant stress in this segment of the Mexico subduction zone, including the area between the seismogenic zone and the region where deep non-volcanic tremor occurs. The models that best fit rapid postseismic deformation after the 1995 earthquake favor mantle viscosities of 5×10^{18} Pa·s to 2×10^{19} Pa·s (Maxwell times of 4 yr to 15 yr), consistent with upper mantle viscosities that have been estimated for other subduction zones. One important outcome of my time-dependent inversions is a unique estimate of the interseismic velocity field of the region fully calibrated for the viscoelastic, coseismic, and afterslip deformation from the 1995 and 2003 earthquakes. The velocity field is fundamental for estimating locking of the subduction interface and thus the seismic hazard.

In Chapter 2, I invert the interseismic velocity fields derived in Chapter 1 to estimate for locking solutions for the Jalisco-Colima subduction interface. To this end, I tested a variety of maximum subduction locking depths and locations for the Rivera-Cocos-North America triple junction. The best fitting solutions have a maximum locking depth of 40 km and the triple junction located ~50 km northwest of the Manzanillo Trough. Although the solution with the best overall fits in the time-dependent and static modeling parts of my study is associated with a mantle viscosity of 2×10^{19} Pa·s (Maxwell time of 15 yr), I cannot exclude viscosities as high as 5×10^{19} Pa·s. The interseismic locking solutions clearly indicate that most of the Rivera-North America subduction interface is strongly locked, at ~90 percent of the full plate convergence rate. They further show that locking is strong but less uniform where transitional oceanic lithosphere between the Rivera and Cocos plates subducts, and that locking is weak-to-moderate along the Michoacán segment of the Cocos-North America interface. The areas of coseismic slip and afterslip from the 1995 and 2003 earthquakes coincide with areas of moderate-to-strong locking.

One goal of this study was to assess the seismic hazard posed by the ~125-km-long segment of the trench segment northeast of the 1995 earthquake rupture, which has not ruptured since 1932 and is located offshore from heavily populated Puerto Vallarta. This strongly locked trench segment accumulates an annual slip deficit of ~20 mm/yr, sufficient to produce a M~8 earthquake if the elastic strain energy that has accumulated since 1932 were released in a single event.

TABLE OF CONTENTS

CHAPTER 1

Modeling of coseismic and transient deformation associated with the 1995 Colima-Jalisco and 2003 Tecomán thrust earthquakes: Mexico subduction zone

SUMMARY

We invert ~25 years of campaign and continuous Global Positioning System records of daily positions at 62 sites in southwestern Mexico to estimate coseismic and postseismic afterslip solutions for the 1995 M_w = 8.0 Colima-Jalisco and the 2003 M_w = 7.5 Tecomán earthquakes, and the long-term velocity of each GPS site. The time-dependent inversions are corrected for the viscoelastic rebound effects of both earthquakes, which are estimated using a 3-D model consisting of an elastic crust, an elastic subducting slab, and a linear Maxwell viscoelastic mantle. Our preferred model, which optimizes the fit to data from several years of rapid postseismic deformation after the larger 1995 earthquake, has a mantle Maxwell time of 15 years (viscosity of 2×10^{19} Pa·s), although an upper mantle viscosity as low as 5×10^{18} Pa·s cannot be excluded. Our geodetic slip solutions for both earthquakes agree well with previous estimates derived from seismic data or via static coseismic offset modelling. Our afterslip solutions predict that most of the postseismic slip coincided with or was downdip from the rupture areas, with cumulative moments similar to or larger than the coseismic moments. Afterslip thus appears to relieve significant stress along the Rivera plate subduction interface, including the area of the interface between a region of deep non-volcanic tremor and the shallower seismogenic zone. We compare the locations of the seismogenic zone, afterslip and tremor in our study area to those of the neighboring Guerrero and Oaxaca segments of the Mexico subduction zone. Our newly derived

interseismic GPS site velocities, the first for western Mexico that are corrected for the coseismic and postseismic effects of the 1995 and 2003 earthquakes, are essential for estimating the interseismic locking and hence seismic hazard of the subduction interface.

1.1 INTRODUCTION

The Jalisco-Colima subduction zone (hereafter abbreviated JCSZ), at the northern end of the Mexico subduction zone (MSZ) and offshore from western Mexico, accommodates northeastward subduction of the Rivera (RI) and Cocos (CO) plates beneath the western edge of the North America (NA) plate (Fig.1.1). The RI plate subducts beneath NA along a 270-km trench segment northwest of the RI-CO-NA trench-trench-fault triple junction, transitioning from 38±4 mm/yr of nearly perpendicular subduction at 104°W to slower, more oblique subduction to the northwest, reaching 15±3 mm/yr at 20.8°N (DeMets & Wilson 1997). The Cocos plate subducts at 51±2 mm/yr southeast of the tectonically complex zone between the Cuyutlán and Coahuayana submarine canyons offshore from the southern Colima Graben (Fig. 1.1 and Bandy *et al*. 2005). For convenience, we refer to this region as the Manzanillo Trough below.

Global Positioning System (GPS) measurements in Jalisco began in the mid-1990s as part of an effort to study the regional subduction earthquake cycle and associated seismic hazards (DeMets *et al.* 1995; Cabral-Cano *et al.* 2018). The Jalisco-Colima subduction interface has produced multiple large subduction thrust earthquakes in the past century, including $M_s \sim 8.2$ and $M_s \sim 7.8$ earthquakes in 1932 (Singh *et al.* 1985), the 1973 $M_w \sim 7.6$ Colima earthquake (Reyes *et al.* 1979), the 1995 $M_w = 8.0$ Colima-Jalisco earthquake, and the 2003 $M_w = 7.5$ Tecomán earthquake. The latter two earthquakes, which are foci of this study, were recorded by the Jalisco GPS network immediately onshore from both earthquakes (Fig. 1.2).

The June 3 and June 18, 1932 earthquakes ruptured the shallow part of the RI-NA interface in a combined area of ~280 km by ~80 km, as estimated from aftershocks (Singh *et al.* 1985). The June 3 event was the largest earthquake in Mexico during the 20th century (Singh *et al.* 2003). Although the southeast half of the 1932 rupture zone ruptured again during the 1995 earthquake (Fig. 1.2), the northwestern ~120 km of the 1932 rupture zone, which is offshore from major tourist resorts along Jalisco's Gold Coast (Fig. 1.1), has been seismically quiescent since 1932 (Ortiz *et al.* 1998). The January 30, 1973 earthquake ruptured ~90 km of the subduction zone immediately southeast of the Manzanillo Trough and Colima graben, where the Cocos plate subducts (Reyes *et al.* 1979).

The October 9, 1995 Colima-Jalisco earthquake, the first along the JCSZ to be geodetically recorded and modeled (Melbourne *et al.* 1997; Hutton *et al.* 2001), was the first large rupture of the JCSZ segment since 1932. Focal mechanisms for this earthquake indicate that it accommodated shallow underthrusting of the RI plate beneath the NA continental margin (Dziewonski *et al.* 1997; Escobedo *et al.* 1998) (Fig. 1.1). Modeling of its local and teleseismic body waveforms (*e.g.*, Courboulex *et al.* 1997; Escobedo *et al.* 1998; Mendoza & Hartzell 1999) indicate that the ~150 km-long rupture initiated at depths of 15-20 km near the northwest edge of the Manzanillo Trough, propagated northwestward, and consisted of several subevents (Fig. 1.2). Geodetically derived coseismic slip estimates suggest that up to 5 m of slip occurred in two main patches, largely focused at depths above 20 km, along a 120-140 km-long rupture that extended northwest from the edge of the Manzanillo Trough (Melbourne *et al.* 1997; Hutton, *et al.* 2001; Schmitt *et al.* 2007), in agreement with the seismic estimates referenced above. The earthquake triggered transient fault afterslip mostly downdip from the coseismic rupture zone, which by 1999 had accumulated an equivalent seismic moment of ~70% of the coseismic moment release (Hutton *et*

al. 2001). Masterlark *et al.* (2001) and Márquez-Azúa *et al.* (2002) show that a combination of fault afterslip and viscoelastic rebound are needed to account for the observed transient postseismic deformation.

The most recent large earthquake along the JCSZ was the January 22, 2003 Tecomán earthquake, which accommodated shallow underthrusting of the offshore oceanic lithosphere beneath the continental margin (Fig. 1.1, Ekström *et al.* 2004; Yagi *et al.* 2004). Modeling of waveforms from local and teleseismic body wave data suggest that this rupture initiated at a depth of ~20 km and propagated up and down-dip (Yagi *et al.* 2004) (Fig. 1.2). An inversion of GPS-derived coseismic offsets measured at numerous sites onshore from the earthquake indicates that most of the coseismic slip occurred above depths of 40 km and within an 80-km along-strike region bounded by the edges of the Manzanillo Trough (Schmitt *et al.* 2007), in agreement with the seismic results. At least 95% of the postseismic deformation recorded with GPS was aseismic based on the small cumulative moment of aftershocks (Schmitt *et al.* 2007). A reversal in the vertical movement of a GPS site directly onshore from the rupture indicates that afterslip propagated down-dip to areas of the subduction interface beneath the coastline within days following the earthquake, similar to the postseismic behavior of the 1995 earthquake (Schmitt *et al.* 2007).

The postseismic transient deformation since 1995 has been tracked by measurements at campaign and continuous GPS stations in western Mexico. As an example, continuous GPS measurements at site COLI onshore from the 1995 and 2003 earthquakes (inset map in Fig. 1.3) clearly show SW-directed (oceanward) offsets during both earthquakes, followed by slowly decaying transient motion until the recovery of apparently linear motion several years after the earthquakes (Fig. 1.3). The observed transient postseismic motion is a superposition of the effects

of three distinct processes: steady interseismic shortening due to fault relocking at the subduction interface, fault afterslip downdip and possibly along the seismogenic zone, and postseismic viscoelastic mantle flow (Márquez-Azúa *et al.* 2002; Wang *et al.* 2012; Bedford *et al.* 2016). The latter two processes decay with different characteristic timescales after the earthquakes. At present, the motions at sites in western Mexico are a superposition of steady interseismic strain accumulation due to frictional locking of the Mexico subduction interface and transient surface deformations from postseismic afterslip and viscoelastic rebound triggered by the 1995 and 2003 earthquakes.

In this first part of a two-part study, we estimate geodetic coseismic slip and post-seismic afterslip solutions for the 1995 Colima-Jalisco and 2003 Tecomán earthquakes via time-dependent modelling of 1993-to-2020 GPS daily station positions from the state of Jalisco and neighboring states, including calibrations for the viscoelastic rebound triggered by these events. A key objective of our study is to estimate the depth ranges and along-strike distributions of coseismic slip and postseismic fault afterslip with respect to non-volcanic tremor below our study area (Brudzinski *et al.* 2016), toward a better understanding of the range of fault slip phenomena that accommodate the long-term plate convergence along the JCSZ and the depths where they occur on the subduction interface. We also estimate the long-term velocities of all the GPS sites fully corrected for the coseismic and postseismic effects of the 1995 and 2003 earthquakes. In the second part of our study we invert the new velocities to estimate interseismic locking along the JCSZ and hence its seismic hazard.

1.2 GPS DATA

We compiled all available GPS data from western Mexico, consisting of daily observations from 36 continuous and 26 campaign GPS sites. The geodetic data used herein span ~25 years, much longer than for any previous study (*e.g.* Melbourne *et al.* 1997; 2002; Hutton *et al.* 2001; Márquez-Azúa *et al.* 2002; Schmitt *et al.* 2007; Selvans *et al.* 2011). The earliest data, which are from continuous sites COLI and INEG (Fig. S1.1), are from early 1993. Fig. 1.2 and Table S1 and Fig. S1.1 contain details about the spatial and temporal coverage of our data set. Highlights of the data include the following:

- Of the fifteen GPS sites with observations before the October 1995 earthquake, two sites (COLI near the coast and INEG farther inland) are continuous and were installed in 1993, and the remaining 13 sites, all campaign stations, were first occupied in March of 1995.
- Thirty-one sites were operational during the January 2003 earthquake, of which six were continuous and two began as campaign stations and were converted to continuous operation after the 2003 earthquake (PURI and COOB).
- Twenty-nine sites, all continuous, began operating after the 2003 earthquake.

Five continuous stations, namely TNCM, TNLC, TNM2, MNZO, and TNMR, were installed at the same locations of earlier discontinued stations: CHMC, GUFI, UCOL, MANZ, and MMIG, respectively.

1.3 DATA ANALYSIS

We analyzed all of the GPS code-phase data with releases 6.3 and 6.4 of the GIPSY software suite from the Jet Propulsion Laboratory. No-net-rotation daily GPS station coordinates

were estimated using the precise point-positioning strategy described by Zumberge *et al.* (1997). Our processing methodology includes constraints on *a priori* tropospheric hydrostatic and wet delays from Vienna Mapping Function parameters (http://ggosatm.hg.tuwien.ac.at), elevation dependent and azimuthally dependent GPS and satellite antenna phase center corrections from IGS08 ANTEX files (available via ftp from sideshow.jpl.nasa.gov), and FES2004 corrections for ocean tidal loading (http://holt.oso.chalmers.se). Phase ambiguities were resolved using GIPSY's single-station ambiguity-resolution feature (Bertiger *et al.* 2010). Daily no-net rotation station location estimates were transformed to IGS14, which conforms to ITRF2014 (Altamimi *et al.* 2016), using daily seven-parameter Helmert transformations from the Jet Propulsion Lab. We estimated daily correlated noise between stations from the coordinate time series of linearly moving continuous stations outside the study area (Márquez-Azúa & DeMets 2003). Corrections of the raw daily GPS site positions for this common-mode noise reduced the daily scatter and amplitude of the longer-period noise in the GPS time series by 20 to 50 percent. All GPS coordinate time series were also corrected for equipment-related offsets and other discontinuities not related to earthquakes. Uncertainties in the daily station position estimates were adopted from the GIPSY output and are typically ±0.6 mm in longitude, ±0.5 mm in latitude, and ±2.5 mm in elevation.

Prior to any modeling, we transformed each GPS position time series from the ITRF14/IGS14 frame of reference to a frame of reference tied to the NA plate, the natural geological frame of reference for this study. To do so, we used the pole located at 7.45ºN, 92.04ºE with angular rate 0.183×10^{-6} degree/yr that best fits the ITRF14 daily position time series for ~1000 GPS sites from the North America plate interior. The formal uncertainties in the NA-IGS14 angular velocity vector propagate into 1-σ uncertainties of only 0.03 mm/yr in the north and east components of the velocity for the North America plate relative to IGS14 at the center of our study

area. For comparison, the likely 1-σ uncertainties in the other velocities used for our analysis are at least ±1 mm/yr, a factor-of-30 larger than the reference frame uncertainties. For this reason, the North America plate reference frame uncertainties are too small to affect any of the results or interpretations that follow.

1.3.1 1993 to 2020 GPS site position time series

Our GPS position time series clearly show the widespread influence of the 1995 and 2003 earthquakes in our study region. Fig. 1.4, which shows the horizontal site motions between the 1995 M_w = 8.0 Colima-Jalisco and 2003 M_w = 7.5 Tecomán earthquakes, reveals that between 1995 and mid-1998 all but two sites moved southwestward toward the 1995 earthquake rupture zone at rates that decreased with time, confirming the pattern previously described by Hutton *et al.* (2001). The postseismic site displacements decrease in magnitude with distance from the rupture, from a maximum of ~200 mm at site PURI ~30 km inland from the rupture to a minimum of ~50 mm at site MCAB ~250 km inland from the earthquake. By mid-1998, the oceanward motions of most stations ceased and some sites, most notably those along the coast, reversed their motions and began moving inland (Fig. 1.4). Hutton *et al.* (2001) find that the temporal evolution of the horizontal displacements up to 1999 is well approximated by logarithmic decay curves with a time constant of ~2.4-3.7 days, consistent with afterslip on the subduction interface. In contrast, Márquez-Azúa *et al.* (2002) show that the observed station motions are better explained via a superposition of linear elastic shortening from locking of the shallow subduction interface, logarithmically-decaying fault afterslip, and postseismic viscoelastic flow. A model of the deformation triggered by the 1995 earthquake that allows for viscoelastic flow but ignores fault afterslip misfits the first few years of deformation at the campaign sites in the Jalisco region

and also misfits the trench-parallel component of the postseismic motion at the continuous site COLI (Sun *et al.* 2018).

Fig. 1.5 shows changes in the GPS site elevations through March of 1999, which were previously described by Hutton *et al.* (2001). Within a few months of the earthquake, the elevations of nearly all the coastal sites and a few inland sites (*i.e.* AUTA, AYUT, and GUFI) increased, whereas most inland sites subsided. The postseismic uplift rates decreased with time at all three sites nearest to the rupture zone (*i.e.* CHAM, CRIP and MELA), with uplift ceasing completely at these sites at varying times between 1999 and 2001. The complex space-time pattern of postseismic uplift likely reflects the time-varying contributions of postseismic afterslip and viscoelastic flow superimposed on steady interseismic elastic shortening due to the locked subduction interface (Márquez-Azúa *et al.* 2002).

Figs. 1.6 and 1.7 display the continuous and campaign GPS horizontal and vertical position changes after the M_w = 7.5 January 22, 2003 Tecomán earthquake. The postseismic effects of this earthquake are weaker than those of the M_w = 8.0 1995 earthquake, with maximum postseismic displacements of a few tens of millimeters, ~25% of those after the 1995 earthquake (Figs 1.4 and 1.5). Continuous observations at station COLI directly onshore from the 2003 rupture (Figs 1.3, 1.6, and 1.7) clearly show that rapid postseismic deformation concluded by mid-2003 and by 2005 the station transitioned back to northeast-directed motion. Continuous measurements at nearby sites COOB, MANZ, and UCOL (Fig. 1.6a) corroborate the short duration of the rapid postseismic deformation. The early postseismic response was complex, with numerous campaign sites near and inland from the rupture moving toward the rupture zone during the first year after the earthquake (Fig. 1.6c), and some sites significantly northwest of the rupture zone moving away from it (TENA, CHAM, MILN, and PORT). The vertical site motions during the months after the

earthquake reveal a similarly complex pattern, with uplift at coastal sites near the rupture transitioning to subsidence at sites farther inland (Fig. 1.7). By 2-2.5 years after the earthquake, the sense of vertical motion at most sites reversed, likely due to the superposition of time-varying vertical effects of fault afterslip and viscoelastic rebound on steady interseismic uplift and/or subsidence at each site.

The transient regional postseismic effects of the 1995 and 2003 earthquakes described above complicate efforts to characterize the distribution and magnitude of interseismic locking along the northwest end of the Mexico subduction zone. Estimating the locking solely from GPS timeseries that predate the October 10, 1995 earthquake is not possible because such observations are limited to 1993-1995 data from continuous sites COLI and INEG (Fig. S1.1). Here, we invert ~25 years of data to separate the long-term steady interseismic motion of each site from the transient deformation components.

1.4 METHODS: TIME-DEPENDENT MODELING

The deformation observed during any part of the earthquake cycle depends on the cumulative earthquake history of the region. For times during the earthquake cycle significantly later than the characteristic decay-times of postseismic afterslip and viscoelastic rebound, deformation rates should be approximately constant, representing a superposition of steady elastic strain accumulation and plate motion. At other times, the deformation will also include transient deformation triggered by large earthquakes, including fault afterslip and viscoelastic rebound. Fault afterslip is typically assumed to be restricted to the brittle upper crust and involves short-term, continued slip around the region of coseismic rupture. Viscoelastic rebound is the surficial response to the long-term viscous relaxation of the ductile media below the seismogenic

zone (lower crust and mantle) (Pollitz *et al.* 1998; Wang 2007). Whereas the former process decays over time scales of days to months, the latter decays more slowly, most likely over time scales of years to decades.

Estimating the degree of interseismic coupling via modeling of GPS position time series requires isolating the steady interseismic elastic strain from instantaneous offsets due to earthquakes and any transient deformation due to fault afterslip and/or viscoelastic rebound. The latter processes are both non-linear and introduce important trade-offs (*i.e.* correlations) between their adjustable parameters (*e.g.*, mantle viscosity, mantle-crust interface depth, and afterslip decay time). Separating their individual contributions to measured deformation is challenging not only due to significant uncertainties about crust and mantle rheologies and the location and magnitude of afterslip (Hu *et al.* 2004; Suito and Freymueller 2009; Hu &Wang 2012; Kogan *et al.* 2013; Sun & Wang 2015; Freed *et al.* 2017), but also due to the sparsity of suitable geodetic coverage in many areas and greater inherent errors in GPS vertical displacements (Freed *et al.* 2017). Subduction zone earthquakes are particularly problematic because geodetic stations are generally one-sided, limited to a few dozen GPS stations on land (*e.g.* Lin *et al.* 2013; Sun *et al.* 2014; Wiseman *et al.* 2015, Freed *et al.* 2017). Extracting unique information about these processes from position GPS time series is thus a complex, time-dependent modeling problem.

We use a two-stage process to estimate possible solutions for the interseismic, coseismic, and postseismic processes that dominate deformation in our study area. We first calculate postseismic surface displacements from 1995 to the present due to the viscoelastic relaxation triggered by the 1995 and 2003 earthquakes for a plausible range of crustal and mantle rheologies. We then subtract the modeled viscoelastic deformation from our GPS position time series and invert the corrected daily site displacements to estimate the postseismic afterslip for each

earthquake and the interseismic site velocities. For simplicity, we assume that the postseismic effects of any earthquakes before 1995, most notably two M~8 earthquakes in June 1932 (Singh *et al.* 1985), are negligible. This assumption is further justified by the results of our modeling of the viscoelastic relaxation from the M_w=8 1995 earthquake (Section 1.5.2). Sites like CHAM and PURI, for which the model predicts large displacements associated with viscoelastic effects, predict slip rates slower than 2 mm/yr in all components for end-member mantle viscosities after 25 years of relaxation, less than half the time between the 1932 and 1995 earthquakes.

We estimate the coseismic slip solution for the 1995 earthquake, which is the basis for estimating the viscoelastic relaxation for that earthquake, from an inversion of all data before the 1995 earthquake and ~3 years of post-earthquake observations, during which any viscoelastic response is small in relation to the postseismic afterslip. Unlike the 1995 coseismic slip solution, the estimate of the 2003 earthquake slip solution from our time-dependent inversion depends on the magnitude and pattern of viscoelastic rebound that we estimate for the 1995 earthquake, and the magnitude and pattern of the 1995 earthquake fault afterslip. Our estimate of the 2003 coseismic slip solution thus entails an exploration of its sensitivity to a range of assumed crustal/mantle rheologies and 1995 fault afterslip solutions.

The coseismic and postseismic slip solutions presented below are limited to our final time-dependent inversion of the full suite of GPS position time series available for our work, suitably corrected for the viscoelastic effects of the 1995 Colima-Jalisco and 2003 Tecomán earthquakes. Results from key intermediate stages of our analysis are presented in a supplementary document, including the sensitivities of our preferred solution to the assumptions that are implicit in our analysis.

1.4.1 Forward modeling of the viscoelastic relaxation

We use RELAX 1.0.7 (Barbot & Fialko 2010a; 2010b; Barbot 2014), published under the GPL3 license, to simulate the coseismic stress changes imparted to the surrounding medium by coseismic slip and the spatiotemporal evolution of surface deformation resulting from the relaxation of linear viscoelastic rheologies underlying an elastic upper crust. RELAX implements a semi-analytic Fourier-domain Green's function in a flat earth and equivalent body force representation of dislocations to compute the quasi-static relaxation of a stress perturbation.

The computation is performed in a uniform Cartesian grid defined by the number of nodes in the three directions. The 2.5-km node spacing in our 512×512×256 element 3-D computational grid (Fig. 1.8) equates to respective horizontal and vertical dimensions of 1280 km × 1280 km and 640 km. Coseismic slip in our model is limited to a collection of slip patches that discretize the fault geometry. Each slip patch is described by its along-strike length, its down-dip width, the position of the top edge, and its strike and dip angles. The dimensions of the along-strike and down-dip slip patches average ~3.5 km (range of 1.7 to 5.2 km) and ~2.4 km (range of 1.1 to 4.8 km), respectively. The slip solutions used to drive the viscoelastic relaxation from the 1995 and 2003 earthquakes were estimated with TDEFNODE (Section 1.3.2). To avoid short-wavelength oscillations near stress concentrations, the coseismic slip solution is smoothed near the fault tip.

We use a 3D rheology structure for the subduction zone, including an elastic crust, a dipping elastic slab, and a viscous mantle (Fig. 1.8). We imposed a shear modulus μ = 40 GPa and a Poisson's ratio υ = 0.25 for the whole domain. Seismicity in the JCSZ concentrates in the continental crust at depths of ~15-35 km (Watkins *et al.* 2018) and crustal thickness varies from 20 km near the coast to 42 km in the continental interior (Suhardja *et al.* 2015). We thus fixed the

thickness of the elastic crust at 35 km. We use the same slab geometry for our subsequent elastic model estimates (Section 1.3.2). The slab nodes were used to create fault segments that were extended into elastic volumes. We matched the slab thickness to that of the elastic crust and assigned a linear viscosity to the mantle, varying the Maxwell time τ_m from 2.5 to 40 yr (viscosities from ~3×10^{18} Pa·s to ~5×10^{19} Pa·s, assuming a shear modulus of 40 GPa). The range of Maxwell times we tested is comparable to the 1-50 year Maxwell times (equivalent to mantle viscosities of order 10^{18}-10^{19} Pa·s) that were used by Suito & Freymueller (2009) to model 30 years of postseismic deformation in Alaska. Our Maxwell times range also include the 8-15 yr mantle relaxation time limits that Johnson & Tebo (2018) identified by modeling fifty years of vertical postseismic deformation in Nankai with a linear Maxwell viscoelastic mantle and afterslip model. Bi-viscous Burger rheologies are not supported by RELAX; we thus only tested linear Maxwell rheologies, similar to Johnson & Tebo (2018). Although we did not test power-law rheologies, which have been used to successfully describe postseismic deformation in other subduction settings (Freed et al. 2006; Peña et al. 2019), results described later in our analysis suggest it might be a useful future approach.

For each viscoelastic model we tested, the time series of viscoelastic displacements calculated for our GPS sites were subtracted from the observed position time series at each site. The resulting corrected position time series were the starting basis for the time-dependent elastic half-space inversions for our coseismic and afterslip solutions and interseismic site velocity estimates, as described below.

1.4.2 Inverse modeling with TDEFNODE

TDEFNODE calculates static and time-dependent elastic deformation using the Okada (1985, 1992) elastic half-space dislocation algorithm. It inverts campaign and continuous GPS position time series and other geodetic, seismologic, and plate kinematic data to estimate simultaneously the long-term linear (steady) motions of sites and short-term transients such as coseismic slip, afterslip, and slow slip events (McCaffrey 2009). In TDEFNODE, the temporal and spatial distributions of slip on a fault during an event are described by

$$s(x, w, t) = AX(x)W(w)S(t) \tag{1.1}$$

where s is the slip on the fault as a function of time t, and position along-strike x and downdip w, A is the amplitude, $X(x)$ and $W(w)$ are the along-strike and downdip spatial functions, and $S(t)$ is the temporal function (McCaffrey 2009).

In this study, coseismic slip locations and amplitudes, afterslip locations, amplitudes, and decay rates, and linear station velocities are estimated. GPS station displacements are modelled in TDEFNODE as

$$d_{ij}(t) = x_{ij}^0 + V_{ij}(t) + H_{t_{\mathrm{eq}}}(t)\left(A_{ij}^{\mathrm{co}} + A_{ij}^{\mathrm{as}} \log_{10}\left(1 + \frac{t - t_{\mathrm{eq}}}{\tau_{\mathrm{c}}}\right)\right) \tag{1.2}$$

where i denotes the i-th component (east, north, and up) of site j, x_{ij}^0 is the initial position, V_{ij} is the steady (interseismic) velocity, A_{ij}^{co} and A_{ij}^{as} are amplitudes related to a site's elastic response to earthquake coseismic slip and afterslip, respectively, $H_{t_{\mathrm{eq}}}$ is the Heaviside function centered at the time of the earthquake t_{eq}, and τ_{c} is the logarithmic relaxation time for the afterslip.

By definition, the time-dependent fitting function described above introduces numerous fitting tradeoffs between the coseismic and afterslip solutions for the 1995 and 2003 earthquakes

studied herein and the interseismic GPS site velocities V_{ij}. More tradeoffs are introduced via the *a priori* corrections we make to every GPS position time series for the viscoelastic effects of both earthquakes, which we explore via viscoelastic models that span mantle Maxwell times τ_m of 2.5 to 40 yr (equivalent to viscosities η of 3.16×10^{18} to 5.05×10^{19} Pa·s for $\mu = 40$ GPa).

Faults are defined in the TDEFNODE elastic half-space by sets of nodes that are placed along depth contours and approximate the fault trace and dip, forming an irregular grid on the fault surface. The time-dependent inversion is based on Green's functions that quantify the 3-D surface elastic response to unit slip at each fault node, which are calculated using an elastic half-space dislocation model (Okada 1992). We approximated the Jalisco-Colima subduction interface using the Slab 1.0 geometry of Hayes *et al.* (2012) and extended the contours to the northwest based on results from local earthquake tomography (Watkins *et al.* 2018) and magnetotelluric imaging (Corbo-Camargo *et al.* 2013). Fault node spacings are ~5-25 km along-strike (~20 km on average) and ~5-25 km down-dip (~10 km on average), located at 5-km depth contours.

In our inversion, slip values for the JCSZ were estimated at each fault node while applying spread smoothing, which penalizes large slip at distances progressively farther from the slip centroid and avoids implausible node-to-node variations in slip values. The misfit F is defined in TDEFNODE as the sum of the reduced chi-squared statistic (χ^2_ν), which is the weighted least-squares misfit normalized by the degrees of freedom, and the penalties associated with smoothing McCaffrey (2005):

$$F = \chi^2_\nu + \text{penalties} = \frac{1}{\nu}\sum_{\mathrm{N}} \frac{r^2}{\sigma^2} + A_1 \sum_x s^2 dx^2 + A_2 \sum_w s^2 dw^2 \qquad (1.3)$$

where ν represents the degrees of freedom (number of observations N minus number of parameters); r are the residuals (observed value minus modeled value); σ are the data uncertainties; x and w denote, respectively, the fault nodes positions in the along-strike and down-dip directions; A_1 and A_2 are the smoothing factors that scale the penalties in each direction, s is the slip; and dx and dw are, respectively, the along-strike and down-dip distances from the slip centroid to the node location. The misfit function F is minimized through simulated annealing and grid search iterations. A measure of the goodness of fit of our solutions is the weighted root-mean-square (McCaffrey 2005):

$$\text{wrms} = \left[\left(\sum_N \frac{r^2}{\sigma^2}\right) / \left(\sum_N \frac{1}{\sigma^2}\right)\right]^{1/2} \tag{1.4}$$

where N is the number of observations, r are the residuals, and σ are the data uncertainties. It has units of mm and measures the weighted scatter in the fits.

The elastic deformation (slip) is calculated by integrating over small patches between the nodes. The segments joining two neighboring nodes are subdivided into five sub-segments, so that each quadrilateral generated by adjacent nodes along-strike and down dip is subdivided into 25 constant-slip patches. In the case of coseismic slip estimations, we adapted this collection of slip patches as input for our forward modeling of the viscoelastic response (Section 1.3.1).

1.5 RESULTS

Outputs of the TDEFNODE inversion described in Section 1.3 that are relevant to our analysis include coseismic slip solutions for the 1995 and 2003 earthquakes, afterslip solutions and logarithmic afterslip decay constants for both earthquakes, and interseismic velocities for all

of the GPS sites included in our data set. Descriptions of the preferred coseismic and afterslip solutions and viscoelastic effects for both earthquakes are found in Sections 1.5.1 to 1.5.5. The interseismic GPS site velocities, which are described and modeled in detail in Chapter 2, are summarized briefly in Section 1.4.6. For completeness, we also inverted the GPS position time series described in Section 1.2 assuming that the viscoelastic effects for the 1995 and 2005 earthquakes were negligible and that fault afterslip was instead the source of all the observed transient postseismic deformation. The results from this latter inversion are summarized entirely within the Supporting Information. Other information applicable to our modeling analysis is also found in the Supporting Information text, figures, and tables.

1.5.1 Coseismic slip solution for the 1995 Colima-Jalisco earthquake

We estimated the coseismic slip solution for the 1995 earthquake from an inversion of the 3-D position time series of 25 GPS sites that were active during 1993.28 to 1999.00. Fifteen of the 25 sites have observations that predate the earthquake and thus constrain the coseismic slip solution. Data from the other 10 sites help constrain the postseismic afterslip. Since the data from this time interval were dominated by campaign measurements, observations up to ~3 years after the earthquake were inverted in order to ensure that sufficient data were available at each site to constrain the transient deformation at the site.

Our preferred time-dependent model for 1993.28 to 1999.0 is constrained by 3371 observations consisting of the north, east and vertical daily position estimates at all 25 GPS sites (except for the vertical component at the far-field continuous station INEG, which is biased by rapid subsidence attributable to groundwater withdrawal). The TDEFNODE model is described by 563 adjustable parameters, which consist of the amplitudes and directions of coseismic slip at

the fault nodes for the 1995 earthquake, the amplitudes and directions of afterslip on the subduction interface, the afterslip decay constant, and the 3-D interseismic velocities for the 25 GPS sites.

The best-fitting coseismic slip solution (Fig. 1.9a) agrees well with previous seismic estimates (*e.g.* Courboulex *et al.* 1997; Escobedo *et al.* 1998; Mendoza & Hartzell 1999). Most of the seismic energy (74%) was released at depths of 5 to 20 km, consistent with seismic constraints. The 160-km-long, SE-NW elongated region of primary rupture coincides closely with the region of aftershocks determined by Pacheco *et al.* (1997) (delineated by the blue line in Fig. 1.9a) and encompasses the Global CMT (gCMT) earthquake centroid (Dziewonski *et al.* 1997), the United States Geological Survey (USGS) estimated epicenter, and the epicenter estimated from local data by Courbolex *et al.* (1997). Our estimated geodetic coseismic moment of 9.71×10^{20} N·m, corresponding to $M_w = 7.92$ for a 40 GPa shear modulus, is close to seismologic estimates of M_o=1.15×10^{21} N·m (Dziewonski *et al.* 1997) and 8.3×10^{20} N·m (Mendoza & Hartzell 1999). Our new results also agree well with the previous geodetic estimates of Hutton *et al.* (2001) and Schmitt *et al.* (2007). For example, the seismic potency estimated in the latter study, $P_0 = 2.5 \times 10^{10}$ m^3, where the potency P_0 is defined as the estimated seismic moment normalized by the shear modulus (Ben-Menahmen & Singh 1981), differs by only 3 percent from $P_0 = 2.43 \times 10^{10}$ m^3 for this study.

Fig. 1.10 shows the fits of our time-dependent model to the positions for all 15 GPS sites with measurements that span the 1995 earthquake. The wrms misfits are 3.1 to 9.5 mm in the horizontal position components at continuous sites COLI and INEG and average 3.3 mm at the 23 campaign GPS sites. The wrms misfits to the noisier vertical daily positions are 11.2 mm at site COLI and average 18.6 mm at the 23 campaign sites. The misfit F (Eq. 1.3) for our best model is

13.4, much larger than the expected value of unity for a well-parameterized model that fits data with correctly determined uncertainties. We interpret this result as evidence that the input daily site position uncertainties, which are typically ±0.7-0.9 mm in the horizontal and ±4 mm in the vertical components, are undervalued. Several factors that may contribute to the undervalued uncertainties include neglecting likely correlations between the daily position components, our approximation of the subduction interface geometry, our simplistic homogeneous elastic half-space assumption, and the elastic properties we assumed for our model (Fig. 1.8).

The horizontal coseismic displacements estimated by TDEFNODE point southwestwards towards the rupture zone and decrease in magnitude with distance from the rupture zone (blue arrows in Fig. 1.9c). Coseismic subsidence is predicted at most sites, decreasing with distance from the large slip zones and transitioning to minor uplift at distances more than 170 km inland from the coast (blue arrows in Fig. 1.9d). The estimated 3-D coseismic offsets, which are tabulated in Table S2, are generally consistent with those derived by Hutton *et al.* (2001) (Fig. S1.2).

For our inversions, we explored variations of the fault-slip smoothing factors and of the length of the time spanned by the postseismic data. We also tested limiting the observations solely to stations with data from both before and after the 1995 earthquake. The results from these numerous inversions indicate that our 1995 coseismic slip solution is robust with respect to all mentioned variations. For example, the estimated coseismic moments and slip amplitudes for models derived from inversions of as little as 2 years of postseismic data differ by only 0.1-2.3% from those for the preferred model and by only 1.8-5.2% for models derived from inversions of all the data gathered between the 1995 and 2003 earthquakes. Inverting the position time series for only those sites with data from before and after the 1995 earthquake changes the estimated coseismic moment and slip amplitude by 1.3% and 2.4%, respectively. Our preferred slip solution

for the 1995 Colima-Jalisco earthquake, which forms the foundation of much of the subsequent analysis, thus appears to be robust.

1.5.2 Viscoelastic deformation from the 1995 Colima-Jalisco earthquake

We modeled the surface displacements produced by the viscoelastic response to the 1995 Colima-Jalisco earthquake using our preferred coseismic slip solution (Fig. 1.9a) and assumed mantle Maxwell times τ_m of 2.5, 4, 8, 15, 25, and 40 yr (equivalent to viscosities η of 3.16×10^{18}, 5.05×10^{18}, 1.01×10^{19}, 1.89×10^{19}, 3.16×10^{19}, 5.05×10^{19} Pa·s for a shear modulus of 40 GPa) for the 3D viscoelastic model described in Section 1.3.1. By 2020, 25 years after the 1995 earthquake, the predicted cumulative viscoelastic relaxation on land includes subsidence along the coast that diminishes with distance from the rupture and turns from subsidence to uplift farther inland (Fig. 1.11). Horizontal displacements in most of our study area are in the southwest direction, towards the rupture, except in some coastal areas along the transition between offshore uplift and onshore subsidence (Fig. 1.11). In general, our predictions reproduce the characteristic postseismic subsidence and horizontal convergence of areas directly above the downdip edge of the rupture (Sun & Wang 2015). At a given location, the magnitudes of the displacements predicted by models that assume values for τ_m of 2.5, 15, and 40 yr vary by factors of 2 to 5 (Fig. 1.12), increasing for models with shorter τ_m (*i.e.* lower viscosities). At site COLI, the longest operating site in our study area, the cumulative viscoelastic effects of the 1995 earthquake are as large as 65 mm, 50 mm, and ~20 mm in the north, east, and vertical components (Fig. 1.13).

We evaluated the robustness of the viscoelastic predictions to plausible variations in the 1995 coseismic slip solutions as follows. For each of the six Maxwell times we tested, we used RELAX to calculate synthetic displacements at our GPS sites for the range of coseismic slip

solutions we derived using postseismic time series that span as little as ~2 years to as long as ~7 years after the earthquake (end of Section 1.4.1). For models with the largest assumed Maxwell time (τ_m = 40 yr), the differences in the magnitudes of the cumulative viscoelastic deformation 25 years after the earthquake predicted by the different coseismic slip solutions were smaller than 25 mm or equivalently 1 mm/yr. For models with the shortest assumed Maxwell time (τ_m = 2.5 yr), the 3-D viscoelastic displacements predicted at nearly all the sites differed by less than 25 mm (1 mm/yr), with only one site exhibiting a difference as large as 1.5 mm/yr. The sites with the largest differences are located along the coast close to the rupture area, where the predicted viscoelastic deformation is sensitive to small variations in the estimated coseismic slip. Our results indicate that uncertainties in the 1995 coseismic slip solution and differences in the Maxwell times we use for our modeling are unlikely to cause systematic biases that are larger than 1 mm/yr in the long-term interseismic site velocities. Biases this small are unlikely to affect any of the results and interpretations related to our modeling of interseismic fault locking.

1.5.3 Coseismic slip solutions for the 2003 Tecomán earthquake

We estimated a coseismic slip solution for the 2003 Tecomán subduction earthquake for each of all six viscoelastic models that are described in the previous section. For each model, we first subtracted the predicted location- and time-dependent viscoelastic movement at each GPS site from the observed daily GPS station positions $d_{ij}(t)$ in Equation (1.2). We then inverted the corrected GPS position time series via TDEFNODE while fixing the 1995 coseismic slip solution to the same preferred estimate as was used to drive the viscoelastic model (Fig. 1.9a).

We evaluated the sensitivity of the 2003 coseismic slip solutions to the length of the postseismic interval spanned by our data, ranging from as little as ~0.5 years to as long as ~4.5

years after the 2003 Tecomán earthquake for each of the six corrected data sets. Fig. S1.14 illustrates best-fitting 2003 coseismic slip solutions from inversions that include 0.5 to 4.5 years of post-earthquake data and shows that the slip location and amplitudes (and earthquake moments) are relatively robust if 2.5 years or more of postseismic data are used to jointly constrain both the coseismic offsets and transient afterslip (the lower four panels in Fig. 1.14 are derived using 2.5 years or more of observations after the January 22, 2003 earthquake). We estimate a preferred slip solution for the 2003 earthquake from GPS data that includes ~2.5 years of postseismic data, the minimum necessary, in order to minimize unavoidable tradeoffs between the relative contributions of fault afterslip and mantle viscoelastic flow to the postseismic deformation.

The six preferred time-dependent models for 1993.28 to 2005.50, each corresponding to one of the mantle rheologies assumed for our viscoelastic models, are constrained by 22,206 observations, consisting of the north, east, and vertical daily position estimates at 35 GPS sites (with the exception of station INEG, see Section 1.1.4.1), including 30 with observations before and after the 2003 earthquake. The models are described by 944 adjustable parameters, namely the amplitudes and directions of coseismic slip at the fault nodes for the 2003 earthquake, the amplitudes and directions of the afterslip of the 1995 and 2003 earthquakes on the subduction interface, separate afterslip decay constants for the two earthquakes, and the 3-D interseismic velocities for the 34 GPS sites. Results for all six of the 2003 Tecomán earthquake coseismic solutions, one for each of the six viscoelastic models we explored, are displayed and tabulated in Figure S1.5 and Tables S1.3 and S1.4. The coseismic slip for all six solutions is concentrated in the Manzanillo Trough and the earthquake moments vary by less than 7.6 percent relative to an average M_o of $1.98 \pm 0.07 \times 10^{20}$ N·m for all six models (Table S1.4), corresponding to M_w = 7.4-7.5. The most important aspects of the slip solution, namely the slip location and earthquake

moment, are thus robust with respect to the range of mantle Maxwell times we explored. Below, we describe in more detail our results for the slip solution for a mantle with τ_m = 15 yr (corresponding to a mantle viscosity of 1.89×10^{19} Pa·s).

Coseismic slip during the 2003 earthquake was largely confined to the Manzanillo Trough (Fig. 1.14a), with more than 97% of the seismic energy released at depths of 10 to 40 km. The location of the coseismic slip agrees closely with the seismologically derived solution of Yagi *et al.* (2004) (shown by the red lines in Fig. 1.14a) and also agrees with the seismologic slip solution of Quintanar *et al.* (2010) and GPS-derived solution of Schmitt *et al.* (2007). The rupture encompasses the Global CMT (gCMT) earthquake centroid (Ekström *et al.* 2004), and epicenters estimated by Yagi *et al.* (2004) and the United States Geological Survey (USGS) (stars in Fig. 1.14a). Our geodetically derived coseismic moment, 1.84×10^{20} N·m (M_w = 7.4), is close to seismologic estimates of $M_o = 2.0 \times 10^{20}$ N·m (Ekström *et al.* 2004), 2.3×10^{20} N·m (Yagi *et al.* 2004), and 1.88×10^{20} N·m (Quintanar *et al.* 2010). This result also agrees with the geodetic estimate of Schmitt *et al.* (2007), who estimate a seismic potency of 5.1×10^9 m^3, which is only ten percent different from the potency found in this study (4.60×10^9 m^3). The potency of the Yagi *et al.* (2004) seismic solution, 4.7×10^9 m^3 (Schmitt *et al.* 2007), differs by only two percent from our estimate.

The fits of the time-dependent model with τ_m = 15 yr are good overall (Fig. 1.15), with wrms misfits of 1.6-2.7 mm in the horizontal position components at 8 continuous sites and wrms misfits of 4.0-4.5 mm at the 27 campaign GPS sites. The wrms misfits to the noisier vertical daily positions are 8.6 mm at 7 continuous sites and 10.7 mm at the 27 campaign sites. Misfit *F* for this model is 11.9, similar to that of the 1995 earthquake (*F* = 13.4). As for the 1995 earthquake, we

interpret the larger than expected weighted misfit as evidence that the data uncertainties are undervalued and that one or more of our modeling assumptions is overly simplistic.

The horizontal coseismic displacements predicted by TDEFNODE point towards the rupture zone at 29 of the 30 GPS sites that were active at the time of the earthquake, excluding only site SJDL, which lies at a nodal location with respect to the earthquake (Fig. 1.14c and Table S4). Coseismic subsidence is predicted at most sites (Fig. 1.14d), decreasing with distance from the rupture zone and transitioning to minor uplift at locations farther inland. Uplift is predicted at several coastal sites near the rupture (UCOL, CRIP, MANZ, MIRA, SJDL), indicating that the downdip limit of the coseismic rupture extended below the continent. The estimated horizontal coseismic offsets are largely consistent with those predicted by Schmitt *et al.* (2007) but differ at some locations in the vertical component (Fig. S1.6), which is sensitive to the estimated location of the downdip edge of the coseismic rupture.

1.5.4 Viscoelastic deformation from the 2003 Tecomán earthquake

We modeled surface displacements produced by the viscoelastic response to the 2003 Tecomán earthquake for all six coseismic slip solutions (Fig. S1.5) using their corresponding mantle Maxwell times (τ_m = 2.5, 4, 8, 15, 25, and 40 yr). Viscoelastic relaxation due to the 2003 earthquake (Fig. 1.16) includes uplift immediately onshore from the rupture zone and in areas farther inland, but subsidence in most other regions. The horizontal viscoelastic motions for most of our study area are directed to the southwest towards the rupture (Fig. 1.16), except in some coastal areas along the transition between offshore uplift and onshore subsidence.

The viscoelastic motions predicted for the 2003 Tecomán earthquake differ from the viscoelastic deformation triggered by the 1995 Colima-Jalisco earthquake in two notable

respects. First, the transitions between postseismic motions –both uplift versus subsidence and landward versus oceanward horizontal motions- are predicted to occur onshore due to the deeper extent of downdip rupture in 2003. Second, significant viscoelastic deformation after the 2003 earthquake affected a much smaller region than for the 1995 earthquake (compare Figs 1.11 and 1.16), as expected given that the 1995 Colima-Jalisco earthquake released a factor-of-five more seismic energy.

Overall, the combined viscoelastic effects of the 1995 and 2003 earthquakes for the 25-year interval spanned by our study constitute a non-negligible fraction of the overall deformation within our study area during the past few decades. At site COLI, the combined viscoelastic effects of the two earthquakes by mid-2020 were as large as 75 mm, 55 mm, and 35 mm in the north, east, and vertical components (Fig. S1.10). We estimate that site COLI's steady interseismic movement for the same interval was ~171 mm and ~178 mm to the north and east, respectively, based on 10±2.5 mm/yr of N46°E-directed interseismic elastic shortening measured at COLI from ~2.5 years of continuous measurements prior to the 1995 Colima-Jalisco earthquake (Márquez-Azúa *et al.* 2002). The combined viscoelastic effects of the two earthquakes thus may be as large as 30-40 percent of the cumulative station motion between 1995 and 2020 (excluding coseismic movements), which are too large to ignore.

1.5.5 Afterslip solutions: 1995 Colima-Jalisco and 2003 Tecomán earthquakes

From TDEFNODE inversions of the north, east and vertical daily position estimates at 62 GPS sites, consisting of 201,506 observations between 1993 and 2020, we estimated afterslip solutions for the 1995 Colima-Jalisco and 2003 Tecomán earthquakes. We first subtracted the combined viscoelastic effects of both earthquakes for each of the six assumed mantle Maxwell

times from all of the daily GPS position time series. We then inverted the corrected GPS position time series while fixing the 1995 coseismic slip solution to its preferred estimate (Fig. 1.9a) and the 2003 coseismic slip solution to the best-fitting estimates corresponding to each assumed Maxwell time (Fig. S1.5). All the other 822 parameters, consisting of 1995 and 2003 afterslip spatial distributions, their associated logarithmic decay constants, and the interseismic GPS site velocities, were estimated via methods described in Section 1.3.2. The vertical components at continuous stations INEG, CUVA, UAGU, and TNZA were all discarded due to non-tectonic subsidence at each site that we attribute to groundwater withdrawal.

Figs 1.9b and 1.14b respectively show the best-fitting 1995 and 2003 earthquake afterslip solutions derived from the GPS positions that were corrected by the representative τ_m = 15 yr viscoelastic model. Misfits for this time-dependent model for selected GPS sites between 1993 and 2020, which are displayed for selected continuous sites in Fig. 1.17 and selected campaign sites in Fig. 1.18, range from 1.9 to 4.9 mm in the horizontal components at the 36 continuous sites and 5.0- 5.1 mm at the 26 campaign sites. The misfit *F* for this model is 14.4, larger than the misfits *F* for the inversions of data that span shorter periods (*e.g.* Section 1.4.3). We attribute the larger misfit to a combination of factors: the sensitivity of the fit to the assumed mantle Maxwell time; our assumption of a Newtonian mantle rheology; and our simple single-layer, linear viscoelastic model. The larger wrms misfits to the campaign site time series (5.0-5.1 mm for the horizontal components and 13.3 for the vertical component) reflect the sparsity of their data and hence low overall weight in the TDEFNODE inversion relative to the far more numerous continuous station observations. Because many more campaign than continuous sites were operating during the early years of this study, when rapid postseismic deformation after the 1995 Colima-Jalisco earthquake occurred, we favored the models that best fit the early campaign observations.

1.5.5.1 1995 Colima-Jalisco earthquake afterslip

The TDEFNODE inversion of the 1993-2020 GPS data corrected for viscoelastic deformation for τ_m = 15 yr indicates that more than 85 percent of the 1995 afterslip moment occurred at depths below 15 km, downdip from the coseismic rupture zone (Fig. 1.9b and Table S1.9) and consistent with deep afterslip reported by Hutton *et al.* (2001). This result is robust with respect to five of the six Maxwell times we explored in our analysis – TDEFNODE inversions of the 1993-2020 data corrected for viscoelastic deformation modeled with Maxwell times equal to or longer than 4 yr all indicate that 80 percent or more of the afterslip occurred below 15 km (Table S1.9).

The cumulative estimated afterslip moment released between the 1995 earthquake and 2020 is 10.8×10^{20} N·m (M_w = 8.0), equivalent to ~110 percent of the coseismic moment release (Table S1.5). The afterslip decays logarithmically with a time constant of 13 days following the 1995 earthquake. During the first ~3.5 years after the earthquake, afterslip released an equivalent of ~80 percent of the coseismic moment, comparable to the afterslip versus coseismic moment release ratio of 70 percent reported by Hutton *et al.* (2001) for the same period.

The cumulative GPS site displacements from the afterslip of the 1995 earthquake (Table S6, magenta arrows in Figs 1.9c and d) were comparable in magnitude to the coseismic slip measured at many of the inland GPS stations, but were significantly smaller than the coseismic slips measured at coastal sites near the rupture. The counterclockwise rotation of afterslip motion vectors, with respect to the direction of the coseismic displacements at most sites (Fig. 1.9c), indicates that most afterslip on the subduction interface was located southeast of the coseismic slip (Figs 1.9a and b). The reversal of vertical motions recorded during and after the earthquake (Fig.

1.9d) further indicates that the main locus of the afterslip was down-dip from the coseismic rupture (Figs 1.9a and b). Both features of our 1995 afterslip model (*i.e.* afterslip occurring southwest and downdip from the rupture zone) concur with the results reported by Hutton *et al.* (2001) from their modeling of the first few years of postseismic data, and with the results from Márquez-Azúa *et al.* (2002) from their modeling of continuous measurements at site COLI.

1.5.5.2 2003 Tecomán earthquake afterslip

The same TDEFNODE inversion indicates that afterslip from the 2003 earthquake was concentrated primarily along and directly downdip from the 2003 earthquake rupture zone (Fig. 1.14b). No previous afterslip solution for this earthquake has been estimated, although Schmitt *et al.* (2007) speculated that the afterslip in 2003 occurred at a downdip location based on an observed reversal in the sense of the coseismic and postseismic vertical movements at two coastal sites in the days after the earthquake.

The cumulative afterslip moment estimated at 2.8×10^{20} N·m ($M_w = 7.6$) is ~1.5 times larger than the coseismic moment. Whereas ~85 percent of the afterslip energy was released at depths of 15-60 km (Fig. 1.14c and Table S1.7), ~5 km farther downdip from the region of coseismic slip (Fig. 1.14a), our inversion implies insignificant (10% or less) afterslip at depths shallower than 15 km for all but one of the models. (Table S1.9). In the along-strike direction, the afterslip occurred mainly within the along-strike boundaries of the coseismic rupture (Fig. 1.14). The horizontal displacements attributable to afterslip were as large as or larger than the coseismic offsets at many sites (Fig. 1.14c and Table S1.8), particularly at inland locations. This result, and the reversal of vertical motions with respect to the coseismic direction, strongly indicate that the fault afterslip was focused downdip of the coseismic rupture (coseismic and afterslip solutions of

Figs 1.14a and b). The vertical displacements associated with afterslip transition from uplift onshore from the rupture to minor subsidence at sites father inland (Fig. 1.14d).

The 2003 earthquake afterslip decayed logarithmically with a time constant of 6 days. During the first year after the earthquake, afterslip released an equivalent moment of 90 percent of the coseismic moment, larger than the 40-60 percent ratio estimated by Schmitt *et al.* (2007) for the same interval from the early postseismic motions at just two sites.

Figs S1.11 and S1.12 respectively display the six best-fitting 1995 and 2003 earthquake afterslip solutions, one for each of the viscoelastic models we explored. Tables S1.5-S1.9 provide relevant information for all the models. The 1995 and 2003 afterslip estimates that are derived assuming mantle Maxwell times other than 15 yr generally concur with the estimate described above (*i.e.* for τ_m = 15 yr) and are thus not discussed further.

1.5.6 The interseismic velocity field

Fig. 1.19 displays GPS site velocities from the TDEFNODE inversion (*i.e.* the V_{ij} term in Eq. 1.2 of Section 1.3.2) with viscoelastic corrections for a mantle Maxwell τ_m of 15 yr. Because each velocity is implicitly corrected for the coseismic, afterslip, and viscoelastic effects of the 1995 and 2003 earthquakes, the velocities constitute our best estimate of the interseismic movement at each site relative to the interior of the North America plate. The horizontal and vertical interseismic site velocities V_{ij} for all six assumed mantle Maxwell times are compared in Figs S1.13 and S1.14 and are tabulated in Table S1.10.

The large misfit values of our solutions (>13) are symptomatic of an undervaluation of the data uncertainties. The formal velocity uncertainties, which are estimated by TDEFNODE solely

from the formal uncertainties in the inverted GPS station positions, are typically less than ±1 mm/yr. They exclude uncertainties that are introduced by our model assumptions and viscoelastic corrections. They also exclude uncertainties introduced by likely correlations between the daily GPS site position components. To account for this, we systematically increased the north and east velocity uncertainties by a factor of three and vertical uncertainties by a factor of five. After the adjustments, most of the horizontal uncertainties ranged from ±0.6-3.5 mm/yr and vertical uncertainties from ±0.9-4 mm/yr.

Detailed descriptions and modeling of the new interseismic velocities are found in Part 2 of our study.

1.6 DISCUSSION AND CONCLUSIONS

1.6.1 Influence of assumed mantle viscosity on coseismic and afterslip solutions

The 1995 and 2003 coseismic slip solutions are both relatively insensitive to the mantle Maxwell times that we used as a basis for correcting our GPS station time series prior to inverting those data with TDEFNODE (Sections 1.4.1 and 1.4.3). In contrast, the postseismic 1995 and 2003 afterslip solutions are more sensitive to the assumed Maxwell time (Section 1.4.5 and Figs S1.11 and S1.12), reflecting the tradeoff between fitting postseismic site motions with a combination of logarithmically decaying afterslip and exponentially decaying viscoelastic deformation. In general, smaller values of τ_m for the viscoelastic corrections, which correspond to larger magnitude short-term viscoelastic deformation, result in smaller estimated afterslip (Figs S1.11 and S1.12).

Previous authors have considered the same tradeoff between afterslip and viscoelastic mantle/crustal responses along subduction zones. Hu & Wang (2012) show that viscoelastic mantle

relaxation and deep afterslip both cause trenchward motion of areas well inland from subduction-thrust rupture zones (Figs 1.11 and 1.16), such that ignoring the viscoelastic relaxation leads to overestimation of the deep afterslip (also see Sun *et al.* 2014). Similarly, postseismic viscoelastic relaxation and shallow afterslip respectively cause landward and seaward (*i.e.* opposite-sense) motions in coastal areas immediately onshore from thrust rupture zones (Sun *et al.* 2014; Sun & Wang 2015; and Figs 1.11 and 1.16). Ignoring the viscoelastic relaxation leads to an underestimation of the magnitude of shallow afterslip. Together, these results imply that neglecting the postseismic viscoelastic effects of large ($M_w \geq 7.5$) thrust earthquakes, including the $M_w = 8.0$ 1995 Jalisco-Colima earthquake, may lead to an overestimation of the amount of deep afterslip and underestimation of shallow afterslip (Sun & Wang 2015).

Our modeling illustrates both of these tradeoffs. The afterslip solutions that are associated with longer Maxwell times, and hence smaller-magnitude viscoelastic deformation, display little or no shallow afterslip and large-magnitude, deep afterslip (Figs S1.11 and S1.12). Conversely, afterslip solutions that are associated with short Maxwell times and hence larger-magnitude viscoelastic deformation include some shallow afterslip and smaller-magnitude deep afterslip (also see Table S1.9).

1.6.2 Implications for subduction along the northernmost Mexico subduction zone

The two earthquakes analyzed in this study ruptured distinctly different areas of the subduction interface (Fig. 1.20). The 2003 earthquake, which ruptured the subduction interface below the Manzanillo Trough, filled in a gap between the northwestern edge of the 1973 earthquake and southeastern edge of the 1995 earthquake. Any overlap between the rupture areas for the 1995 Colima-Jalisco and 2003 Tecomán earthquakes was minimal (Fig. 1.20). Including

the June 1932 M~8 earthquakes, whose rupture areas are known only approximately (Fig. 1.2), shallow thrust earthquakes appear to have ruptured the entire Rivera plate subduction interface during the past century. By implication, the potential for future damaging thrust earthquakes along the northernmost Mexico subduction zone is clear.

Schmitt *et al.* (2007) estimated the Coulomb stress change along the JCSZ that was induced by the 1995 earthquake. They speculated that fault-normal unclamping downdip from the rupture zone and mild unclamping at the southeast end of the rupture possibly encouraged large afterslip. Our estimates of the size and location of the 1995 afterslip (orange area in Fig. 1.20) support this hypothesis. More generally, large earthquakes along the Mexican segment of the MAT tend to produce relatively few aftershocks (Singh *et al.* 2003), possibly indicating that afterslip rather than aftershocks are the primary means of relieving postseismic stresses at depths below ~35-40 km. Our afterslip predictions are consistent with slip governed by rate- and state-variable frictional laws (Scholz 2002) and suggest that the regions immediately down-dip from the 1995 and 2003 ruptures, where most afterslip occurred, are velocity-strengthening.

Inferences about locking of the subduction interface at depths shallower than 15 km are more difficult because shallow slip is typically resolved poorly by GPS networks onshore from subduction zones. Our solutions suggest there was little or possibly no afterslip above depths of 15 km after the 1995 and 2003 earthquakes (Table S1.9). The shallowest regions of the subduction interface may thus be strongly locked between earthquakes (Brudzinski *et al.* 2016).

The 1995 and 2003 earthquakes both triggered unusually large afterslip, with respective afterslip-to-earthquake moment ratios of ~90 per cent and ~120 per cent. Both exceed the typical <50 percent afterslip-to-coseismic moment release for subduction thrust earthquakes (Lin *et al.*

2013). Afterslip may thus accommodate a larger fraction of the plate convergence along the JCSZ than is true along most subduction zones. Although Lin *et al.* (2013) suggest that the relative magnitude of postseismic-to-coseismic moment scales with the magnitude of the mainshock, we observe the converse: The 2003 Tecomán earthquake released proportionally more afterslip than did the 1995 earthquake even though the moment of the 1995 earthquake was five times larger than in 2003.

The apparent coincidence of the edges of the 1995 and 2003 ruptures and their afterslip with the borders of the Manzanillo Trough (Fig. 1.20), which also coincide with the poorly constrained ruptures areas for the 1932 and 1973 earthquakes (Fig. 1.20), suggests that structures within or near the Manzanillo Trough, including the Tecomán trough, Manzanillo horst, and an ensemble of seismically-imaged normal and strike-slip faults (Bandy *et al*. 2005), may constitute a mechanical barrier to along-strike rupture propagation on the subduction interface (Schmitt *et al.* 2007). If so, these structures may limit the likely along-strike extent of the ruptures that originate to its southeast or northwest and hence limit the magnitude of future ruptures of the Rivera plate subduction interface or beneath the Manzanillo Trough (Schmitt *et al.* 2007). Using Hutton *et al.*'s (2001) assumed maximum rupture area of 200 km along-strike by 80 km downdip for the subduction interface northwest of the Manzanillo Trough (16,000 km^2), a hypothetical 4 m uniform rupture of the entire area would have a moment magnitude of M_w = 8.2 (for a shear modulus of 40 GPa). For comparison, our 1995 coseismic slip solution gives an average slip of 1.8 m over an area of ~13,200 km^2. Similarly, using Schmitt *et al.*'s (2007) assumed maximum rupture area of the seismogenic zone beneath the Manzanillo Trough (70 km along-strike and 70 km downdip), a 3 m uniform rupture of the entire area would have a moment magnitude of M_w = 7.8. For comparison,

the mean value of the average slip and the area from our models of the 2003 earthquake rupture were 0.8 m and ~5,800 km^2, respectively.

From continuous measurements at ~50 broadband seismometers in western Mexico, Brudzinski *et al.* (2016) locate numerous instances of tectonic tremor that are apparently associated with the subduction interface and are offset downdip from the seismogenic zone (Fig. 1.20). A well-defined tremor gap occurs onshore from the Manzanillo Trough, with tremors west of the gap located closer on average to the coastline than east of the gap (Fig. 1.20). Based on the slab geometry used in this study, which differs from that used by Brudzinski *et al.* (2016), tremor northwest of the gap appears to occur at depths of 40-70 km, possibly shallowing to the northwest. Tremor east of the gap is instead mostly at depths of 50-70 km (Fig. 1.20). In both areas, our afterslip solutions suggest 0.5-2 meters of afterslip occurred as far downdip as the region of non-volcanic tremor (Fig. 1.20). Our modeling indicates that afterslip is an important mechanism by which plate convergence is accommodated in this transitional region. Further observations are needed to determine how much, if any of the plate convergence is accommodated by slow slip events (SSE). No compelling evidence for SSE below Jalisco has yet emerged after 25 years of continuous GPS measurements in this region (see below).

1.6.3 Comparative subduction along the Jalisco versus Guerrero/Oaxaca segments

A wide variety of seismic phenomena has been observed along the Guerrero and Oaxaca segments of the Mexico subduction zone, including thrust fault earthquakes and their postseismic effects (Singh *et al.* 1985; 2003; Reyes et al 1979, Courboulex *et al.* 1997; Pacheco et al 1997; Hutton *et al.* 2001; Yagi *et al.* 2004; Schmitt *et al.* 2007; Graham *et al.* 2014b), slow slip events (SSE) (Lowry *et al.* 2001; Kostoglodov *et al.* 2003; 2010; Brudzinski *et al.* 2007; Larson *et al.*

2007; Correa-Mora *et al.* 2008, 2009; Vergnolle *et al.* 2010; Radiguet *et al.* 2012; Cavalié *et al.* 2013; Graham *et al.* 2014a; 2016; Bekaert *et al.* 2015; Maubant *et al.* 2020), and non-volcanic tremor (NVT) (Payero *et al.* 2008; Kostoglodov *et al.* 2010; Brudzinski *et al.* 2010; 2016). Below, we summarize and compare the subduction characteristics for our study area as revealed by this and previous studies to those for the Guerrero and Oaxaca segments immediately southeast of our study area, where subduction of the Cocos plate beneath North America at velocities and seafloor ages (< 20 Ma) similar to those for our study area also occurs.

The Guerrero and Oaxaca segments of the Mexico subduction zone are characterized by a flat-to-nearly-flat subduction interface that extends more than 200 km beneath central Mexico, making it one of Earth's shallowest subduction zones (Pérez-Campos *et al.* 2008; Kim *et al.* 2010). Thrust earthquakes below central Mexico occur above depths of ~25 km (Suárez & Sánchez 1996, Pacheco & Singh 2010) and afterslip, which also relieves elastic strain, has been observed at seismogenic depths and deeper areas of the interface as far as 220 km inland from the coast (Graham *et al.* 2014b). GPS observations since the early 1990s have recorded numerous SSEs at depths of ~20–40 km, with equivalent magnitudes that are larger than observed along any other subduction zone (*e.g.* Lowry *et al.* 2001; Kostoglodov *et al.* 2003; 2010; Brudzinski *et al.* 2007; Larson *et al.* 2007; Correa-Mora *et al.* 2008, 2009; Vergnolle *et al.* 2010; Radiguet *et al.* 2012; Cavalié *et al.* 2013; Graham *et al.* 2014a; 2016; Bekaert *et al.* 2015; Maubant *et al.* 2020). Seismic observations have detected widespread NVT on the subduction interface downdip from the source regions of SSEs and offset downdip from the megathrust earthquake rupture zones (Payero *et al.* 2008; Brudzinski *et al.* 2010; Kostoglodov *et al.* 2010).

Despite the geometric similarities of the Guerrero and Oaxaca subduction interfaces, SSEs beneath Guerrero have larger magnitudes (M~7.5) than those beneath Oaxaca (M~6.5-7), and the

SSEs are shallower, possibly intruding the seismogenic zone and releasing a portion of the accumulated shallow elastic strain (Kostoglodov *et al.* 2003; Iglesias *et al.* 2004; Yoshioka *et al.* 2004; Larson *et al.* 2007; Radiguet *et al.* 2012; Cavalié *et al.* 2013; Graham *et al.* 2016). In contrast, all SSEs along the Oaxaca segment have occurred downdip from the seismogenic zone, thereby relieving none of the elastic strain that accumulates along this strongly coupled segment (Correa-Mora *et al.* 2008; Radiguet *et al.* 2012; Graham *et al.* 2016). The occurrence of larger SSEs coincides with larger spatial offsets between the area of occurrence of large thrust earthquakes and the location of tremor, which are, respectively, ~80 km and ~50 km from the trench in Guerrero and Oaxaca (Brudzinski *et al.* 2016).

In contrast to the Guerrero and Oaxaca trench segments, where moderate- to large-magnitude SSEs occur every 2-3 years or more frequently, continuous GPS observations in our study area since the early 1990s have yielded only inconclusive evidence for SSE. Brudzinski *et al.* (2016) describe possible evidence for SSE in our study area in 2008, mid-2011, and 2013. All three of the possible SSEs were associated with GPS position variations that were close to the few millimeter detectability threshold of the GPS observations. Thus, their implied amplitudes were at least an order-of-magnitude smaller than is typical in Guerrero and Oaxaca. To date, the absence (or infrequency) of moderate or large-magnitude SSE appears to be the primary difference between how subduction is accommodated along the JCSZ versus the Guerrero and Oaxaca trench segments.

Brudzinski *et al.* (2016) suggest that the apparent lack of interseismic SSE along the Colima-Jalisco trench segment versus the abundance of large-magnitude SSE below central and southern Mexico may be a consequence of the steeper dips of the subducting Rivera and northwesternmost Cocos plates, as well as the occurrence of significant earthquake afterslip along

the narrow zone between the regions of shallow seismogenesis and downdip non-volcanic tremor in our study area. Specifically, whereas shallow slab dip below central and southern Mexico may allow for larger portions of the subduction interface to have the appropriate temperature, pressure, hydrological, and mineralogical conditions for transient slip, the steeper dips of the Rivera and northwestern Cocos interfaces may reduce the area of the subduction interface with conditions that are conducive to SSE. The offset between the area of NVT and deepest coseismic slip in our study area ranges from only ~5 to 40 km (Fig. 1.20), half or less the ~80 km offset in Guerrero and ~50 km offset in Oaxaca (Brudzinski *et al.* 2016).

Our modeling suggests that afterslip in 1995 and 2003 extended all the way downdip to the region of NVT on the Rivera/Cocos subduction interfaces (Fig. 1.20). If the frictional properties of subduction interfaces differ significantly in areas where postseismic afterslip and interseismic silent slip events occur, as suggested by Malservisi *et al.* (2015) based on the minimal observed overlap between the two slip phenomena beneath the Nicoya Peninsula of Costa Rica, then our modeling results suggest that little or none of the subduction interface below our study area has the conditions suitable for SSE. Alternatively, if frictional conditions do permit SSE and postseismic afterslip to occur along the same parts of a subduction interface, as appears to be true along the Oaxaca segment (Graham *et al.* 2014b), then the significant elastic strain that was discharged by the 1995 and 2003 earthquake afterslips reduced the amount of accumulated strain that was available to drive SSE after 1995 (Section 1.5.5, Tables S1.5 and S1.7).

1.6.4 Challenges and pitfalls of our modelling: model fits and residuals

An important element of this study was to explore the robustness of our solutions and data fits with respect to the tradeoffs between the numerous adjustable parameters. These parameters

include the coseismic and afterslip solutions for the 1995 and 2003 earthquakes, logarithmic decay constants for the afterslip in 1995 and 2003, the interseismic GPS site velocities, and the mantle Maxwell times that were used to estimate *a priori* viscoelastic corrections for the GPS position time series that were inverted within TDEFNODE.

TDEFNODE's misfit F (equation 1.3) should be well suited for identifying the optimal mantle Maxwell time given that the viscoelastic correction that best approximates the mantle's postseismic behavior should allow for the best overall fit to the GPS data. The misfit values varied by only ~10 percent for the wide range of mantle Maxwell times we tested, including an inversion of the GPS position time series without any viscoelastic corrections (Table S1.12). The mantle rheology is thus not strongly constrained by our observations, as expected given the many fitting tradeoffs that exist between the model parameters.

The strongest constraints on the mantle rheology come from the subset of our observations made during the years after the 1995 Colima-Jalisco earthquake when the largest most rapid viscoelastic deformation occurred. The smallest wrms misfit (equation 1.4) to the campaign stations that were mainly active during this time occurs for a Maxwell time of 8 yr (a mantle viscosity of 1×10^{19} Pa·s), the same viscosity that was used by Márquez-Azúa *et al.* (2002) to reconcile a difference in the observed directions of GPS station COLI before and in the years following the 1995 Colima-Jalisco earthquake. The improvements in the fits relative to a model without any viscoelastic correction are particularly notable at sites CHAM, CRIP, MELA, and PURI (compare red and blue residuals for these sites in Fig. 1.21), which were directly onshore from the earthquake in the regions of the greatest postseismic deformation (Fig. 1.4).

Our inversions based on Maxwell times of 4 yr and 15 yr, spanning mantle viscosities of 0.5 to 1.9 × 10^{19} Pa·s, give wrms fits to campaign site data close to that for a Maxwell time of 8 yr (Table S1.12). These values agree with viscosities estimated in similar previous studies, including 3.2 × 10^{19} Pa·s for the 1964 Alaska earthquake (Suito & Freymuller 2009); viscosities on the order of 10^{19} Pa·s for the 1960 Chile, 2006 Sumatra, and ~1700 Cascadia megathrust earthquakes (Wang *et al.* 2012); 5 × 10^{18} Pa·s and 3 × 10^{19} Pa·s respectively for a low-viscosity wedge and the long term mantle viscosity (Trubienco *et al.* 2013); and 0.8-1.5 × 10^{19} Pa·s from modeling of long-term postseismic deformation in Nankai (Johnson & Tebo 2018). We adopt a best viscosity of 1.9 × 10^{19} Pa·s (τ_m = 15 yr), based on results from static modeling of the interseismic motions in the second stage of our analysis (Chapter 2), and the similarities of the wrms misfit values to campaign site data for the 4, 8, and 15 yr Maxwell times.

None of our solutions satisfactorily fits all of the GPS data. For example, significant misfits at some sites during the several years of rapid postseismic deformation after the 1995 earthquake (Fig. 1.21 and Fig. S1.17) may suggest that a single logarithmic decay constant for the postseismic fault afterslip cannot capture the complexity of the postseismic deformation. Alternatively, the misfits may imply that multilayer viscoelastic models (Wiseman *et al.* 2015; Freed *et al.* 2017) or possibly models with different mantle rheologies such as power law (Freed & Bürgmann 2004; Freed *et. al.* 2006; Peña *et al.* 2019) or a Burgers rheology (Hu & Wang 2012; Wang *et al.* 2012; Trubienko *et al.* 2013; Sun *et al.* 2014; 2018) are required to fit the data. Layered models with more realistic values for the elastic properties (e.g. Poisson's ratio, shear modulus) lead to significant differences in deformation rates with respect to homogeneous models (Masterlark *et al.* 2001, Correa-Mora *et al*. 2008). Power-law rheologies, in which viscosity varies spatially with stress and varies temporally with the evolution of stress (Freed & Bürgmann 2004), cause strain

localization, fast early displacement rates at the surface (Freed *et. al.* 2006), discourage deep afterslip, and can produce significantly different motion patterns with respect to Maxwell rheologies, particularly for the vertical component (Peña *et al.* 2019). Burgers rheologies allow for more rapid postseismic deformation over shorter time scales at large distances (Trubienko *et al.* 2013) and favor shallow afterslip (Sun *et al.* 2014; 2018).

Other significant misfits occur at times that are 5 years or more after the earthquakes, possibly pointing to errors or oversimplifications in our viscoelastic model and/or assumptions. In particular, continuous measurements at nearby sites COLI and COOB clearly show that both sites experienced a gradual transition from slow postseismic uplift in the years after the 2003 Tecomán earthquake to slow subsidence after ~2015 (Figs 1.3, 1.7a, 1.13, 1.17, and 1.21). Our model also fails to predict ~6 months of observed postseismic subsidence at site COLI immediately after the 2003 earthquake and prior to the onset of the aforementioned slow uplift. None of the models we explored captured the early postseismic subsidence or gradual reversal in the postseismic vertical motion, once again suggesting an error and/or oversimplification in our models or assumptions.

Overall, improved fits might result from a different geometry for the subduction interface (Pardo & Suárez 1995, Andrews *et al.* 2011; Abbott & Brudzinski 2015), lateral variations in the thickness and/or elastic properties of the crust, different assumed thicknesses/depths for our layered viscous model, and more layering of the upper crust and mantle (Wiseman *et al.* 2015; Freed *et al.* 2017). The incorporation of a low viscosity wedge (Trubienko *et al.* 2013) and/or an elastic cold nose in the mantle wedge (Sun *et al.* 2014; Freed *et al.* 2017; Johnson & Tebo 2018) into our model may improve the fits, as might different viscosities for the mantle below the oceanic and continental crust (Hu & Wang 2012; Li *et al.* 2015; Wiseman *et al.* 2015) or different rheology types (see above). Practical considerations and the limited information in our GPS data,

particularly for the 1995 earthquake, precluded a systematic examination of these many possibilities, which may be better suited to larger magnitude earthquakes for which the signal-to-noise is sufficiently large to discriminate between them.

AKNOWLEDGEMENTS

Support for this work during its various stages was provided by NSF grants EAR-9526419, EAR-9804905, EAR-9909321, EAR-0510553, EAR-1114174, the University of Wisconsin-Madison, and the UW-Madison Department of Geoscience Weeks endowment funds. This material is based on GPS data and services provided by the GAGE Facility, operated by UNAVCO, Inc. and by the TLALOCNet GPS network operated by Servicio de Geodesia Satelital (SGS; Cabral-Cano et al., 2018) at the Instituto de Geofísica-Universidad Nacional Autónoma de México (UNAM). UNAVCO's initial support for TLALOCNet (now part of NOTA) was performed under EAR-1338091 and is currently supported by the National Science Foundation and the National Aeronautics and Space Administration under NSF Cooperative Agreement EAR-1724794. TLALOCNet and other GPS related operations from SGS have also been supported by the Consejo Nacional de Ciencia y Tecnología (CONACyT) projects 253760, 256012 and 2017-01-5955, UNAM-Programa de Apoyo a Proyectos de Investigación e Innovación Tecnológica (PAPIIT) projects IN104213, IN111509, IN109315-3, IN104818-3 and supplemental support from UNAM-Instituto de Geofísica. We are deeply grateful to all personnel from UNAVCO and SGS for station maintenance, data acquisition, IT support and data curation and distribution for these networks and in particular to the following individuals and institutions, whose hard work and resourcefulness were central to the success of this project: Bill Douglass, Neal Lord and Bill Unger at UW-Madison, Oscar Diaz-Molina and Luis Salazar-Tlaczani at SGS, John Galetzka, Adam

Wallace, Shawn Lawrence, Sean Malloy and Chris Walls at UNAVCO, Jesus Pacheco-Martínez at Universidad Autónoma de Aguascalientes, personnel at the Universidad de Guadalajara at campus Guadalajara, Mascota and Ameca, Protección Civil de Jalisco, Universidad de Colima at campus Colima and campus El Naranjo, and Instituto de Biología-UNAM Estacion Chamela. Most figures were produced using Generic Mapping Tools software (Wessel & Smith 1991).

REFERENCES

Abbott, E.R. & Brudzinski, M.R., 2015. Shallow seismicity patterns in the northwestern section of the Mexico Subduction Zone, *J. S. Am. Earth Sci*., **63**, 279-292, http://dx.doi.org/10.1016/j.jsames.2015.07.012.

Altamimi, Z., Rebischung, P., Métivier, L. & Collilieux, X., 2016. ITRF2014: A new release of the International Terrestrial Reference Frame modeling nonlinear station motions, *J. Geophys. Res. – Sol. Ea.*, **121**, 6109–6131,doi:10.1002/2016JB013098.

Álvarez, R. & Yutsis, V., 2015. The elusive Rivera-Cocos plate boundary: not diffuse, in *Magmatic Rifting and Active Volcanism*, eds. Wright, T.J., Ayele, A., Ferguson, D.J., Kidane, T. & Vye-Brown, C., Vol. **420**, Geological Society, London, Special Publications. http://doi.org/10.1144/SP420.8.

Bandy, W.L., Michaud, F., Bourgois, J., Calmus, T., Dyment, J., Mortera-Gutiérrez, C.A., Ortega-Ramírez, J., Pontoise, B., Royer, J.-Y., Sichler, G., Sosson, M., Rebolledo-Vieyra, M., Bigot-Cormier, F., Díaz-Molina, O., Hurtado-Artunduaga, A.D., Pardo-Castro, G., & Trouillard-Perrot, C., 2005. Subsidence and strike-slip tectonism or the upper continental slope off Manzanillo, Mexico, *Tectonophyiscs*, **398**, 115-140, doi:10.1016/j.tecto.2005.01.004.

Bandy, W., Mortera-Gutiérrez, C., Urrutia-Fucugauchi, J. & Hilde, T.W.C., 1995. The subducted Rivera-Cocos plate boundary: Where is it, what is it, and what is its relationship to the Colima rift?, *Geophys. Res. Lett.*, **22**, 22, 3075-3078.

Barbot, S., 2014. RELAX v1.0.7 [software], Computational Infrastructure for Geodynamics, url: https://geodynamics.org/cig/software/relax/.

Barbot, S. & Fialko, Y., 2010a. A unified continuum representation of post-seismic relaxation mechanisms: semi-analytic models of afterslip, poroelastic rebound and viscoelastic flow: Semi-analytic models of postseismic transient, *Geophys. J. Int.*, **182**(3), 1124-1140, doi: 10.1111/j.1365-246X.2010.04678.x.

Barbot, S. & Fialko, Y., 2010b. Fourier-domain Green's function for an elastic semi-infinite solid under gravity, with applications to earthquake and volcano deformation: Fourier-domain elastic solutions, *Geophys. J. Int.*, **182**(2), 568-582, doi: 10.1111/j.1365-246X.2010.04655.x.

Bekaert, D.P.S., Hooper, A. & Wright, T.J., 2015. Reassessing the 2006 Guerrero slow-slip event, Mexico, *J. geophys. Res. – Sol. Ea.*, **120**, 1357–1375. https://doi.org/10.1002/2014JB011558.

Ben-Menahmen, A. & Singh, S.K., 1981. *Seismic Waves and Sources*, Springer-Verlag, New York, NY.

Bertiger, W., Desai, S.D., Haines, B., Harvey, N., Moore, A.W., Owen, S. & Weiss, J.P., 2010. Single receiver phase ambiguity resolution with GPS data, *J. Geodesy*, **94**, 327–337.

Brudzinski, M., Cabral-Cano, E., Correa-Mora, F., DeMets, C. & Márquez-Azúa, B., 2007. Slow slip transients along the Oaxaca subduction segment from 1993 to 2007, *Geophys. J. Int.*, **171**, 523–538.

Brudzinski, M.R., Hinojosa-Prieto, H.R., Schlanser, K.M., Cabral-Cano, E., Arciniega-Ceballos, A., Díaz-Molina, O. & DeMets, C., 2010. Nonvolcanic tremor along the Oaxaca segment of the Middle America subduction zone, *J. geophys. Res. - Sol. Ea.,* **115**, B00A23, http://dx.doi.org/10.1029/2008JB006061.

Brudzinski, M., Schlanser, K.M., Kelly, N.J., DeMets, C., Grand, S.P., Márquez-Azúa, B. & Cabral-Cano, E., 2016. Tectonic tremor and slow slip along the northwestern section of the Mexico subduction zone, *Earth Planet. Sci. Lett.,* **454**, 259–271, http://dx.doi.org/10.1016/j.epsl.2016.08.004.

Cabral-Cano, E., Pérez-Campos, X., Márquez-Azúa, B., Sergeeva, M.A., Salazar-Tlaczani, L., DeMets, C., Adams, D., Galetzka, J., Hodgkinson, K., Feaux, K., Serra, Y.L., Mattioli, G.S. & Miller, M., 2018. TLALOCNet: A continuous GPS-Met backbone in Mexico for seismotectonic and atmospheric research, *Seismol. Res. Lett.,* **89**(2A), 373-381, doi: 10.1785/0220170190.

Cabral-Cano, Enrique, Salazar-Tlaczani, Luis, 2015, *TLALOCNet - UAGU-uagu_tnet_mx2008 P.S., UNAVCO, GPS/GNSS Observations Dataset*, https://doi.org/10.7283/T5513WK7.

Cavalié, O., Pathier, E., Radiguet, M., Vergnolle, M., Cotte, N., Walpersdorf, A., Kostoglodov, V. & Cotton, F. 2013. Slow slip event in the Mexican subduction zone: evidence of shallower slip in the Guerrero seismic gap for the 2006 event revealed by the joint inversion of InSAR and GPS data, *Earth Planet. Sci. Lett.*, **367**, 52–60.

Corbo-Camargo, F., Arzate-Flores, J.A., Álvarez-Béjar, R., Aranda-Gómez, J.J. & Yutsis, V., 2013. Subduction of the Rivera plate beneath the Jalisco block as imaged by magnetotelluric data, *Rev. Mex. Cienc. Geol*., **30**(2), 268–281.

Correa-Mora, F., DeMets, C., Cabral-Cano, E., Díaz-Molina, O. & Márquez-Azúa, B., 2009. Transient deformation in southern Mexico in 2006 and 2007: Evidence for distinct deep-slip patches beneath Guerrero and Oaxaca, *Geochem. Geophys Geosyst*., **10**, Q02S12, doi:10.1029/ 2008GC002211.

Correa-Mora, F., DeMets, C., Cabral-Cano, E., Márquez-Azúa, B. & Díaz-Molina, O., 2008. Interplate coupling and transient slip along the subduction interface beneath Oaxaca, Mexico, *Geophys. J. Int*., **175**, 269-290, doi: 10.1111/j.1365-246X.2008.03910.x.

Courboulex, F., Singh, S.K. & Pacheco, J.F., 1997. The 1995 Colima-Jalixco, Mexico, earthquake (M_w 8): A study of the rupture process, *Geophys. Res. Lett.,* **24**(9), 1019-1022.

DeMets, C., 2007a. *Jalisco GPS Network - FARO-El Faro lighthouse P.S., UNAVCO, GPS/GNSS Observations Dataset*, https://doi.org/10.7283/T5NG4NQB.

DeMets, C., 2007b. *Jalisco GPS Network - PENA-US Gypsum Mine at Pena Colorada P.S., UNAVCO, GPS/GNSS Observations Dataset*, https://doi.org/10.7283/T51R6NMX.

DeMets, C., 2007c. *Jalisco GPS Network - PURI-Purificacion P.S., UNAVCO, GPS/GNSS Observations Dataset*, https://doi.org/10.7283/T5X0655S.

DeMets, C., 2007d. *Jalisco GPS Network - PZUL-Telmex tower near Cruz de Loreto P.S., UNAVCO, GPS/GNSS Observations Dataset*, https://doi.org/10.7283/T5DZ06D2.

DeMets, C., 2007e. *Jalisco GPS Network - TECO-APASCO Cement Factory and quarry P.S., UNAVCO, GPS/GNSS Observations Dataset*, https://doi.org/10.7283/T5S75DF2.

DeMets, C., 2007f. *Jalisco GPS Network - UCOM-Univ. Colima at Manzanillo P.S., UNAVCO, GPS/GNSS Observations Dataset*, https://doi.org/10.7283/T5959FNN.

DeMets, C., Carmichael, I., Melbourne, T., Sánchez, O., Stock, J., Suárez, G. & Hudnut, K., 1995. Anticipating the successor to Mexico's largest historical earthquake, *Eos*, **76**(42), 417-424.

DeMets, C., Gordon, R.G. & Argus, D.F., 2010. Geologically current plate motions, *Geophys. J. Int.*, **181**, 1-80, doi: 10.1111/j.1365-246X.2009.04491.x.

DeMets, C. & Stock, J., 1996. *Jalisco 1996, UNAVCO, GPS/GNSS Observations Dataset*, https://doi.org/10.7283/T5XD0ZS7.

DeMets, C. & Stock, J., 2001a. *Jalisco 1995 03 (March), UNAVCO, GPS/GNSS Observations Dataset*, https://doi.org/10.7283/T5K35RSF.

DeMets, C. & Stock, J., 2001b. *Jalisco 1995 10 (October), UNAVCO, GPS/GNSS Observations Dataset*, https://doi.org/10.7283/T55T3HKM.

DeMets, C. & Stock, J., 2001c. *Jalisco 1997, UNAVCO, GPS/GNSS Observations Dataset*, https://doi.org/10.7283/T5222RWN.

DeMets, C. & Stock, J., 2001d. *Jalisco 1998, UNAVCO, GPS/GNSS Observations Dataset*, https://doi.org/10.7283/T5SN073R.

DeMets, C. & Stock, J., 2001e. *Jalisco 1999, UNAVCO, GPS/GNSS Observations Dataset*, https://doi.org/10.7283/T59K48BS.

DeMets, C. & Stock, J., 2001f. *Jalisco GPS Network - CRIP-Cent. Reg. Inv. Pesqueras P.S., UNAVCO, GPS/GNSS Observations Dataset*, https://doi.org/10.7283/T5RN360T.

DeMets, C. & Stock, J., 2004a. *Jalisco 2000, UNAVCO, GPS/GNSS Observations Dataset*, https://doi.org/10.7283/T5FB512H.

DeMets, C. & Stock, J., 2004b. *Jalisco 2001, UNAVCO, GPS/GNSS Observations Dataset*, https://doi.org/10.7283/T5NV9GCG.

DeMets, C. & Stock, J., 2004c. *Jalisco 2002, UNAVCO, GPS/GNSS Observations Dataset*, https://doi.org/10.7283/T5J38QN2.

DeMets, C. & Stock, J., 2004d. *Jalisco 2003, UNAVCO, GPS/GNSS Observations Dataset*, https://doi.org/10.7283/T5DB7ZXB.

DeMets, C. & Stock, J., 2004e. *Jalisco 2004, UNAVCO, GPS/GNSS Observations Dataset*, https://doi.org/10.7283/T58K775Z.

DeMets, C. & Stock, J., 2006. *Jalisco 2005, UNAVCO, GPS/GNSS Observations Datase*t, https://doi.org/10.7283/T54T6GGP.

DeMets, Charles, 2007, *Jalisco GPS Network - FARO-El Faro lighthouse P.S., UNAVCO, GPS/GNSS Observations Dataset*, https://doi.org/10.7283/T5NG4NQB.

DeMets, Charles, 2007, *Jalisco GPS Network - PENA-US Gypsum Mine at Pena Colorada P.S., UNAVCO, GPS/GNSS Observations Dataset*, https://doi.org/10.7283/T51R6NMX.

DeMets, Charles, 2007, *Jalisco GPS Network - PURI-Purificacion P.S., UNAVCO, GPS/GNSS Observations Dataset*, https://doi.org/10.7283/T5X0655S.

DeMets, Charles, 2007, *Jalisco GPS Network - PZUL-Telmex tower near Cruz de Loreto P.S., UNAVCO, GPS/GNSS Observations Dataset*, https://doi.org/10.7283/T5DZ06D2.

DeMets, Charles, 2007, *Jalisco GPS Network - TECO-APASCO Cement Factory and quarry P.S., UNAVCO, GPS/GNSS Observations Dataset*, https://doi.org/10.7283/T5S75DF2.

DeMets, Charles, 2007, *Jalisco GPS Network - UCOM-Univ. Colima at Manzanillo P.S., UNAVCO, GPS/GNSS Observations Dataset*, https://doi.org/10.7283/T5959FNN.

DeMets, C. & Stock, J., 2008. *Jalisco 2007, UNAVCO, GPS/GNSS Observations Dataset*, https://doi.org/10.7283/T5154F50.

DeMets, C. & Stock, J., 2011. *Jalisco 2009, UNAVCO, GPS/GNSS Observations Dataset,* https://doi.org/10.7283/T5WD3XQR.

DeMets, C. & Wilson, D.S., 1997. Relative motions of the Pacific, Rivera, North American, and Cocos plates since 0.78 Ma, *J. geophys. Res*., **102**, 2789–2806.

Dziewonski, A.M., Ekstrom, G. & Salganik, M.P., 1997. Centroid- moment tensor solutions for October–December 1995, *Phys. Earth planet. Inter*., **101**, 1–12.

Ekström, G., Dziewonski, A.M., Maternovskaya, N.N. & Nettles, M., 2004. Global seismicity of 2003: centroid-moment-tensor solutions for 1087 earthquakes, *Phys. Earth planet. Inter*., **148**, 327-351.

Escobedo, D., Pacheco, J.F. & Suárez, G., 1998. Teleseismic body-wave analysis of the 9 October, 1995 (Mw = 8.0), Colima-Jalisco earthquake, and its largest foreshock and aftershock, *Geophys. Res. Lett.*, **25**(4), 547-550.

Freed, A.M., Bürgmann, R., Calais, E., Freymueller, J., 2006. Stress-dependent power-law flow in the upper mantle following the 2002 Denali, Alaska, earthquake, *Earth Planet. Sci. Lett*., **252**, 481-489, doi:10.1016/j.epsl.2006.10.011.

Freed, A.M., Hashima, A., Becker, T.W., Okaya, D.A., Sato, H. & Hatanaka, Y., 2017. Resolving depth-dependent subduction zone viscosity and afterslip from postseismic displacements following the 2011 Tohoku-oki, Japan earthquake, *Earth Planet. Sci. Lett*., **459**, 279-290, https://doi.org/10.1016/j.epsl.2016.11.040.

Graham, S., DeMets, C., Cabral-Cano, E., Kostoglodov, V., Rousset, B., Walpersdorf, A., Cotte, N., Lasserre, C., McCaffrey, R. & Salazar-Tlaczani, L., 2016. Slow slip history for the MEXICO

subduction zone: 2005 through 2011, *Pure Appl. Geophys.,* **173**, 3445-3465, DOI 10.1007/s00024-015-1211-x.

Graham, S., DeMets, C., Cabral-Cano, E., Kostoglodov, V., Walpersdorf, A., Cotte, N., Brudzinski, M., McCaffrey, R. & and Salazar-Tlaczani, L., 2014a. GPS constraints on the 2011/12 Oaxaca slow slip event that preceded the 20 March 2012 Ometepec earthquake, southern Mexico, *Geophys. J. Int.,* **197**(3), 1593–1607.

Graham, S., DeMets, C., Cabral-Cano, E., Kostoglodov, V., Walpersdorf, A., Cotte, N., Brudzinski, M., McCaffrey, R. & Salazar-Tlaczani, L., 2014b. GPS constraints on the M_w = 7.5 Ometepec earthquake sequence, southern Mexico: coseismic and post-seismic deformation, *Geophys. J. Int*., **199**, 200-218, doi: 10.1093/gji/ggu167.

Hayes, G.P., Wald, D.J. & Johnson, R.L., 2012. Slab1.0: A three-dimensional model of global subduction zone geometries, *J. geophys. Res*., **117**, B01302, doi:10.1029/2011JB008524.

Hu, Y., & Wang, K., 2012. Spherical-Earth finite element model of short-term postseismic deformation following the 2004 Sumatra earthquake, *J. geophys. Res*., **117**, B05404, doi: 10.1029/2012JB009153.

Hu, Y., Wang, K., He, J., Klotz, J. & Khazaradze, G., 2004. Three- dimensional viscoelastic finite element model for post-seismic deformation of the great 1960 Chile earthquake, *J. geophys. Res.*, **109**, B12403, doi:10.1029/2004JB003163.

Hutton, W., DeMets, C., Sánchez, O., Suárez, G. & Stock, J., 2001. Slip kinematics and dynamics during and after the 1995 October 9 Mw=8.0 Colima-Jalisco earthquake, Mexico, from GPS geodetic constraints, *Geophys. J. Inter*., **146**, 637–658.

Iglesias, A., Singh, S., Lowry, A., Santoyo, M., Kostoglodov, V., Larson, K. & Franco-Sánchez, S., 2004. The silent earthquake of 2002 in the Guerrero seismic gap, Mexico (M_w = 7.6): inversion of slip on the plate interface and some implications, *Geofis. Int.*, **43**, 309–317.

Johnson, K.M. & Tebo, D., 2018. Capturing 50 years of postseismic mantle flow at Nankai subduction zone, *J. geophys. Res. – Sol. Ea.*, **123**, 10091–10106. https://doi.org/10.1029/2018JB016345.

Kim, Y., Clayton, R.W. & Jackson, J.M., 2010. Geometry and seismic properties of the subducting Cocos plate in central Mexico, *J. geophys. Res*., **115**, B06310, doi:10.1029/2010JB006942.

Kogan, M.G., Vasilenko, N.F., Frolov, D.I., Freymueller, J.T., Steblov, G.M., Prytkov, A.S. & Ekstrom, G., 2013. Rapid postseismic relaxation after the great 2006-2007 Kuril earthquakes from GPS observations in 2007-2011, *J. geophys. Res*., **118**, 3691–3706.

Kostoglodov, V., Singh, S.K., Santiago, J.A., Franco, S.I., Larson, K.M., Lowry, A.R. and Bilham, R., 2003. A large silent earthquake in the Guerrero seismic gap, Mexico, *Geophys. Res. Lett*., **30**, 1807, doi:10.1029/2003GL017219.

Kostoglodov, V., Husker, A., Shapiro, N.M., Payero, J.S., Campillo, M., Cotte, N. & Clayton, R., 2010. The 2006 slow slip event and nonvolcanic tremor in the Mexican subduction zone, *Geophys. Res. Lett*., **37**, L24301, doi:10.1029/2010GL045424.

Larson, K.M., Kostoglodov, V., Miyazaki, S.I. & Santiago, J.A.S., 2007. The 2006 aseismic slow slip event in Guerrero, Mexico: new results from GPS, *Geophys. Res. Lett*., **34**, L13309, doi:10.1029/2007GL029912.

Li, S., Moreno, M., Bedford, J., Rosenau, M. & Oncken, O., 2015. Revisiting viscoelastic effects on interseismic deformation and locking degree: A case study of the Peru-North Chile subduction zone, *J. Geophys. Res. – Sol. Ea*., **120**, 4522–4538, doi:10.1002/ 2015JB011903.

Lin, Y.-n. N., Sladen, A., Ortega-Culaciati, F., Simons, M., Avouac, J.P., Fielding, E.J., Brooks, B.A., Bevis, M., Genrich, J., Rietbrock, A., Vigny, C., Smalley, R. & Socquet, A., 2013. Coseismic and postseismic slip associated with the 2010 Maule Earthquake, Chile: Characterizing the Arauco Peninsula barrier effect, *J. Geophys. Res. - Sol. Ea.*, **118**, 3142–3159, doi:10.1002/jgrb.50207.

Lowry, A., Larson, K., Kostoglodov, V. & Bilham, R., 2001. Transient fault slip in Guerrero, southern Mexico, *Geophys. Res. Lett*., **28**, 3753–3756.

Malservisi, R., Schwartz, S.Y., Voss, N., Protti, M., González, V., Dixon, T., Jiang, Y., Newman, A.V., Richardson, J., Walter, J.I. & Voyenko, D., 2015. Multiscale post- seismic behavior on a megathrust: the 2012 Nicoya earthquake, Costa Rica, *Geochem. Geophys. Geosyst*., **16**, http://dx.doi.org/10.1002/2015GC005794.

Márquez-Azúa, B. & DeMets, C., 2003. Crustal velocity field of Mexico from continuos GPS measurements, 1993 to June, 2001: Implications for the neotectonics of Mexico, *J. geophys. Res*., **108**(B9), 2450.

Márquez-Azúa, B., DeMets, C., Cabral-Cano, E. & Salazar-Tlaczani, L., 2015. *TLALOCNet - UGEO-ugeo_tnet_mx1998 P.S., UNAVCO, GPS/GNSS Observations Dataset*, https://doi.org/ 10.7283/T58S4N9N.

Márquez-Azúa, B., DeMets, C. & Masterlark, T., 2002. Strong interseismic coupling, fault afterslip, and viscoelastic flow before and after the Oct. 9, 1995 Colima-Jalisco earthquake: Continuous GPS measurements from Colima, Mexico, *Geophys. Res. Lett*., **29**, 10.1029/ 2002GL014702.

Masterlark, T., DeMets, C., Wang, H.F., Sánchez, O. & Stock, J., 2001. Homogeneous vs heterogeneous subduction zone models: Coseismic and postseismic deformation, *Geophys. Res. Lett.*, **28**(21), 4047-4050.

Maubant, L., Pathier, E., Daout, S., Radiget, M., Doin, M.-P., Kazachkina, E., Kostoglodov, V., Cotte, N. & Walpersdorf, A., 2020. Independent Component Analysis and Parametric Approach for Source Separation in InSAR Time Series at Regional Scale: Application to the 2017-2018 Slow Slip Event in Guerrero (Mexico), *J. geophys. Res. - Sol. Ea.*, **25**, e2019JB018187, https://doi.org/10.1029/2019JB018187.

McCaffrey, R., 2005. Block kinematics of the Pacific-North America plate boundary in th southwestern United States from inversion of GPS, seismological, and geologic data, *J. geophys. Res.*, **110**, B07401, doi:10.1029/2004JB003307.

McCaffrey, R., 2009. Time-dependent inversion of three-component continuous GPS for steady and transient sources in northern Cascadia, *Geophys. Res. Lett*., **36**, L07304, doi:10.1029/2008GL036784.

Melbourne, T., Carmichael, I., DeMets, C., Hudnut, K., Sánchez, O., Stock, J., Suárez, G. & Webb, F., 1997. The geodetic signature of the M=8.0 October 9, 1995, Jalisco subduction earthquake, *Geophys. Res. Lett*., **24**, 715–718.

Mendoza, C. & Hartzell, S., 1999. Fault-slip distribution of the 1995 Colima-Jalisco, Mexico, earthquake, *Bull. Seismol. Soc. Am*., **89**(5) 1338-1344.

Okada, Y., 1985. Surface deformation to shear and tensile faults in a half-space, *Bull. Seismol. Soc. Am*., **75**, 1135-1154.

Okada, Y., 1992. Internal deformation due to shear and tensile faults in a half-space, *Bull*. *Seismol. Soc. Am*., **82**, 1018-1040.

Ortiz, M., Singh, S.K., Pacheco, J. & Kostoglodov, V., 1998. Rupture length of the October 9, 1995 Colima-Jalisco earthquake (M_w 8) estimated from tsunami data, *Geophys. Res. Lett*., **25**(15), 2857-2860.

Pacheco, J.F. & Singh, S.K., 2010. Seismicity and state of stress in Guerrero segment of the Mexican subduction zone, *J. Geophys. Res. - Sol. Ea.*, **115**, B01303, doi:10.1029/2009JB006453.

Pacheco, J., Singh, S.K., Domínguez, J., Hurtado, A., Quintanar, L., Jiménez, Z., Yamamoto, J., Gutiérrez, C., Santoyo, M., Bandy, W., Guzmán, M., & Kostoglodov, V., 1997. The October 9, 1995 Colima-Jalisco, Mexico earthquake (M_w 8): An aftershock study and a comparison of the earthquake with those of 1932, *Geophys. Res. Lett.*, **24**(17), 2223-2226.

Pardo, M. & Suárez G., 1995. Shape of the subducted Rivera and Cocos plates in southern Mexico: Seismic and tectonic implications, *J. geophys. Res*., **100**, B7, 12357-12373.

Payero, J.S., Kostoglodov, V., Shapiro, N., Mikumo, T., Iglesias, A., Pérez-Campos, X. & Clayton, R.W., 2008. Nonvolcanic tremor observed in the Mexican subduction zone, *Geophys. Res. Lett*., **35**, L07305. http://dx.doi.org/10.1029/2007GL032877.

Peña, C., Heidbach, O., Moreno, M., Bedford, J., Ziegler, M., Tassara, A. & Oncken, O., 2019. Role of Lower Crust in the Postseismic Deformation of the 2010 Maule Earthquake: Insights from a Model with Power-Law Rheology, *Pure Appl. Geophys*., **176**, 3913-3928, https://doi.org/ 10.1007/s00024-018-02090-3.

Pérez-Campos, X., Kim, Y.H., Husker, A., Davis, P.M., Clayton, R.W., Iglesias, A., Pacheco, J., Singh, S.K., Manea, V.C. & Gurnis, M., 2008. Horizontal subduction and truncation of the Cocos Plate beneath central Mexico, *Geophys. Res. Lett.,* **35**, L18303, doi:10.1029/2008GL035127.

Pollitz, F.F., Burgmann, R. & Segall P., 1998. Joint estimation of afterslip rate and postseismic relaxation following the 1989 Loma Prieta earthquake, *J. geophys. Res*., **103**(B11), 26,975–26,992.

Quintanar, L., Rodríguez-Lozoya, H.E., Ortega, R., Gómez-González, J.M., Domínguez, T., Javier, C., Alcántara, L. & Rebollar, C.J., 2010. Source characteristics of the 22 January 2003 M_w = 7.5 Tecomán, Mexico, Earthquake: New insights, *Pure Appl. Geophys*., **168**, 1339–1353, DOI 10.1007/s00024-010-0202-1.

Radiguet, M., Cotton, F., Vergnolle, M., Campillo, M., Walpersdorf, A., Cotte, N. & Kostoglodov, V., 2012. Slow slip events and strain accumulation in the Guerrero gap, Mexico, *J. geophys. Res*., **117**, B04305, doi:10.1029/2011JB008801.

Reyes, A., Brune, J.N. & Lomnitz, C., 1979. Source mechanism and aftershock study of the Colima, Mexico earthquake of January 30, 1973, *Bull. Seismol. Soc. Am*., **69**, 1819-1840.

Schmitt, S. V., DeMets, C., Stock, J., Sánchez, O., Márquez-Azúa, B. & Reyes, G., 2007. A geodetic study of the 2003 January 22 Tecomán, Colima, Mexico earthquake, *Geophys. J. Int.,* **169**, 389–406, doi: 10.1111j.1365-246X.2006.03322.x.

Scholz, C.H., 2002. *The Mechanics of Earthquakes and Faulting*. Cambridge University Press.

Selvans, M.M., Stock, J.M., DeMets, C., Sánchez, O. & Márquez-Azúa, B., 2011. Constraints on Jalisco Block Motion and Tectonics of the Guadalajara Triple Junction from 1998–2001 Campaign GPS Data, *Pure Appl. Geophys*., **168**, 1435–1447, https://doi.org/10.1007/s00024-010-0201-2.

Singh, S.K., Pacheco, J.F., Alcántara, L., Reyes, G., Ordaz, M., Iglesias, A., Alcocer, S.M., Gutiérrez, C., Valdés, C., Kostoglodov, V., Reyes, C., Mikumo, T., Quaas, R. & Anderson, G.,

2003. A Preliminary Report on the Tecomán, Mexico Earthquake of 22 January 2003 (M_W 7.4) and its Effects, *Sesimol. Res. Lett*., **74**(3), 279-289.

Singh, S.K., Ponce, L. & Nishenko, S.P., 1985. The great Jalisco, Mexico, earthquakes of 1932: Subduction of the Rivera plate, *Bull. Seismol. Soc. Am*., **75**, 1301-1314.

Suárez, G. & Sánchez, O., 1996. Shallow depth of seismogenic coupling in southern Mexico: implications for the maximum size of earthquakes in the subduction zone, *Phys. Earth planet. Inter.,* **93**, 53–61.

Suhardja, S.K., Grand, S.P., Wilson, D., Guzman-Speziale, M., Gómez- González, J.M., Domínguez-Reyes, T. & Ni, J., 2015. Crust and subduction zone structure of Southwestern Mexico, *J. Geophys. Res. – Sol. Ea.*, **120**, 1020–1035, doi:10.1002/2014JB011573.

Suito, H. & Freymueller, J.T., 2009. A viscoelastic and afterslip postseismic deformation model for the 1964 Alaska earthquake, *J. geophys. Res.*, **114**, B11404, doi:1029/2008JB005954.

Sun, T. & Wang K., 2015. Viscoelastic relaxation following subduction earthquakes and its effects on afterslip determination, *J. Geophys. Res. – Sol. Ea.*, **120**, 1329–1344, doi:10.1002/ 2014JB011707.

Sun, T., Wang, K. & He, J., 2018. Crustal deformation following great subduction earthquakes controlled by earthquake size and mantle rheology, *J. Geophys. Res. – Sol. Ea.*, **123**, 5323-5345, https://doi.org/10.1029/2017JB015242.

Sun, T., Wang, K., Iinuma, T., Hino, R., He, J., Fujimoto, H., Kido, M., Osada, Y., Miura, S., Ohta, Y. & Hu, Y., 2014. Prevalence of viscoelastic relaxation after the 2011 Thoku-oki earthquake, *Nature*, **514**, 84-87, doi:10.1038/nature13778.

Trubienko, O., Fleitout, L., Garaud, J.-D. & Vigny, C., 2013. Interpretation of interseismic deformations and the seismic cycle associated with large subduction earthquakes, *Tectonophysics*, **589**, 126–141.

UNAVCO Community, 2014, *TLALOCNet - TNCM-TNCM_TNET_MX2014 P.S., UNAVCO, GPS/GNSS Observations Dataset*, https://doi.org/10.7283/T5B856FW.

UNAVCO Community, 2014, *TLALOCNet - TNMR-TNMR_TNET_MX2014 P.S., UNAVCO, GPS/GNSS Observations Dataset*, https://doi.org/10.7283/T5Z036FZ.

UNAVCO Community, 2015, *TLALOCNet - PENA-PENA-TNET-MX2015 P.S., UNAVCO, GPS/GNSS Observations Dataset*, https://doi.org/10.7283/T5891464.

UNAVCO Community, 2015, *TLALOCNet - TNCC-TNCC_TNET_MX2015 P.S., UNAVCO, GPS/GNSS Observations Dataset*, https://doi.org/10.7283/T50R9MSK.

UNAVCO Community, 2015, *TLALOCNet - TNLC-TNLC_TNET_MX2015 P.S., UNAVCO, GPS/GNSS Observations Dataset*, https://doi.org/10.7283/T5CZ35J8.

UNAVCO Community, 2015, *TLALOCNet - TNMZ-Manzanilo_TNET_MX_2015 P.S., UNAVCO, GPS/GNSS Observations Dataset*, https://doi.org/10.7283/03FG-YJ81.

UNAVCO Community, 2017, TLALOCNet - *TNCT-Chalacatepec__TNET_MX_2017 P.S., UNAVCO, GPS/GNSS Observations Dataset*, https://doi.org/10.7283/JCTK-TZ92.

UNAVCO Community, 2017, *TLALOCNet - TNTM-Tamarindo_TNET_MX_2017 P.S., UNAVCO, GPS/GNSS Observations Dataset*, https://doi.org/10.7283/PN65-9M91.

UNAVCO Community & DeMets, C., 2007. *Jalisco GPS Network - PENA-US Gypsum Mine at Pena Colorada P.S., UNAVCO, GPS/GNSS Observations Dataset*, https://doi.org/10.7283/T5K35S10.

Vergnolle, M., Walpersdorf, A., Kostoglodov, V., Tregoning, P., Santiago, J.A., Cotte, N., and Franco, S.I., 2010. Slow slip events in Mexico revised from the processing of 11 year GPS observations, *J. geophys. Res*., **115**, B08403, doi:10.1029/2009JB006852.

Wang, K., 2007. Elastic and viscoelastic models of crustal deformation in subduction earthquake cycles, in *The Seismogenic Zone Experiment*, ed. Dixon, T., Columbia Univ. Press.

Wang, K., Hu, Y. & He, J., 2012. Deformation cycles of subduction earthquakes in a viscoelastic Earth, *Nature,* **484**, 327-332, doi:10.1038/nature11032.

Watkins, W.D., Thurber, C.H., Abbott, E.R. & Brudzinski, M.R., 2018. Local earthquake tomography of the Jalisco, Mexico region, *Tectonophysics*, **724–725**, 51–64, https://doi.org/10.1016/j.tecto.2018.01.002.

Wessel, P. & Smith, W.H.F., 1991. Free software helps map and display data, *EOS Trans. AGU*, **72**(41), 445–446. doi:10.1029/90EO00319.

Wiseman, K., Bürgmann, R., Freed, A.M. & Banerjee, P., 2015. Viscoelastic relaxation in a heterogeneous Earth following the 2004 Sumatra-Andaman earthquake, *Earth Planet. Sci. Lett.,* **431**, 308–317, http://dx.doi.org/10.1016/j.epsl.2015.09.024.

Yagi, Y., Mikumo, T., Pacheco, J. & Reyes, G., 2004. Source rupture process of the Tecomán, Colima, Mexico Earthquake of 22 January 2003, determined by joint inversion of teleseismic body-wave and near-source data, *Bull. Seismol. Soc. Am.,* **94**(5), 1795-1807.

Yoshioka, S., Mikumo, T., Kostoglodov, V., Larson, K., Lowry, A. & Singh, S., 2004. Interplate coupling and a recent aseismic slow slip event in the Guerrero seismic gap of the Mexican subduction zone, as deduced from GPS data inversion using a Bayesian information criterion, *Phys. Earth planet. Inter*., **146**, 513–530.

Zumberge, J.F., Heflin, M.B., Jefferson, D.C., Watkins, M.M. & Webb, F.H., 1997. Precise point positioning for the efficient and robust analysis of GPS data from large networks, *J. geophys. Res*., **102**, 5005–5017.

FIGURES

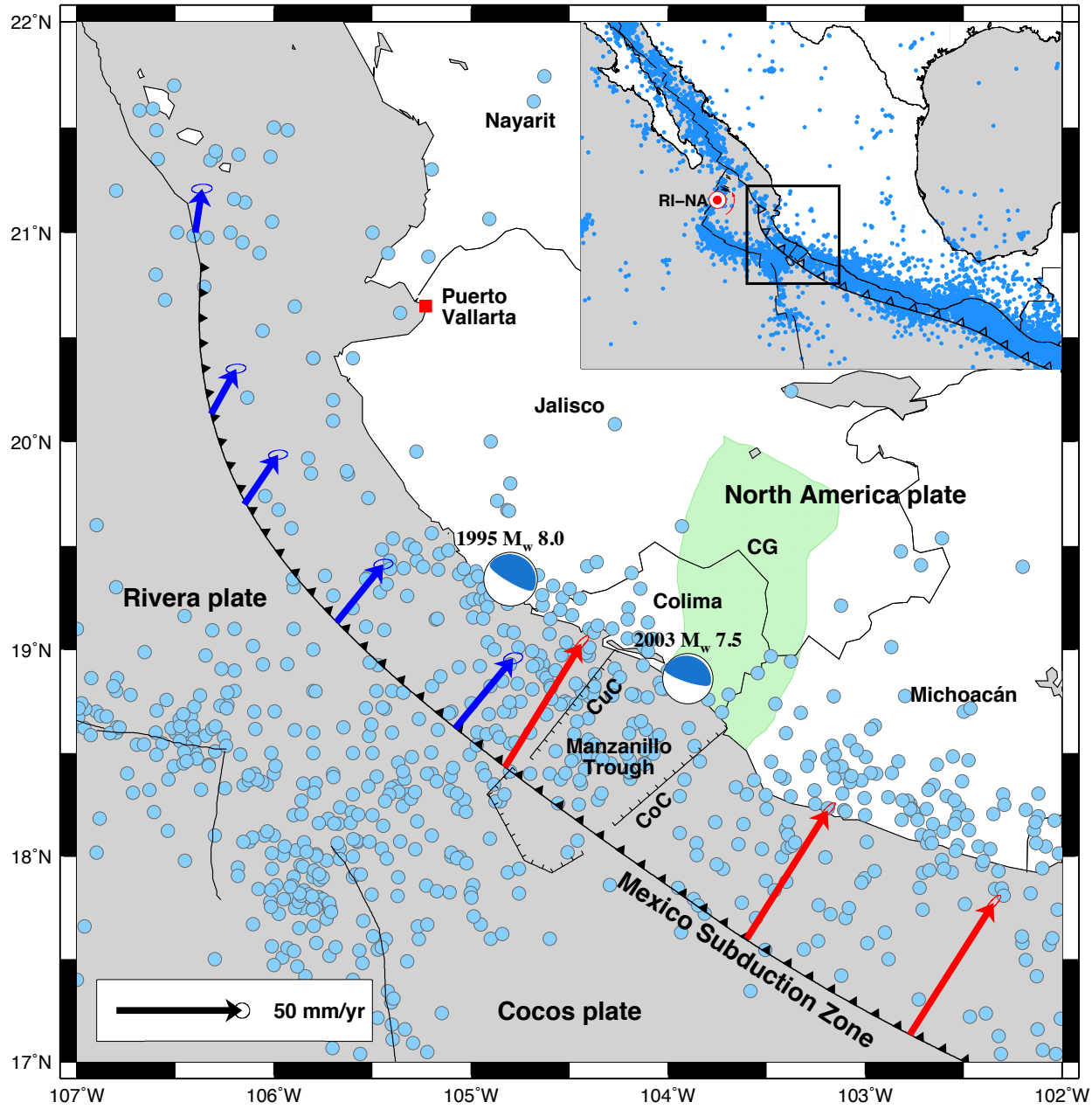

Figure 1.1. Tectonic setting. Focal mechanisms from the Global Centroid Moment Tensor (gCMT) catalog. Arrows indicate velocities of Cocos (red) and Rivera (blue) plates relative to North America plate, as predicted by the MORVEL global plate motion model (DeMets *et al*. 2010). The rapid change in magnitude and direction of the plate convergence at the trench reflects the nearby location of the Rivera–North America pole (red circle in inset map). Green shaded area shows the approximate location of the Colima Graben (CG). CoC: Coahuayana canyon. CuC: Cuyutlán canyon. Blue circles show the M ≥ 3.0 earthquakes with depths ≤ 60 km from 1962 to 2017 from the United States Geologic Survey (USGS) catalog. The seismicity suggests distributed shear across a diffuse Rivera–Cocos plate boundary (DeMets & Wilson 1997).

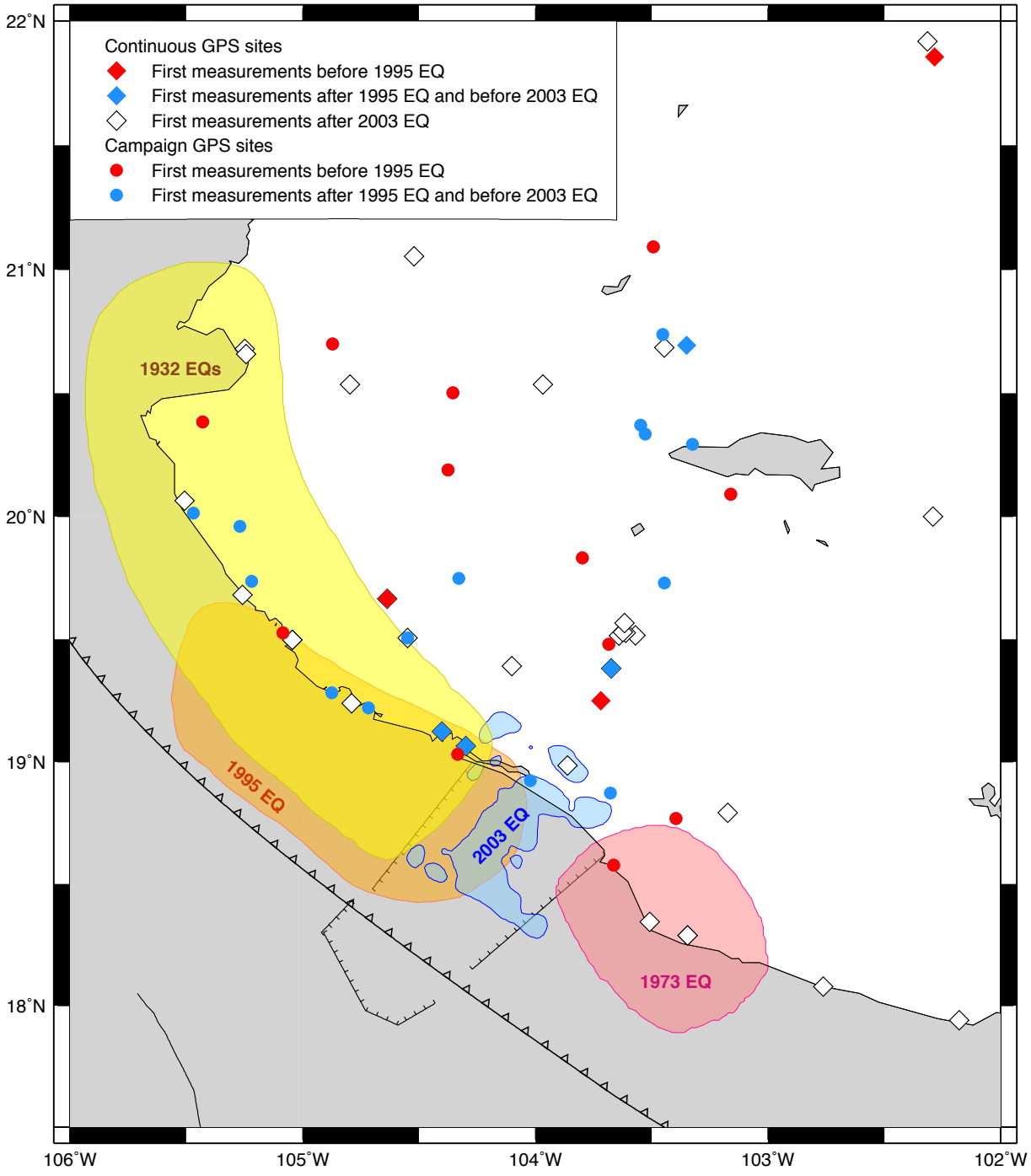

Figure 1.2. Locations of the GPS stations used in this study. The yellow patch is the total estimated aftershock area of the 3 and 18 June 1932 earthquakes (Singh *et al*. 1985). Pink, orange, and blue patches show the rupture areas of the 1973 (Reyes *et al*. 1979), 1995 (Pacheco *et al*. 1997) and 2003 (Yagi *et al*. 2004) earthquakes, respectively.

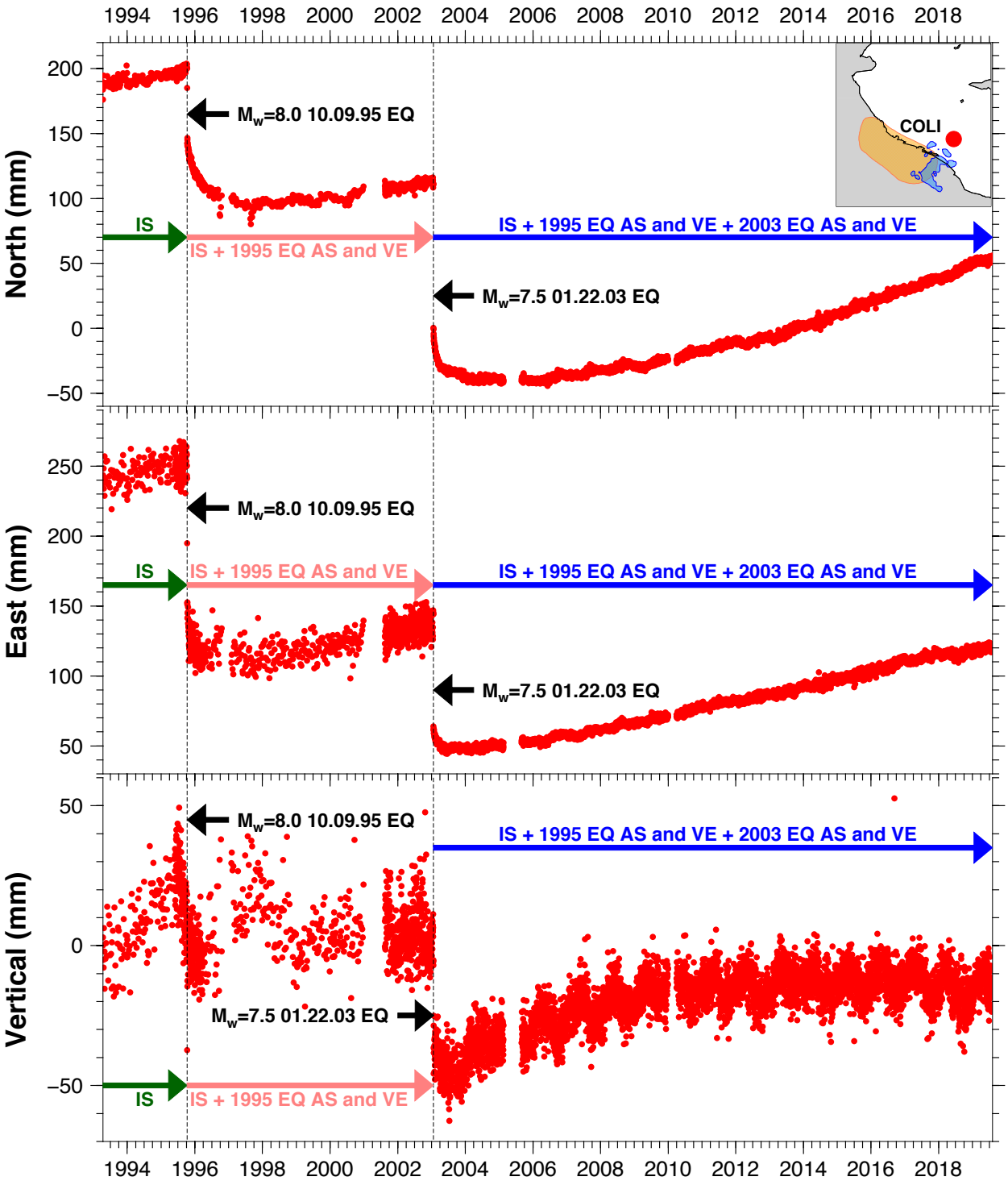

Figure 1.3. GPS station COLI daily positions (north, east and vertical) from 1993 to 2019 (location on inset, along with rupture areas of the 1995 and 2003 earthquakes from Fig. 1.2). IS: interseismic, EQ: earthquake, AS: postseismic afterslip, VE: postseismic viscoelastic rebound. The green arrow delimits a period in which only interseismic motion is present. The pink arrow indicates the appearence of the postseismic effects triggered by the 1995 EQ superimposed over the interseismic motion. The blue arrow indicates the appearance of the postseismic effects triggered by the 2003 EQ superimposed over the interseismic motion and the postseismic effects of the 1995 EQ.

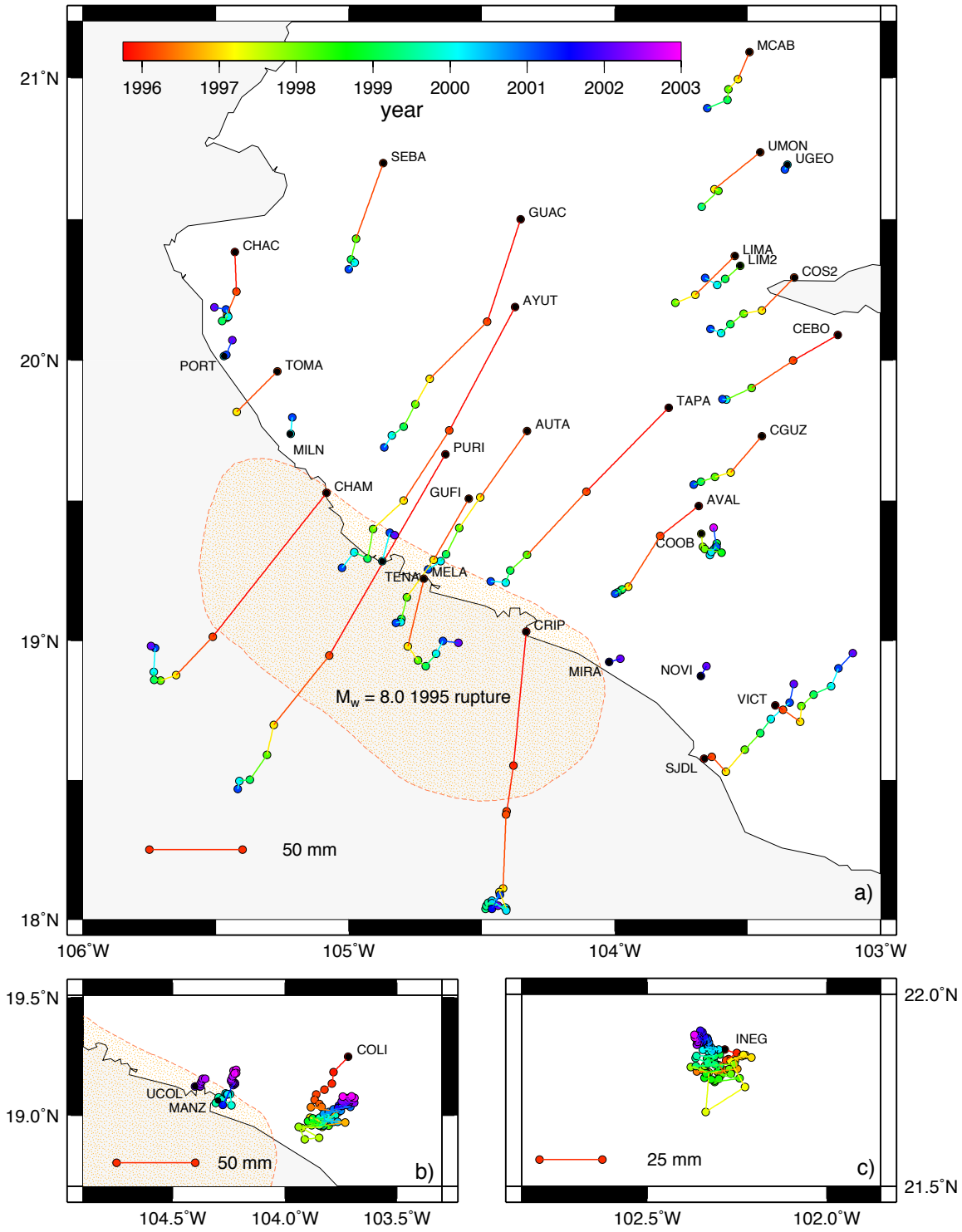

Figure 1.4. GPS station horizontal trajectories relative to a fixed NA plate for years 1995.77–2003.00. Color scale specifies time–progressive color coding along the site trajectories. Black dots mark the time series origins at the site locations. Dashed orange line delimits the 1995 earthquake rupture area. a) Campaign sites. b) Continuous sites: each point shows the 30 day mean location for a site. c) Continuous site farther inland.

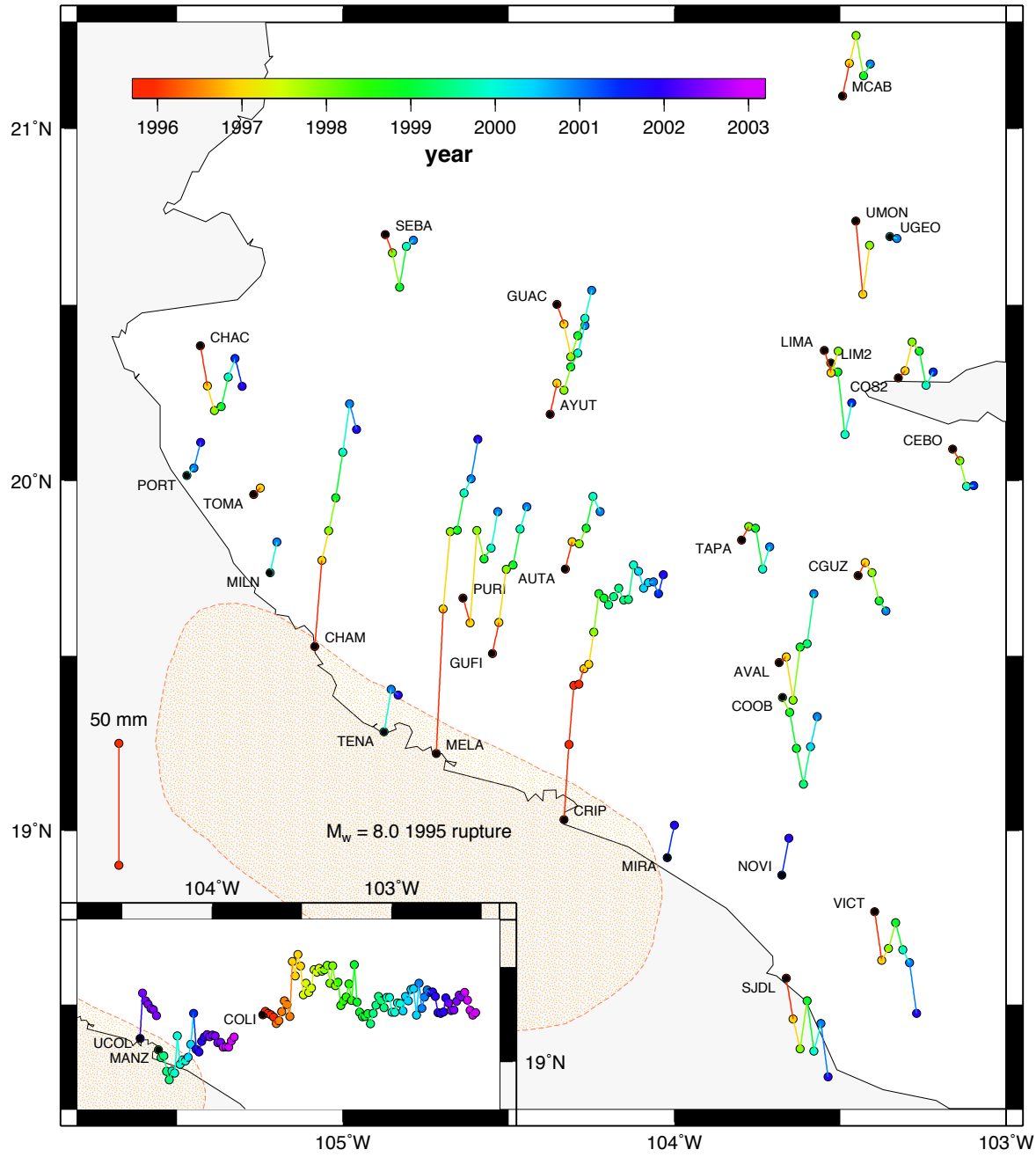

Figure 1.5. GPS station vertical trajectories for 1995.77–2003.00. Positions are progressively shifted to the right to help visualization. Color scale specifies time–progressive color coding along the site trajectories. Site displacements with increasing time toward the northern map boundary indicate station uplift, whereas displacements toward the southern boundary indicate site subsidence, with time increasing eastward (to the right) on the map. Black dots mark the time series origins at the site locations. Dashed orange line delimits the 1995 earthquake rupture area. Campaign sites are shown in the main figure. Continuous sites are shown in the inset, where each point shows the 30 day mean location for a site.

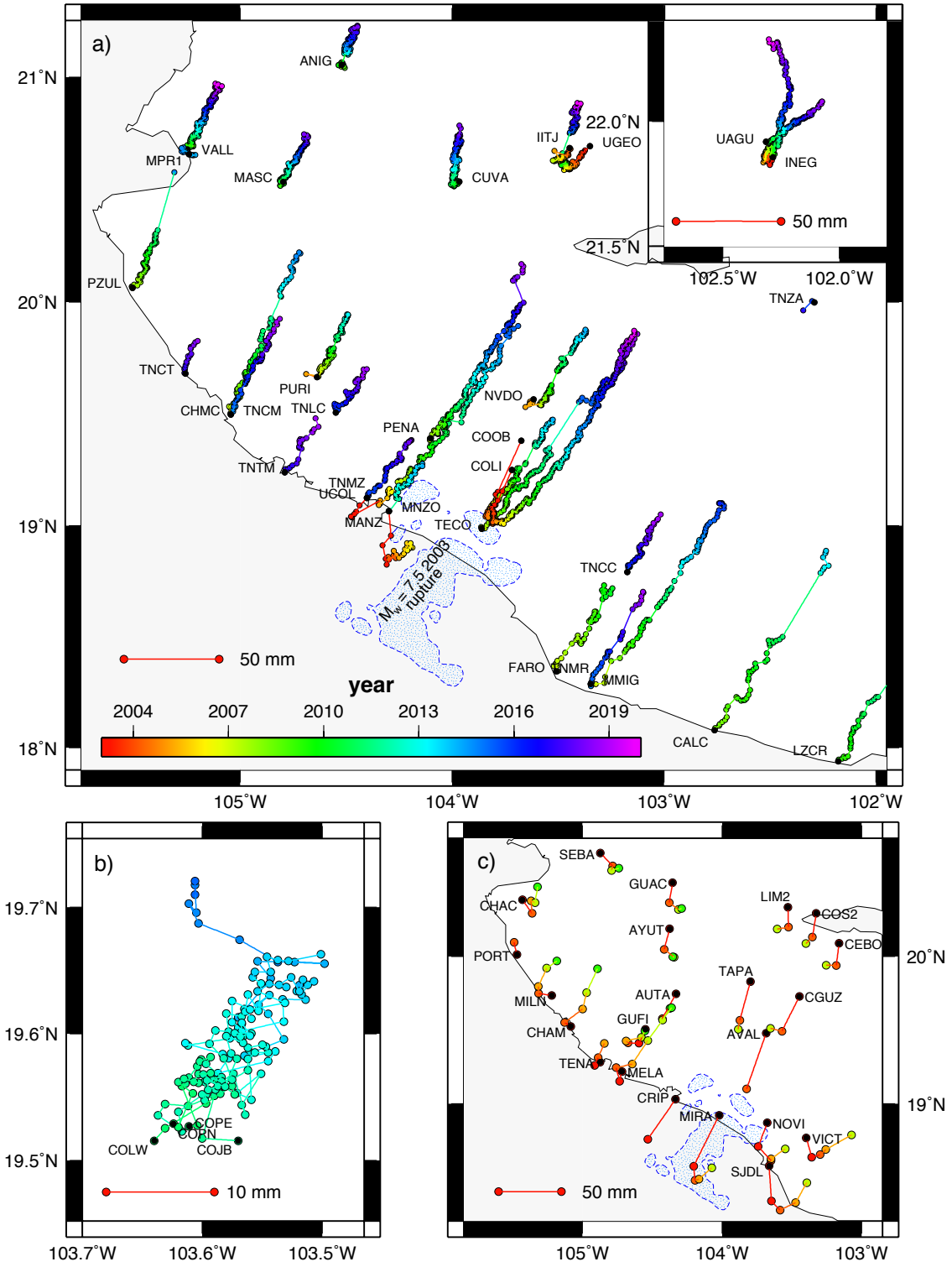

Figure 1.6. GPS station horizontal trajectories relative to a fixed NA plate for years 2003.08–2020.00. Color scale specifies time–progressive color coding along the site trajectories. Black dots mark the time series origins at the site locations. The 2003 earthquake rupture area is shown in blue. a) Continuous GPS sites: each point shows the 30 day mean position for a given site. Inset shows two continuous sites farther inland. b) Continuous sites installed near the Nevado de Colima volcano. c) Campaign sites.

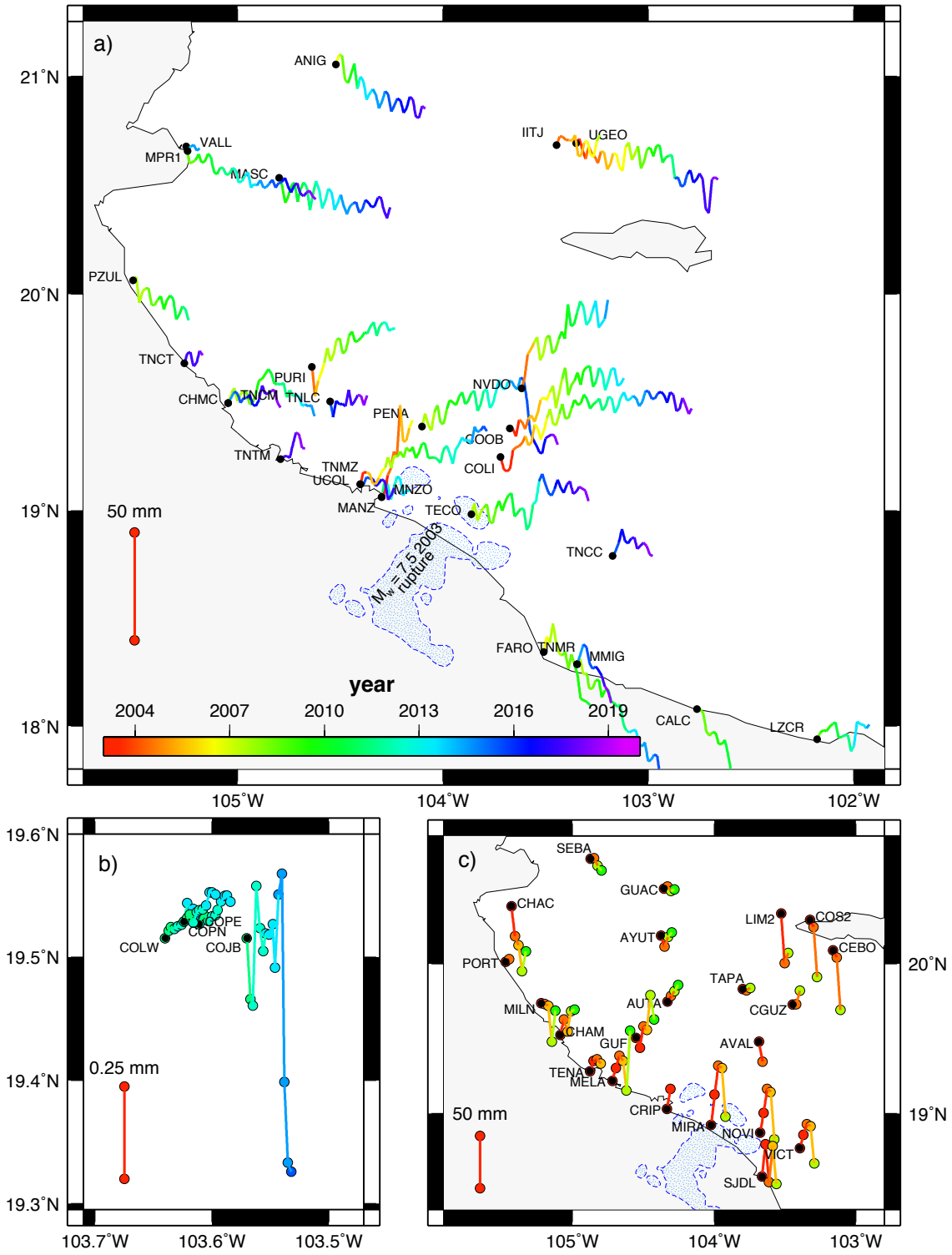

Figure 1.7. GPS station vertical trajectories for years 2003.08–2020.00. Color scale specifies time–progressive color coding along the site trajectories. Black dots mark the time series origins at the site locations. Site displacements toward the northern map boundary indicate station uplift, whereas displacements toward the southern boundary indicate site subsidence, with time increasing eastward on the map. Blue dashed line delimits the 2003 earthquake rupture area. a) Continuous sites: 0.25 year mean positions. b) Continuous sites installed near the Nevado de Colima volcano. c) Campaign sites.

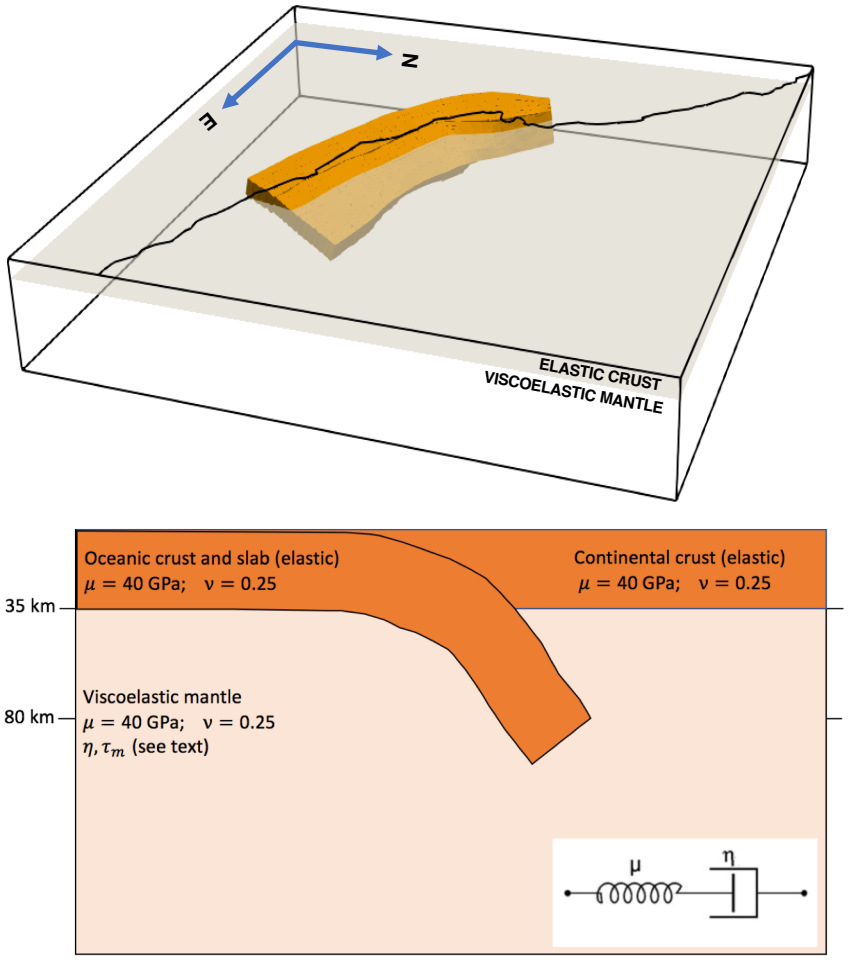

Figure 1.8: Geometry of the computational domain and rheological structure in RELAX modeling. Top: The 3D computational domain is a rectangular grid 512 × 512 × 256 with horizontal and vertical grid steps of 2.5 km. The domain is several times larger than the length of coseismic rupture (not shown). It includes an elastic upper layer (oceanic and continental crust), an elastic subducting slab, and a viscoelastic mantle with characteristic Maxwell time τ_m and viscosity η. Bottom: trench-normal cross section of the model domain (not to scale). The thickness of the elastic crust and slab is 35 km.

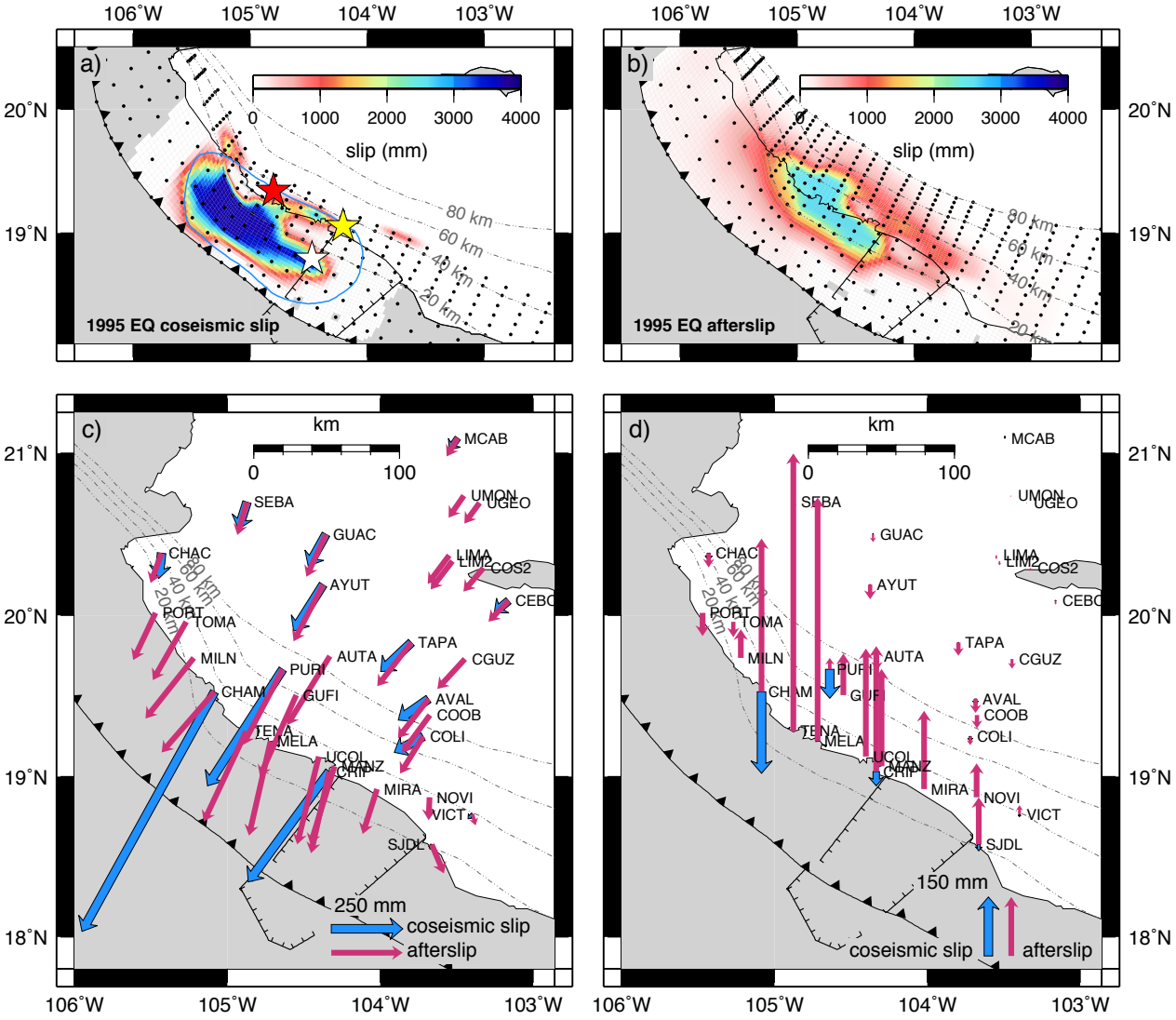

Figure 1.9. TDEFNODE slip solution for a) the 1995 Colima–Jalisco earthquake and b) its postseismic afterslip (integrated over the 1995.77–2020.00 interval) for a model using time series corrected for the viscoelastic effects of a mantle with τ_m = 15 years (see main text). EQ: earthquake. Dashed lines show the slab contours (extended from Hayes *et al*. (2012), see main text) every 20 km. Black dots locate the fault nodes where slip is estimated. The blue line delimits the earthquake aftershock area (Pacheco *et al*. 1997). White, yellow and red stars are the epicenters from Courboulex *et al*. (1997) and USGS, and the centroid from the gCMT catalog (Dziewonski *et al*. 1997), respectively. Panels c) and d) respectively show the horizontal and vertical site motions that are predicted by the coseismic and afterslip solutions from panels a) and b) at sites active during the earthquake for panel c) and sites active between 1995 and 2003 for panel d).

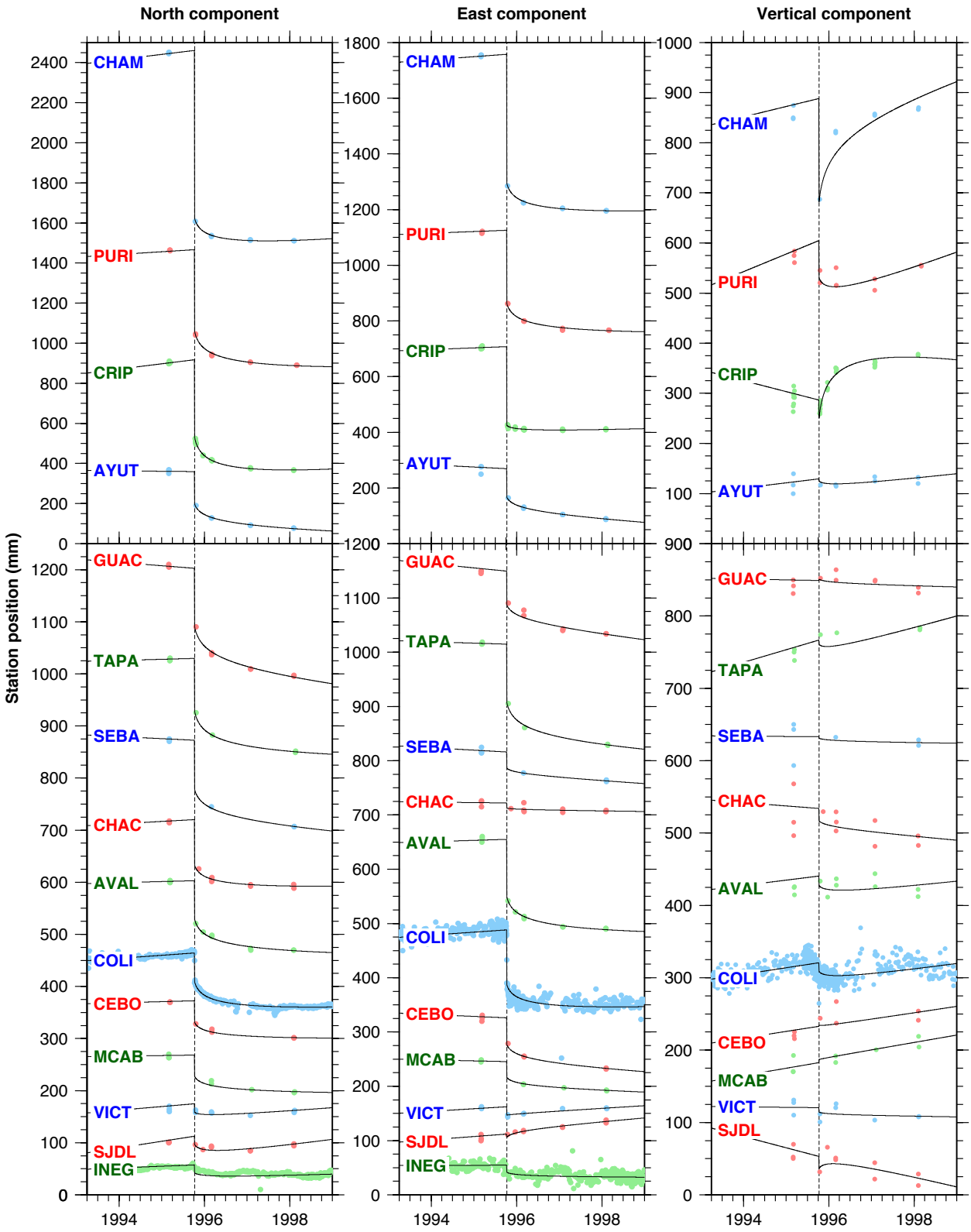

Figure 1.10. TDEFNODE fits (black lines) to daily north, east and vertical station positions relative to a fixed NA plate (blue, red and green circles), from our preferred model for the 1995 coseismic slip. Intercepts are arbitrary. Dashed vertical lines mark the time of the earthquake. Only stations that where operating during the earthquake are shown.

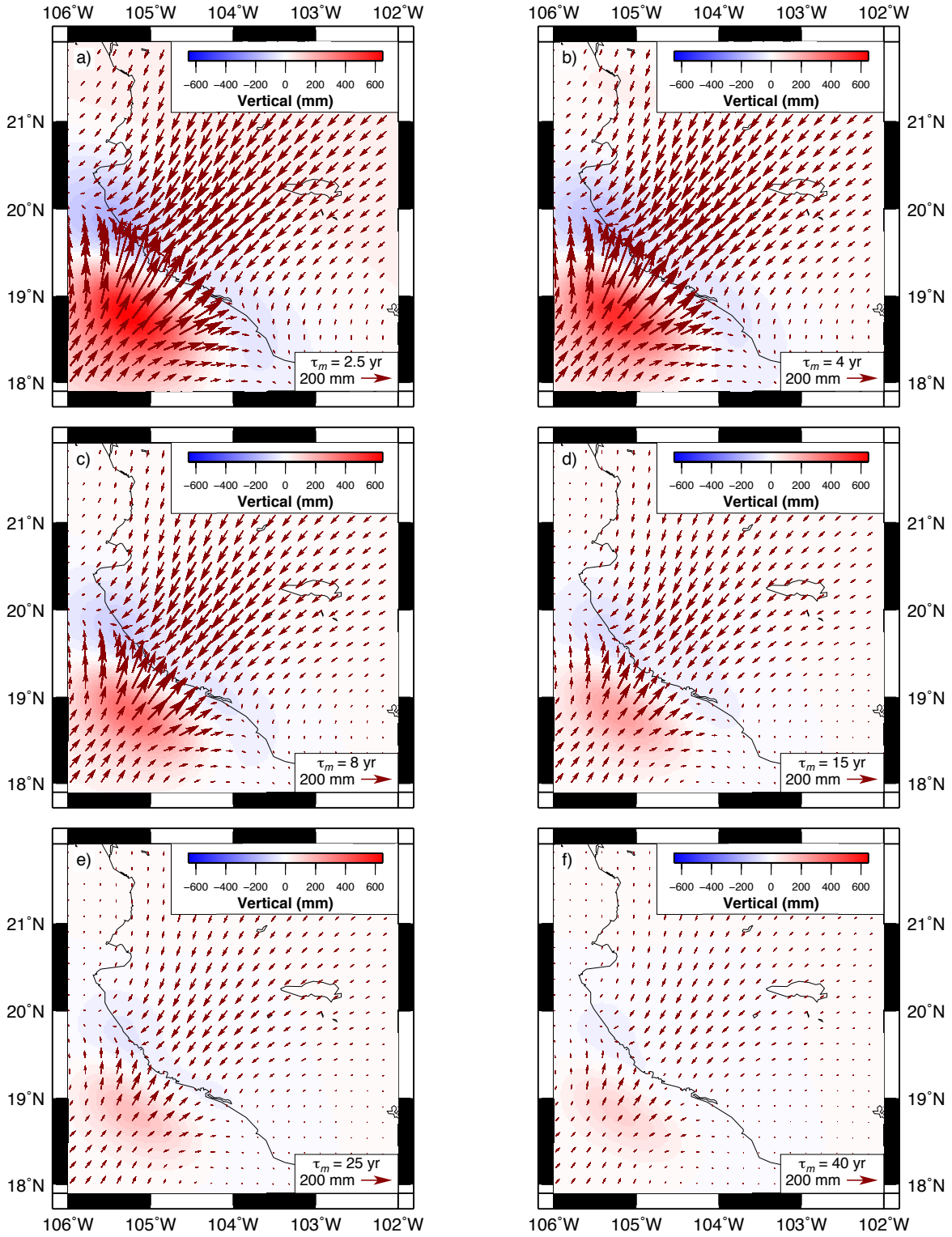

Figure 1.11. Cumulative viscoelastic displacements for the 25–year–long period from 1995.77 to 2020.27 triggered by the 1995 Colima–Jalisco earthquake, as predicted with RELAX software using the preferred 1995 coseismic slip solution from Fig. 1.9a. The displacements shown in each panel were determined using the mantle Maxwell time given in the lower right corner of each panel. Arrows show the horizontal displacements and colors indicate the vertical displacements.

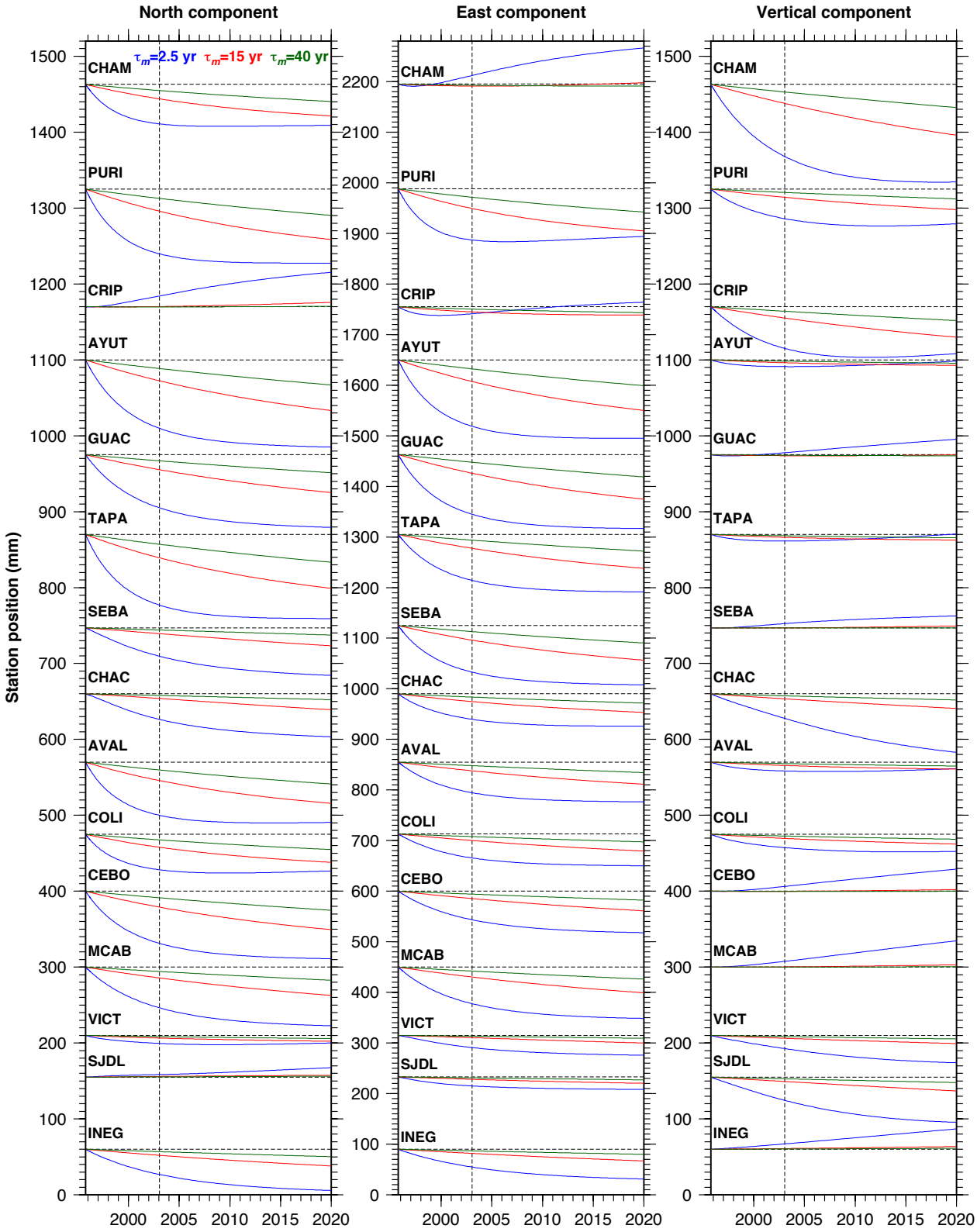

Figure 1.12. Modeled viscoelastic deformation for the 1995 Colima–Jalisco earthquake at GPS sites active during the earhtquake for mantle rheologies corresponding to Maxwell times of 2.5 (blue), 15 (red), and 40 years (green). The dashed vertical lines mark the time of the 2003 Tecomán earthquake.

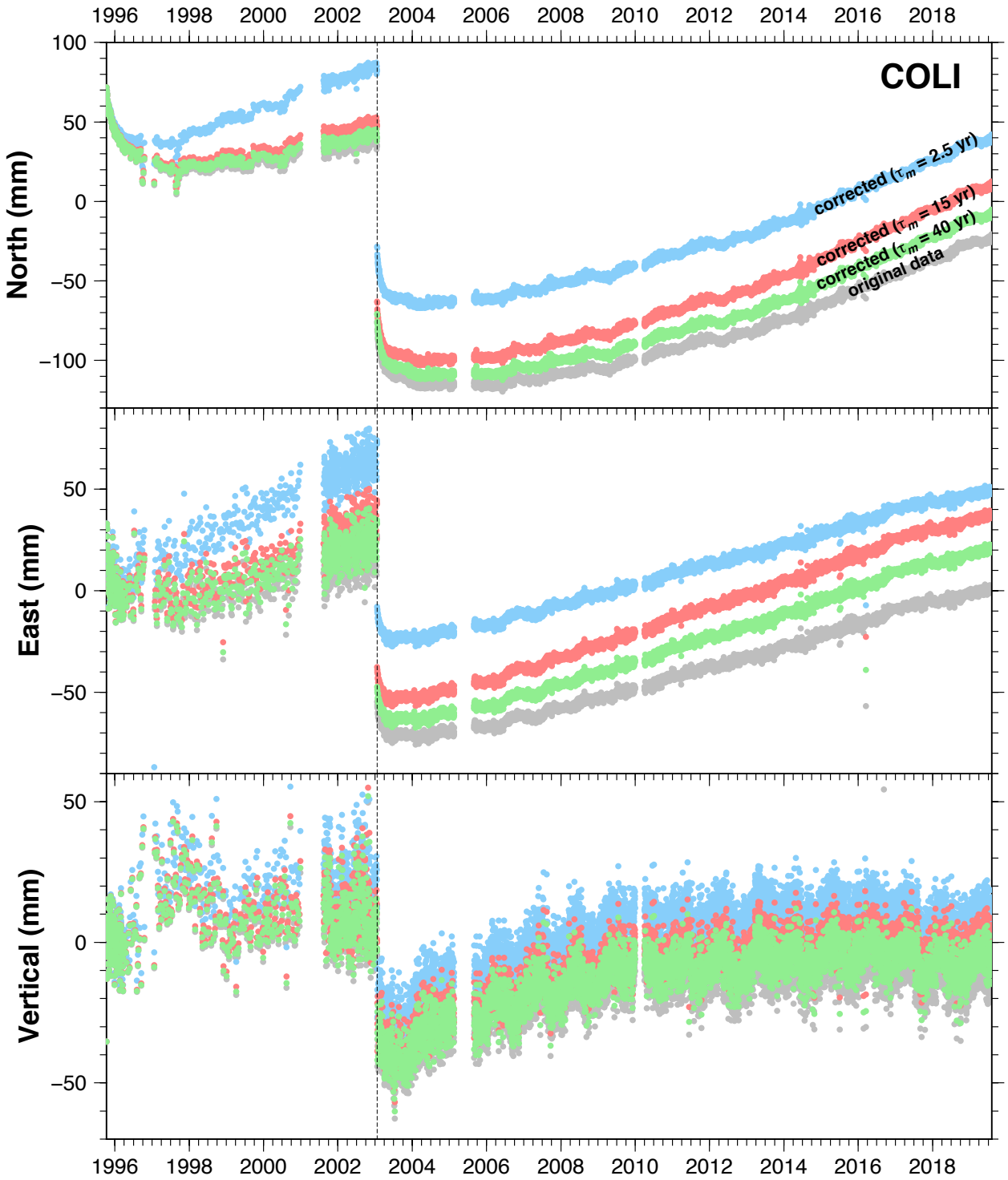

Figure 1.13. Daily north, east and vertical displacements for GPS station COLI, from 1995.77 to 2019.50. Gray dots correspond to the original time series. Blue, red, and green dots correspond to the corrected time series for the 1995 earthquake viscoelastic deformation models using τ_m = 2.5, 15, and 40 years, respectively. The black dashed line marks the time of the 2003 Tecomán earthquake.

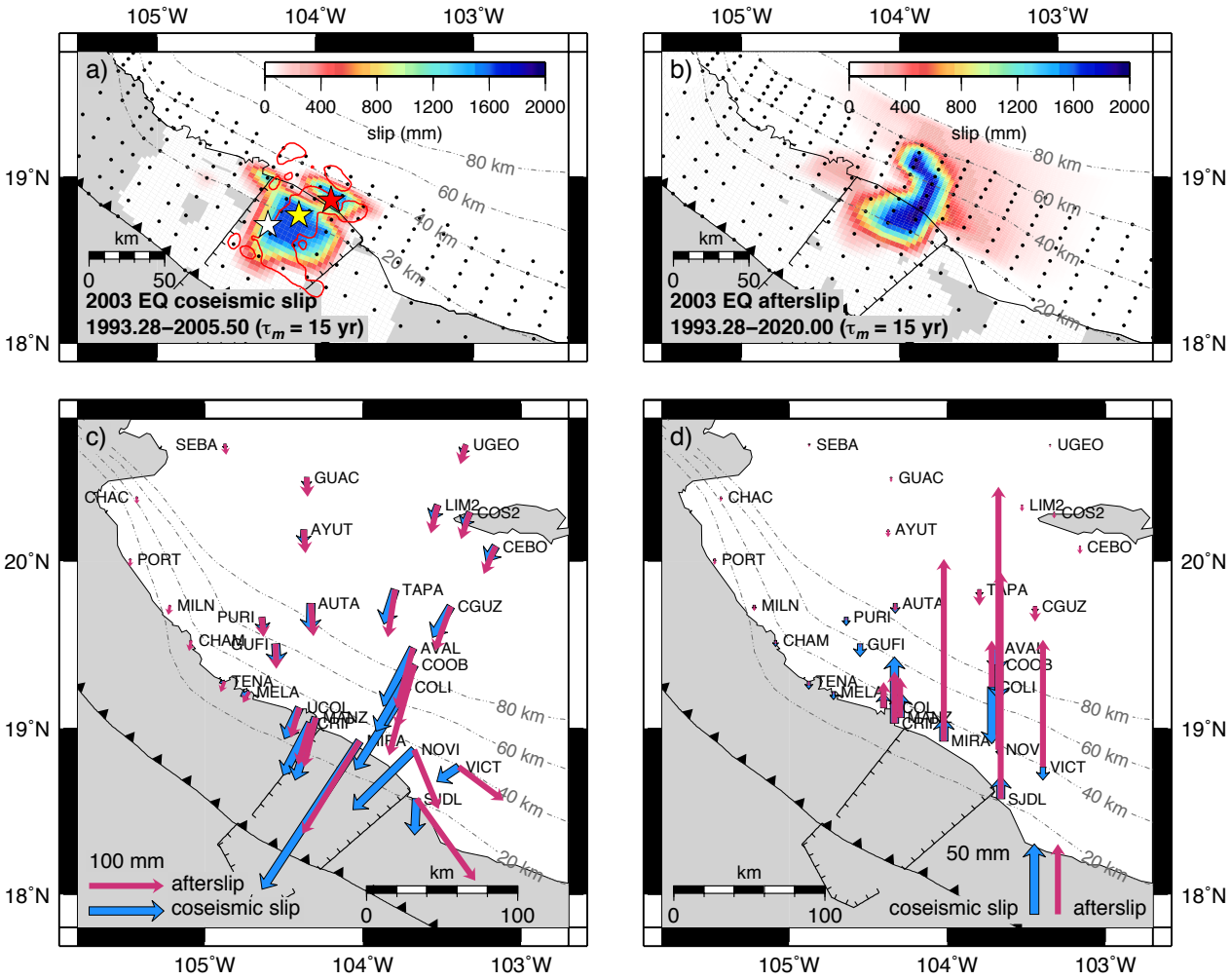

Figure 1.14. TDEFNODE slip solution for a) the 2003 Tecomán earthquake and b) its postseismic afterslip (integrated over the 2003.06–2020.00 interval) for a model using time series corrected for the viscoelastic effects of a mantle with τ_m = 15 years. The inversion used observations from the intervals indicated in panels a) and b) (see main text on details on how these distributions were estimated). EQ: earthquake. Dashed lines show the slab contours every 20 km. Black dots locate the fault nodes where slip is estimated. The red line delimits the rupture area for the earthquake (Yagi *et al*. 2004). White, yellow and red stars are the epicenters from Yagi *et al*. (2004) and USGS, and the centroid from the gCMT catalog (Ekström *et al*. 2004), respectively. Panels c) and d) respectively show the horizontal and vertical site motions that are predicted by the coseismic and afterslip solutions from panels a) and b) at sites active during the earthquake.

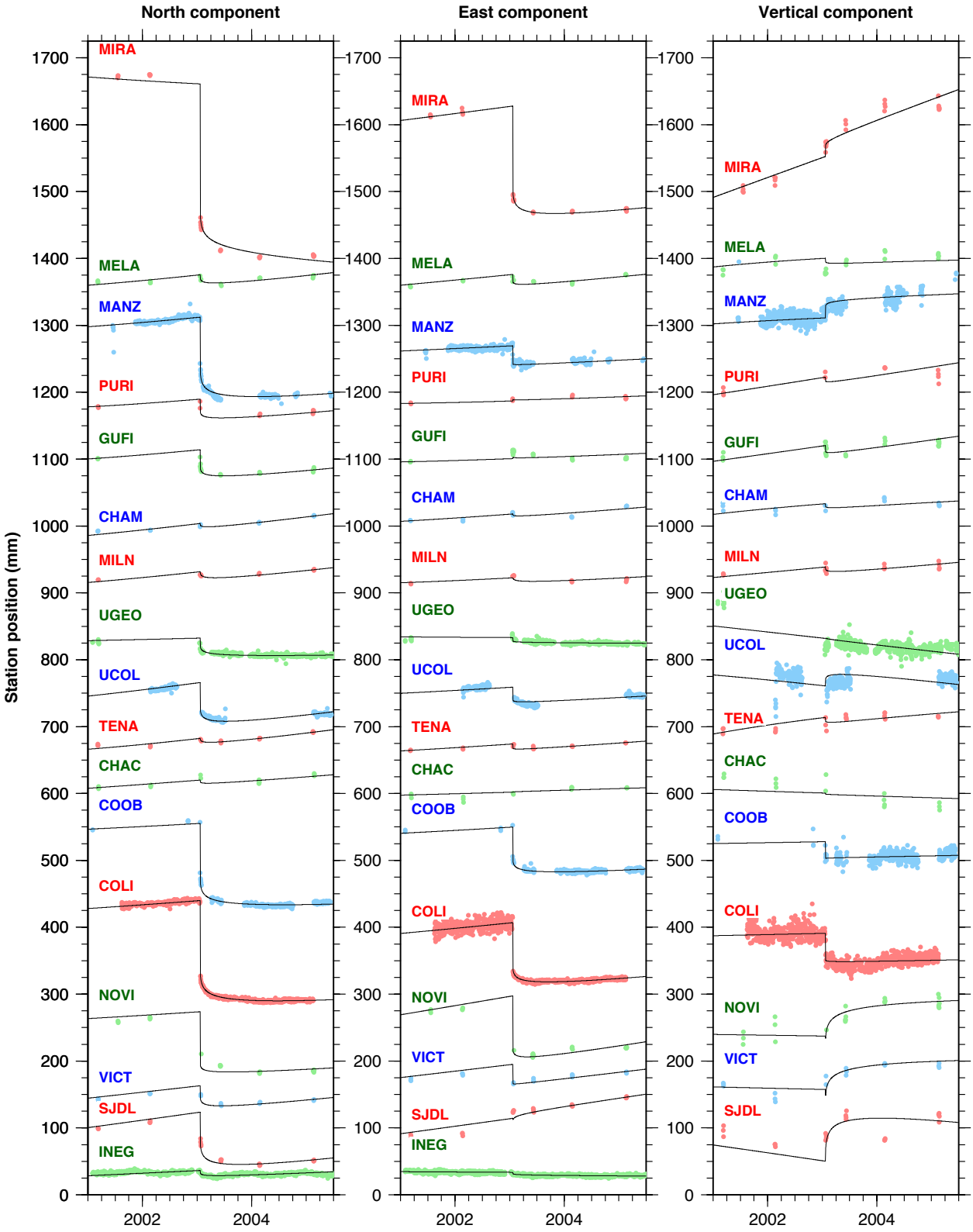

Figure 1.15. TDEFNODE fits (blue, red and green lines) to daily north, east and vertical station positions relative to a fixed NA plate for selected stations with observations spanning the 2003 Tecomán earthquake. Intercepts are arbitrary. The data set has been corrected for the viscoelastic effects of the 1995 Colima–Jalisco earthquake using τ_m = 15 years for the mantle.

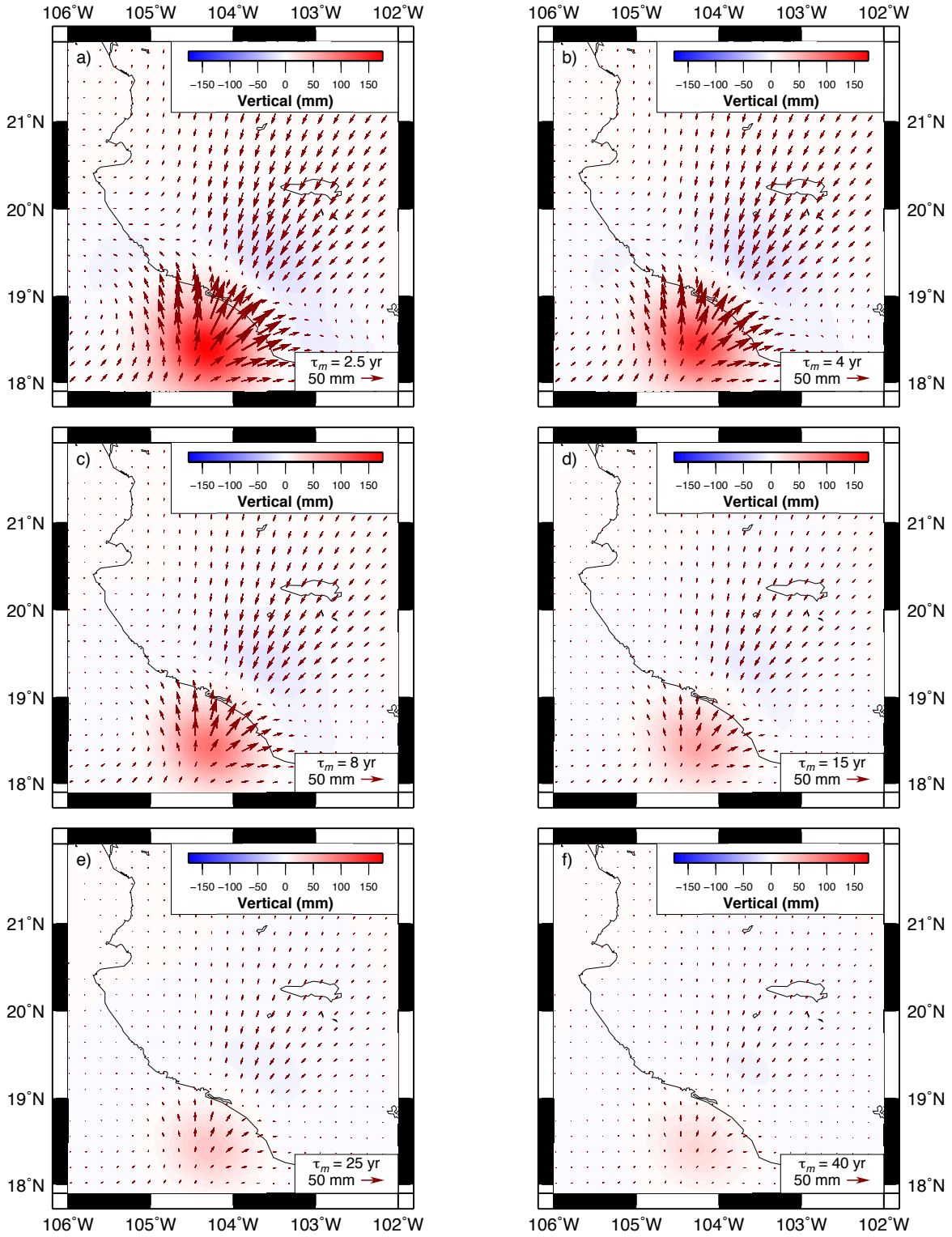

Figure 1.16. Cumulative viscoelastic displacements for the ~17–year–long period 2003.06 to 2020.25 triggered by the 2003 Tecomán earthquake, as predicted with RELAX software using our preferred 2003 coseismic slip solutions. The displacements shown in each panel were determined using the mantle Maxwell time given in the lower right corner of each panel. Arrows show the horizontal dispacements and colors indicate the vertical displacements.

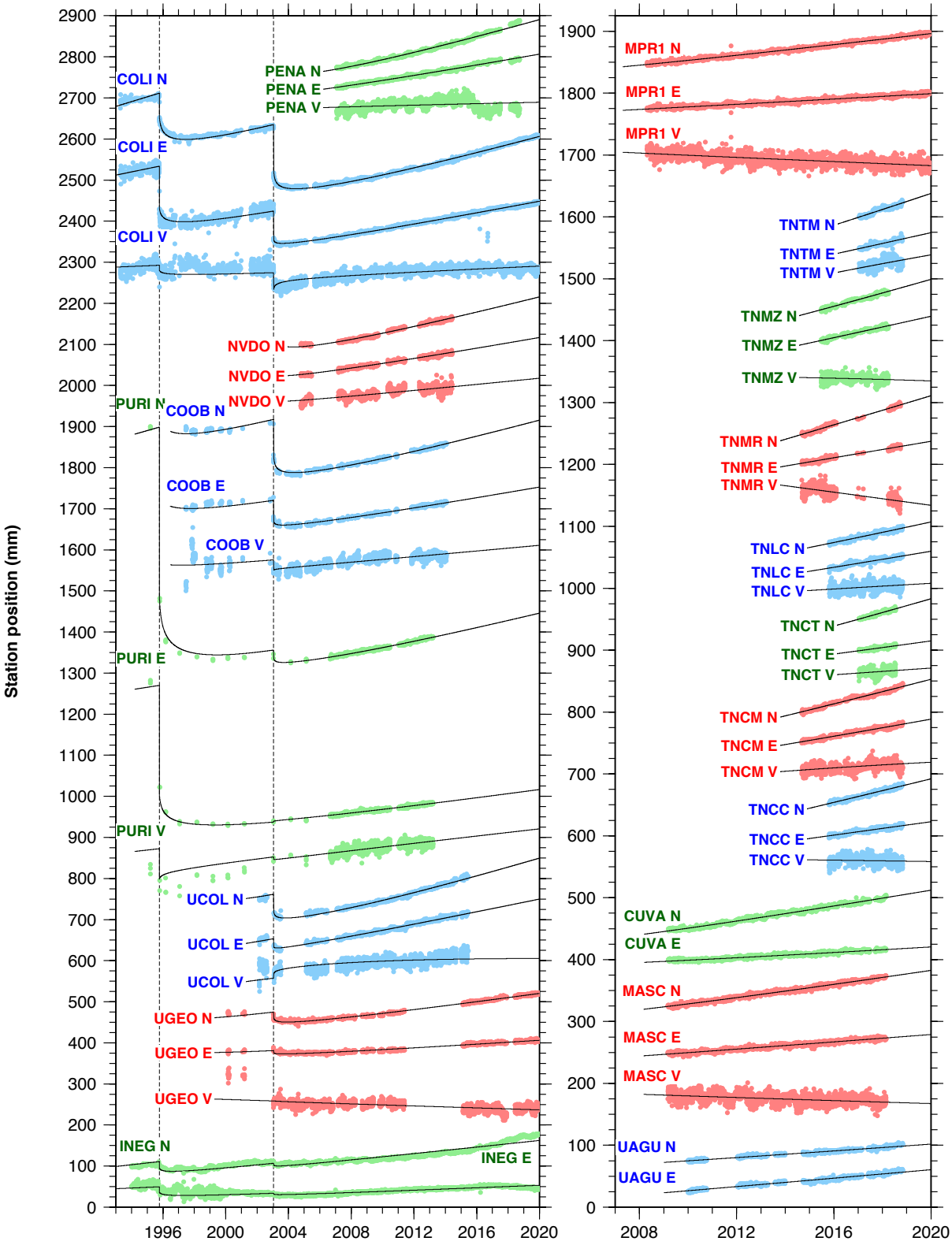

Figure 1.17. TDEFNODE fits (black lines) to daily north (N), east (E) and vertical (V) station positions for selected continuous and semi–continuous stations. Intercepts are arbitrary. The data set has been corrected for the viscoelastic effects of the 1995 Colima–Jalisco and the 2003 Tecomán earthquakes using τ_m = 15 years for the mantle.

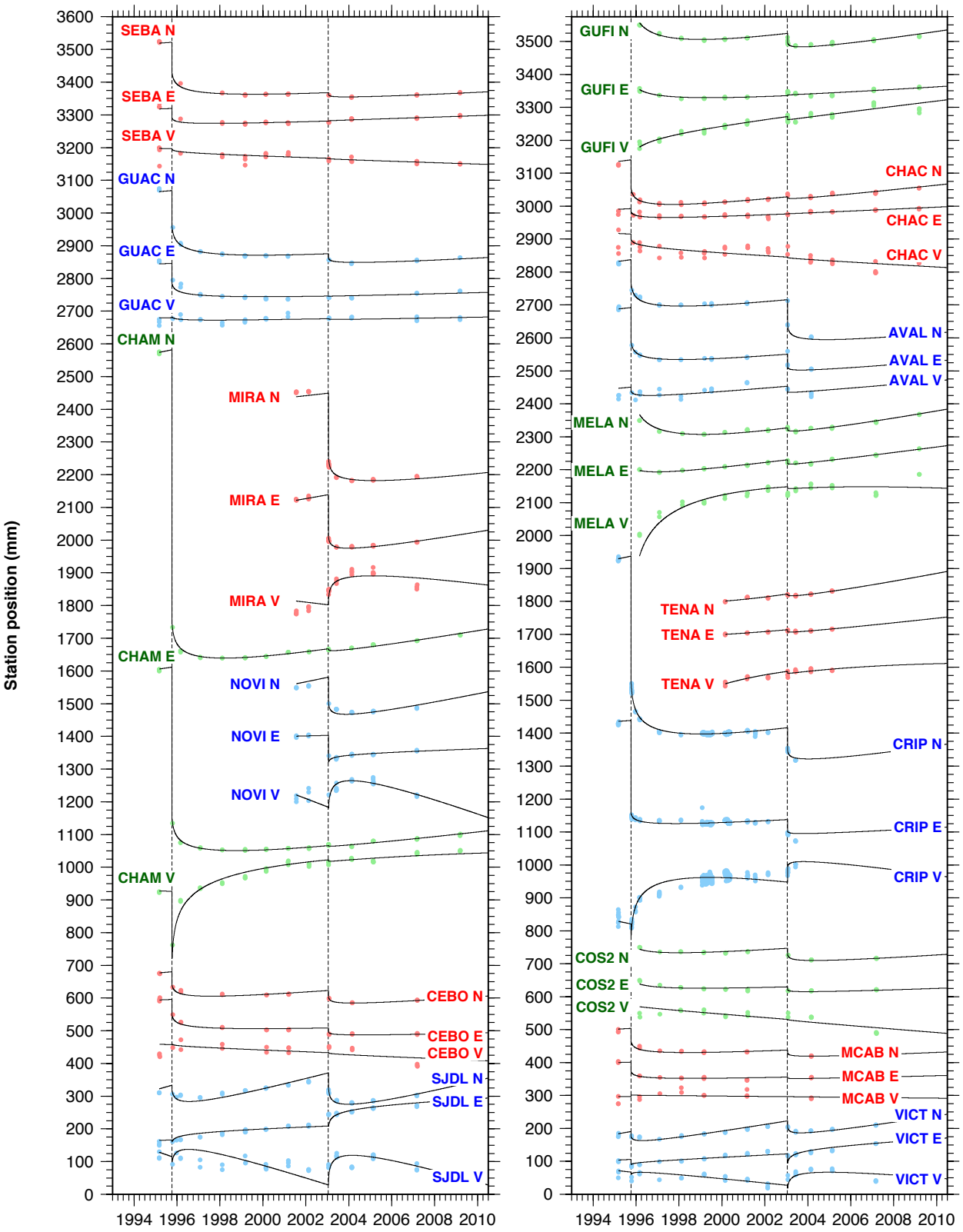

Figure 1.18. TDEFNODE fits (black lines) to daily north (N), east (E), and vertical (V) station positions for selected campaign stations. Intercepts are arbitrary. The data set has been corrected for the viscoelastic effects of the 1995 Colima–Jalisco and the 2003 Tecomán earthquakes using τ_m = 15 years for the mantle.

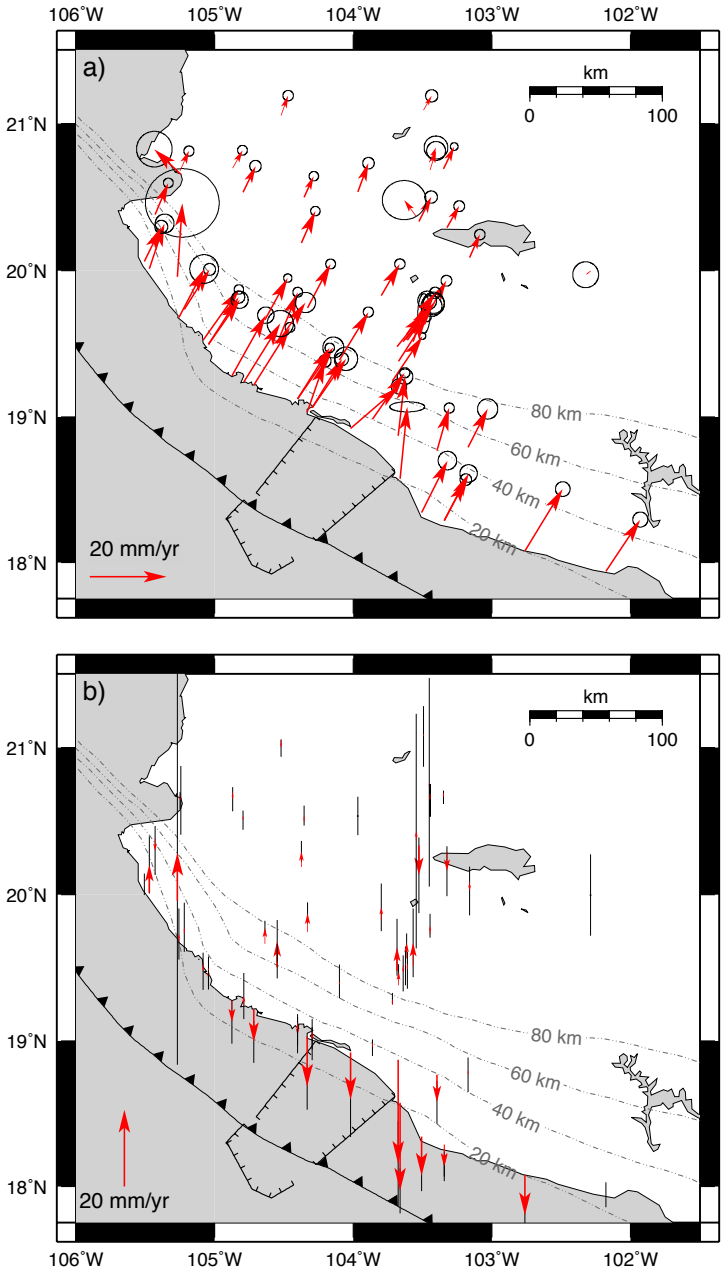

Figure 1.19. Best–fitting GPS site velocities from the time–dependent inversion of GPS position time series that were corrected using a mantle Maxwell time of 15 years (Section 1.4.6 and Table S1.10). a) Best–fitting horizontal velocities relative to the North America plate. The velocity ellipses show thee 2–D 1–σ uncertainties. b) Vertical velocities. Thin black lines represent 1–σ uncertainties.

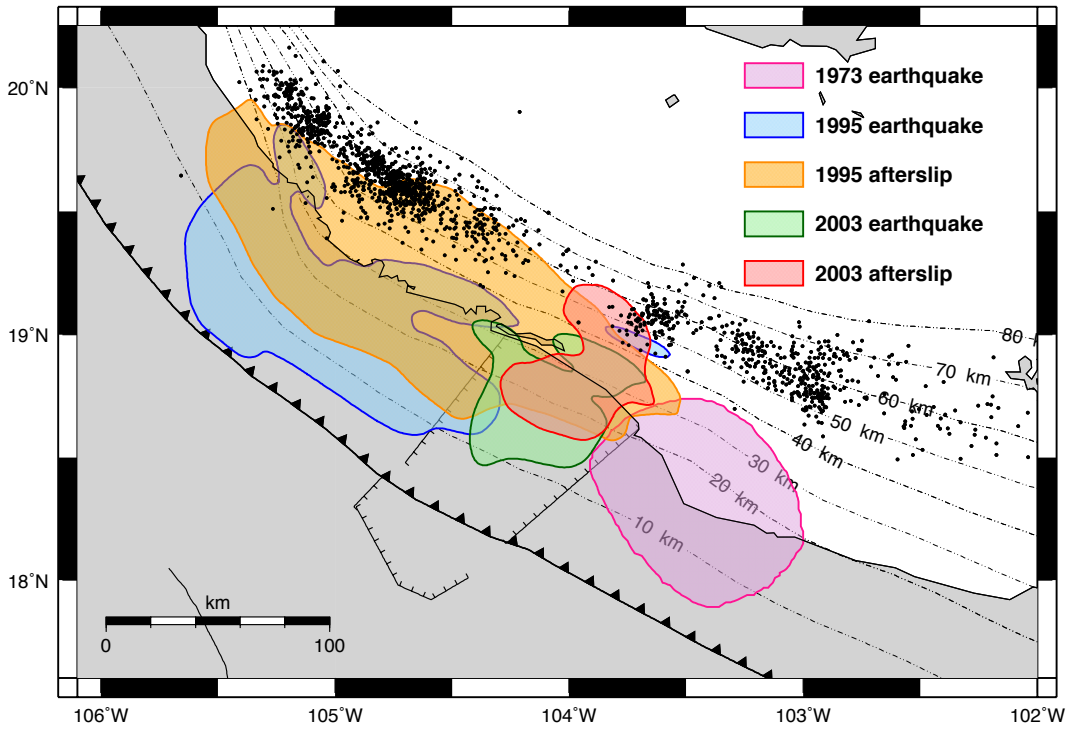

Figure 1.20. Locations of recent large thrust earthquakes (1973: purple, 1995: blue, 2003: green), afterslip (1995: orange, 2003: red), and non volcanic tremor (black dots) along the Jalisco–Colima subduction interface. The 1973 rupture is from Reyes *et al*. (1979). The 1995 and 2003 coseismic ruptures and afterslip correspond to the 0.5 m contour of the coseismic slip and afterslip solutions from our model with viscoelastic rebound corrections using τ_m = 15 years. Tremor locations are from Brudzinski *et al*. (2016).

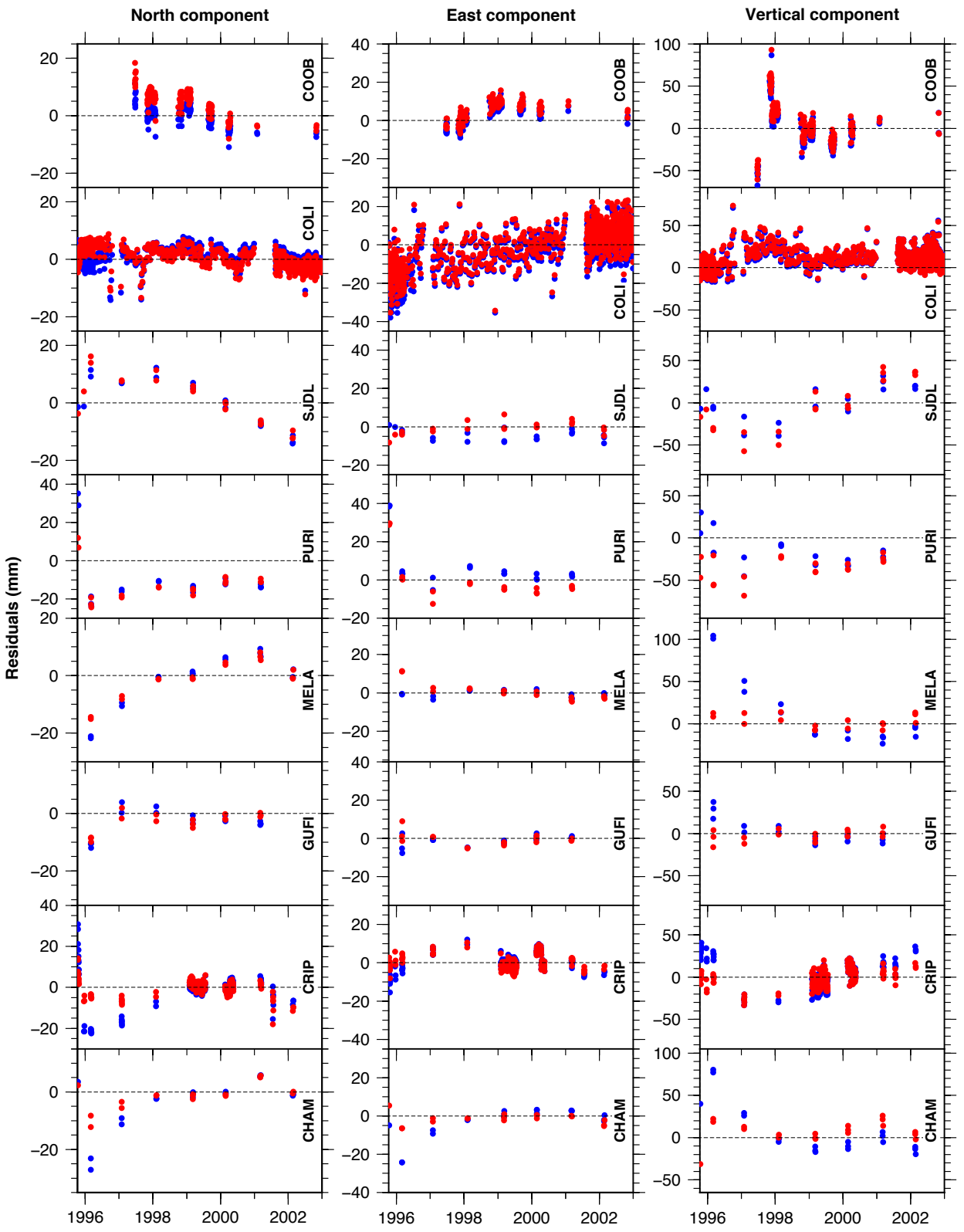

Figure 1.21. Residuals at selected sites from our model with viscoelastic response corrections using τ_m = 8 years for the mantle (red) and with no corrections for viscoelastic effects (blue), for the period between the 1995 and 2003 earthquakes.

SUPPLEMENTARY INFORMATION

The supplementary materials in this document include:

- A summary of the results from the inversion of the GPS position time series without corrections for the viscoelastic effects from the 1995 Colima-Jalisco and the 2003 Tecomán earthquakes.
- Supplementary Tables S1.1 to S1.12, which are referenced in the main document.
- Supplementary Figures S1.1 to S1.17, which are referenced in the main document.

S1.1 MODEL WITH NO VISCOELASTIC GPS TIME SERIES CORRECTIONS

As is described in the main document, we used TDEFNODE to invert our GPS position time series absent any corrections for the viscoelastic effects of the 1995 and 2003 earthquakes to create a baseline reference model and its associated fits for comparison to the six models that we derived with viscoelastic corrections. Similar to those six TDEFNODE models, the parameters estimated for this afterslip-only model include the 1995 and 2003 coseismic and afterslip solutions, logarithmic decay constants for the afterslip after each earthquake, and an interseismic velocity at each GPS site represented in the input data. Overall, the TDEFNODE output consisted of 1166 estimated parameters constrained by 201,510 observations, consisting of the north, east and vertical daily position estimates at 62 GPS sites (excluding all vertical observations at continuous stations INEG, CUVA, UAGU, and TNZA, where the vertical rates appear to be biased by rapid subsidence attributable to groundwater withdrawal). Misfit F (Eq. 1.3) for this best-fitting model is 14.7. The wrms misfits for the model are 1.9-4.9 mm in the horizontal position components at

continuous sites and 5.4-5.8 mm at the campaign sites. The wrms misfits to the noisier vertical daily positions are 7.4 mm at the continuous sites and 15.3 mm at the campaign sites.

The best-fitting coseismic slip solution for the 1995 Colima-Jalisco earthquake (Figs S1.3h and S1.15) agrees well with previous seismic estimates (*e.g.* Courboulex *et al.* 1997; Escobedo *et al.* 1998; Mendoza and Hartzell 1999) and with the GPS-derived solution from Hutton *et al.* (2001). Most of the seismic energy (~66%) was released at depths of 5 to 20 km, consistent with seismic constraints and deeper than our estimate using shorter time series (Section 1.4.1). The region of primary rupture coincides closely with the region of aftershocks determined by Pacheco *et al.* (1997). The geodetic coseismic moment we estimate is 9.8×10^{20} N·m, corresponding to M_w = 7.9 for a standard value of 40 GPa for the shear modulus.

The cumulative estimated moment released by the afterslip triggered by the 1995 Colima-Jalisco earthquake was 13.2×10^{20} N·m (M_w = 8.0), equivalent to ~130 percent of the coseismic moment release (Table S1.5). Eighty seven percent of that moment occurred at depths below 15 km, downdip from the coseismic rupture zone (Fig. S1.15 and Table S1.9). This result agrees with respect to five of the six Maxwell times we explored in our analysis: our inversions of the 1993-2020 data corrected for viscoelastic deformation modeled with Maxwell times equal to or longer than 4 yr all indicate that 80 percent or more of the afterslip occurred below 15 km (Table S1.9). Absent any correction for likely viscoelastic deformation, the estimated logarithmic decay constant for afterslip is 82±1 days, 6-16 times longer than the 5-14 day decay times estimated for the six models we derived with viscoelastic rebound corrections (Table S1.5). The much longer decay constant is required because viscoelastic deformation that decays over time scales of years to decades is not corrected for in this afterslip-only model.

The coseismic slip estimated for the 2003 earthquake was largely confined to the Manzanillo Trough (Figs S1.4 and S1.16a), with 91% of the seismic energy released between depths of 10 and 40 km (Table S1.3). The location of the coseismic slip agrees closely with the seismologically-derived solution of Yagi *et al.* (2004) (shown by the red lines in Fig. 1.16a) and also with the seismologic slip solution of Quintanar *et al.* (2010) and the GPS-derived solution of Schmitt *et al.* (2007), as well as with our solutions with viscoelastic corrections (Fig. S1.4). The estimated coseismic moment of 2.49×10^{20} N·m ($M_w = 7.5$) is ~25 percent larger than the estimates derived when applying viscoelastic corrections to the data (Table S1.3).

For the afterslip triggered by the 2003 earthquake, the estimated cumulative moment was of 3.0×10^{20} N·m ($M_w = 7.6$), equivalent to 120 percent of the coseismic moment release (Table S1.7). Eighty-nine percent of the afterslip energy was released at depths of 15-60 km (Fig. S1.16 and Table S1.9), *i.e.* at the same depths as, or downdip from, the 2003 earthquake rupture zone and mostly confined along strike by the lateral boundaries of the coseismic rupture. The energy released by afterslip at depths shallower than 15 km amounts only to 11 percent of the total (Table S1.9). The decay constant estimated for the afterslip triggered by the 2003 earthquake is 64.4±0.8 days, much longer than 3-15 day estimates for TDEFNODE models derived from the GPS data with viscoelastic rebound corrections (Table S1.7). As is true for the 1995 afterslip decay constant that was estimated without any viscoelastic correction to the underlying GPS data (see above), the 64-day estimated decay constant is much longer because viscoelastic deformation that decays over time scales of years to decades is ignored in this afterslip-only model.

REFERENCES

Courboulex, F., Singh, S.K., & Pacheco, J.F., 1997. The 1995 Colima-Jalixco, Mexico, earthquake (M_w 8): A study of the rupture process, *Geophys. Res. Lett.,* **24**(9), 1019-1022.

Escobedo, D., Pacheco, J.F. & Suárez, G., 1998. Teleseismic body-wave analysis of the 9 October, 1995 (Mw = 8.0), Colima-Jalisco earthquake, and its largest foreshock and aftershock, *Geophys Res Lett*, **25**(4), 547-550.

Hutton, W., DeMets, C., Sánchez, O., Suárez, G. & Stock, J., 2001. Slip kinematics and dynamics during and after the 1995 October 9 Mw=8.0 Colima-Jalisco earthquake, Mexico, from GPS geodetic constraints, *Geophys. J. Inter.*, **146**, 637–658.

Mendoza, C. & Hartzell, S., 1999. Fault-slip distribution of the 1995 Colima-Jalisco, Mexico, earthquake, *Bull. Seismol. Soc. Am.*, **89**(5), 1338-1344.

Pacheco, J., Singh, S.K., Domínguez, J., Hurtado, A., Quintanar, L., Jiménez, Z., Yamamoto, J., Gutiérrez, C., Santoyo, M., Bandy, W., Guzmán, M. & Kostoglodov, V., 1997. The October 9, 1995 Colima-Jalisco, Mexico earthquake (M_w 8): An aftershock study and a comparison of the earthquake with those of 1932, *Geophys. Res. Lett.*, **24**(17), 2223-2226.

Quintanar, L., Rodríguez-Lozoya, H.E., Ortega, R., Gómez-González, J.M., Domínguez, T., Javier, C., Alcántara, L. & Rebollar, C.J., 2010. Source characteristics of the 22 January 2003 M_w = 7.5 Tecomán, Mexico, Earthquake: New insights, *Pure Appl. Geophys.*, **168**, 1339–1353, DOI 10.1007/s00024-010-0202-1.

Schmitt, S.V., DeMets, C., Stock, J., Sánchez, O., Márquez-Azúa, B. & Reyes, G., 2007. A geodetic study of the 2003 January 22 Tecomán, Colima, Mexico earthquake, *Geophys. J. Int.,* **169**, 389–406, doi: 10.1111j.1365-246X.2006.03322.x.

Yagi, Y., Mikumo, T., Pacheco, J. & Reyes, G., 2004. Source rupture process of the Tecomán, Colima, Mexico Earthquake of 22 January 2003, determined by joint inversion of teleseismic body-wave and near-source data, *Bull. Seismol. Soc. Am.,* **94**(5), 1795-1807.

S1.2 SUPPLEMENTARY TABLES

Table S1.1: GPS site information

Site ID	Latitude* °N	Longitude* °E	Elevation† m	Time span	Observation days
ANIG	21.0538	-104.5207	1000.18	2006.8411 - 2018.3260	1880
AUTA	19.7482	-104.3293	870.83	1996.1803 - 2009.1863	26
AVAL	19.4808	-103.6841	1618.24	1995.1890 - 2004.1585	24
AYUT	20.1885	-104.3745	1650.03	1995.1671 - 2009.1863	28
CALC	18.0790	-102.7619	32.22	2007.9397 - 2013.6548	1111
CEBO	20.0896	-103.1608	2004.38	1995.1890 - 2007.1918	21
CGUZ	19.7300	-103.4461	1736.02	1996.1612 - 2007.1890	20
CHAC	20.3835	-105.4289	272.10	1995.1781 - 2009.1781	38
CHAM	19.5271	-105.0842	-11.90	1995.1671 - 2009.1890	39
CHMC	19.4980	-105.0448	82.85	2006.8329 - 2014.8027	1893
COJB	19.5155	-103.5699	2326.52	2011.6192 - 2015.0712	1007
COLI	19.2491	-103.7182	512.93	1993.2822 - 2019.5945	6604
COLW	19.5154	-103.6399	2814.90	2011.3315 - 2014.0822	951
COOB	19.3814	-103.6744	1212.48	1997.4685 - 2014.0712	2583
COPE	19.5269	-103.6109	3161.53	2011.3288 - 2014.0000	968
COPN	19.5289	-103.6240	3042.24	2011.3342 - 2013.9973	966
COS2	20.2930	-103.3246	1727.72	1996.1694 - 2007.1945	20
CRIP	19.0313	-104.3328	-5.75	1995.1671 - 2003.4438	327
CUVA	20.5356	-103.9669	1222.78	2009.1945 - 2018.1507	3154
FARO	18.3446	-103.5087	35.73	2006.7233 - 2010.3342	1281
GUAC	20.5006	-104.3540	1575.01	1995.1671 - 2009.1781	28
GUFI	19.5062	-104.5495	265.50	1996.1667 - 2009.1945	46
IITJ	20.6845	-103.4460	1656.99	2003.9562 - 2007.3342	1061
INEG	21.8562	-102.2842	1889.09	1995.1233 - 2019.5945	7321
LIM2	20.3346	-103.5282	1653.29	1998.1260 - 2007.1918	17
LIMA	20.3700	-103.5476	2106.51	1996.1913 - 1998.0849	5
LZCR	17.9394	-102.1783	-8.50	2008.9290 - 2014.4329	1010
MANZ	19.0639	-104.2981	-14.18	1999.2986 - 2006.4000	1165
MASC	20.5347	-104.7967	1221.62	2009.1726 - 2018.1507	3064
MCAB	21.0916	-103.4935	1680.06	1995.1671 - 2004.1667	17
MELA	19.2202	-104.7179	57.46	1996.1612 - 2009.1945	36
MILN	19.7369	-105.2194	9.71	2000.1503 - 2009.1890	29
MIRA	18.9227	-104.0210	-0.61	2001.5479 - 2007.1781	32
MMIG	18.2885	-103.3455	41.44	2006.8274 - 2016.2760	1829
MNZO	19.0639	-104.2982	-13.88	2011.8411 - 2014.1151	659
MPR1	20.6790	-105.2492	10.94	2008.3142 - 2019.5945	3922
NOVI	18.8722	-103.6764	95.19	2001.5534 - 2007.1699	25
NVDO	19.5656	-103.6165	4004.38	2004.8005 - 2014.4247	2237
PENA	19.3905	-104.1014	1489.98	2007.0849 - 2018.7260	3753
PORT	20.0145	-105.4699	9.00	2000.1421 - 2004.1393	13
PURI	19.6651	-104.6371	376.41	1995.1890 - 2013.2137	2215
PZUL	20.0640	-105.5076	183.79	2007.2000 - 2014.6877	1565
SEBA	20.6989	-104.8710	1971.67	1995.1781 - 2009.1753	25
SJDL	18.5765	-103.6629	24.94	1995.1671 - 2007.1699	43
TAPA	19.8311	-103.7971	1961.73	1995.1890 - 2007.1918	25
TECO	18.9845	-103.8610	213.53	2007.1397 - 2018.8329	3100

Continued on next page

Table S1.1 – continued from previous page

Site ID	Latitude* °N	Longitude* °E	Elevation† m	Time span	Observation days
TENA	19.2829	-104.8750	-5.82	2000.1503 - 2005.1315	23
TNCC	18.7911	-103.1730	1074.24	2015.8027 - 2018.8329	912
TNCM	19.4981	-105.0448	83.09	2014.6877 - 2018.8329	1207
TNCT	19.6811	-105.2588	-8.68	2017.0384 - 2018.5479	508
TNLC	19.5061	-104.5492	267.85	2015.8137 - 2018.8329	907
TNMR	18.2885	-103.3455	41.30	2014.6904 - 2018.7479	660
TNMZ	19.1236	-104.4015	-5.81	2015.4767 - 2018.2466	651
TNTM	19.2391	-104.7899	12.74	2017.0466 - 2018.8329	616
TNZA	19.9989	-102.2903	1556.78	2015.4575 - 2017.4849	57
TOMA	19.9603	-105.2693	20.46	1996.1639 - 1997.0877	3
UAGU	21.9185	-102.3150	1860.63	2010.0000 - 2018.8329	1995
UCOL	19.1241	-104.4015	-9.71	2002.1425 - 2015.4740	3407
UGEO	20.6939	-103.3500	1533.79	2000.1612 - 2019.5945	3303
UMON	20.7373	-103.4532	1622.48	1996.1913 - 1999.4575	13
VICT	18.7675	-103.3961	880.32	1995.1781 - 2007.1726	36
VALL	20.6579	-105.2429	-17.83	2013.8493 - 2014.8384	354

*Site coordinates are in IGS14/ITRF2014 for the first day of measurements at each site.

†Site elevations are specified relative to the WGS84 reference ellipsoid for the first day of measurements at each site.

Table S1.2: Coseismic displacements from the 1995 Colima-Jalisco earthquake at GPS sites active during the earthquake.

Site	North (mm) $\pm$1 mm	East (mm) $\pm$1 mm	Vertical (mm) $\pm$2 mm
AVAL	-74	-106	-13
AYUT	-162	-103	-4
CEBO	-42	-50	1
CHAC	-88	-10	-17
CHAM	-837	-463	-207
COLI	-55	-101	-12
CRIP	-386	-283	-37
GUAC	-112	-62	2
INEG	-15	-13	3
MCAB	-41	-29	4
PURI	-407	-263	-74
SEBA	-94	-30	-2
SJDL	-16	-6	-17
TAPA	-101	-107	-6
VICT	-17	-15	-6

Table S1.3: Comparative 2003 earthquake sizes for models using time series corrected for viscoelastic relaxation from a mantle using different Maxwell times (t_m).

	t_m = 2.5 yr	t_m = 4 yr	t_m = 8 yr	t_m = 15 yr	t_m = 25 yr	t_m = 40 yr	no correction
$M_o(10^{20}$ N m)	2.05	1.98	2.00	1.84	2.00	2.00	2.49
Potency (10^9 m^3)	5.13	4.95	5.00	4.60	5.00	5.00	6.23
M_w	7.5	7.5	7.5	7.4	7.5	7.5	7.5
M_o^{1995}/M_o^{2003}	4.7	4.9	4.5	5.2	4.5	4.5	4.0‡
$\%M_o^{10-40km}$†	91	93	92	97	93	93	91

† Percentage of coseismic moment relased betwen depths of 10 and 40 km.

‡ 1995 coseismic moment from the model without viscoelastic relaxation corrections.

Table S1.4: Coseismic displacements from the 2003 Tecomán earthquake at GPS sites active during the earthquake.

	Maxwell time for the mantle used in the corrections for postseismic viscoelastic deformation																	
	t_m = 2.5 yr			t_m = 4 yr			t_m = 8 yr			t_m = 15 yr			t_m = 25 yr			t_m = 40 yr		
Site	North	East	Vert.	North	East	Vert.	North	East	Vert.	North	East	Vert.	North	East	Vert.	North	East	Vert.
	mm	mm	mm	mm	mm	mm	mm	mm	mm	mm	mm	mm	mm	mm	mm	mm	mm	mm
	±1	±1	±2	±1	±1	±2	±1	±1	±2	±1	±1	±2	±1	±1	±2	±1	±1	±2
AUTA	-41	-2	-7	-40	-2	-7	-40	-1	-7	-38	-1	-7	-40	-1	-7	-40	-1	-7
AVAL	-81	-43	-16	-80	-41	-16	-82	-42	-17	-78	-40	-18	-81	-42	-17	-81	-42	-17
AYUT	-21	-1	-2	-20	-1	-2	-21	-1	-2	-19	-1	-2	-20	-1	-2	-21	-1	-2
CEBO	-22	-14	-0	-22	-14	-0	-22	-14	-0	-21	-13	-1	-22	-14	-0	-22	-14	-0
CGUZ	-43	-26	-4	-43	-25	-4	-43	-26	-5	-41	-24	-5	-43	-25	-5	-43	-25	-5
CHAC	-3	0	-2	-3	0	-2	-3	0	-2	-3	0	-2	-3	0	-2	-3	0	-2
CHAM	-3	-2	-5	-3	-2	-5	-3	-2	-5	-2	-2	-4	-3	-2	-5	-3	-2	-5
COLI	-118	-75	-39	-116	-73	-39	-119	-75	-41	-111	-70	-41	-117	-73	-41	-118	-74	-41
COOB	-93	-55	-23	-92	-53	-23	-94	-54	-24	-89	-51	-25	-93	-54	-24	-93	-54	-24
COS2	-21	-10	0	-20	-10	0	-21	-10	-0	-20	-9	-0	-21	-10	-0	-21	-10	-0
CRIP	-74	-38	56	-71	-37	53	-76	-37	48	-70	-36	47	-75	-37	53	-75	-37	54
GUAC	-15	-1	-1	-14	-1	-1	-15	-1	-1	-14	-1	-1	-15	-1	-1	-15	-1	-1
GUFI	-33	1	-10	-31	1	-10	-31	2	-9	-28	2	-9	-31	2	-10	-31	2	-10
INEG	-4	-2	1	-4	-2	0	-4	-2	0	-4	-2	0	-4	-2	0	-4	-2	0
LIM2	-22	-9	-0	-21	-8	-0	-22	-8	-0	-21	-8	-0	-22	-8	-0	-22	-8	-0
MANZ	-91	-28	17	-88	-28	16	-91	-26	18	-84	-28	18	-90	-27	19	-89	-27	20
MCAB	-10	-3	1	-10	-3	0	-10	-3	0	-10	-3	0	-10	-3	0	-10	-3	0
MELA	-9	-15	-7	-7	-14	-6	-8	-11	-6	-6	-12	-5	-7	-13	-6	-7	-13	-6
MILN	-3	-1	-4	-3	-1	-4	-3	-0	-4	-3	-1	-3	-3	-1	-4	-3	-1	-4
MIRA	-201	-147	-11	-196	-139	2	-205	-140	5	-198	-130	17	-199	-137	15	-199	-137	14
NOVI	-82	-100	-21	-84	-96	-16	-81	-90	-14	-80	-82	-4	-83	-91	-10	-83	-91	-11
PORT	-2	-0	-2	-2	-0	-2	-2	-0	-2	-2	-0	-2	-2	-0	-2	-2	-0	-2
PURI	-23	1	-7	-22	2	-6	-22	2	-6	-20	2	-6	-22	2	-6	-22	2	-6
SEBA	-7	0	-1	-7	0	-1	-7	0	-1	-7	0	-1	-7	0	-1	-7	0	-1
SJDL	-53	1	28	-53	-5	21	-51	7	24	-48	-2	16	-54	-5	21	-53	-4	19
TAPA	-48	-17	-5	-47	-16	-5	-48	-16	-5	-46	-15	-5	-48	-16	-5	-48	-16	-5
TENA	-4	-8	-7	-3	-8	-6	-3	-7	-6	-2	-7	-6	-3	-7	-6	-3	-7	-6
UCOL	-46	-22	12	-44	-21	10	-46	-19	11	-42	-20	10	-46	-20	12	-45	-20	12
UGEO	-14	-6	1	-14	-6	0	-14	-6	0	-13	-5	0	-14	-6	0	-14	-6	0
VICT	-20	-38	-14	-21	-36	-13	-20	-32	-12	-19	-29	-9	-21	-33	-11	-21	-34	-11

Table S1.5: Comparison of 1995 afterslip solutions for models corrected for viscoelastic relaxation.

	t_m = 2.5 yr	t_m = 4 yr	t_m = 8 yr	t_m = 15 yr	t_m = 25 yr	t_m = 40 yr	no correction
$M_o(10^{20}$ N m)	5.07	6.37	8.91	10.80	12.00	11.90	13.2
Equivalent M_w	7.7	7.8	7.9	8.0	8.0	8.0	8.0
$M_o^{as}/M_o^{co}(\%)$	52	66	92	111	124	124	134
t_c (days)	5	8	11	13	14	14	82

t_m: Mantle Maxwell time used for the viscoelastic corrections.
co: coseismic, as: afterslip, t_c: logarithmic decay constant.

Table S1.6: Cumulative 1995 Colima-Jalisco earthquake afterslip displacements (1995.77-2020.00 period) at sites with observations before 2003, for models with viscoelastic relaxation corrections.

	Maxwell time for the mantle used in the corrections for postseismic viscoelastic deformation																	
	t_m = 2.5 yr			t_m = 4 yr			t_m = 8 yr			t_m = 15 yr			t_m = 25 yr			t_m = 40 yr		
Site	North	East	Vert.	North	East	Vert.	North	East	Vert.	North	East	Vert.	North	East	Vert.	North	East	Vert.
	mm	mm	mm	mm	mm	mm	mm	mm	mm	mm	mm	mm	mm	mm	mm	mm	mm	mm
	±1	±1	±2	±1	±1	±2	±1	±1	±2	±1	±1	±2	±1	±1	±2	±1	±1	±2
AUTA	-94	-49	1	-135	-73	-13	-199	-109	-30	-241	-150	-37	-258	-163	-33	-262	-167	-39
AVAL	-55	-40	0	-80	-57	-13	-118	-82	-27	-137	-107	-35	-150	-118	-39	-146	-118	-37
AYUT	-76	-39	-11	-113	-58	-20	-159	-77	-28	-198	-103	-38	-215	-113	-40	-216	-114	-40
CEBO	-29	-27	-2	-41	-38	-4	-60	-52	-6	-73	-70	-10	-82	-78	-11	-80	-77	-11
CGUZ	-41	-37	-4	-59	-52	-11	-88	-73	-18	-104	-96	-25	-117	-107	-29	-113	-106	-27
CHAC	-30	-6	-11	-56	-16	-23	-89	-26	-31	-104	-38	-36	-112	-42	-38	-114	-43	-38
CHAM	-175	-101	169	-175	-129	237	-201	-157	258	-212	-185	390	-223	-192	420	-225	-194	425
COLI	-64	-31	11	-87	-42	-6	-118	-63	-14	-130	-81	-22	-136	-88	-20	-135	-90	-18
COOB	-56	-36	4	-80	-52	-12	-116	-76	-25	-132	-97	-34	-144	-108	-37	-140	-108	-34
COS2	-34	-27	-2	-47	-39	-4	-67	-52	-5	-83	-70	-8	-94	-78	-10	-91	-78	-9
CRIP	-250	-48	159	-265	-46	218	-287	-52	277	-286	-63	319	-288	-67	352	-292	-69	349
GUAC	-58	-26	-6	-86	-38	-11	-118	-50	-14	-149	-69	-20	-163	-75	-22	-162	-76	-21
GUFI	-128	-40	52	-164	-50	78	-249	-88	64	-285	-127	105	-312	-150	128	-313	-150	112
INEG	-10	-7	1	-14	-10	1	-19	-14	2	-24	-18	2	-27	-20	2	-27	-20	2
LIM2	-40	-29	-2	-56	-42	-5	-79	-57	-7	-100	-76	-11	-111	-84	-12	-109	-84	-12
LIMA	-40	-29	-2	-56	-42	-5	-79	-55	-6	-100	-75	-10	-111	-83	-12	-109	-82	-11
MANZ	-219	-50	136	-235	-48	185	-262	-66	216	-273	-84	247	-292	-101	265	-289	-94	262
MCAB	-26	-15	1	-36	-22	0	-50	-29	0	-64	-39	-0	-71	-43	-1	-70	-43	-0
MELA	-224	-88	55	-242	-48	210	-300	-29	395	-331	-76	620	-345	-84	640	-363	-85	656
MILN	-93	-65	41	-131	-96	46	-196	-128	0	-212	-169	73	-230	-185	88	-237	-188	79
MIRA	-171	-57	11	-185	-48	38	-233	-48	122	-157	-50	199	-173	-78	224	-183	-66	192
NOVI	-79	-37	-11	-84	-27	0	-114	-24	38	-80	-3	86	-62	13	132	-71	-5	109
PORT	-30	-9	-8	-74	-28	-23	-139	-45	-50	-165	-78	-59	-186	-93	-69	-190	-93	-71
PURI	-100	-42	30	-143	-64	33	-225	-105	9	-264	-139	29	-281	-159	42	-289	-161	29
SEBA	-44	-10	-6	-66	-17	-9	-92	-23	-12	-115	-34	-16	-125	-38	-18	-126	-38	-18
SJDL	-59	-23	-8	-61	2	79	-90	-5	133	-101	43	120	-107	38	129	-102	37	112
TAPA	-62	-46	-7	-88	-65	-16	-126	-89	-24	-153	-119	-34	-170	-132	-38	-167	-132	-36
TENA	-231	-49	80	-254	-56	292	-300	-80	492	-317	-149	706	-333	-164	760	-344	-158	769
TOMA	-55	-20	-5	-100	-48	-18	-170	-74	-52	-204	-117	-39	-228	-137	-43	-234	-137	-45
UCOL	-207	-86	161	-227	-76	192	-272	-72	201	-308	-76	275	-314	-102	283	-323	-95	286
UGEO	-29	-21	-0	-41	-30	-1	-58	-40	-1	-73	-53	-3	-81	-59	-4	-80	-59	-3
UMON	-31	-21	-0	-44	-30	-1	-61	-39	-2	-77	-53	-3	-86	-59	-4	-84	-58	-3
VICT	-47	-26	-15	-45	-18	-18	-67	-14	-2	-40	11	22	-41	25	38	-39	19	33

Table S1.7: Comparison of 2003 afterslip solutions for models corrected for viscoelastic relaxation.

	t_m = 2.5 yr	t_m = 4 yr	t_m = 8 yr	t_m = 15 yr	t_m = 25 yr	t_m = 40 yr	no correction
$M_o(10^{20}$ N m)	1.55	1.77	2.48	2.84	3.16	3.05	3.00
M_w	7.4	7.4	7.5	7.6	7.6	7.6	7.6
$M_o^{as}/M_o^{co}(\%)$	76	89	124	154	158	153	121
t_c (days)	11	3	7	6	16	15	64

t_m: Mantle Maxwell time used for the viscoelastic corrections.
co: coseismic, as: afterslip, t_c: logarithmic decay constant.

Table S1.8: Cumulative 2003 Tecomán earthquake afterslip displacements (2003.06-2020.00 period) at sites with observations before 2005.

	Maxwell time for the mantle used in the corrections for postseismic viscoelastic deformation																	
	t_m = 2.5 yr			t_m = 4 yr			t_m = 8 yr			t_m = 15 yr			t_m = 25 yr			t_m = 40 yr		
Site	North	East	Vert.	North	East	Vert.	North	East	Vert.	North	East	Vert.	North	East	Vert.	North	East	Vert.
	mm	mm	mm	mm	mm	mm	mm	mm	mm	mm	mm	mm	mm	mm	mm	mm	mm	mm
	±1	±1	±2	±1	±1	±2	±1	±1	±2	±1	±1	±2	±1	±1	±2	±1	±1	±2
AUTA	-23	2	-2	-28	3	-3	-29	1	-2	-44	3	-6	-55	7	-8	-54	5	-7
AVAL	-28	-2	14	-46	-8	3	-64	-13	-1	-81	-21	-5	-88	-23	-3	-87	-24	-3
AYUT	-17	2	-2	-20	3	-3	-23	1	-4	-32	2	-5	-38	4	-7	-37	3	-6
CEBO	-13	-6	-1	-20	-9	-3	-32	-13	-5	-37	-16	-6	-39	-16	-6	-38	-16	-6
CGUZ	-20	-6	1	-33	-11	-4	-51	-17	-9	-59	-21	-11	-61	-21	-10	-60	-21	-10
CHAC	-4	1	-1	-5	1	-1	-6	-0	-3	-9	0	-3	-12	1	-4	-11	1	-3
CHAM	-7	1	-2	-6	-1	-3	-8	-4	-0	-14	-3	-3	-19	-2	-4	-18	-2	-4
COLI	-46	4	37	-56	-2	33	-72	-14	35	-92	-24	33	-91	-24	35	-92	-26	33
COOB	-32	1	22	-48	-6	12	-67	-14	8	-84	-23	5	-88	-25	8	-88	-26	7
COS2	-14	-5	-1	-21	-7	-2	-30	-10	-4	-36	-12	-4	-39	-13	-5	-38	-13	-5
CRIP	-66	-2	10	-58	-5	16	-52	-13	26	-56	-16	37	-50	-21	51	-49	-21	53
GUAC	-13	1	-1	-16	1	-2	-19	1	-3	-26	1	-3	-31	2	-4	-30	2	-4
GUFI	-19	0	0	-20	1	-1	-21	-3	3	-33	1	-2	-43	5	-6	-43	4	-6
INEG	-3	-1	0	-5	-2	0	-7	-3	0	-8	-4	0	-9	-4	0	-9	-4	0
LIM2	-16	-4	-1	-22	-6	-3	-31	-7	-4	-38	-9	-5	-42	-10	-6	-41	-10	-5
LIMA	-16	-4	-1	-22	-5	-2	-30	-7	-4	-37	-9	-4	-41	-9	-5	-40	-9	-5
MANZ	-67	-4	16	-63	-7	19	-57	-16	24	-66	-16	29	-61	-18	39	-61	-19	39
MCAB	-9	-2	-0	-12	-2	-0	-16	-3	-1	-19	-4	-1	-22	-4	-1	-21	-4	-1
MELA	-19	-0	-3	-10	-3	-2	-9	-9	2	-15	-8	-2	-20	-6	-6	-20	-7	-6
MILN	-6	1	-2	-6	-0	-3	-8	-3	-2	-13	-2	-4	-18	-1	-5	-16	-1	-5
MIRA	-137	-17	26	-131	-43	55	-124	-77	65	-124	-76	130	-95	-69	262	-96	-66	242
NOVI	-78	-3	25	-71	18	77	-102	-7	142	-80	33	187	-67	99	244	-66	87	228
PORT	-4	1	-1	-5	0	-2	-7	-1	-3	-11	-0	-4	-14	1	-5	-13	0	-5
PURI	-16	2	-2	-16	3	-2	-16	-1	1	-26	2	-2	-34	6	-4	-33	5	-4
SEBA	-8	2	-1	-9	2	-1	-11	1	-2	-15	2	-2	-18	3	-3	-17	3	-3
SJDL	-78	7	15	-67	42	93	-102	29	181	-110	79	162	-110	76	129	-110	78	136
TAPA	-26	-5	-2	-38	-6	-6	-48	-6	-8	-64	-10	-11	-73	-10	-13	-70	-11	-12
TENA	-12	1	-3	-7	-2	-4	-8	-6	-1	-15	-5	-4	-20	-3	-7	-20	-4	-6
TOMA	-5	2	-1	-6	1	-2	-8	-2	-3	-12	-1	-4	-16	1	-4	-15	0	-4
UCOL	-45	-4	10	-37	-6	12	-33	-12	19	-40	-11	18	-40	-10	18	-40	-11	17
UGEO	-11	-3	-0	-15	-4	-1	-22	-6	-2	-26	-7	-2	-29	-8	-2	-28	-8	-2
UMON	-11	-3	-0	-15	-4	-1	-21	-5	-2	-26	-6	-2	-29	-7	-2	-28	-7	-2
VICT	-31	4	5	-34	27	32	-57	27	73	-45	60	91	-48	81	105	-47	77	98

Table S1.9: Down-dip distribution of afterslip for all models corrected for viscoelastic relaxation in percentage of total afterslip moment release at the indicated depth intervals.

t_m	1995 afterslip depth intervals				2003 afterslip depth intervals			
(years)	$0-15$ km	$15-40$ km	$40-60$ km	below 60 km	$0-15$ km	$15-40$ km	$40-60$ km	below 60 km
2	43	37	15	4	39	31	18	11
4	19	58	19	4	10	52	27	12
8	18	62	17	3	7	54	28	12
15	12	64	19	4	4	57	27	12
25	11	64	20	5	6	54	23	17
40	12	64	19	4	6	55	23	16
no correction	13	59	21	7	11	50	21	18

t_m: Mantle Maxwell time used for the viscoelastic relaxation corrections.

Table S1.10: Site velocities for all models with viscoelastic relaxation corrections.[†]

Site	Maxwell time for the mantle used in the corrections for postseismic viscoelastic deformation								
	t_m = 2.5 yr			t_m = 4 yr			t_m = 8 yr		
	North (mm/yr)	East (mm/yr)	Vert. (mm/yr)	North (mm/yr)	East (mm/yr)	Vert. (mm/yr)	North (mm/yr)	East (mm/yr)	Vert. (mm/yr)
ANIG	3.6 ± 0.9	2.0 ± 0.9	-3.8 ± 1.5	4.6 ± 0.9	2.3 ± 0.9	-3.2 ± 1.5	5.4 ± 0.9	2.2 ± 0.9	-2.6 ± 1.5
AUTA	8.4 ± 0.8	5.3 ± 0.8	4.7 ± 1.8	10.5 ± 0.8	6.3 ± 0.8	5.2 ± 1.8	11.2 ± 0.8	6.6 ± 0.8	4.9 ± 1.8
AVAL	5.7 ± 3.4	6.5 ± 1.1	3.3 ± 4.9	6.9 ± 3.4	6.8 ± 1.1	4.6 ± 4.9	8.3 ± 3.4	6.8 ± 1.1	5.5 ± 4.9
AYUT	7.6 ± 0.8	4.8 ± 0.8	2.9 ± 1.8	8.9 ± 0.8	5.1 ± 0.8	3.5 ± 1.8	8.8 ± 0.8	4.4 ± 0.8	3.8 ± 1.8
CALC	16.1 ± 1.3	10.1 ± 1.3	-9.2 ± 2.1	16.3 ± 1.3	9.9 ± 1.3	-9.8 ± 2.1	16.4 ± 1.3	9.7 ± 1.3	-10.3 ± 2.1
CEBO	6.7 ± 0.9	3.9 ± 0.9	-4.3 ± 4.2	6.5 ± 0.9	3.8 ± 0.9	-3.5 ± 4.2	6.4 ± 0.9	3.1 ± 0.9	-2.8 ± 4.2
CGUZ	7.3 ± 0.9	4.7 ± 0.9	0.3 ± 2.0	7.9 ± 0.9	5.1 ± 0.9	1.1 ± 2.0	8.2 ± 0.9	4.8 ± 0.9	1.8 ± 2.0
CHAC	7.0 ± 0.8	4.8 ± 0.8	-1.4 ± 4.2	7.8 ± 0.8	4.4 ± 0.8	-2.1 ± 4.2	8.2 ± 0.8	3.7 ± 0.8	-2.8 ± 4.2
CHAM	6.8 ± 0.8	6.7 ± 0.8	14.2 ± 3.2	8.6 ± 0.8	8.1 ± 0.8	9.9 ± 3.2	11.7 ± 0.8	9.0 ± 0.8	6.1 ± 3.2
CHMC	8.4 ± 1.1	5.7 ± 1.1	-0.8 ± 1.8	9.1 ± 1.1	6.5 ± 1.1	-0.3 ± 1.8	11.1 ± 1.1	7.5 ± 1.1	-0.6 ± 1.8
COJB	7.9 ± 1.6	1.0 ± 1.6	5.0 ± 5.9	9.3 ± 1.6	2.1 ± 1.6	5.7 ± 5.9	10.8 ± 1.6	3.4 ± 1.6	5.9 ± 5.9
COLI	9.0 ± 0.6	5.0 ± 0.6	1.1 ± 0.9	10.1 ± 0.6	6.2 ± 0.6	1.9 ± 0.9	11.5 ± 0.6	7.5 ± 0.6	1.8 ± 0.9
COLW	6.1 ± 1.8	4.5 ± 1.8	-3.0 ± 3.1	7.7 ± 1.8	5.7 ± 1.8	-2.2 ± 3.1	9.4 ± 1.8	7.0 ± 1.8	-1.9 ± 3.1
COOB	9.0 ± 0.8	4.9 ± 0.8	3.0 ± 1.2	10.4 ± 0.8	6.2 ± 0.8	3.8 ± 1.2	11.7 ± 0.8	7.2 ± 0.8	3.8 ± 1.2
COPE	6.8 ± 1.8	4.1 ± 1.8	-2.5 ± 3.2	8.3 ± 1.8	5.3 ± 1.8	-1.8 ± 3.2	9.8 ± 1.8	6.6 ± 1.8	-1.6 ± 3.2
COPN	6.2 ± 1.8	4.6 ± 1.8	-1.5 ± 3.3	7.8 ± 1.8	5.8 ± 1.8	-0.8 ± 3.3	9.4 ± 1.8	7.1 ± 1.8	-0.6 ± 3.3
COS2	7.1 ± 0.9	5.0 ± 0.9	-6.9 ± 4.3	7.0 ± 0.9	5.0 ± 0.9	-6.0 ± 4.3	6.3 ± 0.9	4.0 ± 0.9	-5.4 ± 4.3
CRIP	10.1 ± 1.1	1.1 ± 1.1	9.3 ± 3.9	12.2 ± 1.1	2.0 ± 1.1	1.4 ± 3.9	14.4 ± 1.1	3.4 ± 1.1	-7.2 ± 3.9
CUVA	5.1 ± 1.0	1.6 ± 1.0	—	6.4 ± 1.0	2.3 ± 1.0	—	7.6 ± 1.0	2.9 ± 1.0	—
FARO	12.6 ± 1.6	5.1 ± 1.6	-8.6 ± 2.7	13.0 ± 1.6	5.8 ± 1.6	-9.4 ± 2.7	14.4 ± 1.6	6.3 ± 1.6	-11.3 ± 2.7
GUAC	6.2 ± 0.8	4.2 ± 0.8	-0.2 ± 1.7	6.8 ± 0.8	4.0 ± 0.8	0.6 ± 1.7	6.1 ± 0.8	3.1 ± 0.8	1.1 ± 1.7
GUFI	7.8 ± 0.8	4.0 ± 0.8	10.1 ± 3.6	10.1 ± 0.8	4.7 ± 0.8	9.3 ± 3.6	12.6 ± 0.8	5.6 ± 0.8	8.4 ± 3.6
IITJ	6.7 ± 1.6	2.5 ± 1.6	-3.5 ± 2.8	6.8 ± 1.6	2.7 ± 1.6	-2.6 ± 2.8	6.1 ± 1.6	2.3 ± 1.6	-1.9 ± 2.8
INEG	5.2 ± 0.6	2.3 ± 0.6	—	5.2 ± 0.6	2.4 ± 0.6	—	4.8 ± 0.6	2.1 ± 0.6	—
LIM2	7.5 ± 1.1	4.9 ± 1.1	-9.7 ± 6.5	7.8 ± 1.1	5.0 ± 1.1	-8.8 ± 6.5	7.1 ± 1.1	4.1 ± 1.1	-8.1 ± 6.5
LIMA	9.0 ± 3.4	3.1 ± 3.8	1.1 ± 20.1	6.2 ± 3.4	0.2 ± 3.8	1.8 ± 20.1	4.2 ± 3.4	-2.9 ± 3.8	2.0 ± 20.1
LZCR	13.8 ± 1.3	9.0 ± 1.3	0.2 ± 2.1	13.9 ± 1.3	8.9 ± 1.3	0.1 ± 2.1	13.7 ± 1.3	8.8 ± 1.3	0.1 ± 2.1
MANZ	9.8 ± 1.1	3.6 ± 1.1	4.8 ± 1.9	11.2 ± 1.1	5.1 ± 1.1	3.5 ± 1.9	12.6 ± 1.1	6.9 ± 1.1	0.9 ± 1.9
MASC	4.1 ± 1.0	3.1 ± 1.0	-1.5 ± 1.6	5.3 ± 1.0	3.5 ± 1.0	-1.4 ± 1.6	6.6 ± 1.0	3.6 ± 1.0	-1.2 ± 1.6
MCAB	6.5 ± 1.1	4.8 ± 1.1	-1.8 ± 5.2	5.7 ± 1.1	4.0 ± 1.1	-1.2 ± 5.2	4.3 ± 1.1	2.7 ± 1.1	-0.8 ± 5.2
MELA	6.8 ± 0.8	7.1 ± 0.8	8.9 ± 3.6	8.6 ± 0.8	7.2 ± 0.8	5.1 ± 3.6	12.7 ± 0.8	7.9 ± 0.8	-1.4 ± 3.6
MILN	4.5 ± 1.0	4.8 ± 1.0	6.4 ± 4.2	6.6 ± 1.0	6.0 ± 1.0	6.0 ± 4.2	9.3 ± 1.0	6.7 ± 1.0	4.6 ± 4.2
MIRA	12.2 ± 1.3	3.0 ± 1.3	14.9 ± 6.4	12.4 ± 1.3	7.3 ± 1.3	7.1 ± 6.4	13.6 ± 1.3	14.0 ± 1.3	2.9 ± 6.4
MMIG	10.1 ± 1.0	5.0 ± 1.0	-4.0 ± 1.6	10.3 ± 1.0	5.2 ± 1.0	-4.7 ± 1.6	11.0 ± 1.0	5.3 ± 1.0	-5.9 ± 1.6
MNZO	9.5 ± 2.0	6.4 ± 2.0	-3.1 ± 3.5	9.9 ± 2.0	6.9 ± 2.0	-2.0 ± 3.5	11.7 ± 2.0	8.2 ± 2.0	-1.4 ± 3.5
MPR1	3.9 ± 0.9	2.7 ± 0.9	-1.2 ± 1.4	4.6 ± 0.9	2.9 ± 0.9	-1.4 ± 1.4	5.2 ± 0.9	2.7 ± 0.9	-1.6 ± 1.4
NOVI	16.9 ± 1.3	9.3 ± 1.4	3.6 ± 7.4	16.3 ± 4.4	6.0 ± 1.4	-5.8 ± 7.4	20.2 ± 4.4	9.2 ± 1.4	-17.2 ± 7.4
NVDO	8.5 ± 1.0	5.0 ± 1.0	3.3 ± 1.6	10.1 ± 1.0	6.3 ± 1.0	3.9 ± 1.6	11.3 ± 1.0	7.4 ± 1.0	4.1 ± 1.6
PENA	8.0 ± 0.9	4.6 ± 0.9	-1.2 ± 2.9	9.6 ± 0.9	5.6 ± 0.9	0.2 ± 2.9	11.8 ± 0.9	7.1 ± 0.9	0.8 ± 2.9
PORT	7.3 ± 1.6	3.9 ± 1.6	12.9 ± 4.9	9.1 ± 1.6	4.2 ± 1.6	11.2 ± 4.9	10.9 ± 1.6	4.0 ± 1.6	8.9 ± 4.9
PURI	5.0 ± 0.7	3.6 ± 0.7	3.9 ± 1.2	7.1 ± 0.7	4.7 ± 0.7	4.6 ± 1.2	10.0 ± 0.7	5.9 ± 0.7	4.8 ± 1.2
PZUL	6.3 ± 1.1	4.2 ± 1.1	2.5 ± 1.9	7.5 ± 1.1	4.5 ± 1.1	2.6 ± 1.9	8.8 ± 1.1	4.6 ± 1.1	1.5 ± 1.9
SEBA	4.7 ± 0.8	4.4 ± 0.8	-3.2 ± 2.1	5.4 ± 0.8	4.0 ± 0.8	-2.8 ± 2.1	5.2 ± 0.8	3.1 ± 0.8	-2.2 ± 2.1
SJDL	14.7 ± 0.9	9.7 ± 0.9	-1.6 ± 3.9	14.2 ± 0.9	6.6 ± 0.9	-13.6 ± 3.9	17.9 ± 0.9	7.3 ± 0.9	-25.5 ± 3.9
TAPA	6.8 ± 0.9	5.4 ± 0.9	1.4 ± 4.1	7.9 ± 0.9	5.8 ± 0.9	2.3 ± 4.1	8.1 ± 0.9	5.1 ± 0.9	2.6 ± 4.1
TECO	10.2 ± 0.9	5.8 ± 0.9	0.7 ± 1.4	10.7 ± 0.9	6.6 ± 0.9	0.9 ± 1.4	12.2 ± 0.9	8.2 ± 0.9	-0.1 ± 1.4
TENA	6.8 ± 1.4	3.6 ± 1.4	10.2 ± 3.7	8.7 ± 1.4	5.0 ± 1.4	6.2 ± 3.7	12.9 ± 1.4	7.0 ± 1.4	0.1 ± 3.7
TNCC	9.5 ± 1.7	4.7 ± 1.7	-0.3 ± 3.0	9.8 ± 1.7	5.0 ± 1.7	-0.2 ± 3.0	10.4 ± 1.7	5.3 ± 1.7	-0.5 ± 3.0
TNCM	9.1 ± 1.5	6.3 ± 1.5	-0.8 ± 2.5	9.2 ± 1.5	6.8 ± 1.5	0.0 ± 2.5	10.5 ± 1.5	7.6 ± 1.5	0.6 ± 2.5
TNCT	10.2 ± 2.5	5.1 ± 2.5	1.0 ± 4.4	10.5 ± 2.5	5.5 ± 2.5	2.3 ± 4.4	11.8 ± 2.5	6.1 ± 2.5	3.2 ± 4.4
TNLC	6.3 ± 1.7	5.1 ± 1.7	-0.0 ± 3.0	7.1 ± 1.7	5.6 ± 1.7	1.0 ± 3.0	9.3 ± 1.7	6.8 ± 1.7	1.9 ± 3.0
TNMR	11.8 ± 1.5	5.9 ± 1.5	-4.7 ± 2.5	11.9 ± 1.5	6.0 ± 1.5	-4.8 ± 2.5	12.5 ± 1.5	6.2 ± 1.5	-5.6 ± 2.5
TNMZ	10.6 ± 1.8	7.8 ± 1.8	-5.0 ± 3.1	10.7 ± 1.8	8.0 ± 1.8	-3.7 ± 3.1	12.1 ± 1.8	8.8 ± 1.8	-2.6 ± 3.1
TNTM	13.0 ± 2.2	8.4 ± 2.2	3.9 ± 4.0	12.8 ± 2.2	8.2 ± 2.2	4.1 ± 4.0	13.9 ± 2.2	8.6 ± 2.2	4.1 ± 4.0
TNZA	-1.1 ± 2.2	-2.1 ± 2.2	—	-0.7 ± 2.2	-1.6 ± 2.2	—	-0.6 ± 2.2	-1.1 ± 2.2	—
TOMA	0.7 ± 5.9	-6.2 ± 6.3	20.8 ± 36.5	5.2 ± 5.9	-5.7 ± 6.3	17.0 ± 36.5	14.6 ± 5.9	-4.9 ± 6.3	17.7 ± 36.5
UAGU	3.1 ± 1.0	3.7 ± 1.0	—	3.5 ± 1.0	4.0 ± 1.0	—	3.4 ± 1.0	3.9 ± 1.0	—
UCOL	8.5 ± 0.8	6.1 ± 0.8	-1.3 ± 1.4	9.4 ± 0.8	6.8 ± 0.8	-0.3 ± 1.4	11.9 ± 0.8	8.0 ± 0.8	-0.4 ± 1.4
UGEO	5.2 ± 0.7	2.3 ± 0.7	-2.9 ± 1.1	6.0 ± 0.7	2.9 ± 0.7	-2.2 ± 1.1	6.3 ± 0.7	3.1 ± 0.7	-1.5 ± 1.1
UMON	9.4 ± 2.0	7.1 ± 2.0	0.0 ± 17.9	7.1 ± 2.0	5.1 ± 2.0	0.6 ± 17.9	4.7 ± 2.0	2.6 ± 2.0	0.9 ± 17.9
VALL	5.1 ± 3.1	-6.7 ± 3.1	-0.2 ± 5.9	5.8 ± 3.1	-6.4 ± 3.1	-0.4 ± 5.9	6.5 ± 3.1	-6.5 ± 3.1	-0.7 ± 5.9
VICT	12.8 ± 0.9	11.1 ± 0.9	4.5 ± 3.7	12.5 ± 0.9	8.6 ± 0.9	1.4 ± 3.7	14.3 ± 0.9	7.8 ± 0.9	-3.5 ± 3.7

Table S1.10: Continued from previous page.

Site	Maxwell time for the mantle used in the corrections for postseismic viscoelastic deformation								
	t_m = 15 yr			t_m = 25 yr			t_m = 40 yr		
	North (mm/yr)	East (mm/yr)	Vert. (mm/yr)	North (mm/yr)	East (mm/yr)	Vert. (mm/yr)	North (mm/yr)	East (mm/yr)	Vert. (mm/yr)
ANIG	5.2 ± 0.9	1.8 ± 0.9	-2.2 ± 1.5	4.9 ± 0.9	1.6 ± 0.9	-2.0 ± 1.5	4.4 ± 0.9	1.4 ± 0.9	-2.0 ± 1.5
AUTA	11.4 ± 0.8	6.0 ± 0.8	4.9 ± 1.8	11.4 ± 0.8	5.0 ± 0.8	4.5 ± 1.8	10.3 ± 0.8	4.4 ± 0.8	4.4 ± 1.8
AVAL	8.7 ± 3.4	7.0 ± 1.1	6.1 ± 4.9	9.1 ± 3.4	6.9 ± 1.1	6.0 ± 4.9	8.2 ± 3.4	6.3 ± 1.1	5.7 ± 4.9
AYUT	8.3 ± 0.8	3.6 ± 0.8	4.1 ± 1.8	7.8 ± 0.8	2.8 ± 0.8	4.2 ± 1.8	6.6 ± 0.8	2.2 ± 0.8	4.1 ± 1.8
CALC	16.1 ± 1.3	9.8 ± 1.3	-10.5 ± 2.1	16.1 ± 1.3	9.8 ± 1.3	-10.6 ± 2.1	15.9 ± 1.3	9.9 ± 1.3	-10.6 ± 2.1
CEBO	6.0 ± 0.9	2.6 ± 0.9	-2.5 ± 4.2	5.8 ± 0.9	2.2 ± 0.9	-2.3 ± 4.2	5.1 ± 0.9	1.5 ± 0.9	-2.4 ± 4.2
CGUZ	7.7 ± 0.9	4.2 ± 0.9	2.2 ± 2.0	7.3 ± 0.9	3.6 ± 0.9	2.1 ± 2.0	6.5 ± 0.9	2.9 ± 0.9	1.9 ± 2.0
CHAC	8.2 ± 0.8	3.4 ± 0.8	-3.2 ± 4.2	8.2 ± 0.8	3.2 ± 0.8	-3.4 ± 4.2	7.9 ± 0.8	3.0 ± 0.8	-3.6 ± 4.2
CHAM	13.2 ± 0.8	9.3 ± 0.8	-1.9 ± 3.2	14.2 ± 0.8	8.9 ± 0.8	-4.3 ± 3.2	14.2 ± 0.8	8.6 ± 0.8	-5.3 ± 3.2
CHMC	12.3 ± 1.1	7.9 ± 1.1	-2.8 ± 1.8	13.0 ± 1.1	7.7 ± 1.1	-3.8 ± 1.8	13.0 ± 1.1	7.4 ± 1.1	-4.4 ± 1.8
COJB	10.7 ± 1.6	3.7 ± 1.6	6.0 ± 5.9	10.5 ± 1.6	3.5 ± 1.6	5.8 ± 5.9	9.9 ± 1.6	3.1 ± 1.6	5.6 ± 5.9
COLI	11.6 ± 0.6	7.8 ± 0.6	1.6 ± 0.9	11.6 ± 0.6	7.8 ± 0.6	1.1 ± 0.9	11.1 ± 0.6	7.5 ± 0.6	1.0 ± 0.9
COLW	9.3 ± 1.8	7.3 ± 1.8	-1.9 ± 3.1	9.2 ± 1.8	7.2 ± 1.8	-2.1 ± 3.1	8.5 ± 1.8	6.7 ± 1.8	-2.3 ± 3.1
COOB	11.5 ± 0.8	7.4 ± 0.8	3.6 ± 1.2	11.5 ± 0.8	7.2 ± 0.8	3.1 ± 1.2	10.8 ± 0.8	6.7 ± 0.8	2.9 ± 1.2
COPE	9.7 ± 1.8	6.8 ± 1.8	-1.6 ± 3.2	9.5 ± 1.8	6.7 ± 1.8	-1.8 ± 3.2	8.9 ± 1.8	6.2 ± 1.8	-1.9 ± 3.2
COPN	9.3 ± 1.8	7.4 ± 1.8	-0.5 ± 3.3	9.2 ± 1.8	7.2 ± 1.8	-0.7 ± 3.3	8.5 ± 1.8	6.8 ± 1.8	-0.9 ± 3.3
COS2	5.6 ± 0.9	3.2 ± 0.9	-5.0 ± 4.3	5.2 ± 0.9	2.6 ± 0.9	-5.0 ± 4.3	4.5 ± 0.9	1.9 ± 0.9	-5.0 ± 4.3
CRIP	13.4 ± 1.1	4.6 ± 1.1	-13.1 ± 3.9	13.3 ± 1.1	5.0 ± 1.1	-17.6 ± 3.9	13.4 ± 1.1	5.3 ± 1.1	-17.9 ± 3.9
CUVA	7.5 ± 1.0	2.8 ± 1.0	—	7.2 ± 1.0	2.4 ± 1.0	—	6.5 ± 1.0	2.0 ± 1.0	—
FARO	13.5 ± 1.6	6.8 ± 1.6	-10.2 ± 2.7	13.5 ± 1.6	7.1 ± 1.6	-10.2 ± 2.7	13.4 ± 1.6	7.3 ± 1.6	-10.2 ± 2.7
GUAC	5.5 ± 0.8	2.5 ± 0.8	1.5 ± 1.7	5.0 ± 0.8	1.9 ± 0.8	1.6 ± 1.7	3.8 ± 0.8	1.4 ± 0.8	1.6 ± 1.7
GUFI	13.3 ± 0.8	5.4 ± 0.8	6.8 ± 3.6	14.1 ± 0.8	4.8 ± 0.8	6.0 ± 3.6	13.2 ± 0.8	4.3 ± 0.8	6.1 ± 3.6
IITJ	5.0 ± 1.6	1.6 ± 1.6	-1.7 ± 2.8	4.7 ± 1.6	1.0 ± 1.6	-1.5 ± 2.8	3.8 ± 1.6	0.5 ± 1.6	-1.5 ± 2.8
INEG	4.3 ± 0.6	1.7 ± 0.6	—	4.0 ± 0.6	1.4 ± 0.6	—	3.7 ± 0.6	1.2 ± 0.6	—
LIM2	6.4 ± 1.1	3.2 ± 1.1	-7.7 ± 6.5	6.0 ± 1.1	2.5 ± 1.1	-7.6 ± 6.5	5.1 ± 1.1	1.9 ± 1.1	-7.7 ± 6.5
LIMA	4.3 ± 3.4	-3.1 ± 3.8	2.5 ± 20.1	4.5 ± 3.4	-3.4 ± 3.8	2.6 ± 20.1	3.5 ± 3.4	-4.2 ± 3.8	2.5 ± 20.1
LZCR	13.4 ± 1.3	8.9 ± 1.3	0.1 ± 2.1	13.3 ± 1.3	9.0 ± 1.3	0.2 ± 2.1	13.2 ± 1.3	9.1 ± 1.3	0.2 ± 2.1
MANZ	12.7 ± 1.1	7.8 ± 1.1	-1.7 ± 1.9	12.8 ± 1.1	8.3 ± 1.1	-4.0 ± 1.9	12.5 ± 1.1	8.1 ± 1.1	-4.4 ± 1.9
MASC	6.8 ± 1.0	3.3 ± 1.0	-1.0 ± 1.6	6.5 ± 1.0	2.9 ± 1.0	-0.9 ± 1.6	6.0 ± 1.0	2.7 ± 1.0	-0.9 ± 1.6
MCAB	3.7 ± 1.1	2.1 ± 1.1	-0.6 ± 5.2	3.4 ± 1.1	1.7 ± 1.1	-0.6 ± 5.2	2.7 ± 1.1	1.3 ± 1.1	-0.6 ± 5.2
MELA	15.0 ± 0.8	9.4 ± 0.8	-8.6 ± 3.6	16.3 ± 0.8	9.6 ± 0.8	-9.6 ± 3.6	16.9 ± 0.8	9.7 ± 0.8	-10.6 ± 3.6
MILN	10.4 ± 1.0	6.6 ± 1.0	1.6 ± 4.2	11.2 ± 1.0	6.1 ± 1.0	0.2 ± 4.2	11.1 ± 1.0	5.7 ± 1.0	-0.4 ± 4.2
MIRA	10.9 ± 1.3	12.7 ± 1.3	-12.3 ± 6.4	5.6 ± 4.3	12.5 ± 1.3	-33.9 ± 6.4	5.8 ± 4.3	11.9 ± 1.3	-30.4 ± 6.4
MMIG	10.7 ± 1.0	5.7 ± 1.0	-5.8 ± 1.6	10.7 ± 1.0	5.8 ± 1.0	-6.0 ± 1.6	10.6 ± 1.0	5.9 ± 1.0	-6.1 ± 1.6
MNZO	12.8 ± 2.0	8.8 ± 2.0	-2.1 ± 3.5	13.3 ± 2.0	9.2 ± 2.0	-2.7 ± 3.5	13.3 ± 2.0	9.2 ± 2.0	-2.9 ± 3.5
MPR1	5.2 ± 0.9	2.3 ± 0.9	-1.5 ± 1.4	5.0 ± 0.9	2.0 ± 0.9	-1.4 ± 1.4	4.7 ± 0.9	1.8 ± 0.9	-1.4 ± 1.4
NOVI	15.4 ± 1.3	1.8 ± 1.4	-27.1 ± 7.4	12.9 ± 1.3	-6.6 ± 1.4	-34.9 ± 7.4	12.6 ± 1.3	-4.7 ± 1.4	-32.2 ± 7.4
NVDO	10.8 ± 1.0	7.5 ± 1.0	4.1 ± 1.6	10.6 ± 1.0	7.2 ± 1.0	3.9 ± 1.6	9.9 ± 1.0	6.6 ± 1.0	3.7 ± 1.6
PENA	12.5 ± 0.9	7.6 ± 0.9	0.7 ± 2.9	13.0 ± 0.9	7.5 ± 0.9	0.5 ± 2.9	12.4 ± 0.9	7.2 ± 0.9	0.3 ± 2.9
PORT	11.8 ± 1.6	3.9 ± 1.6	7.3 ± 4.9	12.3 ± 1.6	3.7 ± 1.6	6.5 ± 4.9	12.1 ± 1.6	3.4 ± 1.6	5.8 ± 4.9
PURI	10.9 ± 0.7	5.9 ± 0.7	4.2 ± 1.2	10.9 ± 0.7	5.5 ± 0.7	3.8 ± 1.2	10.4 ± 0.7	5.1 ± 0.7	3.7 ± 1.2
PZUL	9.0 ± 1.1	4.4 ± 1.1	0.3 ± 1.9	9.2 ± 1.1	4.2 ± 1.1	-0.3 ± 1.9	9.0 ± 1.1	4.0 ± 1.1	-0.8 ± 1.9
SEBA	4.6 ± 0.8	2.6 ± 0.8	-1.9 ± 2.1	4.2 ± 0.8	2.2 ± 0.8	-1.8 ± 2.1	3.4 ± 0.8	2.0 ± 0.8	-1.7 ± 2.1
SJDL	18.7 ± 0.9	1.9 ± 3.0	-22.9 ± 3.9	19.0 ± 0.9	3.3 ± 3.0	-20.6 ± 3.9	18.5 ± 0.9	3.2 ± 3.0	-20.3 ± 3.9
TAPA	8.2 ± 0.9	4.8 ± 0.9	3.2 ± 4.1	8.3 ± 0.9	4.2 ± 0.9	3.2 ± 4.1	7.2 ± 0.9	3.5 ± 0.9	3.0 ± 4.1
TECO	12.1 ± 0.9	8.4 ± 0.9	-1.1 ± 1.4	11.4 ± 0.9	8.0 ± 0.9	-3.6 ± 1.4	11.4 ± 0.9	8.1 ± 0.9	-3.1 ± 1.4
TENA	15.8 ± 1.4	8.8 ± 1.4	-5.8 ± 3.7	17.8 ± 1.4	8.9 ± 1.4	-7.4 ± 3.7	18.3 ± 1.4	8.9 ± 1.4	-8.2 ± 3.7
TNCC	10.0 ± 1.7	5.1 ± 1.7	-0.9 ± 3.0	9.9 ± 1.7	4.9 ± 1.7	-1.2 ± 3.0	9.7 ± 1.7	4.9 ± 1.7	-1.2 ± 3.0
TNCM	11.6 ± 1.5	8.1 ± 1.5	-0.7 ± 2.5	12.2 ± 1.5	8.1 ± 1.5	-1.5 ± 2.5	12.4 ± 1.5	7.9 ± 1.5	-2.0 ± 2.5
TNCT	12.7 ± 2.5	6.6 ± 2.5	2.0 ± 4.4	13.2 ± 2.5	6.6 ± 2.5	1.1 ± 4.4	13.4 ± 2.5	6.4 ± 2.5	0.6 ± 4.4
TNLC	10.6 ± 1.7	7.4 ± 1.7	1.6 ± 3.0	11.1 ± 1.7	7.4 ± 1.7	1.3 ± 3.0	10.8 ± 1.7	7.2 ± 1.7	1.2 ± 3.0
TNMR	12.3 ± 1.5	6.4 ± 1.5	-5.7 ± 2.5	12.3 ± 1.5	6.5 ± 1.5	-5.8 ± 2.5	12.2 ± 1.5	6.6 ± 1.5	-5.9 ± 2.5
TNMZ	13.4 ± 1.8	9.3 ± 1.8	-3.2 ± 3.1	14.0 ± 1.8	9.7 ± 1.8	-3.5 ± 3.1	14.2 ± 1.8	9.7 ± 1.8	-3.8 ± 3.1
TNTM	15.3 ± 2.2	9.5 ± 2.2	2.6 ± 4.0	16.1 ± 2.2	9.8 ± 2.2	2.1 ± 4.0	16.6 ± 2.2	9.9 ± 2.2	1.8 ± 4.0
TNZA	-1.0 ± 2.2	-1.2 ± 2.2	—	-1.2 ± 2.2	-1.4 ± 2.2	—	-1.4 ± 2.2	-1.7 ± 2.2	—
TOMA	19.2 ± 5.9	1.3 ± 6.3	12.5 ± 36.5	23.0 ± 5.9	4.3 ± 6.3	12.1 ± 36.5	23.7 ± 5.9	3.8 ± 6.3	11.7 ± 36.5
UAGU	3.0 ± 1.0	3.6 ± 1.0	—	2.7 ± 1.0	3.4 ± 1.0	—	2.5 ± 1.0	3.2 ± 1.0	—
UCOL	13.3 ± 0.8	8.3 ± 0.8	-1.8 ± 2.7	13.9 ± 0.8	8.7 ± 0.8	-2.4 ± 2.7	13.9 ± 0.8	8.6 ± 0.8	-2.8 ± 2.7
UGEO	5.8 ± 0.7	2.8 ± 0.7	-1.2 ± 1.1	5.4 ± 0.7	2.4 ± 0.7	-1.0 ± 1.1	4.8 ± 0.7	2.0 ± 0.7	-1.0 ± 1.1
UMON	3.9 ± 2.0	1.8 ± 2.0	1.1 ± 17.9	3.5 ± 2.0	1.3 ± 2.0	1.1 ± 17.9	2.7 ± 2.0	0.7 ± 2.0	1.1 ± 17.9
VALL	6.5 ± 3.1	-6.9 ± 3.1	-0.6 ± 5.9	6.3 ± 3.1	-7.2 ± 3.1	-0.5 ± 5.9	6.0 ± 3.1	-7.4 ± 3.1	-0.5 ± 5.9
VICT	11.2 ± 0.9	3.2 ± 0.9	-7.1 ± 3.7	11.2 ± 0.9	1.5 ± 0.9	-8.7 ± 3.7	10.8 ± 0.9	2.1 ± 0.9	-8.0 ± 3.7

† Velocities are relative to the North America plate and, as described in section 1.2.1, were converted from IGS14/ITRF14 to the North America plate frame of reference using the angular velocity 7.45°N, 92.04°E, 0.183°/ Myr.

Table S1.11: Site velocities for model with no viscoelastic relaxation corrections.†

Site	North (mm/yr)	East (mm/yr)	Vertical (mm/yr)
ANIG	3.5 ± 0.9	1.1 ± 0.9	-1.9 ± 1.5
AUTA	9.9 ± 0.8	3.8 ± 0.8	3.6 ± 1.8
AVAL	8.4 ± 3.4	5.7 ± 1.1	5.2 ± 4.9
AYUT	6.2 ± 0.8	2.0 ± 0.8	4.3 ± 1.8
CALC	15.9 ± 1.3	10.0 ± 1.3	-10.6 ± 2.1
CEBO	5.2 ± 0.9	1.0 ± 0.9	-2.2 ± 4.2
CGUZ	7.1 ± 0.9	2.7 ± 0.9	2.2 ± 2.0
CHAC	8.9 ± 0.8	3.9 ± 0.8	-3.2 ± 4.2
CHAM	17.0 ± 0.8	10.1 ± 0.8	-12.1 ± 3.2
CHMC	14.2 ± 1.1	7.6 ± 1.1	-8.5 ± 1.8
COJB	9.2 ± 1.6	2.2 ± 1.6	5.2 ± 5.9
COLI	10.9 ± 0.6	6.8 ± 0.6	-0.4 ± 0.9
COLW	7.8 ± 1.8	5.8 ± 1.8	-2.9 ± 3.1
COOB	10.6 ± 0.8	6.0 ± 0.8	1.8 ± 1.2
COPE	8.2 ± 1.8	5.3 ± 1.8	-2.4 ± 3.2
COPN	7.8 ± 1.8	5.8 ± 1.8	-1.4 ± 3.3
COS2	4.7 ± 0.9	1.7 ± 0.9	-4.8 ± 4.3
CRIP	15.8 ± 1.1	7.7 ± 1.1	-31.3 ± 3.9
CUVA	5.5 ± 1.0	1.3 ± 1.0	—
FARO	13.8 ± 1.6	7.5 ± 1.6	-10.6 ± 2.7
GUAC	3.5 ± 0.8	1.3 ± 0.8	1.8 ± 1.7
GUFI	13.4 ± 0.8	3.3 ± 0.8	2.6 ± 3.6
IITJ	3.4 ± 1.6	-0.1 ± 1.6	-1.5 ± 2.8
INEG	3.4 ± 0.6	0.9 ± 0.6	—
LIM2	5.1 ± 1.1	1.6 ± 1.1	-7.5 ± 6.5
LIMA	5.7 ± 3.4	-3.0 ± 3.8	3.1 ± 20.1
LZCR	13.2 ± 1.3	9.1 ± 1.3	0.3 ± 2.1
MANZ	14.1 ± 1.1	9.1 ± 1.1	-11.7 ± 1.9
MASC	5.0 ± 1.0	2.4 ± 1.0	-0.8 ± 1.6
MCAB	2.5 ± 1.1	1.1 ± 1.1	-0.5 ± 5.2
MELA	17.9 ± 0.8	9.9 ± 0.8	-18.0 ± 3.6
MILN	12.5 ± 1.0	6.5 ± 1.0	-3.9 ± 4.2
MIRA	9.4 ± 1.3	8.4 ± 1.3	-33.6 ± 6.4
MMIG	10.7 ± 1.0	6.0 ± 1.0	-6.3 ± 1.6
MNZO	13.9 ± 2.0	9.7 ± 2.0	-6.2 ± 3.5
MPR1	4.3 ± 0.9	1.8 ± 0.9	-1.2 ± 1.4
NOVI	13.5 ± 1.3	-4.0 ± 1.4	-35.6 ± 7.4
NVDO	9.2 ± 1.0	5.6 ± 1.0	3.2 ± 1.6
PENA	12.1 ± 0.9	6.5 ± 0.9	-0.9 ± 2.9
PORT	15.9 ± 1.6	6.0 ± 1.6	5.3 ± 4.9
PURI	9.4 ± 0.7	4.1 ± 0.7	2.0 ± 1.2
PZUL	9.7 ± 1.1	4.1 ± 1.1	-1.7 ± 1.9
SEBA	3.2 ± 0.8	2.2 ± 0.8	-1.5 ± 2.1
SJDL	20.0 ± 0.9	4.7 ± 0.9	-21.5 ± 3.9
TAPA	6.9 ± 0.9	2.9 ± 0.9	3.0 ± 4.1
TECO	11.2 ± 0.9	7.3 ± 0.9	-5.5 ± 1.4
TENA	21.4 ± 1.4	9.8 ± 1.4	-16.5 ± 3.7
TNCC	9.7 ± 1.7	4.6 ± 1.7	-1.6 ± 3.0
TNCM	13.3 ± 1.5	7.9 ± 1.5	-5.2 ± 2.5
TNCT	14.2 ± 2.5	6.5 ± 2.5	-1.7 ± 4.4
TNLC	10.1 ± 1.7	6.3 ± 1.7	-0.2 ± 3.0
TNMR	12.3 ± 1.5	6.7 ± 1.5	-6.1 ± 2.5
TNMZ	14.5 ± 1.8	9.8 ± 1.8	-6.3 ± 3.1
TNTM	17.6 ± 2.2	10.1 ± 2.2	-1.1 ± 4.0
TNZA	-1.6 ± 2.2	-2.2 ± 2.2	—
TOMA	27.1 ± 5.9	9.6 ± 6.3	5.0 ± 36.5
UAGU	2.1 ± 1.0	2.8 ± 1.0	—
UCOL	14.6 ± 0.8	8.9 ± 0.8	-6.5 ± 2.7
UGEO	4.1 ± 0.7	1.4 ± 0.7	-0.9 ± 1.1
UMON	3.9 ± 2.0	1.2 ± 2.0	1.3 ± 17.9
VALL	5.6 ± 3.1	-7.5 ± 3.1	-0.4 ± 5.9
VICT	10.9 ± 0.9	1.6 ± 0.9	-12.9 ± 3.7

† See footnote in Table S1.10.

Table S1.12: Misfit F (Eq. 1.3) and weighted root mean square error wrms (Eq. 1.4) for all models with viscoelastic relaxation corrections.

t_m	F	wrms (campaign sites) mm
2.5 years	13.6	5.8
4 years	13.1	5.4
8 years	13.8	5.3
15 years	14.4	5.4
25 years	14.6	5.7
40 years	14.9	5.6
no correction	14.7	6.1

S1.3 SUPPLEMENTARY FIGURES

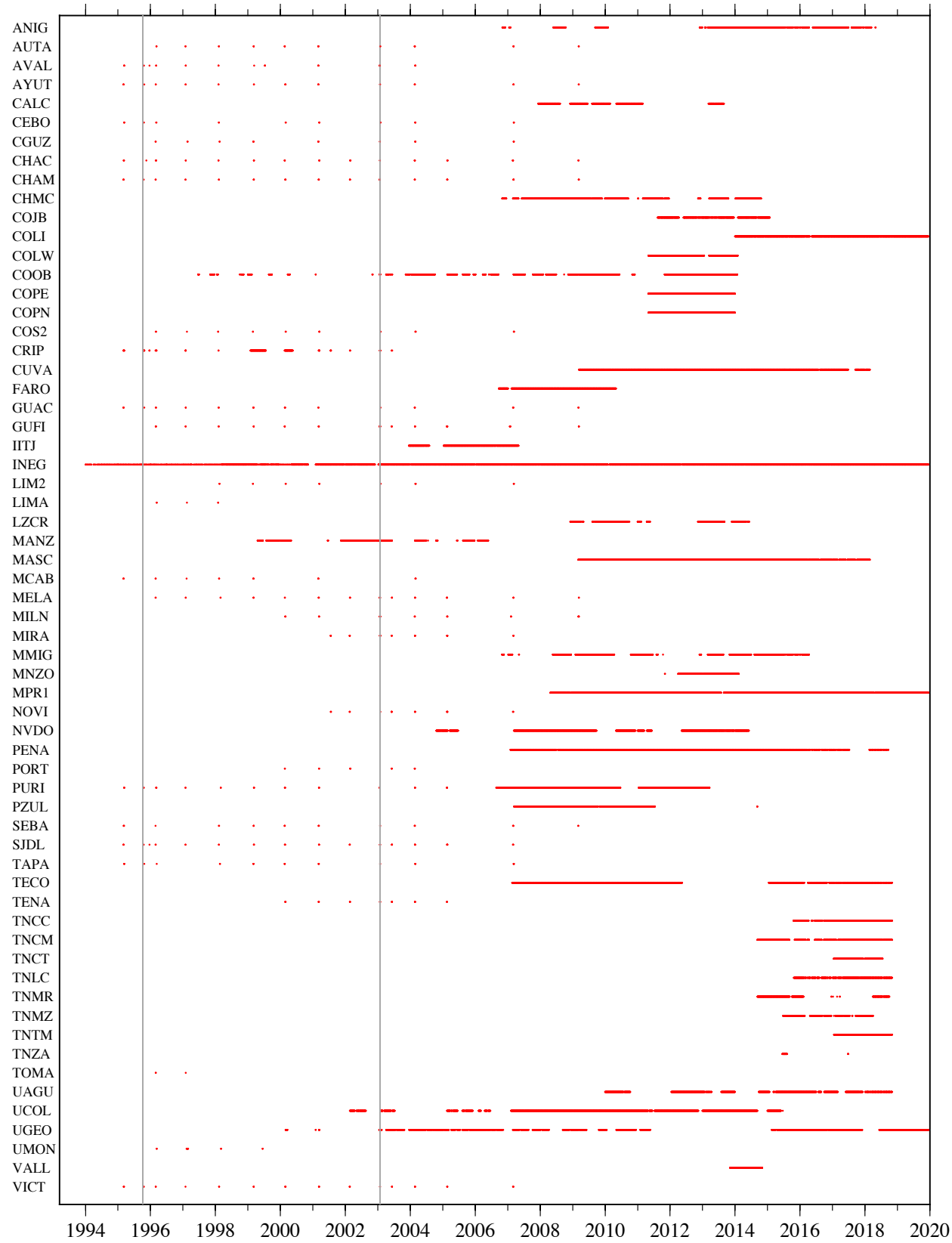

Figure S1.1. Time coverage of the GPS sites. Vertical lines indicate earthquake dates.

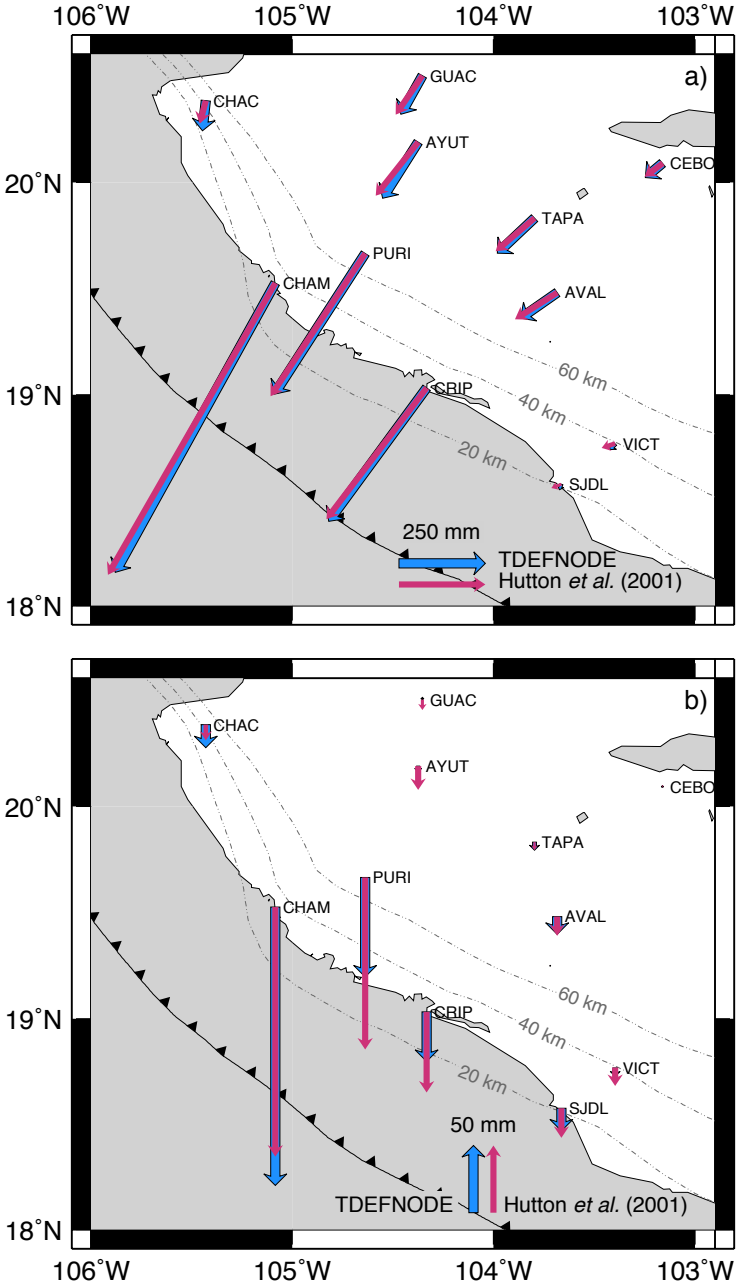

Figure S1.2. Coseismic GPS site displacements from the 1995 Jalisco–Colima earthquake, predicted by our preferred slip solution (blue arrows) and by the model from Hutton *et al*. (2001) (magenta arrows).

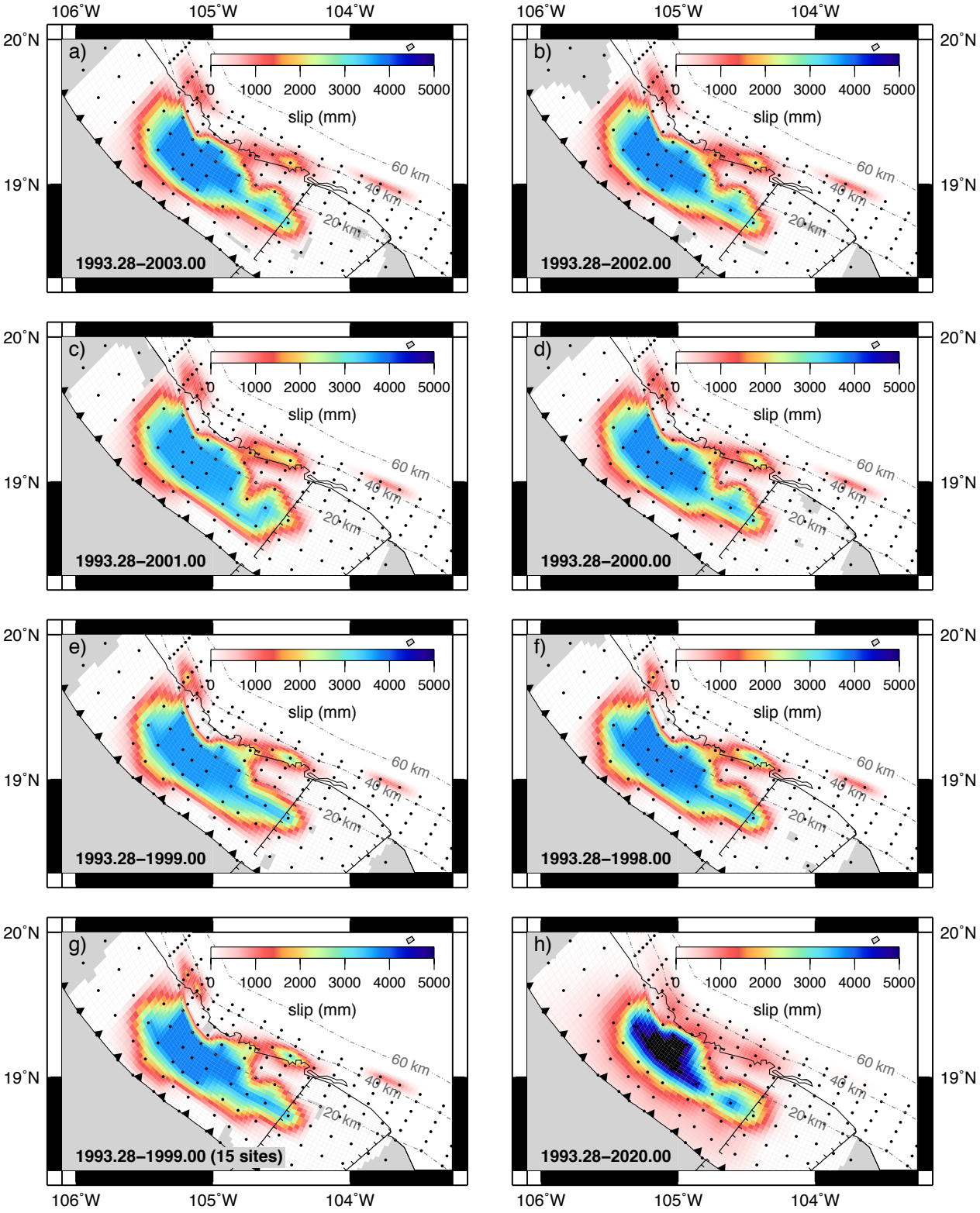

Figure S1.3. TDEFNODE slip solutions for the 1995 Colima–Jalisco earthquake using observations from the interval indicated on each panel. "15 sites" refers to the use of the sites active during the earthquake exclusively. Dashed lines show the slab contours every 20 km. Black dots locate the fault nodes where slip is estimated.

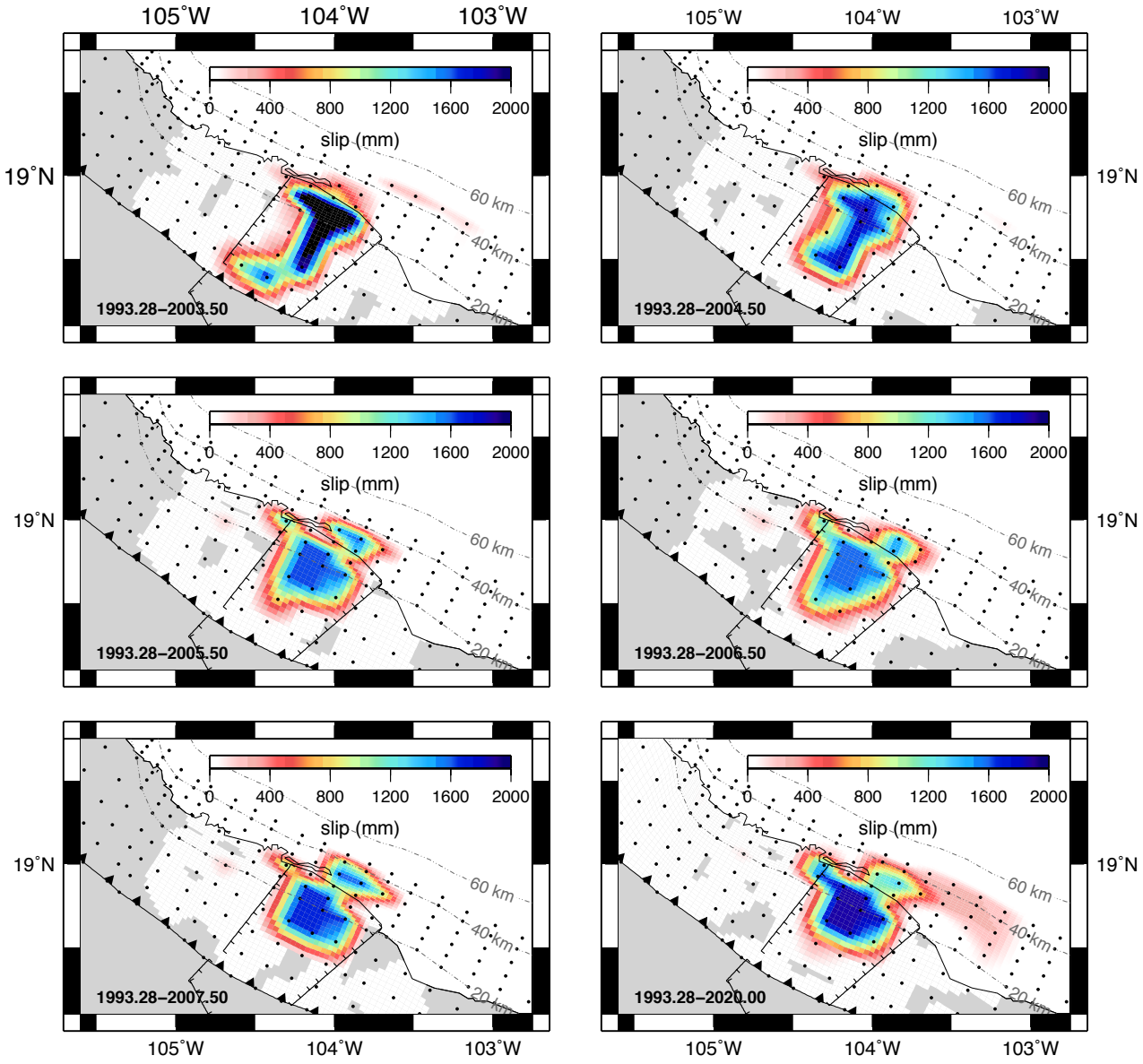

Figure S1.4. TDEFNODE geodetic slip solutions for the 2003 Colima–Jalisco earthquake using time series corrected for the viscoelastic effects of the 1995 Tecoman earthquake with τ_m = 15 years for the mantle. The interval used for the inversion is shown on each panel. Bottom right panel (1993.28–2020.00) corresponds to a model with no viscoelastic corrections. Dashed lines show the slab contours every 20 km. Black dots locate the fault nodes where slip is estimated.

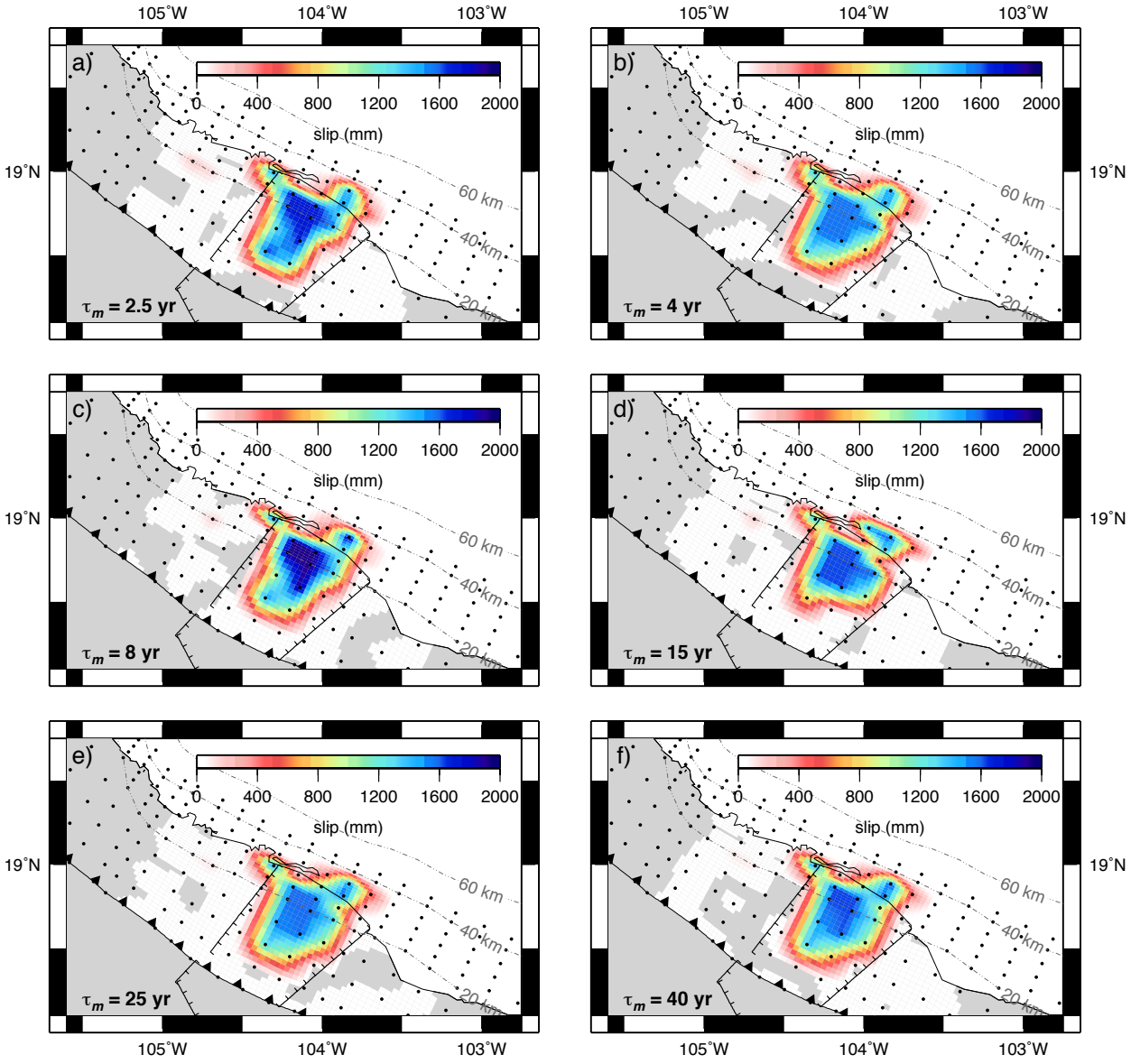

Figure S1.5. TDEFNODE slip solutions for the 2003 Tecoman earthquake using time series corrected for the viscoelastic effects of the 1995 Colima–Jalisco earthquake. The Maxwell time τ_m for the mantle corresponding to the correction is indicated on each panel. The interval used for the inversion was 1993.28–2005.50. Dashed lines show the slab contours every 20 km. Black dots locate the fault nodes where slip is estimated.

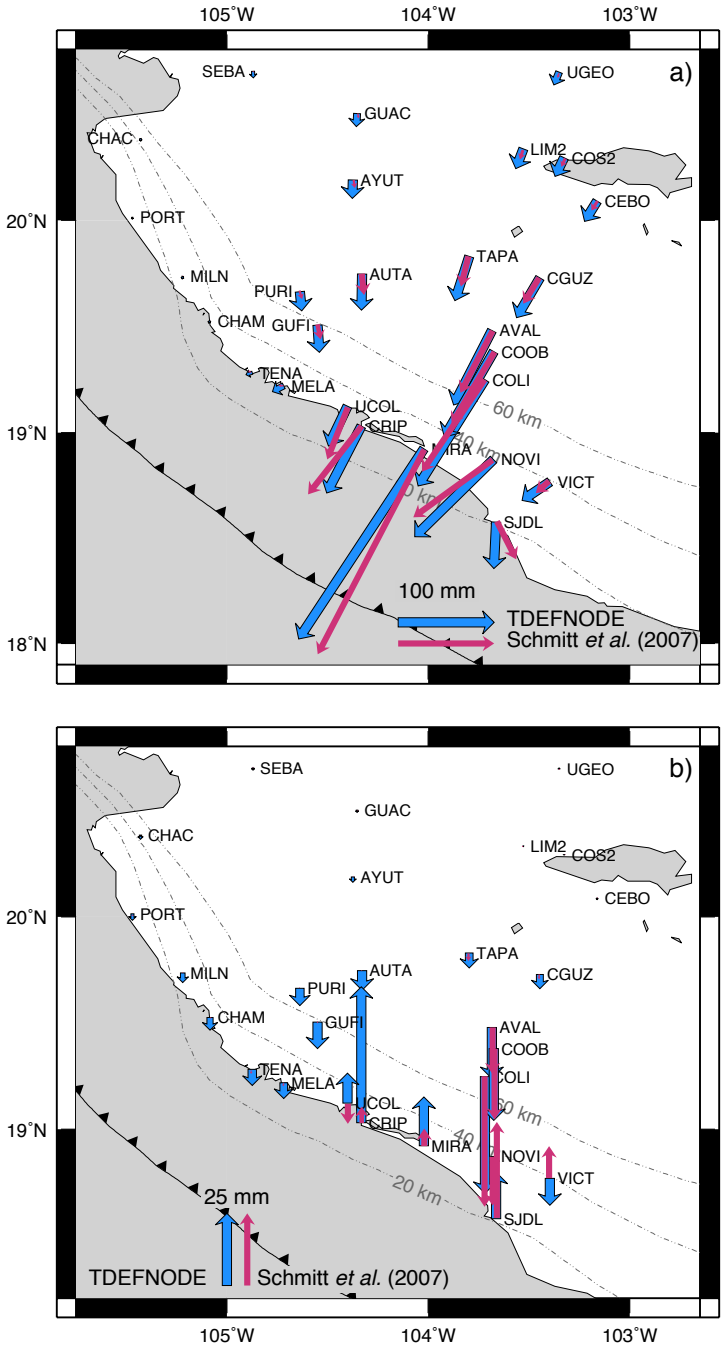

Figure S1.6. Coseismic GPS site displacements from the 2003 Tecomán earthquake, predicted by Schmitt *et al*. (2007) (magenta arrows) and by our preferred slip solution for the model corresponding to the correction for the viscoelastic effects of a mantle with τ_m = 15 years (blue arrows).

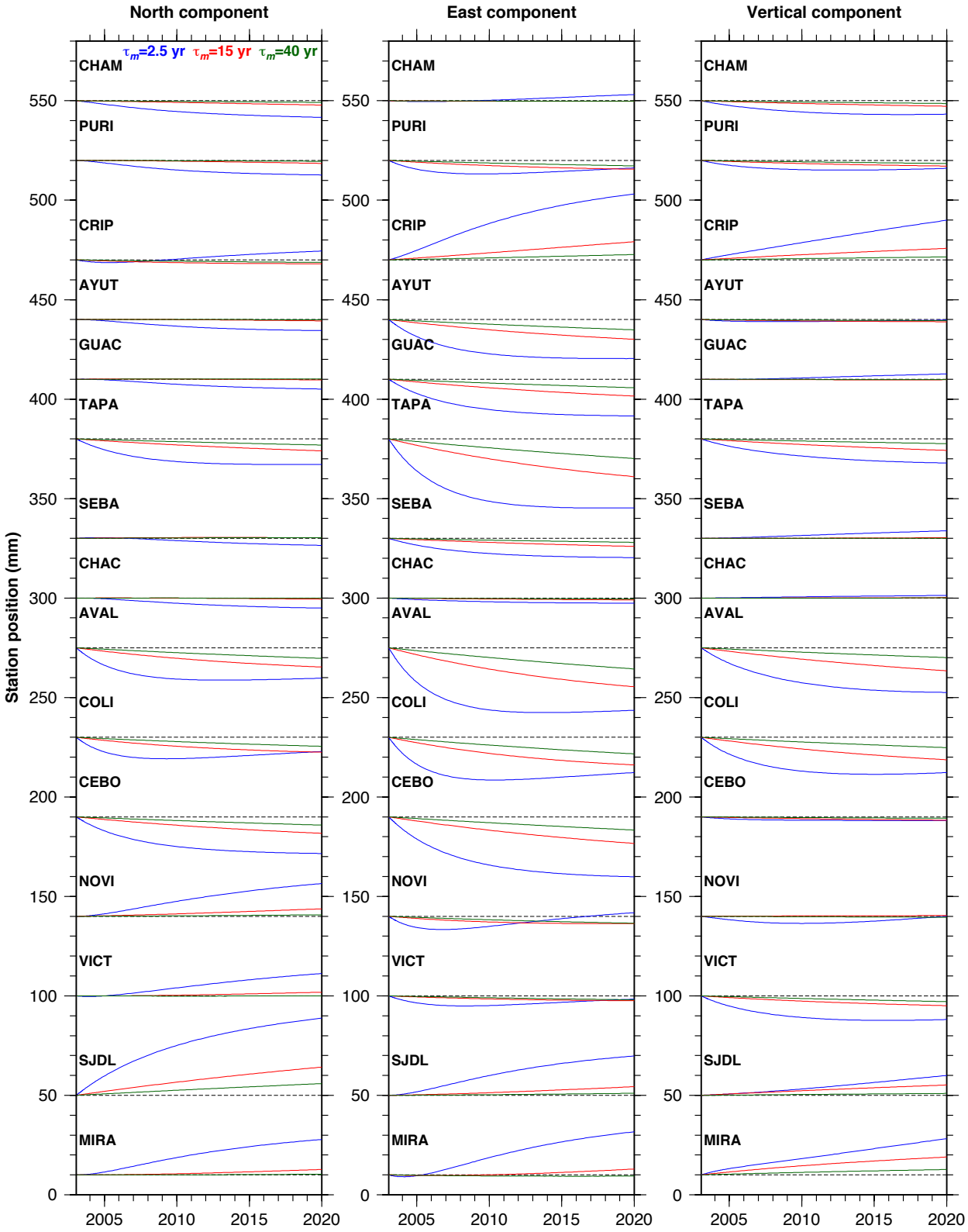

Figure S1.7. Modeled viscoelastic deformation for the 2003 Tecomán earthquake at selected GPS sites, for mantle rheologies corresponding to Maxwell times of 2.5 (blue), 15 (red), and 40 years (green).

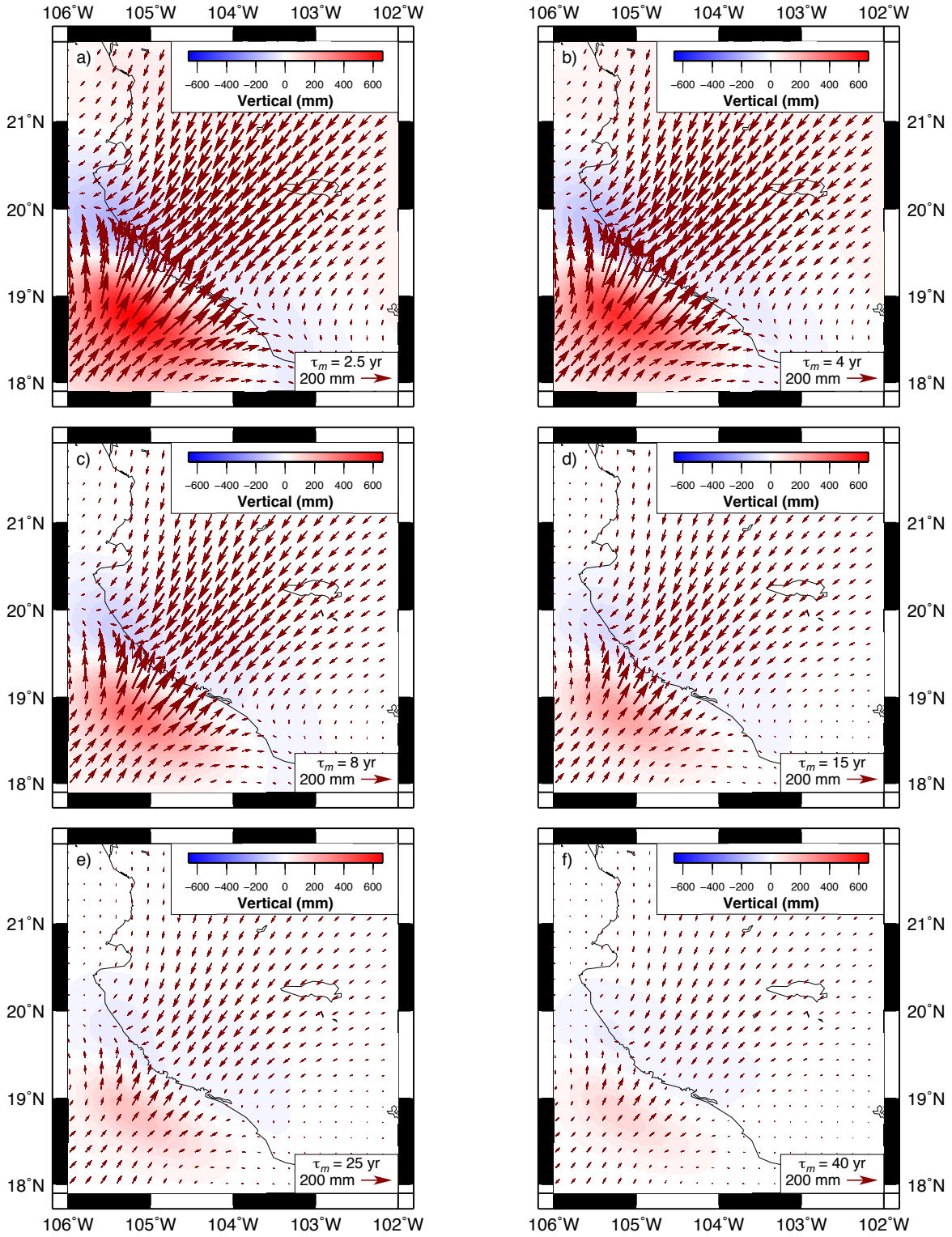

Figure S1.8. Cumulative viscoelastic displacements for the ~25–year–long period 1995.77 to 2020.27 triggered by the 1995 Colima–Jalisco and the 2003 Tecomán earthquakes, as predicted with RELAX software using our preferred coseismic slip solutions. The displacements shown in each panel were determined using the mantle Maxwell time given in the lower right corner of each panel. Arrows show the horizontal displacements and colors indicate the vertical displacements.

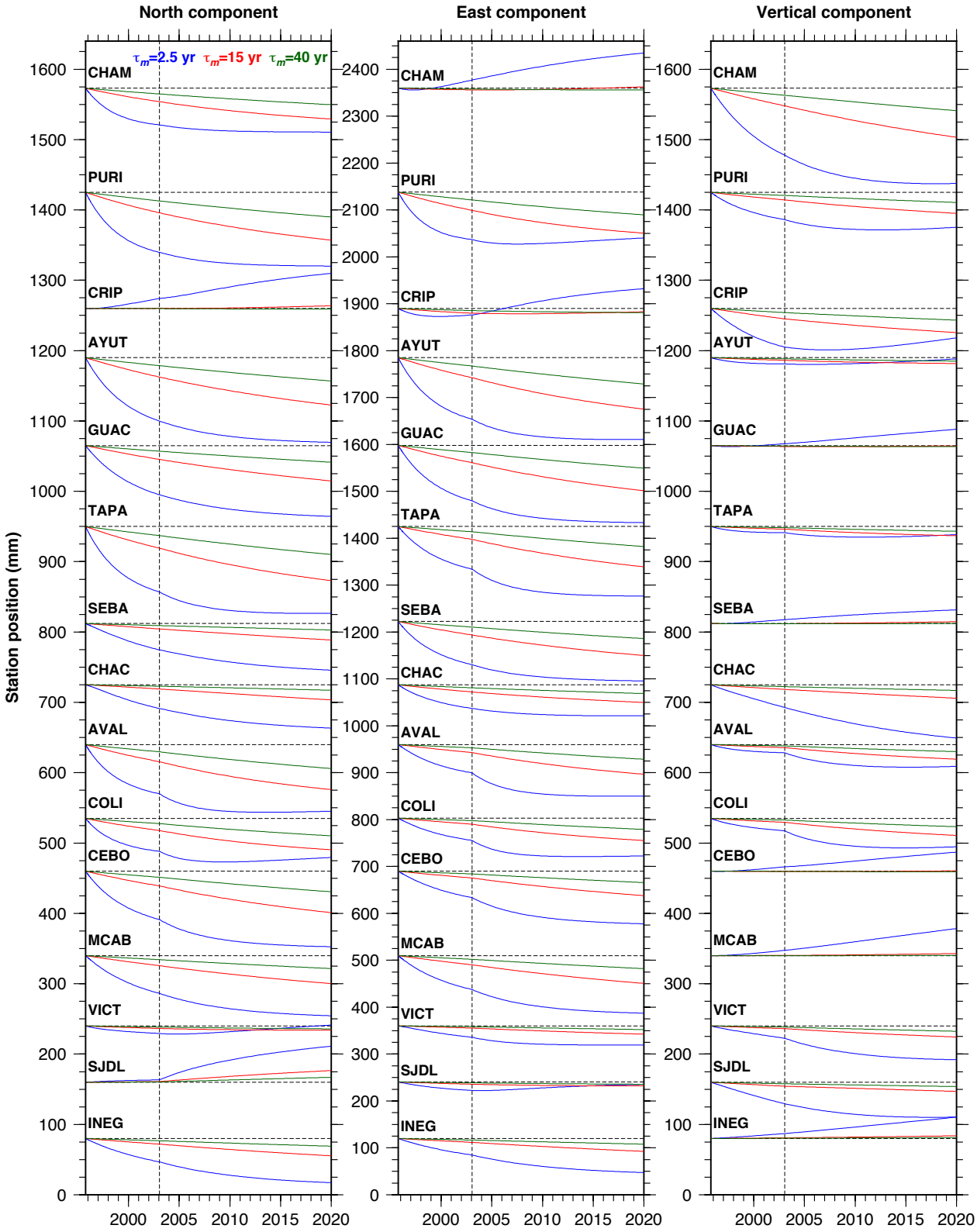

Figure S1.9. Modeled viscoelastic deformation for the 1995 Colima–Jalisco and the 2003 Tecomán earthquakes at selected GPS sites, for mantle rheologies corresponding to Maxwell times of 2.5 (blue), 15 (red), and 40 years (green). The dashed vertical lines mark the time of the 2003 Tecomán earthquake.

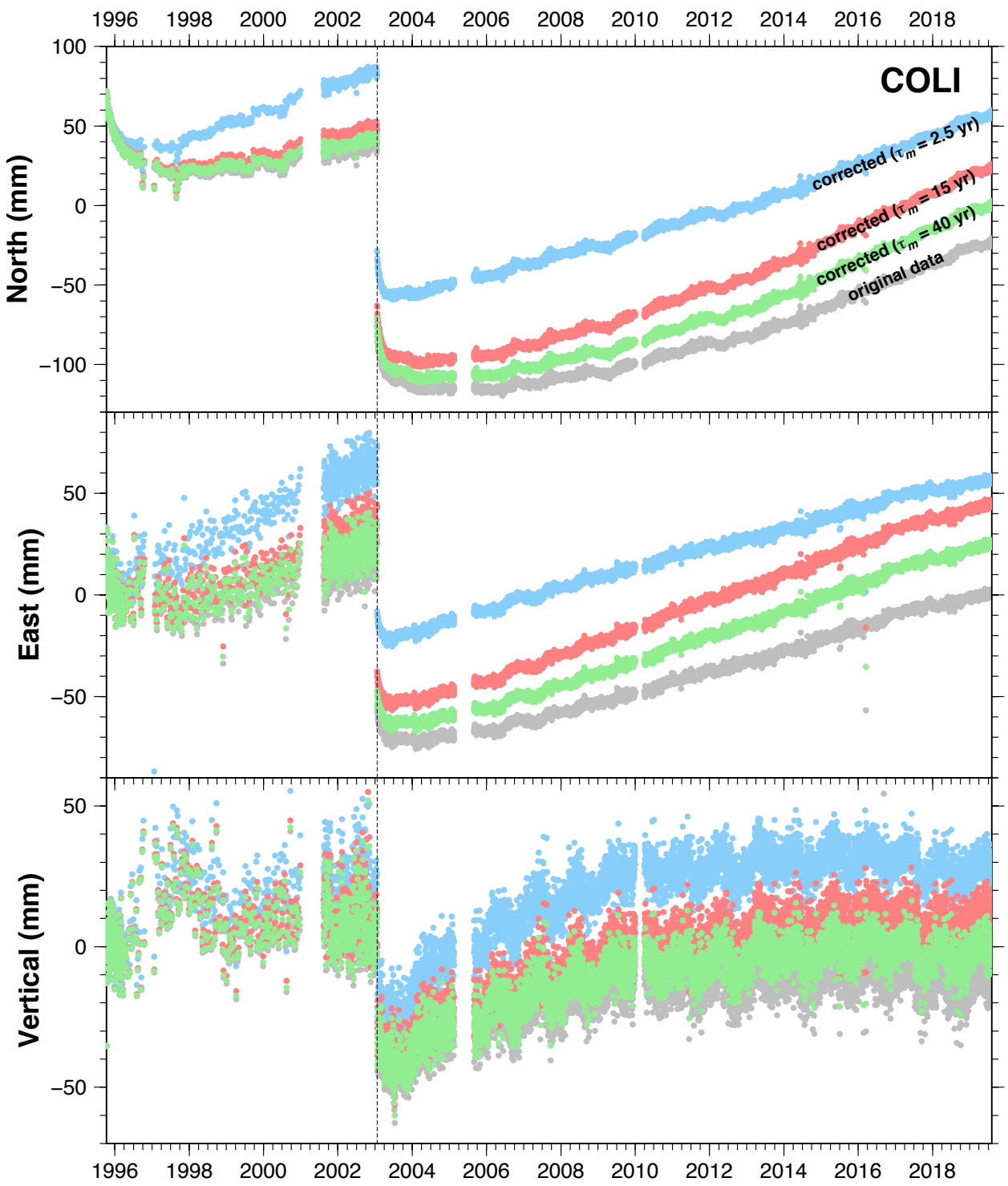

Figure S1.10. Daily north, east and vertical displacements for GPS station COLI, from 1993 to 2019. Gray dots correspond to the original time series. Blue, red and green dots correspond to the time series corrected for the viscoelastic deformation response from the 1995 and 2003 earthquakes, using τ_m = 2.5, 15, and 40 years, respectively. The black dashed line marks the time of the 2003 Tecomán earthquake.

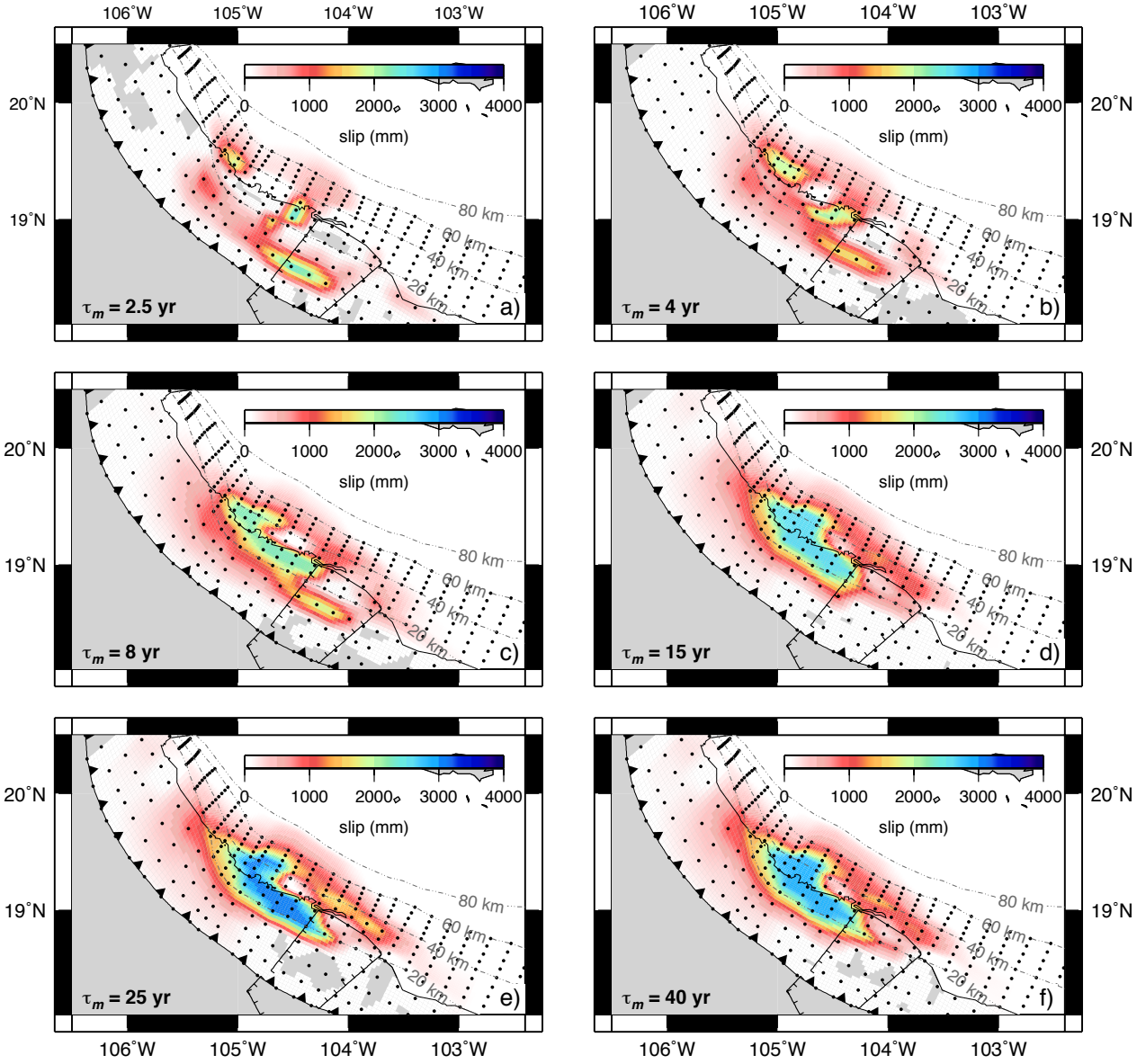

Figure S1.11. TDEFNODE slip solutions for the 1995 Colima–Jalisco earthquake afterslip (integrated over the 1995.77–2020.00 interval) using time series corrected for the viscoelastic effects of the 1995 Colima–Jalisco and the 2003 Tecomán earthquakes. The mantle Maxwell times τ_m used for the corrections are indicated on each panel. The interval of observations used for the inversions was 1993.28–2020.00. Dashed lines show the slab contours every 20 km. Black dots locate the fault nodes where slip is estimated.

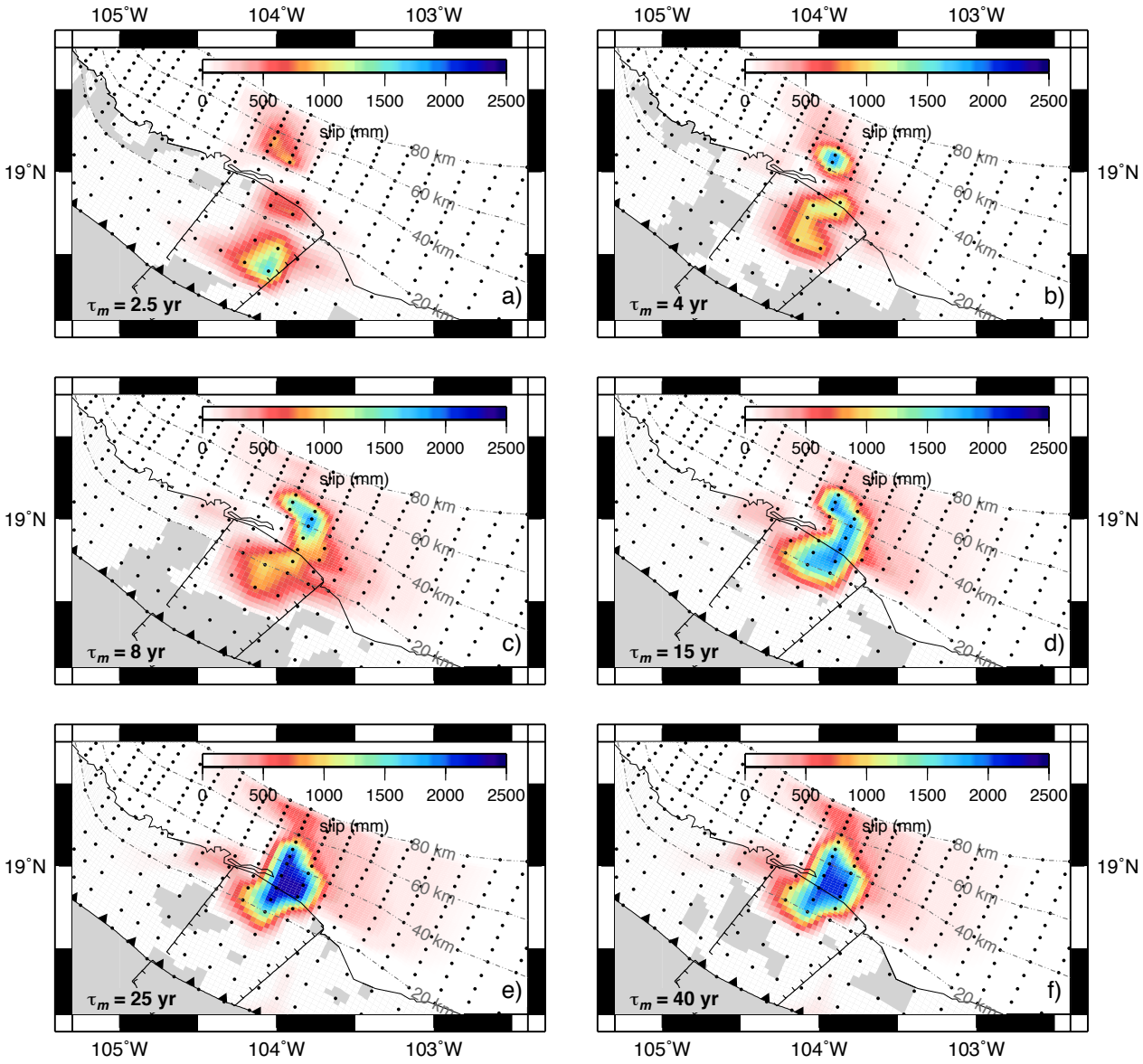

Figure S1.12. TDEFNODE solutions for the 2003 Tecoman earthquake afterslip (integrated over the 2003.06–2020.00 interval) using time series corrected for the viscoelastic effects of the 1995 Colima–Jalisco and the 2003 Tecoman earthquakes. The mantle Maxwell times τ_m used for the corrections are indicated on each panel. The interval of observations used for the inversions was 1993.28–2020.00. Dashed lines show the slab contours every 20 km. Black dots locate the fault nodes where slip is estimated.

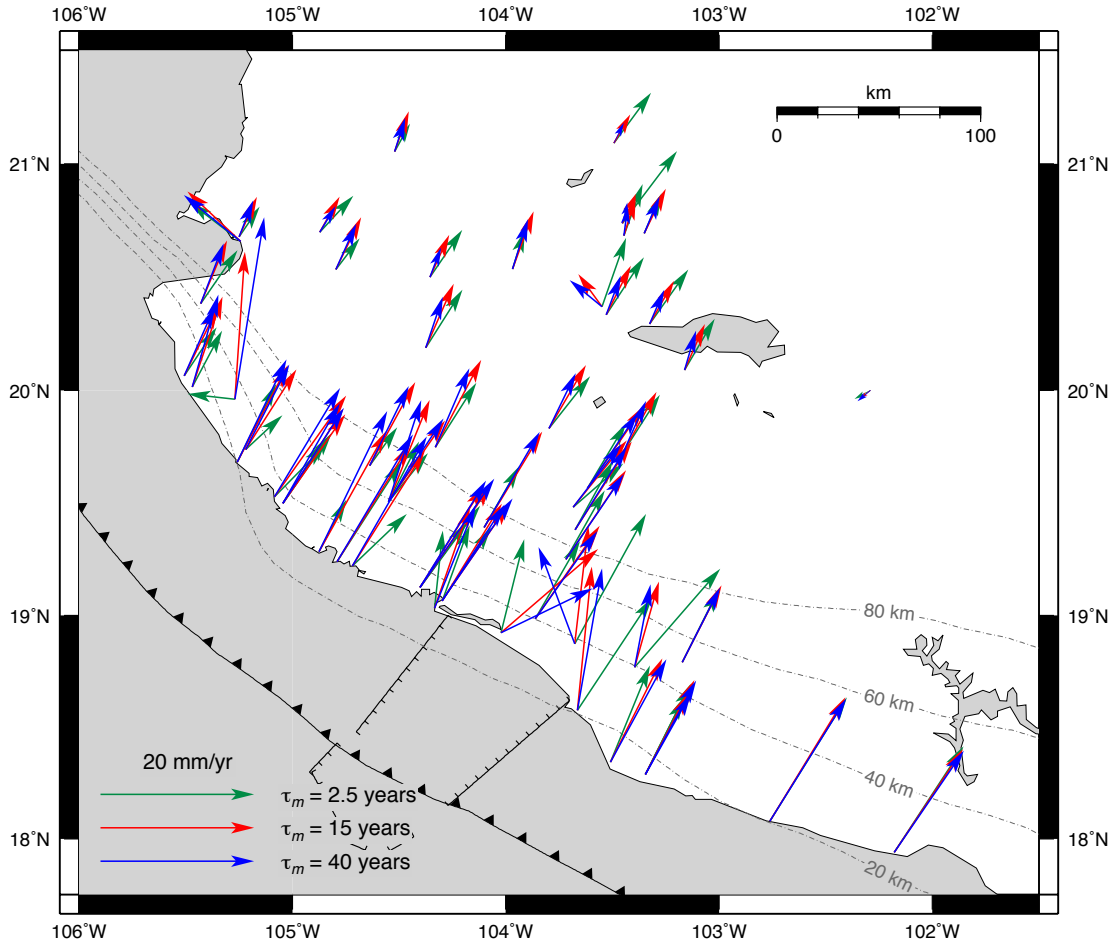

Figure S1.13. Best fitting horizontal site velocities relative to the North America plate, from the time–dependent inversion of GPS position time series that were corrected for viscoelastic effects using mantle Maxwel times of 2.5 (green), 15 (red), and 40 (blue) years. Uncertainties have been omitted for clarity.

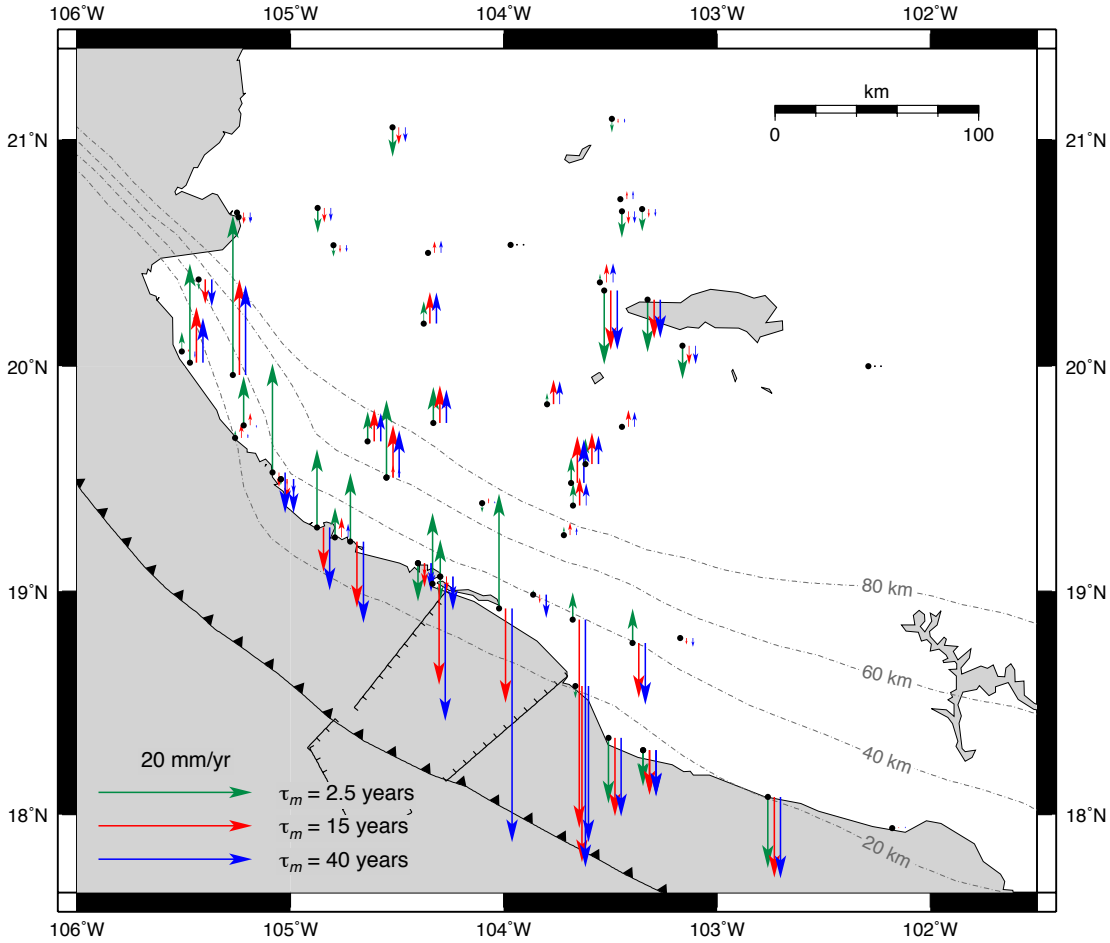

Figure S1.14. Best fitting vertical site velocities from the time–dependent inversion of GPS position time series that were corrected for viscoelastic effects using mantle Maxwel times of 2.5 (green), 15 (red), and 40 (blue) years. Black dots show the site locations. Superposing velocity vectors are shifted to the right to help visualization. Uncertainties have been omitted for clarity.

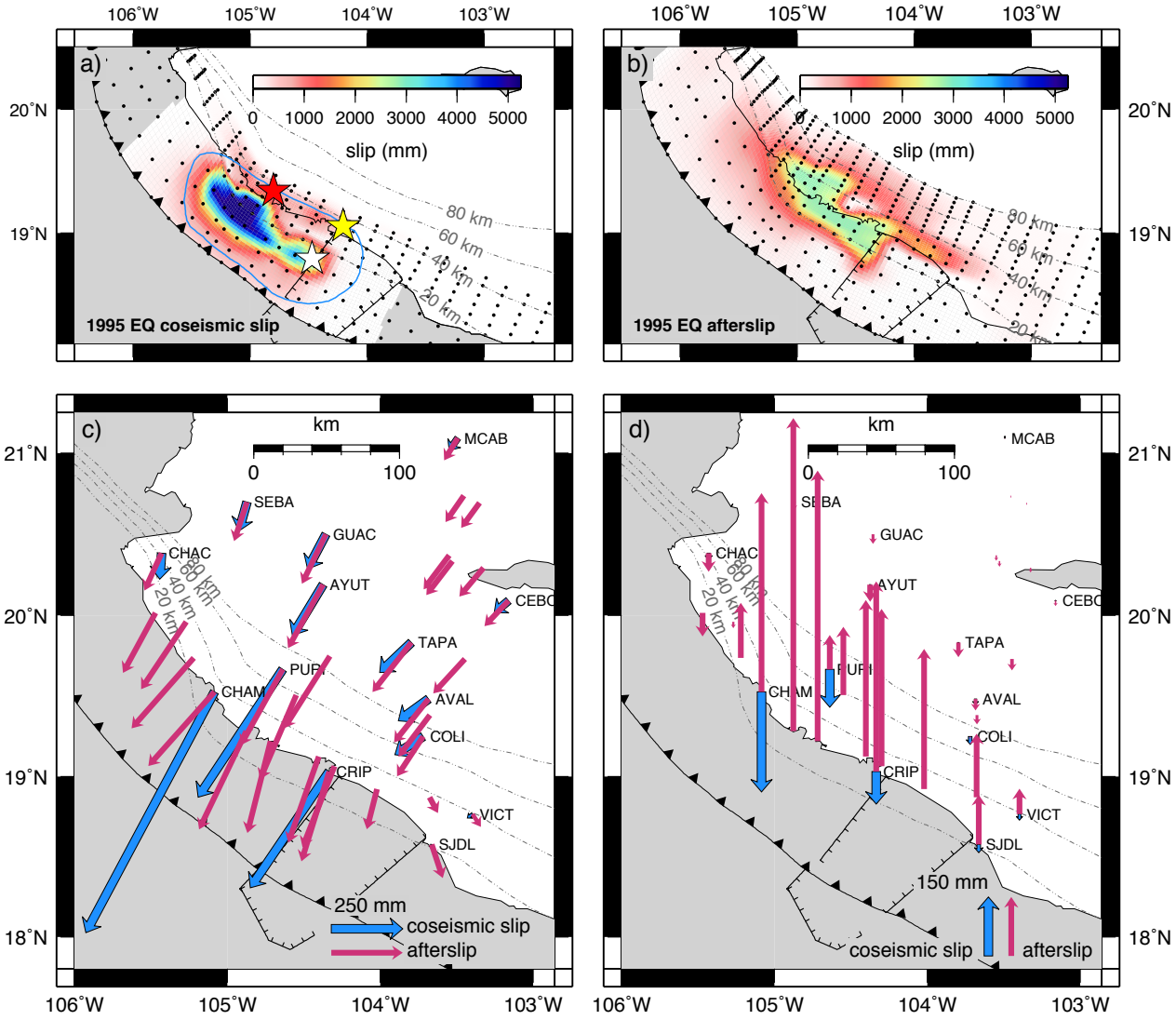

Figure S1.15. TDEFNODE slip solution for a) the 1995 Colima–Jalisco earthquake and b) its postseismic afterslip for a model without viscoelastic effects corrections. EQ: earthquake. Dashed lines show the slab contours every 20 km. Black dots locate the fault nodes where slip is estimated. The blue line delimits the earthquake aftershock area (Pacheco *et al*. 1997). White, yellow and red stars are the epicenters from Courboulex *et al*. (1997) and USGS, and the centroid from the gCMT catalog (Dziewonski *et al*. 1997), respectively. Panels c) and d) respectively show the horizontal and vertical site motions that are predicted by the coseismic and afterslip solutions from panels a) and b) at sites active during the earthquake for panel c) and sites active between 1995 and 2003 for panel d).

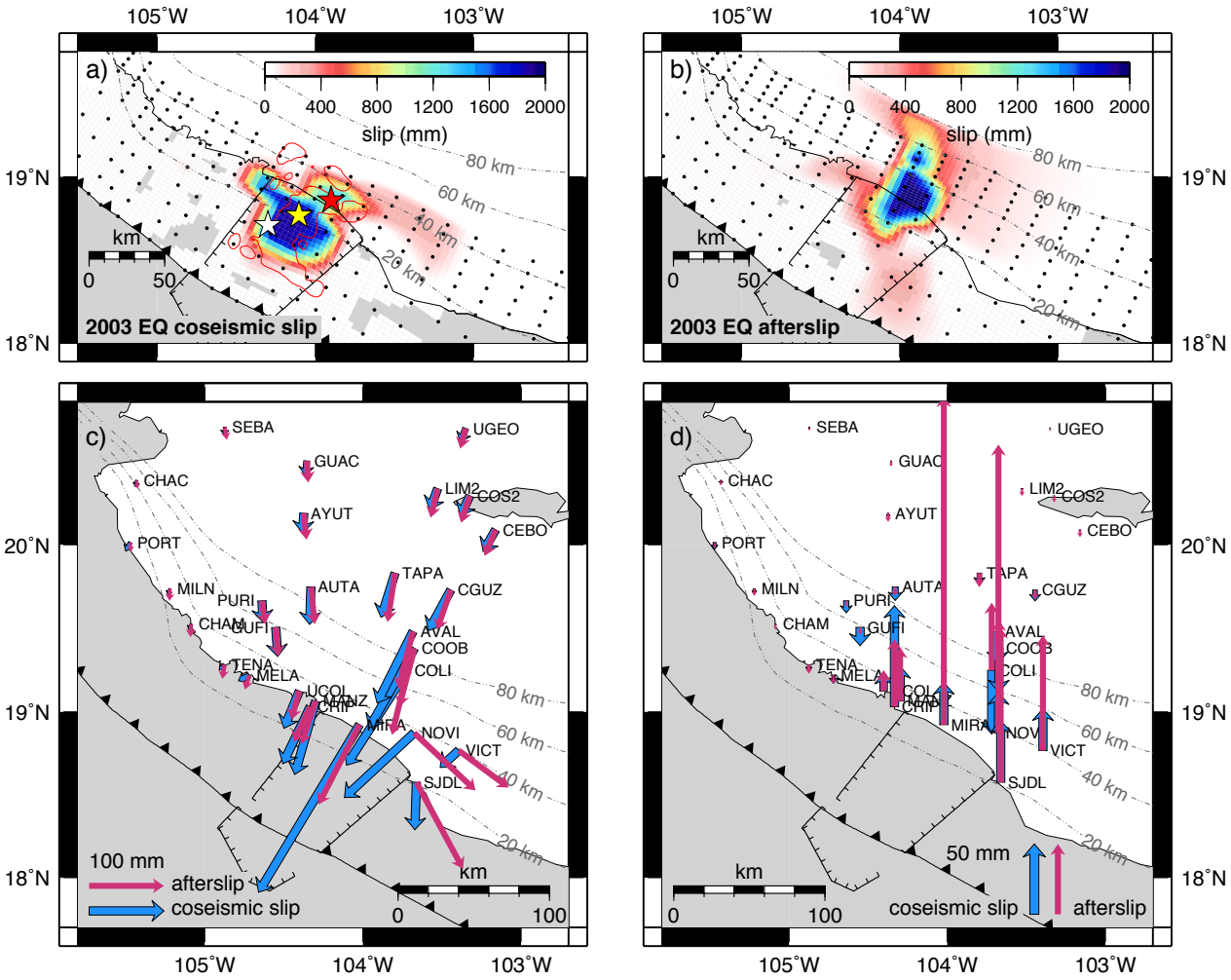

Figure S1.16. TDEFNODE slip solution for a) the 2003 Tecomán earthquake and b) its postseismic afterslip for a model without viscoelastic effects corrections. EQ: earthquake. Dashed lines show the slab contours every 20 km. Black dots locate the fault nodes where slip is estimated. The red line delimits the rupture area for the earthquake (Yagi *et al*. 2004). White, yellow and red stars are the epicenters from Yagi *et al*. (2004) and USGS, and the centroid from the gCMT catalog (Ekström *et al*. 2004), respectively. Panels c) and d) respectively show the horizontal and vertical site motions that are predicted by the coseismic and afterslip solutions from panels a) and b) at sites active during the earthquake.

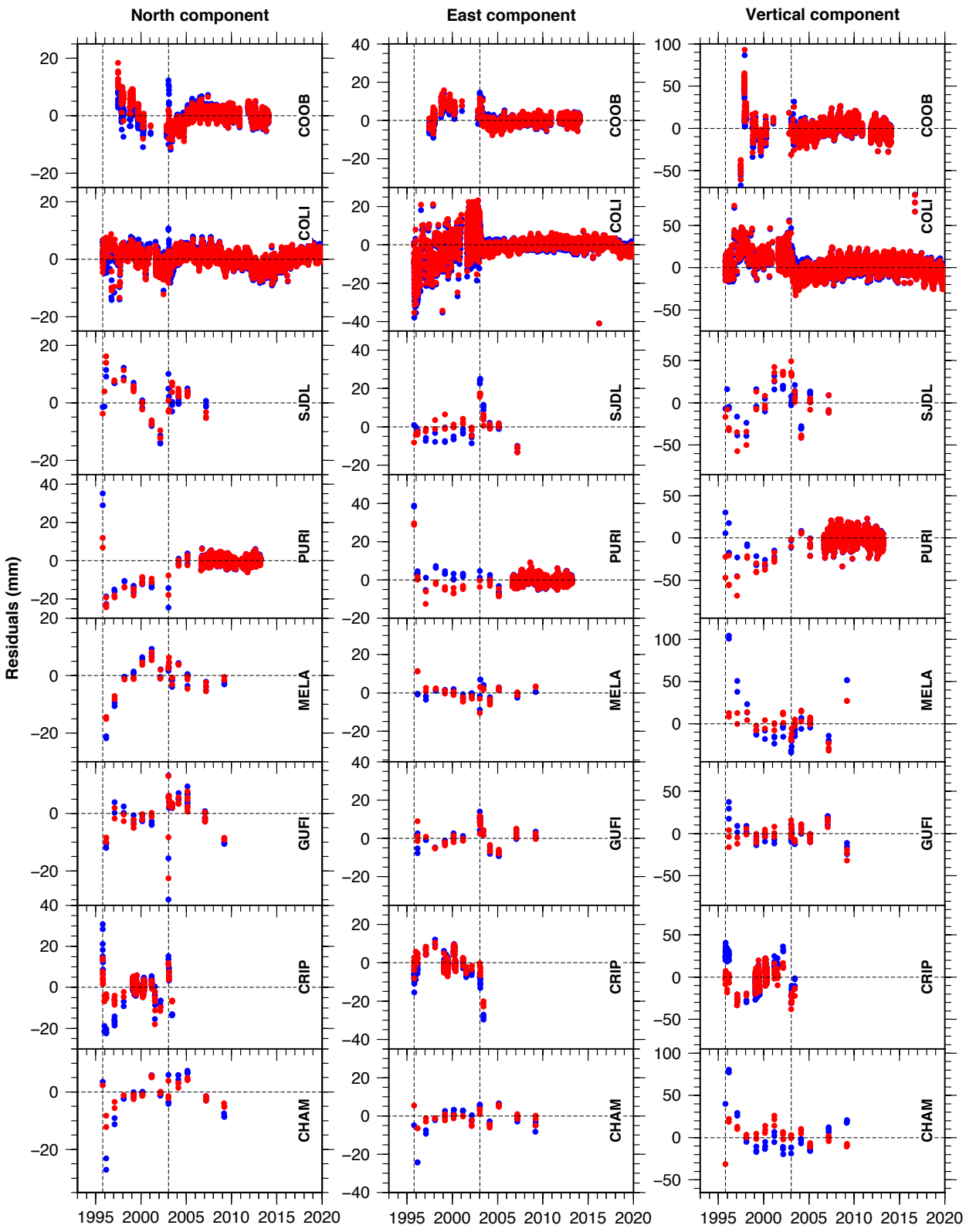

Figure S1.17. Residuals at selected sites from our model with viscoelastic corrections using τ_m = 8 years for the mantle (red) and with no corrections for viscoelastic effects (blue). Dashed vertical lines mark the time of the 1995 and 2003 earthquakes.

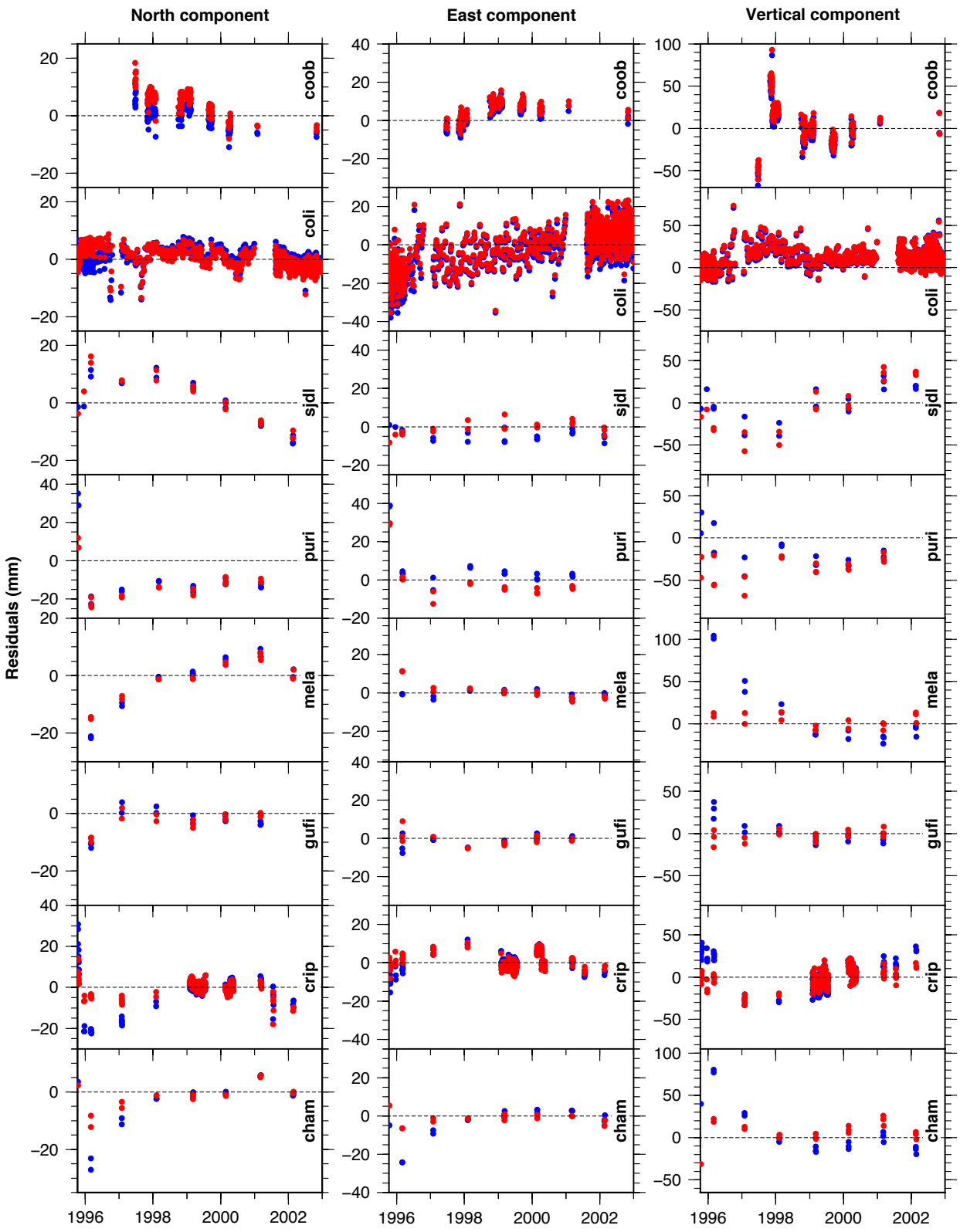

Figure 1.21. Residuals at selected sites from our model with viscoelastic response corrections using t_m = 8 years for the mantle (red) and with no corrections for viscoelastic effects (blue), for the period between the 1995 and 2003 earthquakes.

CHAPTER 2

GPS-derived interseismic fault locking along the Jalisco-Colima segment of the Mexico subduction zone

SUMMARY

Northeastward subduction of the oceanic Rivera and Cocos plates in western Mexico poses a poorly understood seismic hazard to the overlying areas of the North America plate. We estimate the magnitude and distribution of interseismic locking along the northern ~500 km of the Mexico subduction zone, with a series of elastic half-space inversions that optimize the fits to the velocities of 57 GPS stations in western Mexico. All velocities were corrected for the coseismic, afterslip and viscoelastic rebound effects of the 1995 Colima-Jalisco and 2003 Tecomán earthquakes. We explore the robustness of interseismic locking estimates to a variety of mantle Maxwell times that are required for the viscoelastic corrections, to the maximum permitted depth for locking of the subduction interface, and to the location assigned to the Rivera-Cocos-North America plate triple junction offshore from western Mexico. The best fitting locking solutions are associated with a maximum locking depth of 40 km, a triple junction location ~50 km northwest of the Manzanillo Trough, and a mantle Maxwell time of 15 yr (viscosity of 2×10^{19} Pa·s). Checkerboard tests show that the locking distribution is best resolved at intermediate depths (10-40 km). All of our inversions define a gradual transition from strong locking (i.e. 70-100 percent) of most (70%) of the Rivera-North America subduction interface to strong but less uniform locking below the Manzanillo Trough, where oceanic lithosphere transitional between the Cocos and Rivera plate subducts, to weak to moderate locking (averaging 55 percent) of the Michoacán segment of the

Cocos-North America interface. Strong locking of the ~125-km-long trench segment offshore from Puerto Vallarta and other developed coastal areas, where our modeling indicates an average annual elastic slip-rate deficit of ~20 mm/yr, implies that ~1.8 m of unrelieved plate slip has accrued since the segment last ruptured in 1932, sufficient for a M~8.0 earthquake.

2.1 INTRODUCTION

Geodetic studies of the Jalisco-Colima Subduction Zone (JCSZ) began in the mid-1990s with aims of monitoring interseismic strain accumulation and crustal deformation associated with the subduction of the Rivera (RI) and Cocos (CO) plates beneath the North America (NA) plate (Fig. 2.1). At the time, the Rivera plate subduction zone had been relatively aseismic since the destructive June 3 1932 (M_w = 8.2) and June 18 1932 (M_w = 7.8) earthquakes, most likely indicating that the subduction interface was relocked and accumulating strain for a future large earthquake. DeMets *et al.* (1995) suggested that the seismic energy that was released by the 1932 earthquakes could reaccumulate in ~80 years given an average estimated plate kinematic convergence rate of 20-30 mm y^{-1} (DeMets & Stein 1990). Since then, two large earthquakes, the M = 8.0 October 9, 1995 Colima-Jalisco and M = 7.4 January 22, 2003 Tecomán earthquakes have ruptured roughly half of the subduction interface that ruptured in 1932. The northwestern ~120 km of the 1932 rupture zone, offshore from Puerto Vallarta and other major tourist resorts along Jalisco's Gold Coast, has however remained seismically quiescent (Fig. 1.2) and presumably remains a seismic hazard.

Significant, long-lasting transient deformation associated with the 1995 and 2003 earthquakes (*e.g*. Figs 1.3-1.7 and Márquez-Azúa *et al.* 2002) has impeded progress in quantifying the steady-state interseismic strain accumulation and interseismic coupling across the Rivera-

North America (RI/NA) subduction interface and northwesternmost few hundred km of the Cocos-North America (CO/NA) subduction interface, which are essential for understanding the regional seismic hazard. To date, only two studies have estimated interseismic locking in this region. From the velocity of a single continuous GPS site COLI that operated for ~2.5 years before the 1995 Colima-Jalisco earthquake, Márquez-Azúa *et al.* (2002) estimated that the shallow regions of the RI/NA subduction interface (depths < 25 km) were fully locked prior to the earthquake. Selvans *et al.* (2010) approximated the steady interseismic velocity field by assuming that transient deformation associated with the 1995 earthquake had decayed to negligible levels by early 1998 and estimating site velocities from GPS data gathered between 1998 and 2001. However, most of the 1998-2001 average site velocities pointed towards the subduction zone, opposite to that expected for a region with interseismic elastic shortening (Márquez-Azúa *et al.* 2002). They concluded that the estimated site velocities were qualitatively consistent with a combination of locking along the subduction interface and a continued viscoelastic response to the 1995 earthquake.

In this second stage of our two-part seismotectonic study of northwestern Mexico, we describe and invert newly determined interseismic velocities at 57 GPS sites in Jalisco, Colima and neighboring states. Our objective is to estimate interseismic locking of the entire northernmost ~500 km of the Mexico subduction zone, including the whole RI/NA subduction interface and northwestern CO/NA interface below the state of Michoacán (Fig. 2.1). The interseismic velocities we used are results of the first stage of our analysis (Chapter 1), in which we inverted the daily position time-series at 62 GPS sites to estimate time-dependent coseismic slip and post-seismic afterslip solutions for the 1995 Colima-Jalisco and 2003 Tecomán earthquakes, and interseismic

GPS site velocities fully corrected for viscoelastic deformation from six assumed models for the mantle (Section 1.2.1, Fig. 1.8).

Given that interseismic locking solutions for this part of the Mexico subduction zone have not been estimated previously, much of our analysis focuses on evaluating how the best-fitting locking solutions vary with respect to four key assumptions in our analysis, as follows: 1) the mantle viscosities that were used to correct the GPS time series in the first stage of our analysis; 2) the location assumed for the poorly understood, offshore boundary between the subducting Rivera and Cocos plates; 3) the maximum depth for interseismic locking of the subduction interface; 4) the estimated convergence rate between the Rivera and North America plates (RI-NA). Our principal goals are to estimate: 1) the magnitude of and along-strike variations in interseismic locking along the subduction interface; 2) differences in locking between the CO/NA and RI/NA subduction interfaces; 3) where interseismic locking occurs with respect to the depth ranges of postseismic afterslip and non-volcanic tremor.

2.2 DATA

2.2.1 Raw GPS data and processing

For our two-part study we compiled all available GPS data from western Mexico, including all the data that were used in previous geodetic studies of this region (*e.g.* Melbourne *et al.* 1997; 2002; Hutton *et al.* 2001; Márquez-Azúa *et al.* 2002; Schmitt *et al.* 2007; Selvans *et al.* 2010) and all subsequent observations. Readers are referred to Chapter 1 for descriptions of our methods for processing the raw GPS data, details about the GPS site locations, data time spans, and site position time series, and information about the inversions we used to determine 3-D interseismic station velocities via modeling of the instantaneous coseismic offsets for the 1995 and 2003

earthquakes and time-dependent postseismic fault afterslip and viscoelastic rebound triggered by the two earthquakes.

The horizontal velocities used herein are specified relative to the North America plate, which is the geodetic frame of reference adopted for our study and whose motion is given by an angular velocity constrained by the motions of ~1000 continuous stations in the plate interior (Section 1.2.1). The formal velocity uncertainties estimated from inversions that are described in Chapter 1 do not account for likely errors or biases that might be introduced by our modeling assumptions and viscoelastic corrections. We thus systematically increased the formal uncertainties, which were typically only fractions of a mm y^{-1}, to more typical magnitudes of ±13 mm y^{-1} in the horizontal components and larger in the vertical component (Section 1.4.6). All of the velocities and uncertainties that were used for this analysis are found in Tables S1.10 and S1.11.

2.2.2 GPS site velocities

Sixty-two GPS sites were active in our study area between 1993 and 2020, consisting of 36 continuous and 26 campaign sites. Of these, we excluded from this analysis the velocities of four sites with too few observations to be useful (LIMA, TNZA, TOMA, and VALL) and one site (NOVI) with a velocity that disagreed significantly with the velocities of other more reliable nearby sites. Fig. 2.2 displays the horizontal and vertical velocities of the remaining 57 sites. All velocities are corrected for the coseismic and afterslip effects of the 1995 and 2003 earthquakes and the viscoelastic effects of each earthquake calculated for an assumed mantle Maxwell time of 15 yr (with an equivalent mantle viscosity of 2×10^{19} Pa·s for a shear modulus of 40 GPa). The velocities that were calibrated for a viscoelastic response with a τ_m = 15 yr are associated

with the best average least-squares model fits for our two-stage analysis and are thus adopted here as the basis for much of the ensuing analysis. The horizontal velocities (Fig. 2.2a) are dominated by northeastward motion toward the plate interior at rates that diminish rapidly inland from the trench (Figs 2.3a and b). The vertical rates transition from subsidence in coastal areas to slow uplift at locations farther inland (Figs 2.2b, 2.3c and d). The observed margin normal shortening is consistent with elastic strain that arises from partial to full coupling of the Mexico subduction interface.

As is described in Chapter 1, we also derived interseismic site velocities based on viscoelastic corrections that use assumed mantle Maxwell times of 2.5, 4, 8, 25, and 40 years, corresponding to upper mantle viscosities η of 3×10^{18}, 5×10^{18}, 1×10^{19}, 3×10^{19}, and 5×10^{19} Pa·s. The velocity fields derived for all of these viscoelastic corrections and a velocity field without any viscoelastic correction are displayed in Figs S2.1-S2.6. Although the interseismic velocity fields are dominated by northeast-directed station motions, consistent with non-zero subduction interface coupling, the velocity magnitudes and velocity gradients differ significantly for the different applied viscoelastic corrections. For example, the trench-normal rates of sites in areas of coastal Jalisco (Figs S2.7a and b) average 14-19 mm/yr for the $\tau_m = 40$ yr velocities, but only 7-10 mm/yr for the $\tau_m = 2.5$ yr velocities, a factor of two difference. The $\tau_m = 40$ yr velocities diminish from as high as 20 mm/yr at the coast to only 3 mm/yr ~250 km inland, much more than for the $\tau_m = 2.5$ yr velocities, which diminish from 10 mm/yr to only 5-7 mm/yr over the same distance (Figs S2.1, S2.5 and S2.7).

Similar large differences occur for the $\tau_m = 2.5$ yr versus $\tau_m = 40$ yr vertical rates (Figs S2.5, S2.7c and d). Whereas the $\tau_m = 2.5$ yr vertical rates for a trench-normal transect of the Jalisco

region transition from coastal subsidence to inland uplift (Fig. S2.1), the τ_m = 40 yr vertical rates transition from rapid coastal uplift to slow or no uplift farther inland (Fig. S2.5). Thus, estimates of the 3-D velocities and the interseismic locking models we derive from them are sensitive to the mantle Maxwell time (or viscosity) used to calibrate those velocities for the viscoelastic effects of the 1995 and 2003 earthquakes.

2.3 METHODS

2.3.1 TDEFNODE inversions

In general, interseismic GPS velocity fields are well approximated by models that incorporate rotating blocks that deform internally via interseismic elastic strain due to interactions with other blocks across the bounding faults (McCaffrey 2002). The motion of a block *i* rotating in the reference frame R is described by its angular velocity ${}_{\mathrm{R}}\boldsymbol{\Omega}_i = (\lambda_p, \phi_p, \omega)$, where $\lambda_p, \phi_p,$ and ω specify the angular velocity's latitude, longitude, and rotation rate, respectively. The horizontal velocity of each point **X** on block *i* relative to reference frame R is given by ${}_{\mathrm{R}}\mathbf{V}_i = {}_{\mathrm{R}}\boldsymbol{\Omega}_i \times \mathbf{X}$, where **X** is the vector that points from the geocenter to said point. The difference in the constant velocities of blocks *i* and *j*, ${}_j\mathbf{V}_i = {}_{\mathrm{R}}\mathbf{V}_i - {}_{\mathrm{R}}\mathbf{V}_j$, calculated at point **X** on the fault that separates the two blocks gives the long-term slip rate at that point. Friction along a boundary between two blocks gives rise to an accruing elastic slip deficit with respect to the expected long-term block motion. The fractional part of relative plate motion that is not accommodated by steady, aseismic slip is referred to as "locking" (McCaffrey 2002). When parts of the fault are locked, the motions everywhere within the bounding blocks due to their rotations in reference frame R are modified by elastic strain whose magnitude and direction depend on the orientation and configuration of the locked boundary faults and the rate and sense of slip across those faults.

We use TDEFNODE to estimate interseismic locking of the Jalisco-Colima subduction interface from the GPS site velocities described above. When applied in its static mode, TDEFNODE simultaneously estimates block rotations, fault locking, and block strain-rate tensors (for blocks with long-term internal deformation) (McCaffrey 2002). Elastic deformation is determined using backslip methods (Savage 1983) and half-space dislocation equations (Okada 1985) that quantify the direction and rate of elastic deformation given the orientations, locations, and slip sense/rate of locked faults. Faults (and hence fault locking) are parameterized by nodes that follow fault depth contours. At each fault node, a long-term fault slip-rate vector **V** is determined from the angular velocity that specifies the relative motion of the two fault-bounding blocks; backslip is applied to the fault as $\varphi\mathbf{V}$, where φ is the fault locking.

For blocks without long-term internal deformation, as we assume for this analysis, the velocities V_i at locations **X** within our study area are given by (McCaffrey 2002)

$$V_i(\mathbf{X}) = \sum_{b=1}^{B} H(\mathbf{X} \in \Delta_b)\,[{}_{\mathrm{R}}\boldsymbol{\Omega}_b \times \mathbf{X}] \cdot \hat{\mathbf{i}} - \sum_{k=1}^{F} \sum_{n=1}^{N_k} \sum_{j=1}^{2} \varphi_{nk}\, G_{ij}(\mathbf{X}, \mathbf{X}_{nk})[\,{}_{h}\boldsymbol{\Omega}_f \times \mathbf{X}_{nk}]\,] \cdot \hat{\mathbf{j}} \quad (2.1)$$

where i is the index for velocity component (x, y, or z); B is the number of blocks; Δ is the subset of the model domain within block b; $H = 1$ if the point **X** is contained within block b, $H = 0$ otherwise; $\hat{\mathbf{i}}$ is the unit vector in the i direction; ${}_{\mathrm{R}}\boldsymbol{\Omega}_b$ is the Euler pole of block b relative to the reference frame; ${}_{h}\boldsymbol{\Omega}_f = {}_{h}\boldsymbol{\Omega}_{\mathrm{R}} - {}_{f}\boldsymbol{\Omega}_{\mathrm{R}}$ is the Euler pole of the footwall block f of fault relative to the hanging wall block h; F is the number of faults; N_k is the number of nodes defining fault k; $\mathbf{X}_{nk}$ is the position of node n on fault k; φ_{nk} is the locking fraction at node n on fault k, as defined above;

$\hat{\mathbf{j}}$ is the unit vector in j^{th} direction on fault surface (downdip or along-strike); and $G_{ij}(\mathbf{X}, \mathbf{X}_{nk})$ is the elastic response function that specifies the i^{th} component of velocity at surface point $\mathbf{X}$ due to a unit slip velocity along fault surface at node $\mathbf{X}_{nk}$ in the j^{th} direction. The components of G_{ij} are the Green's functions that quantify the theoretical elastic response at each GPS site due to assumed unit slip at each fault node within the model domain (Okada, 1985).

The Jalisco-Colima subduction interface was approximated as described in Section 1.3.2. Laplacian smoothing was applied during the inversions to avoid short-wavelength artifacts in our locking solutions. We explored a variety of smoothing factors to mitigate the tradeoff between the misfit and the model complexity.

Misfit F is defined in TDEFNODE as the sum of the reduced chi-squared statistic (χ_ν^2), which is a data misfit penalty function, and the penalties associated with smoothing (McCaffrey 2002; 2005):

$$F = \chi_\nu^2 + \text{penalties} = \frac{1}{\nu}\boldsymbol{R}^{\mathrm{T}}\boldsymbol{C}^{-1}\boldsymbol{R} + A_1\left(\frac{d^2\varphi}{dx^2}\right)^2 + A_2\left(\frac{d^2\varphi}{dw^2}\right)^2 \tag{2.2}$$

where ν represents the degrees of freedom (number of observations N minus number of parameters); $\boldsymbol{R}$ is the matrix of velocity residuals (R_e, R_n, R_v), T indicates the transpose of the matrix, $\boldsymbol{C}$ is the east-north-vertical covariance matrix, x and w denote, respectively, the along-strike and down-dip directions; A_1 and A_2 are the smoothing factors that scale the penalties in each direction, and φ is the locking coefficient. The misfit function F is minimized through simulated annealing and grid search iterations.

Our model includes the North America, Cocos, and Rivera plates. For our best-fitting models, we apply the MORVEL Cocos-North America (CO-NA) and Rivera-North America (RI-NA) plate angular velocities (DeMets *et al.* 2010) as *a priori* constraints. Later in the analysis, we evaluate how relaxing the constraint on the RI-NA angular velocity, which is the more poorly known of the two, influences our results.

The Jalisco-Colima subduction interface was approximated as described in Section 1.3.2. Laplacian smoothing was applied during the inversions to avoid short-wavelength artifacts in our locking solutions. We explored a variety of smoothing factors to mitigate the tradeoff between the misfit and the model complexity.

2.3.2 Model resolution

We tested the capability of the GPS network in western Mexico to resolve locking along the JCSZ via a checkerboard test, with locking distributed in rectangular patches of alternating constant values of 0 and 0.5 (Fig. S2.8). We calculated synthetic 3-D velocities from two different starting models at each site of the GPS network, perturbed the synthetic velocities with random noise of 1 mm/yr (1-sigma) for the east and north components and 2 mm/yr for the vertical component, and inverted the noisy velocities while applying the same smoothing as was used for our preferred solutions. Figure S2.8 shows both starting models, their associated synthetic velocities, and the models recovered from inversions of those velocities.

The resolution tests indicate that our locking solutions are the least reliable offshore southeastern Michoacán, where only two GPS stations are located, both on the coast. Elsewhere, the recovery of the starting locking values at depths shallower than 10 km is better but erratic, as expected from a network of land-based instruments. In contrast, at depths below 10 km, the starting

locking values and in particular their along-strike variations are well recovered from southwestern Michoacán to the southwestern Jalisco coast.

2.3.3 Model parameter exploration

As part of our analysis, we evaluated the effect of the assumed maximum interface locking depth on our results. Pardo & Suárez (1995) estimate a ~40 km downdip limit for seismogenic coupling of the RI/NA subduction interface and ~25 km downdip limit for the CO/NA subduction interface below Michoacán, both from earthquake hypocenter locations and focal mechanisms. More recently, Martínez-López & Mendoza (2016) estimate a maximum coupling depth of ~40 km for both segments using an augmented data base from that of Pardo & Suárez (1995), modestly deeper than the 35 km downdip limit of the interpolate seismogenic zone estimated from seismic tomographic imaging of the subduction interface below Jalisco (Watkins *et al.* 2018). Based on the above estimates, we tested the effect of varying the maximum locking depth of the subduction interface from 25 to 55 km.

We also evaluated how the fits and results are affected by the assumed location of the offshore oceanic boundary between the Rivera and Cocos plates (RI/CO), which determines which of the two plates is located offshore from and beneath different parts of our study region. Based on evidence of a broad zone of diffuse seismicity and shear within the seafloor offshore from the Manzanillo Trough (Fig. 2.1, 2.4a). DeMets & Wilson (1997) suggest that the two plates are separated by a diffuse offshore plate boundary. Northeast of this diffuse seismic zone, large-scale, fault-controlled subsidence within the North America plate offshore from the southern Colima Graben (e.g. Bandy et al. 2005) coincides with a series of submarine canyons (Alvarez and Yutsis 2015). For simplicity, we refer to this region as the Manzanillo Trough (Fig. 2.1), which is bounded

by the Cuyutlán and Coahuayana submarine canyons. Singh *et al.* (1995), Bandy *et al.* (1995), and Bandy *et al.* (1998) propose that the Manzanillo Trough and southern Colima Graben are located above the subducted RI/CO plate boundary. From modeling of gravimetric data, Alvarez & Yutsis (2015) propose that the RI/CO offshore boundary intersects the trench near the middle of the Manzanillo Trough.

Based on the range of proposed locations for the RI-CO-NA triple junction, we tested three potential locations: one each near the eastern and western limits of the Manzanillo Trough and one ~50 km farther northwest (indicated respectively by locations 1, 2, and 3 in the map inset in Fig. 2.4a). We did not test a model that approximates the boundary as diffuse, as seems most likely given the diffuse seismic zone where the two plates intersect and absence of any well-defined discrete offshore fault that might constitute the boundary (DeMets & Wilson 1997, Fig. 2.4a).

2.4 RESULTS

Below, we describe variations in the fits and interseismic locking solutions from TDEFNODE inversions of the 57-site GPS velocity fields described in Section 2.2 and the Supplementary Information as a function of four maximum assumed locking depths, the Rivera-North America (RI-NA) convergence rate, three assumed locations for Rivera-Cocos (RI/CO) plate boundary, and the mantle Maxwell times that were used to estimate the site velocities.

2.4.1 Model fits and determination of a best-fitting solution

Figure 2.4 summarizes the misfits F (Eq. 2.2) for all the velocity fields, maximum locking depths, and RI/CO boundary locations that were considered for our analysis, totaling 84 distinct inverse solutions. The worst fits occur for models that restrict interseismic locking to depths

shallower than 25 km (Figs 2.4b-d), independent of the RI/CO boundary location that was adopted and the mantle Maxwell time that was used for the velocity field calibration. For six of the seven velocity fields (and hence Maxwell times), the best velocity field fits occurred for a 40-km maximum locking depth (Figs 2.4b-d), with ~40 percent reductions in misfit F for the inversions with 40-km versus 25-km locking depths. The data thus strongly favor a maximum subduction locking depth of 40 km independent of the assumed mantle Maxwell time and RI/CO plate boundary location.

For the subset of models with a maximum 40-km locking depth, the worst fits all occur for velocity fields with no correction for viscoelastic deformation (black symbols in Figs 2.4b-d) or short Maxwell times (τ_m = 2.5 and 4 years, corresponding to upper mantle viscosities of 3-5 $\times$ 10^{18} Pa·s). This result corroborates those from the first part of our analysis, in which the worst fits from our time-dependent inversions of the GPS position time series for these sites were associated with data that were corrected assuming a 2.5 yr Maxwell time or that were not corrected for any viscoelastic deformation (corresponding to an infinite Maxwell time). As is shown in Figs 2.4b-d, the misfits for velocities associated with a 4-year Maxwell time are 35-100 percent higher than for the best models. Together, the poor fits for these three sets of velocities suggest that the upper mantle viscosity for our study area is unlikely to be less than 1 $\times$ 10^{19} Pa·s or greater than 1 $\times$ 10^{20} Pa·s (*i.e.* τ_m > 80 yr).

The fits to velocities that were derived for mantle Maxwell times of 15, 25, and 40 years are all nearly equivalent, with differences of ~10 percent or less (Figs 2.4b-d) independent of the assumed maximum locking depth or RI/CO boundary location. The best fitting model, with F = 4.0 and weighted root mean squared (wrms) velocity misfit of 1.4 mm/yr, is for an inversion of

velocities that were corrected using τ_m = 40 years. Inversions of velocities that were corrected using τ_m = 15 yr (F = 4.4 and wrms = 1.4 mm/yr) and τ_m = 25 yr (F = 4.6 and wrms = 1.5 mm/yr) give nearly equivalent fits. Time-dependent inversions (described in Chapter 1) of the GPS position time series that are corrected using Maxwell times of τ_m = 15, 25, and 40 yr yield respective wrms misfits of 5.4 mm, 5.7 mm, and 5.6 mm. The best overall fits for the time-dependent and static modeling are thus associated with a mantle Maxwell time of 15 years and viscosity of 2×10^{19} Pa·s.

We adopt as our preferred model the GPS site velocities that were calibrated using a mantle Maxwell time of 15 years, a 40-km maximum permitted locking depth, and a Rivera-Cocos plate boundary that intersects the trench ~50 km northwest of the Manzanillo Trough, based on a comparison of the fits for the static elastic half space models we explored above and the time-dependent fits described in Part 1 of our analysis (Chapter 1). Fig. 2.5 shows the observed and predicted horizontal and vertical velocities for this model their misfits, and subduction interface locking (φ) and slip-rate deficit ($-\varphi V$) solutions, all of which are described in more detail below. Comparisons of the model predictions and observations for trench-normal transects of subsets of the GPS sites above the Rivera and Cocos plates are shown in Fig. 2.6. In the following sections we describe the preferred model results and fits in more detail and also compare the outcomes of our alternative models in order to evaluate the robustness of the preferred solution with respect to plausible variations in the assumed model parameters.

2.4.2 Comparison of the best-fitting and alternative solutions: Model robustness

The most prominent and robust outcome of our analysis is the evidence for strong locking of the RI/NA subduction interface versus weak-to-moderate locking of the CO/NA interface (Fig.

2.5a). We distinguish three segments: 1) the Jalisco segment, which corresponds to the RI-NA interface along the Jalisco coast and offshore areas; 2) the Michoacán segment, where the Cocos plate subducts below North America along the state of Michoacán and offshore areas; and 3) the Colima segment, where oceanic lithosphere with velocities likely to be transitional between the Rivera and Cocos plate motions subducts offshore from the Mexico state of Colima (Fig. 2.1).

More than 40 percent of the area of the Michoacán segment subduction interface has locking values in our preferred solution that are below 50% (Fig. 2.5a). In contrast, the locking values for ~70 percent of the areas of the Jalisco and Colima segments are 70-100%. The first-order difference between the strong-versus-weak locking of the Jalisco and Michoacán segments arises from the fact that the coastal GPS stations above the Rivera plate move northeastward at similar rates or 2-3 mm/yr faster than the coastal stations above the Cocos plate (Figs 2.2a, 2.3a and b) even though the Cocos plate subducts at rates that are nearly 50 percent faster than the Rivera plate (Fig. 1). We thus consider the weak-versus-strong locking outcomes for the CO/NA and RI/NA subduction interfaces to be a robust outcome of our analysis.

The locking at depths shallower than ~5 km, where our model has the least ability to resolve locking values, is strong everywhere along-strike. Along the Jalisco segment, average locking is ~75% and is distributed uniformly along-strike, compared to the patchier locking distributions for the other two segments (Fig. 2.5a). Offshore from Jalisco, the interseismic locking is strong (≥ ~90 percent) but diminishes abruptly to less than 35 percent below the coast and continent. In contrast, locking offshore and near the coast on the Michoacán segment (depths between 5 and 25 km) is moderate (~65 percent) and transitions to weak locking (< 15 percent) below the continent, at depths of 25 to 40 km. The weak deep locking along the Michoacán segment changes abruptly to strong locking (≥ ~80 percent) at most locations along the Colima segment. Strong locking of

much of the interface northwest of and including the Manzanillo Trough is required to match the rapid northeastward velocities of the GPS sites inland from this segment (also see Fig. 2.3a).

Our best-fitting model also predicts that the average locking values diminish with depth (Fig. 2.5a), from ~90 percent at 0-10 km depths to 70 percent at 10-25 km depths and 40 percent below depths of 25 km. Our estimates of depth-dependent locking variations are the most reliable along the RI/NA subduction interface, where the trench-normal velocity gradient critical for defining depth-dependent variations in interseismic locking is constrained by numerous GPS sites (Fig. 2.6). Further, strong locking all the way to the surface appears to be necessary to fit the rapid inland velocities that are observed everywhere onshore from the subducting Rivera plate (*e.g*. Fig. 2.6b). Our estimates of the locking variations with depth are the least reliable along the subduction interface east of the Manzanillo Trough, where there are too few GPS sites to define the trench-normal velocity gradient (Fig. 2.1).

The fits for our preferred model (*i.e.* τ_m = 15 yr) to the horizontal velocity components are good, with wrms east and north velocity components misfits of 1.2 mm/yr and 1.1 mm/yr, respectively (Fig. 2.5c). The sites with the largest misfits are situated along the coast near the limits of the 1995 and 2003 earthquake ruptures (Fig. 2.5c), where the estimated site velocities are the most sensitive to the accuracy of the time-dependent coseismic, afterslip, and viscoelastic corrections that were required in order to estimate the long-term station motions. We ascribe these larger misfits to likely inaccuracies in those corrections and likely oversimplifications in our models and assumptions. In general, the velocities for sites above the subducting Cocos plates are fit within their estimated uncertainties (Figs 2.6a and 2.6c). In contrast, the velocities of sites in Jalisco above the subducting Rivera plate are systematically faster by 1-2 mm/yr than the predicted velocities everywhere between the coast and regions far inland (Figs 2.5a and 2.6b). In the

following sections, we examine possible reasons for this systematic misfit, including whether the present RI-NA convergence rate is faster than that estimated with the MORVEL angular velocity.

In general, the more poorly constrained vertical rates are well fit in our entire study area (Figs 2.5d, 2.6c and d). The good fits to the vertical rates above the Cocos plate, which define a clear transition from rapid coastal subsidence to slow inland uplift (Fig. 2.6c), is encouraging given that nearly half of the rates in the Cocos plate transect are based on continuous measurements and thus have uncertainties smaller than ±1-2 mm/yr.

2.4.2.1 Influence of viscoelastic corrections on model outcomes and fits

Figure 2.7 shows the locking solutions from models with a fixed maximum interface locking depth of 40 km, a RI/CO boundary location ~50 km northwest of the Manzanillo Trough (location 3), and varying mantle Maxwell times. The main features of the preferred locking distribution (Figs 2.5a and 2.7d) are reproduced for all models with Maxwell times > 8 yr (Figs 2.5c, e, and f). A comparison of the residuals that are shown in Fig. 2.7 and the velocity transects in Figs 2.8a and b clearly show that the fits to the horizontal velocities and their trench-normal components are significantly worse for shorter Maxwell times (2.5 and 4 years) than for Maxwell times longer than 8 years. The systematic misfits for the models based on inversions of the velocities that were corrected assuming mantle Maxwell times of 2.5, 4, or 8 years (Figs 2.7a, b, and c) either indicate that the average mantle viscosity is greater than 1×10^{19} Pa·s or that one or more of our model assumptions are incorrect. Overall, as is discussed in Section 2.4.1, the models with 15 yr $\leq \tau_m \leq$ 40 yr fit the data best as measured by their misfit F and wrms values.

2.4.2.2 Influence of the maximum locking depth of the subduction interface

Figure 2.9 illustrates how the locking solutions vary as a function of the maximum allowed locking depth, assuming that the RI/CO plate boundary is located at its preferred site (location 3 in Fig. 2.4a) and τ_m =15 yr. Models with progressively deeper maximum locking depths give rise to progressively deeper strong locking, particularly on the Colima and southeastern Jalisco segments, reflecting the expected inverse tradeoff between locking strength and the area of the subduction interface available for locking. The model with maximum locking depth of 25 km predicts trench-normal velocities that are systematically too slow (Figs 2.9a and 2.10ab), indicating that the measured shortening rates are faster than can be matched via full locking of the subduction interface at the maximum plate tectonic convergence rates (Fig. 2.10a and b). In contrast, models with maximum locking depths of 35, 40, and 45 km fit the data well, with the lowest misfit value *F* and hence best overall fit associated with a maximum locking depth of 40 km (Fig. 2.4). The along-strike change from weak to strong coupling in our preferred model is reproduced independent of our choice of maximum locking depth (Fig. 2.9), illustrating the robustness of this result. Varying the maximum locking depth from 35 to 45 km changed the vertical and horizontal predictions of our TDEFNODE model by 1 mm/yr or less everywhere in our study area (Fig. 2.10), close to or below the resolution threshold of our data. In contrast, the model predictions for an assumed 25-km locking depth differed by as much as 10 mm/yr at some locations from the rates predicted by the other models (Fig. 2.10c), large enough to resolve within the uncertainties of our velocities.

2.4.2.3 Influence of the RI/CO plate boundary location

For all of the models we tested, the lowest values of the misfit *F* are associated with models in which the RI/CO plate boundary intersects the trench ~50 km NW of the Manzanillo Trough (Fig. 2.4a). Figure 2.11 shows how the best-fitting locking solutions vary with the assumed location for the RI/CO plate boundary for a model with a 40-km maximum locking depth and for velocities calibrated using a mantle Maxwell time of 15 years. For all three assumed boundary locations, the best-fitting solutions require full locking of the eastern RI/NA trench segment and weak-to-moderate locking of the eastern CO/NA segment (Fig. 2.11).

For all three assumed boundary locations, their fits to the velocities of sites that are the farthest northwest and southeast in our study area (Fig. 2.11, 2.12) and fits to all the vertical velocities (Fig. 2.12c and d) are equally good. Those subsets of the velocity field thus cannot discriminate between the alternative RI/CO boundary locations. Instead, the critical subset of our velocities is located along the coast and inland from 105°W-104°W, at the center of our study area (Fig. 2.11). Here, a transition occurs between the onland areas that are above the subducting Cocos versus the Rivera plates. For the models that were derived using assigned locations 1 and 2 within and on the eastern edge of the Manzanillo Trough, the horizontal motions of the stations in the transitional region are fit poorly (Fig. 2.11b and c), versus a good fit for our preferred model (Fig. 2.11a). The site velocities are thus more consistent with models in which the oceanic lithosphere that subducts beneath the Manzanillo Trough is part of the Cocos rather than Rivera plate. Based on the broadly scattered seismicity that occurs outboard from the trench in this transitional area (Fig. 2.4a), our discrete-boundary assumption is clearly an approximation. The boundary instead more likely includes multiple active faults that accommodate a gradual transition in the plate motion.

2.4.2.4 Influence of the RI angular velocity with respect to NA

As we discussed in Section 2.4.2 and illustrate in Figs 2.5a and 2.6b, none of our models predict horizontal velocities onshore from the Rivera plate that are as fast as observed. This result includes solutions for a fully locked subduction interface and locking depth that maximizes the potential locking area (45 km). We thus explored how much the misfit (F) of the models could be reduced via a systematic increase in the RI-NA convergence rate based on the presumption that the rate either accelerated during the past 0.78 Myr or is underestimated by the MORVEL 0.78-Myr-average RI-NA angular velocity. We inverted velocity fields that were calibrated for mantle Maxwell times of 2.5 to 40 years and for a negligible viscoelastic response, and for TDEFNODE models with a 40-km maximum locking depth and all three RI/CO plate boundary locations (Figs 2.13a, b, and c). We explored angular rates up to 35% faster than the MORVEL angular rate, which has a formal 95% uncertainty equal to ±15% of the 4.37º/Myr angular rate (defined by the yellow area in Figs 2.13a-c).

Relative to the fit of the best fitting model identified above (F = 4.0 indicated by the solid purple line in Figs 2.13a-c), 10 of the 147 models with the faster RI-NA angular rates we explored yielded superior fits (Figs 2.13a-c). Of these ten models, four had the same characteristics as our preferred model: 1) the GPS velocities were calibrated for our preferred mantle time of 15 years; 2) the maximum interface locking depth was 40 km; and 3) the RI/CO plate boundary intersects the trench ~50 km northwest of the Manzanillo Trough. The RI-NA angular rates that were required to achieve better fits for these four models, which are 20-35 percent faster than the MORVEL estimate, exceed the 95% upper bound on the MORVEL angular rotation rate.

All six of the remaining models that improved the fit were derived from velocities that were calibrated for a Maxwell time of 40 years (Figs 2.13a-c). None of the TDEFNODE models that were derived from velocities calibrated for values of $\tau_m \leq 8$ yr or from velocities that were determined without any calibration for viscoelastic deformation improved on the fit of our preferred model. The latter result reinforces the unsuitability of mantle viscosities less than or equal to 1×10^{19} Pa·s for our viscoelastic modeling. All of the models with a RI/CO boundary located at position 3 give fits superior to those for the other two boundary locations, reinforcing the evidence that the transition from subducting Cocos to subducting Rivera plate occurs northwest of the Manzanillo Trough.

Our exploration of alternative, faster angular rates for the Rivera-North America plate pair thus identifies two classes of models that improve on the fit of our preferred model. If the upper mantle is well approximated using a Maxwell time of 15 years, then models with RI-NA angular rates that are 20% or more faster than the 0.78-Myr MORVEL estimate are required to improve the fit. If a Maxwell time of 40 years is more appropriate, then all RI-NA angular rates faster than the MORVEL estimate progressively improve the fit (red symbols in Fig. 2.13c). Given the similarities of the 15-yr and 40-yr Maxwell time fits for the time-dependent modeling described in Chapter 1, we cannot exclude the possibility that the upper mantle Maxwell time is closer to 40 years than 15 years.

If the RI-NA America convergence has accelerated 20-30% since 0.78 Ma, then enforcing closure of the Pacific-North America-Rivera plate circuit requires that one or both of Pacific-North America or Pacific-Rivera plate motion has changed over the same time frame. A comparison of Pacific-North America plate motion at present (via GPS) to reconstructions that span the past 20

Ma reveals no significant change in motion for this plate pair since 4.2 Ma (DeMets & Merkouriev 2016). A 20-30% acceleration of RI-NA plate convergence thus implies that Pacific-Rivera plate motion has changed. As a test, we summed the present-day Pacific-North America angular velocity estimated by DeMets & Merkouriev (2016) with the MORVEL Rivera-North America pole and an angular rate 25% faster than the MORVEL estimate. The resulting Pacific-Rivera angular velocity predicts present-day slip directions along the Rivera transform fault that are 2-10 degrees anticlockwise from its well-mapped fault trace. The difference between the predicted slip directions and the trace of the active fault is 2-3 times larger than the uncertainties in the fault azimuths estimated by DeMets *et al.* (2010). A recent 25% acceleration of RI-NA convergence rates thus seems implausible.

2.5 DISCUSSION

2.5.1 Earthquake cycle implications for the Jalisco/Colima/Michoacán trench segments

Our new interseismic locking solution is constrained by GPS station velocities that extend to the northwesternmost limit of the Mexico subduction zone. This solution indicates that the subduction interface northwest of the limits of the 1995 Colima-Jalisco earthquake, where the interface has not ruptured since 1932, is strongly locked (Fig. 2.5a) and accumulates an annual elastic slip deficit of ~20 mm/yr (Fig. 2.5b). By implication, ~1.8 meters of unrelieved interface slip has accumulated since 1932, sufficient to cause a M>7 earthquake depending on the lateral and downdip extent of the future earthquake. For a slip area of ~15,500 km^2 (a ~125-km-long rupture northwest of the 1995 Colima-Jalisco earthquake zone), the release of all the accumulated slip deficit to date would produce a M~8 earthquake. Elsewhere in our study area, the annual slip-rate deficits range from as little as 10 mm/yr to ~60 mm/yr (Fig. 2.5b), sufficient to generate M~7

or larger earthquakes at least once per century. The hazards from subduction thrust earthquakes are thus significant everywhere in our study area, including the areas of weak-to-moderate interface locking east of the Manzanillo Trough.

Pacheco *et al.* (1993) suggest that variations in seismic coupling are associated with differences in frictional behavior along the subduction interface, which may be caused by the subduction of large bathymetric features, the presence of unstable triple junctions, sediment composition, and other factors. The most robust feature of our locking solutions, namely the along-strike change from weak locking southeast of the Manzanillo Trough to strong locking northwest of the trough (Fig. 2.5a), coincides well with the limits of the 1932, 1973, 1995 and 2003 earthquake rupture zones and afterslip after the latter two earthquakes (Fig. 2.14). It also correlates with the along-strike gap in nonvolcanic tremor that occurs downdip from the seismogenic zone (Fig. 2.14, Brudzinski *et al.* 2016). Together, these suggest that the Manzanillo Trough may be a mechanical barrier for along-strike rupture propagation (*e.g.*, Schmitt *et al.* 2007), and may mark a transition in the physical or possibly kinematic properties that affect the frictional behavior of the subduction interface.

Our interplate locking solution for the northernmost ~500 km of the Mexico subduction zone and the Rousset *et al.* (2015) interseismic locking solution for the ~700-km-long Guerrero and Oaxaca trench segments that extend east from our study area collectively reveal multiple significant along-strike variations in the locking of the Cocos and Rivera plate subduction interfaces at depths above 25 km. These variations include alternating areas with locking greater than 0.7 and areas with locking less than 0.3. The only significant along-strike variation in locking occurs near an offshore upper plate structural discontinuity, the Manzanillo Trough, and coincides with a transition from subducting Cocos to Rivera plate oceanic lithosphere. In contrast, Rousset

et al. (2015) find a strong spatial correlation between trench-to-coast distance and regions of strong versus weak shallow coupling for the Guerrero and Oaxaca segments, which they attribute to along-strike variations in the mechanical properties of the upper plate. A single explanation for the lateral locking variations along the entire subduction zone is thus unclear and beyond the scope of this work.

Non-volcanic tremor in our study region occurs at depths of ~40-70 km, only ~10 km farther downdip from the deepest extents of interseismic locking and coseismic slip in 1995 and 2003 (Fig. 2.14). If slow slip events (SSE) originate on the interface in the region between non-volcanic tremor and coseismic slip, as may be the case along the Oaxaca segment (Brudzinski *et al.* 2010), then relatively little of the subduction interface may have the appropriate frictional conditions for slow slip events with amplitudes large enough to be detected with GPS, as suggested by Brudzinski *et al.* (2016). Better GPS coverage in the state of Michoacán and in western Guerrero, where security is a concern, is needed to determine whether slow slip events offshore from or beneath the state of Michoacán are relieving a significant fraction of the accumulating interseismic strain, thereby explaining the apparently weaker locking along this segment of the trench.

2.5.2 Model misfits and sensitivities

The most persistent misfit in the many models we tested for this study was to the velocities in coastal and inland areas of Jalisco above the Rivera plate, which were 1-2 mm/yr systematically faster than was predicted by any of our models (Figs 2.6b, 2.10b, and 2.11b). We suspect the misfit is evidence for an error and/or oversimplification in one or more of our model assumptions. As is described in Section 1.6, a variety of modifications to our assumptions or models might improve

the fits. These include the following: 1) a different subduction interface geometry; 2) lateral variations in the thickness and/or elastic properties of the crust; 3) use of a multi-layered viscoelastic model; 4) use of a low viscosity wedge and/or an elastic cold nose in the mantle wedge; and 5) use of different mantle rheologies such as power law or Burgers body.

The largest sensitivity in our locking solutions is associated with the location that is assigned to the intersection of the poorly understood RI/CO plate boundary with the trench. This location determines the *a priori* rate of interplate convergence that is applied to each node on the subduction interface and hence the magnitude of locking required to fit the nearby GPS site velocities. Our modeling shows that the Cocos plate subducts rapidly enough to match and/or exceed the onshore surface deformation even for partial locking of the interface. In contrast, full locking of most of the RI/NA interface is required to match the GPS-measured surface velocities in areas above the more slowly subducting Rivera plate. Models in which the offshore RI/CO plate boundary intersects the trench northwest of the Manzanillo Trough fit our velocities more successfully because larger areas of the subduction interface are driven by faster Cocos plate subduction and thus fit the measured surface deformation even under conditions of partial coupling. Although the offshore RI/CO plate boundary is more likely to be diffuse than discrete, approximating a diffuse boundary in our elastic model would require hard-to-justify assumptions and additional tradeoffs between the existing model parameters and new hard-to-resolve parameters associated with the newly introduced diffuse boundary.

2.6 CONCLUSIONS

We inverted GPS station velocities derived from nearly 25 years of GPS measurements onshore from the northern ~500 km of the Mexico subduction zone to estimate an interseismic

locking solution for this region (Fig. 2.5a). Our preferred model requires an average of ~70% percent interseismic locking between the surface and depths of 40 km, non-uniformly distributed along the interface. The most robust features of the locking solution are:

- Transitions along the trench from strong locking (> 90%) of the Jalisco segment subduction interface at depths shallower than ~20 km to moderate-to-strong locking (average of ~80%) of the Colima segment below the Manzanillo Trough to weak-to-moderate locking (average ~55 %) of the CO/NA subduction interface southeast of the Manzanillo Trough (Michoacán segment).

- Strong locking of the subduction interface to depths of 40 km along the trench segments ruptured by the 1995 Colima-Jalisco and 2003 Tecomán thrust earthquakes, at depths where afterslip relieved significant accumulated elastic strain after both earthquakes.

- Evidence that elastic strain that has accumulated along the ~125-km-long trench segment offshore from Puerto Vallarta and other developed coastal areas, where the last large thrust earthquake occurred in 1932, is sufficient to release a M~8.0 earthquake if all of the stored elastic energy was released simultaneously.

These features are robust with respect to the mantle Maxwell times that are equal to or longer than 8 yr, in particular for τ_m = 15, 25, and 40 years, which give rise to the lowest misfits. They are also robust with respect to variations in the maximum depth that is permitted for interseismic locking and the location where the poorly understood Rivera-Cocos plate boundary is assumed to intersect the trench. The relatively small 1.2 mm/yr north and 1.1 mm/yr east GPS velocity component misfits for our preferred model suggest that most of our model assumptions, including the linear viscoelastic rheology we use for the upper mantle, are adequate. We interpret

a 1-2 mm/yr systematic misfit to the subset of our data located above the subducting Rivera plate as evidence that one or more of our modeling assumptions require refinements.

The mantle viscosity of 2×10^{19} Pa·s gives the best overall fit for both the time-dependent and static modeling in our two stage analysis. Further, this viscosity is similar to viscosities estimated in previous studies, including 3.2×10^{19} Pa·s (τ_m = 20 years, μ = 50 GPa) for the 1964 Alaska earthquake (Suito & Freymuller 2009), viscosities of the order of 10^{19} Pa·s for the 1960 Chile, 2006 Sumatra and ~1700 Cascadia megathrust earthquakes (Wang *et al.* 2012), 0.5×10^{19} Pa·s and 3×10^{19} Pa·s respectively for a low-viscosity wedge and the long-term mantle viscosity (Trubienco *et al.* 2013), and 0.8-1.5 $\times 10^{19}$ Pa·s (8 yr $\leq \tau_m \leq$ 15 yr, μ = 30 GPa), from modeling of long-term postseismic deformation in Nankai (Johnson & Tebo 2018).

ACKNOWLEDGEMENTS

Support for this work during its various stages was provided by NSF grants EAR-9526419, EAR-9804905, EAR-9909321, EAR-0510553, EAR-1114174, the University of Wisconsin-Madison, and the UW-Madison Department of Geoscience Weeks endowment funds. This material is based on GPS data and services provided by the GAGE Facility, operated by UNAVCO, Inc. and by the TLALOCNet GPS network operated by Servicio de Geodesia Satelital (SGS; Cabral-Cano et al., 2018) at the Instituto de Geofísica-Universidad Nacional Autónoma de México (UNAM). UNAVCO's initial support for TLALOCNet (now part of NOTA) was performed under EAR-1338091 and is currently supported by the National Science Foundation and the National Aeronautics and Space Administration under NSF Cooperative Agreement EAR-1724794. TLALOCNet and other GPS related operations from SGS have also been supported by the Consejo Nacional de Ciencia y Tecnología (CONACyT) projects 253760, 256012 and 2017-

01-5955, UNAM-Programa de Apoyo a Proyectos de Investigación e Innovación Tecnológica (PAPIIT) projects IN104213, IN111509, IN109315-3, IN104818-3 and supplemental support from UNAM-Instituto de Geofísica. We are deeply grateful to all personnel from UNAVCO and SGS for station maintenance, data acquisition, IT support and data curation and distribution for these networks and in particular to the following individuals and institutions, whose hard work and resourcefulness were central to the success of this project: Bill Douglass, Neal Lord and Bill Unger at UW-Madison, Oscar Diaz-Molina and Luis Salazar-Tlaczani at SGS, John Galetzka, Adam Wallace, Shawn Lawrence, Sean Malloy and Chris Walls at UNAVCO, Jesus Pacheco-Martínez at Universidad Autónoma de Aguascalientes, personnel at the Universidad de Guadalajara at campus Guadalajara, Mascota and Ameca, Protección Civil de Jalisco, Universidad de Colima at campus Colima and campus El Naranjo, and Instituto de Biología-UNAM Estacion Chamela. Most figures were produced using Generic Mapping Tools software (Wessel & Smith 1991).

REFERENCES

Álvarez, R. & Yutsis, V., 2015. The elusive Rivera-Cocos plate boundary: not diffuse, in *Magmatic Rifting and Active Volcanism*, eds. Wright, T.J., Ayele, A., Ferguson, D.J., Kidane, T. & Vye-Brown, C., Vol. **420**, Geological Society, London, Special Publications. http://doi.org/10.1144/SP420.8.

Bandy, W.L., Kostoglodov, V. & Mortera-Gutiérrez, C.A., 1998. Structure of the southern Jalisco subduction zone, Mexico, as inferred from gravity and seismicity, *Geofís. Int.*, **37**, 3, 153-169.

Bandy, W.L., Michaud, F., Bourgois, J., Calmus, T., Dyment, J., Mortera-Gutiérrez, C.A., Ortega-Ramírez, J., Pontoise, B., Royer, J.-Y., Sichler, G., Sosson, M., Rebolledo-Vieyra, M., Bigot-Cormier, F., Díaz-Molina, O., Hurtado-Artunduaga, A.D., Pardo-Castro, G., & Trouillard-Perrot, C., 2005. Subsidence and strike-slip tectonism or the upper continental slope off Manzanillo, Mexico, *Tectonophyiscs*, **398**, 115-140, doi:10.1016/j.tecto.2005.01.004.

Bandy, W., Mortera-Gutiérrez, C., Urrutia-Fucugauchi, J. & Hilde, T.W.C., 1995. The subducted Rivera-Cocos plate boundary: Where is it, what is it, and what is its relationship to the Colima rift?, *Geophys. Res. Lett.*, **22**, 22, 3075-3078.

Brudzinski, M.R., Hinojosa-Prieto, H.R., Schlanser, K.M., Cabral-Cano, E., Arciniega-Ceballos, A., Díaz-Molina, O. & DeMets, C., 2010. Nonvolcanic tremor along the Oaxaca segment of the Middle America subduction zone, *J. geophys. Res*. - *Sol. Ea.*, **115**, B00A23. http://dx.doi.org/10.1029/2008JB006061.

Brudzinski, M., Schlanser, K.M., Kelly, N.J., DeMets, C., Grand, S.P., Márquez-Azúa, B. & Cabral-Cano, E., 2016. Tectonic tremor and slow slip along the northwestern section of the Mexico subduction zone, *Earth Planet. Sc. Lett*., **454**, 259–271.

DeMets, C., Carmichael, I., Melbourne, T., Sánchez, O., Stock, J., Suárez, G. & Hudnut, K., 1995. Anticipating the successor to Mexico's largest historical earthquake, *Eos*, **76**, 42, 417-424.

DeMets, C., Gordon, R.G. & Argus, D.F., 2010. Geologically current plate motions, *Geophys. J. Int.*, **181**, 1-80, doi: 10.1111/j.1365-246X.2009.04491.x.

DeMets, C. & Merkouriev, S., 2016. High-resolution reconstructions of Pacific-North America plate motion: 20 Ma to present, *Geophys. J. Int*., 207, 741-773.

DeMets, C., & Stein S., 1990. Present-day kinematics of the Rivera plate and implications for tectonics in southwestern Mexico, *J. geophys. Res*., **95**, B13, 21931-21948.

DeMets, C., & Wilson, D.S., 1997. Relative motions of the Pacific, Rivera, North American, and Cocos plates since 0.78 Ma, *J. geophys. Res*., **102**, 2789–2806.

Hutton, W., DeMets, C., Sánchez, O., Suárez, G. & Stock, J., 2001. Slip kinematics and dynamics during and after the 1995 October 9 M_w=8.0 Colima-Jalisco earthquake, Mexico, from GPS geodetic constraints, *Geophys. J. Inter*., **146**, 637–658.

Johnson, K.M., & Tebo, D., 2018. Capturing 50 years of postseismic mantle flow at Nankai subduction zone, *J. Geophys. Res.* - *Sol. Ea.*, **123**, 10091–10106. https://doi. org/10.1029/2018JB016345.

Márquez-Azúa, B., DeMets, C. & Masterlark, T., 2002. Strong interseismic coupling, fault afterslip, and viscoelastic flow before and after the Oct. 9, 1995 Colima-Jalisco earthquake: Continuous GPS measurements from Colima, Mexico, *Geophys. Res. Lett*., **29**, 10.1029/2002GL014702.

Martínez-López, M. R. & Mendoza, C., 2016. Acoplamiento sismogénico en la zona de subducción de Michoacán-Colima-Jalisco, México, *B. Soc. Geol. Mex*., **68**, 2, 199-214.

McCaffrey, R., 2002. Crustal block rotations and plate coupling, in *Plate Boundary Zones*, Vol. **30**, pp. 101-122, Geodynamics Series 30, eds. Stein, S. & Freymueller, J.T, Am. Geophys. Un., Washington, DC.

McCaffrey, R., Long, M.D., Goldfinger, C., Zwick, P.C., Nabelek, J.L., Johnson, C.K. & Smith, C., 2000. Rotation and plate locking at the southern Cascadia subduction zone, *Geophys. Res. Lett.*, **27**, 19, 3117-3120.

Melbourne, T., Carmichael, I., DeMets, C., Hudnut, K., Sánchez, O., Stock, J., Suárez, G. & Webb, F., 1997. The geodetic signature of the M=8.0 October 9, 1995, Jalisco subduction earthquake, *Geophys. Res. Lett.*, **24**, 715–718.

Okada, Y., 1985. Surface deformation to shear and tensile faults in a half-space, *Bull. Seismol. Soc. Am.*, **75**, 1135-1154.

Pacheco, J.F., Sykes, L.R. & Scholz, C.H., 1993. Nature of seismic coupling along simple plate boundaries of the subduction type, *J. geophys. Res.*, **98**, B8, 14133-14159.

Pardo, M. & Suárez G., 1995. Shape of the subducted Rivera and Cocos plates in southern Mexico: Seismic and tectonic implications, *J. geophys. Res.*, **100**, B7, 12357-12373.

Rousset, B., Lasserre, C., Cubas, N., Graham, S., Radiguet, M., DeMets, C., Socquet, A., Campillo, M., Kostoglodov, V., Cabral-Cano, E., Cotte, N. & Walpersdorf, A., 2015. Lateral variations of interplate coupling along the Mexican subduction interface: relationships with long-term morphology and fault zone mechanical properties, *Pure Appl. Geophys.*, **172**, 12, 3265-3670, DOI 10.1007/s00024-015-1215-6.

Savage, J.C.,1983. A dislocation model of strain accumulation and release at a subduction zone, *J. geophys. Res.*, **88**, 4984-4996.

Schmitt, S.V., DeMets, C., Stock, J., Sánchez, O., Márquez-Azúa, B. & Reyes, G., 2007. A geodetic study of the 2003 January 22 Tecoman, Colima, Mexico earthquake, *Geophys. J. Int.*, **169**, 389–406, doi: 10.1111j.1365-246X.2006.03322.x.

Selvans, M.M., Stock, J.M., DeMets, C., Sánchez, O. & Márquez-Azúa, B., 2011. Constraints on Jalisco Block motion and tectonics of the Guadalajara triple junction from 1998–2001 Campaign GPS Data, *Pure Appl. Geophys.*, **168**, 1435–1447. https://doi.org/10.1007/s00024-010-0201-2.

Singh, S.K., Ponce, L. & Nishenko, S.P., 1985. The great Jalisco, Mexico, earthquakes of 1932: Subduction of the Rivera plate, *Bull. Seismol. Soc. Am.*, **75**, 1301-1314.

Suito, H., & Freymueller, J.T., 2009. A viscoelastic and afterslip postseismic deformation model for the 1964 Alaska earthquake, *J. geophys. Res.*, **114**, B11404, doi:1029/2008JB005954.

Trubienko, O., Fleitout, L., Garaud, J-D. & Vigny, C., 2013. Interpretation of interseismic deformations and the seismic cycle associated with large subduction earthquakes, *Tectonophysics,* **589**, 126–141.

Wang, K., Hu, Y. & He, J., 2012. Deformation cycles of subduction earthquakes in a viscoelastic Earth, *Nature,* **484**, 327-332, doi:10.1038/nature11032.

Watkins, W.D., Thurber, C.H., Abbott, E.R. & Brudzinski, M.R., 2018. Local earthquake tomography of the Jalisco, Mexico region, *Tectonophysics*, **724–725**, 51–64, https://doi.org/10.1016/j.tecto.2018.01.002.

Wessel, P. & Smith, W.H.F., 1991. Free software helps map and display data, *EOS Trans. AGU*, **72**(41), 445–446. doi:10.1029/90EO00319.

FIGURES

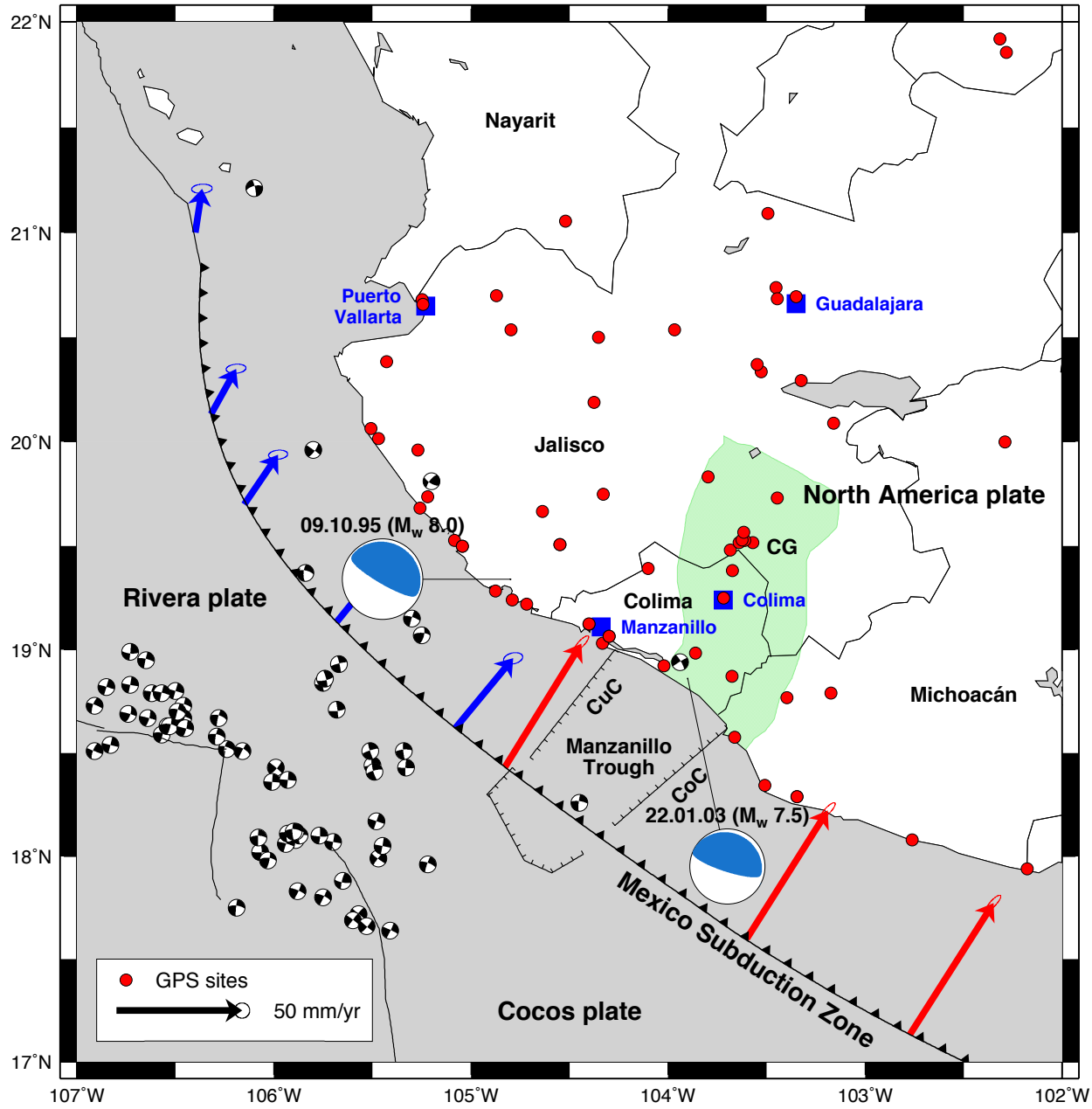

Figure 2.1. Tectonic setting with focal mechanisms from the Global Centroid Moment Tensor (gCMT) catalog. Arrows indicate velocities of Cocos (red) and Rivera (blue) plates relative to North America plate, as predicted by the MORVEL global plate motion model (DeMets *et al*. 2010). Red dots show the location of the GPS sites. Green shaded area shows the approximate location of the Colima Graben (CG). CoC: Coahuayana canyon. CuC: Cuyutlán canyon. Focal mechanisms are $M_w \geq 4.0$ strike–slip earthquakes with depths ≤ 60 km from 1976 to 2020 from the gCMT catalog. The seismicity suggests distributed shear across a diffuse Rivera–Cocos plate boundary (DeMets & Wilson 1997).

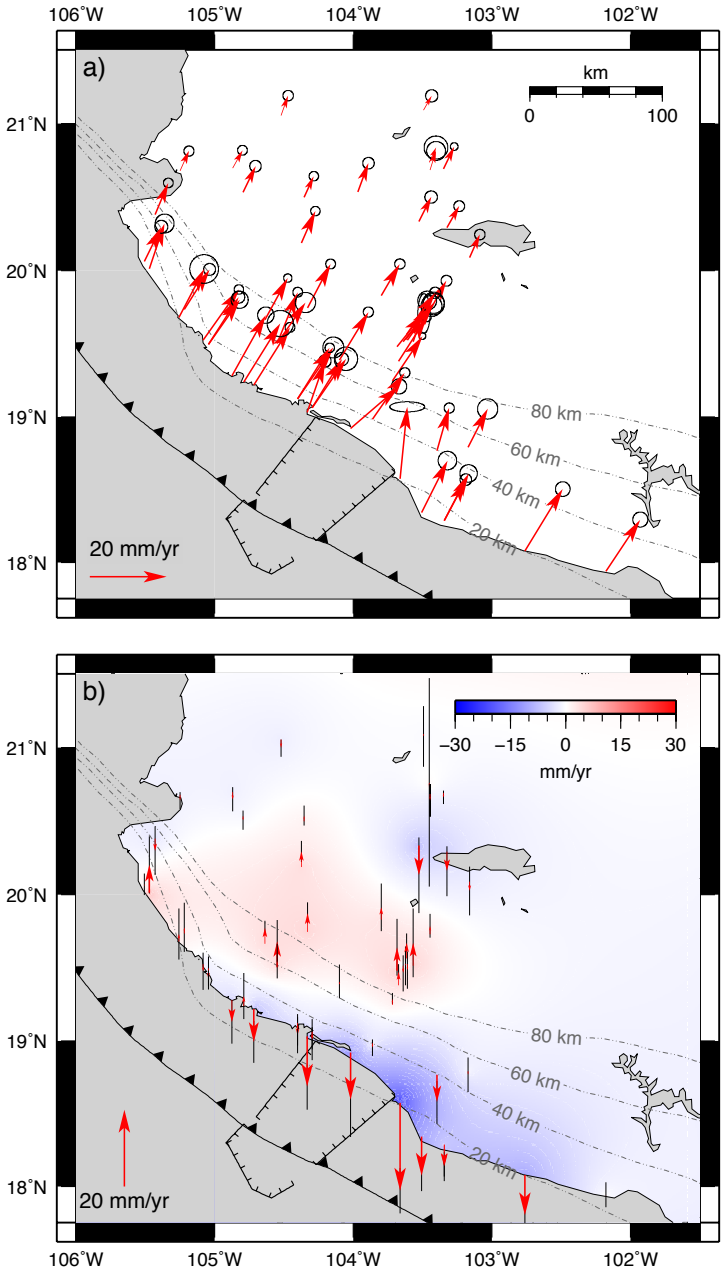

Figure 2.2. Best fitting GPS site velocities from the time–dependent inversion of GPS position time series that were corrected for the viscoelastic effects of the 1995 Colima–Jalisco and 2003 Tecomán earthquakes using a mantle Maxwell time of 15 years. a) Horizontal velocities relative to a fixed North America plate frame of reference. Ellipses represent 2D, 1–σ uncertainties. b) Vertical velocites. Thin black lines represent 1–σ uncertainties. Color shows the interpolated surface vertical velocities over the region.

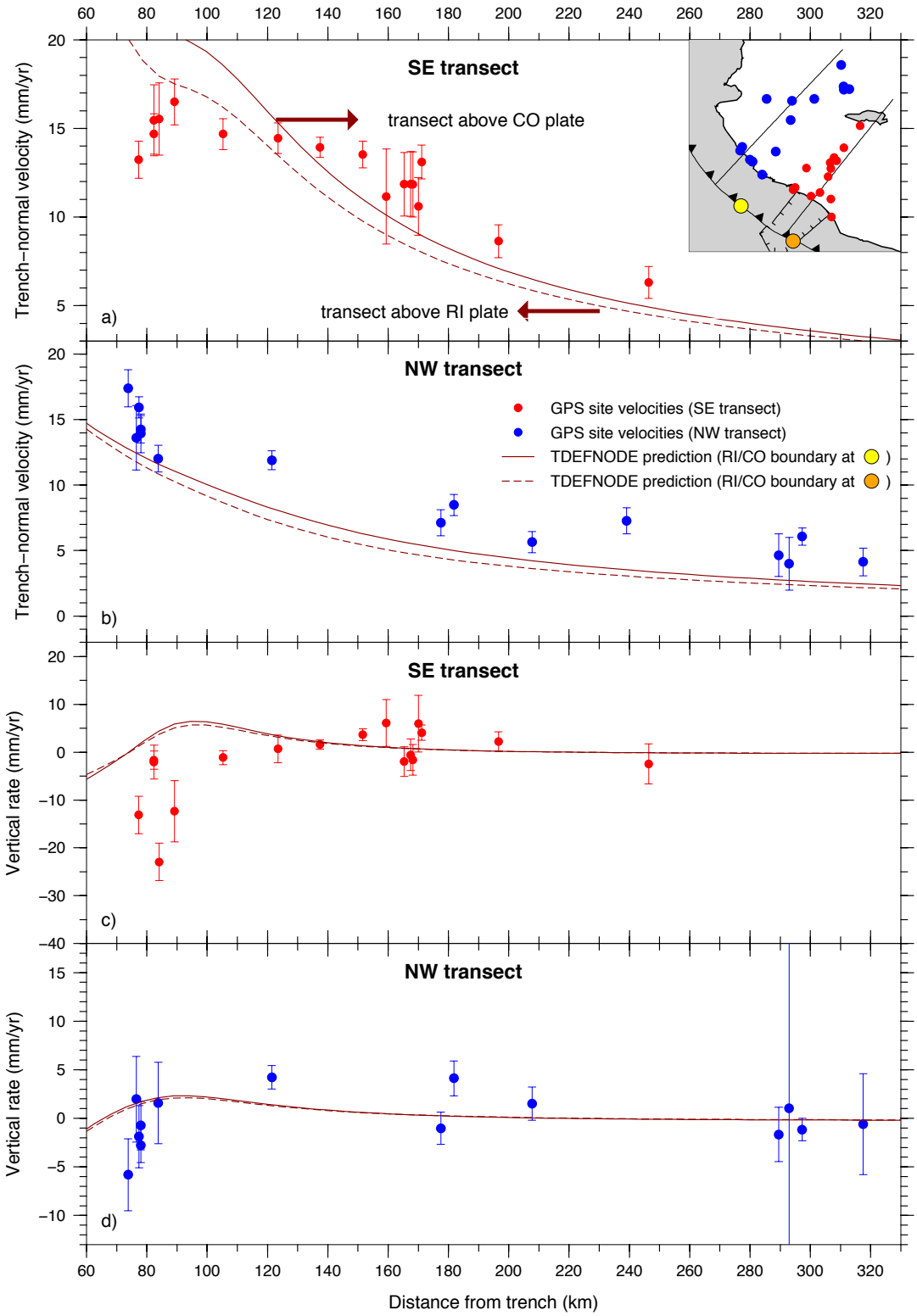

Figure 2.3. Trench–normal (a and b) and vertical (b and d) velocity components with 1–σ uncertainties, corrected for viscoelastic effects from a mantle with τ_m = 15 yr, along the northwestern (N45°E, blue) and southeastern (N40°E, red) transects in inset map. Dashed and continuous lines show TDEFNODE predictions for a fully locked interface between depths of 0–25 km, using RI/CO boundary locations 1 (orange circle) and 3 (yellow circle), respectively.

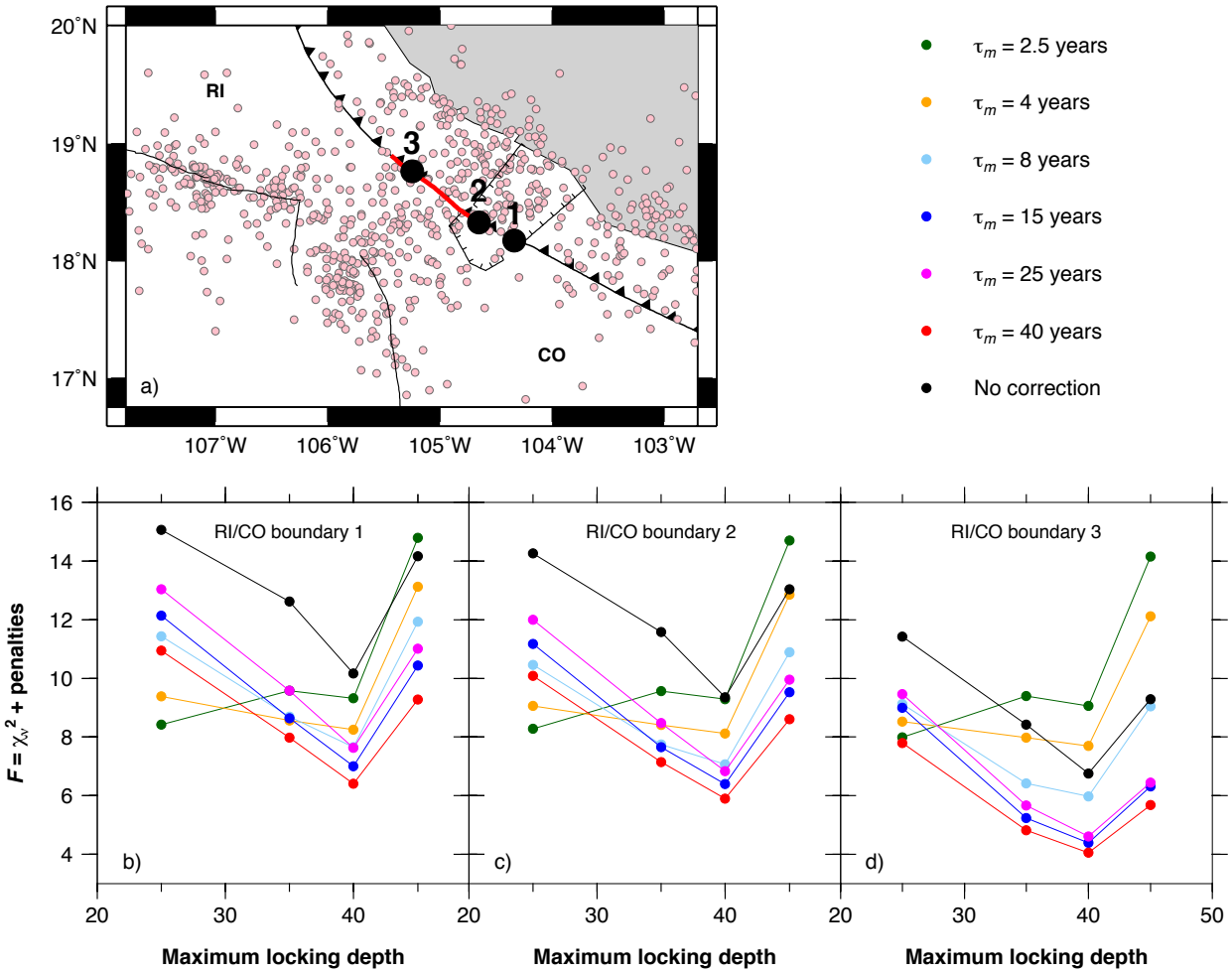

Figure 2.4. Misfit *F* vs maximum interface locking depth for models using locations 1 (b), 2 (c) and 3 (d) for the RI/CO plate boundary as shown by the black circles in a). Red segment in a) is the intersection of the trench with the zone of distributed shear proposed by DeMets and Wilson (1997) as a diffuse RI/CO plate boundary. Pink circles show the 1963–2017 seismicity (USGS). Symbol colors correspond to data sets corrected for viscoelastic effects using different mantle Maxwell times τ_m as defined in the legend.

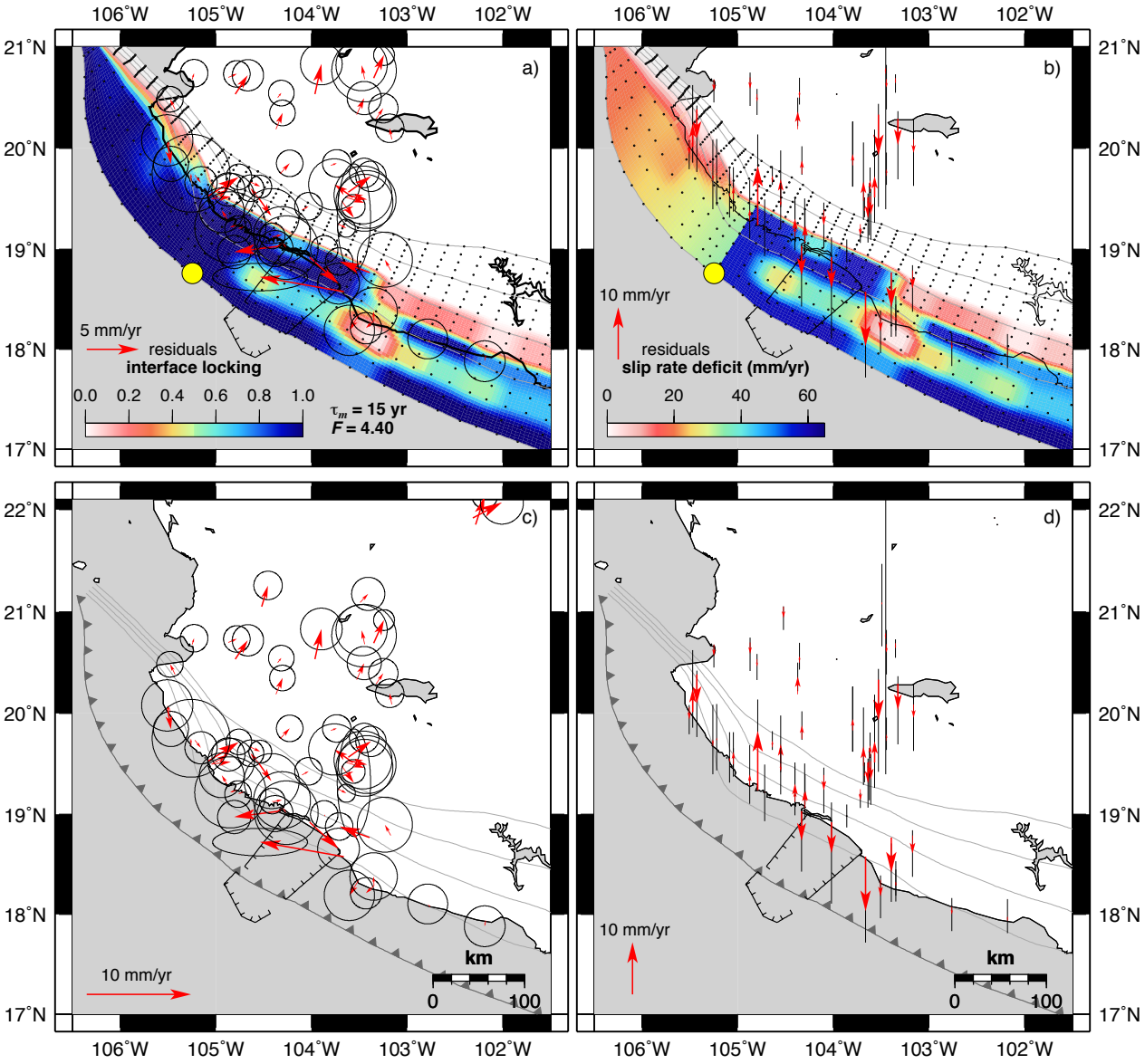

Figure 2.5. Interface locking (a) and slip rate deficit (b) along the Jalisco–Colima subduction zone from the best fitting model (maximum locking depth of 40 km and RI/CO plate boundary 3 from Fig. 2.4a, for GPS velocities that were corrected for viscoelastic effects using τ_m = 15 yr for the mantle. Yellow circle marks the location of the RI/CO plate boundary at the trench. Arrows show the horizontal (c) and vertical (d) velocity residuals (observed minus calculated by the model) with 1–σ uncertainties (ellipses and vertical lines).

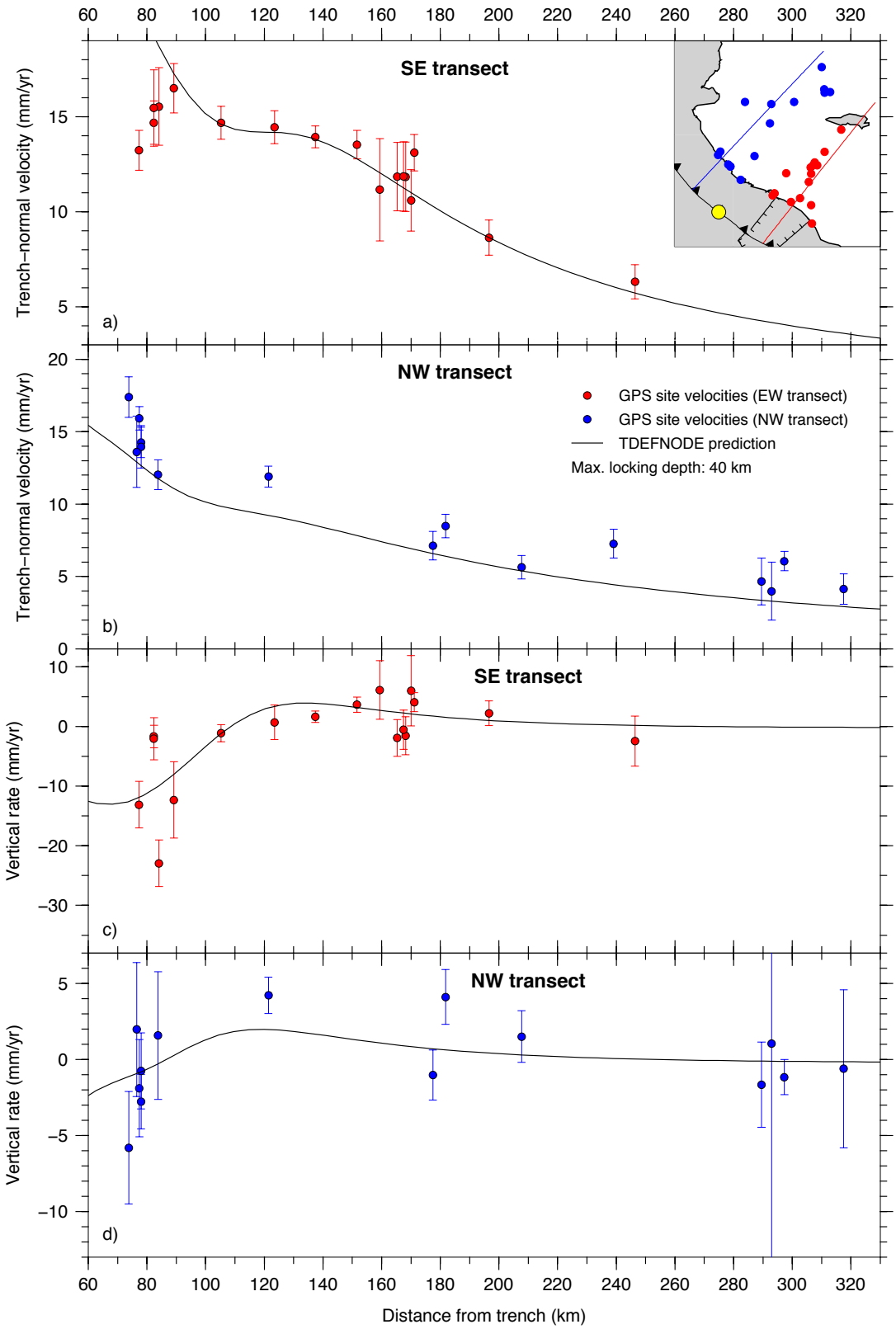

Figure 2.6. Predictions from our preferred model (black line) for the trench–normal (a, b) and vertical (b, d) velocity components with 1–σ errors, along the southeastern (N40°E, red) and northwestern (N45°E, blue) transects shown on inset. Yellow circle shows the location of the RI/CO boundary.

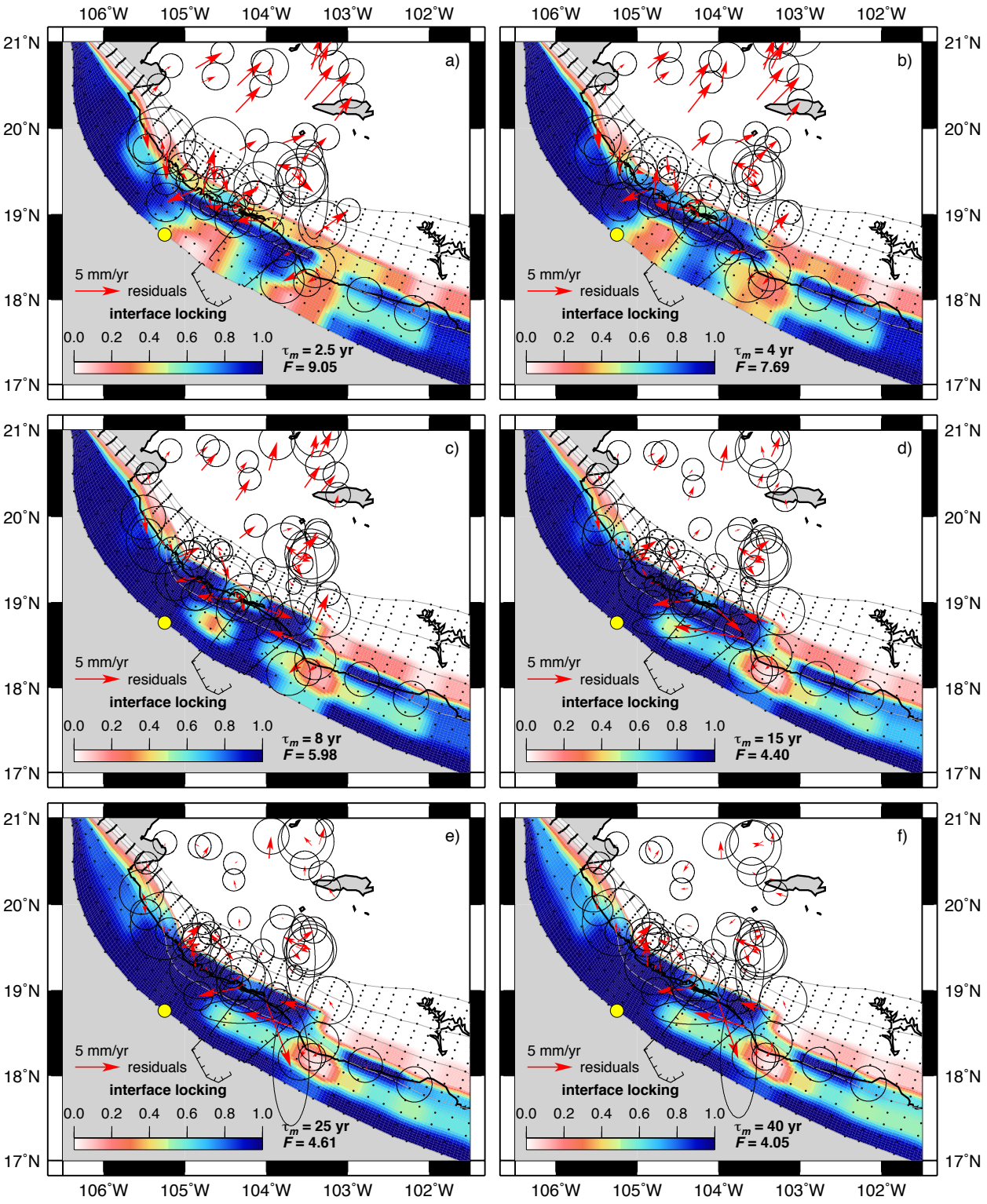

Figure 2.7. Effect of the viscoelastic corrections for the mantle Maxwell times indicated in each panel. All locking solutions have a maximum permitted locking depth of 40 km and use RI/CO boundary location 3 from Fig. 2.4a. The yellow circles identify the intersection of the RI/CO boundary with the trench. The residual velocities in each panel are the observed minus the velocities predicted by the TDEFNODE inversions described in the text. The velocity ellipses show the estimated 2–D, 1–σ uncertainties.

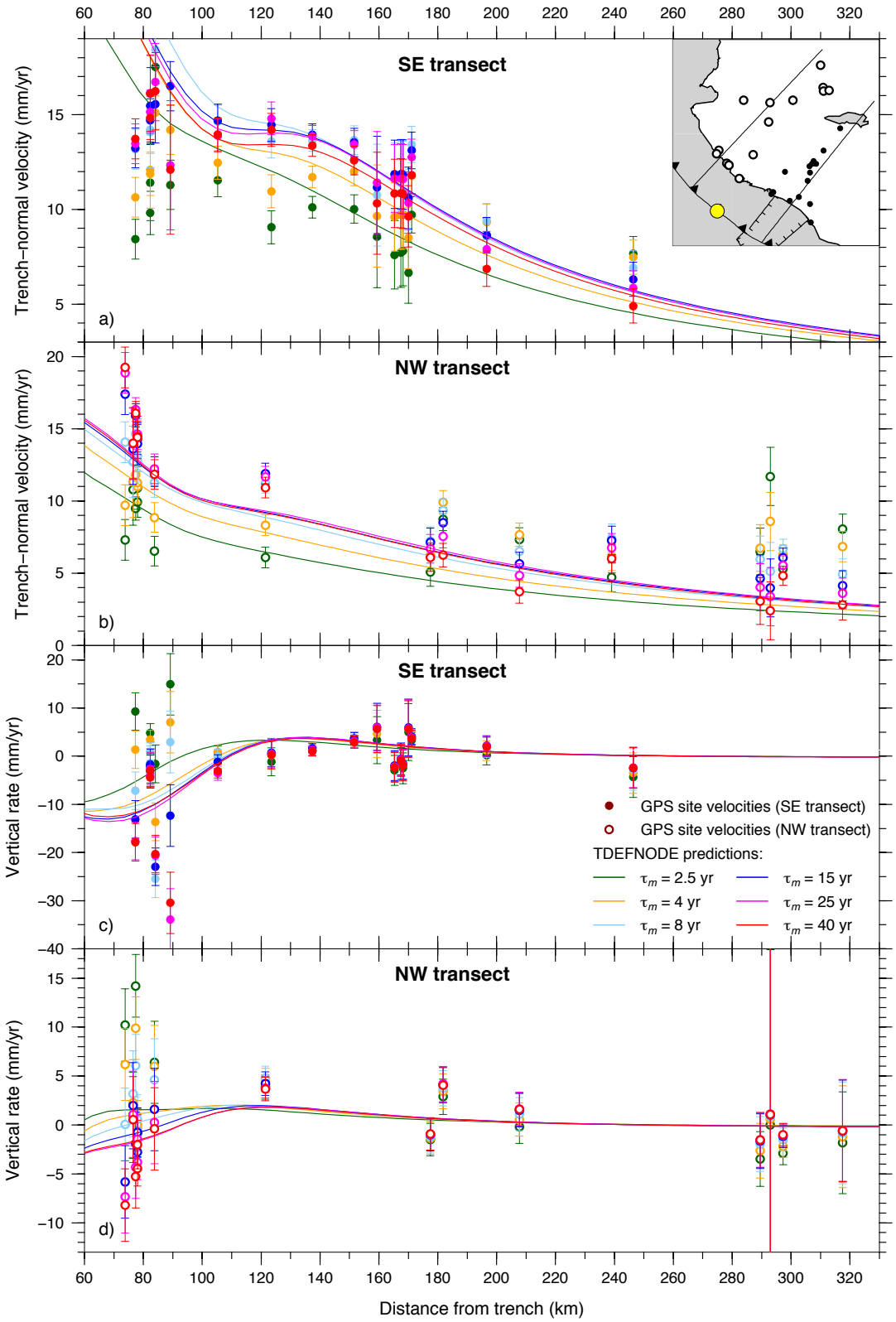

Figure 2.8. Predictions from our models (solid lines) for the trench–normal (a, b) and vertical (b, d) velocity components with 1–σ errors, along the SE (azimuth of N40°E, filled circles) and NW (azimuth of N45°E, open circles) transects shown on inset. Yellow circle locates the RI/CO boundary.

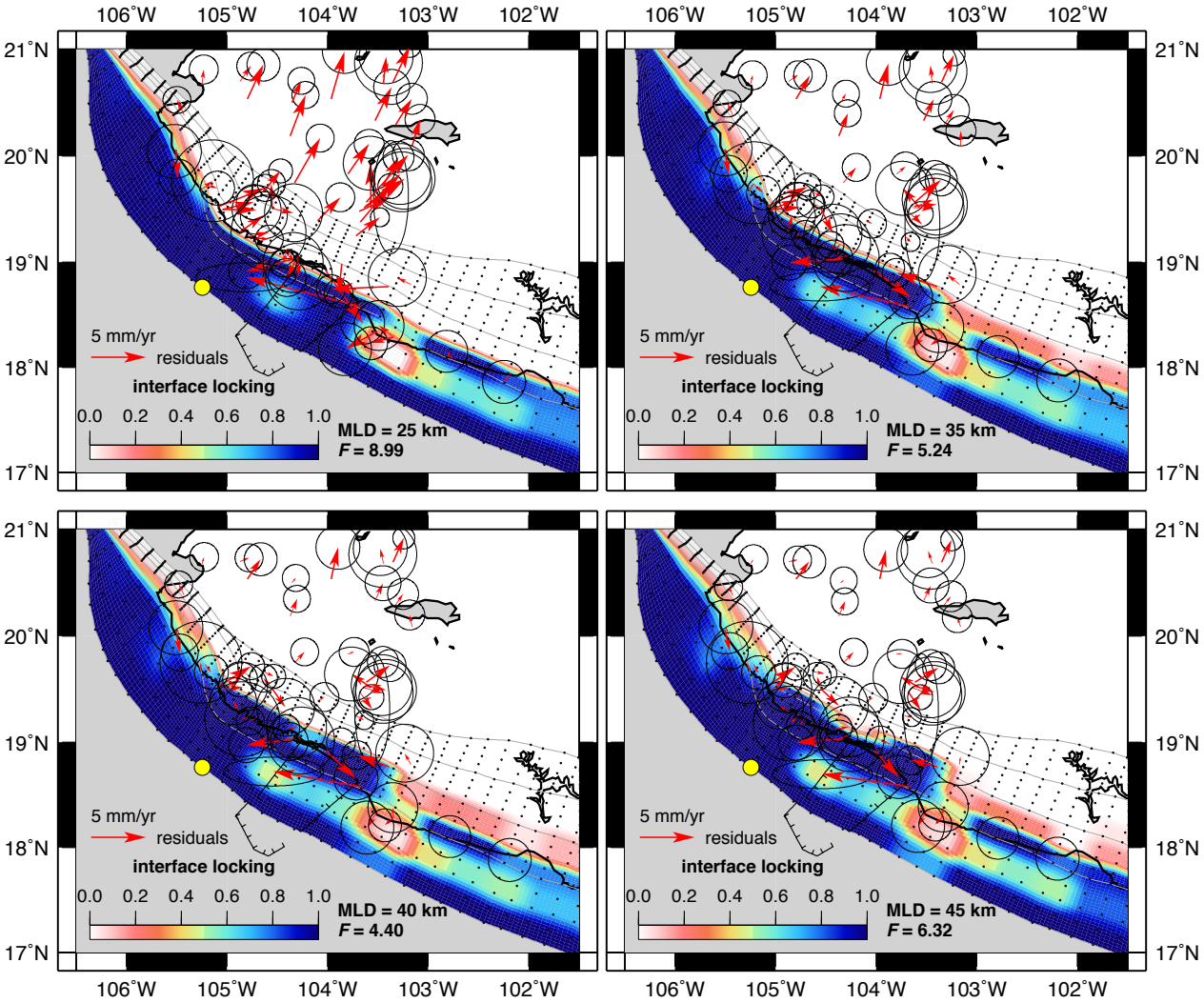

Figure 2.9. Variations of the interface locking solutions with changes in the maximum locking depth (MLD) as labeled on each panel, for the dataset using a mantle Maxwell time of 15 years for the viscoelastic effects corrections and RI/CO plate boundary 3 from Fig. 2.4a (yellow circle). The residual velocities in each panel are the observed minus the and predicted velocities. The velocity ellipses show the estimated 2–D, 1–σ uncertainties.

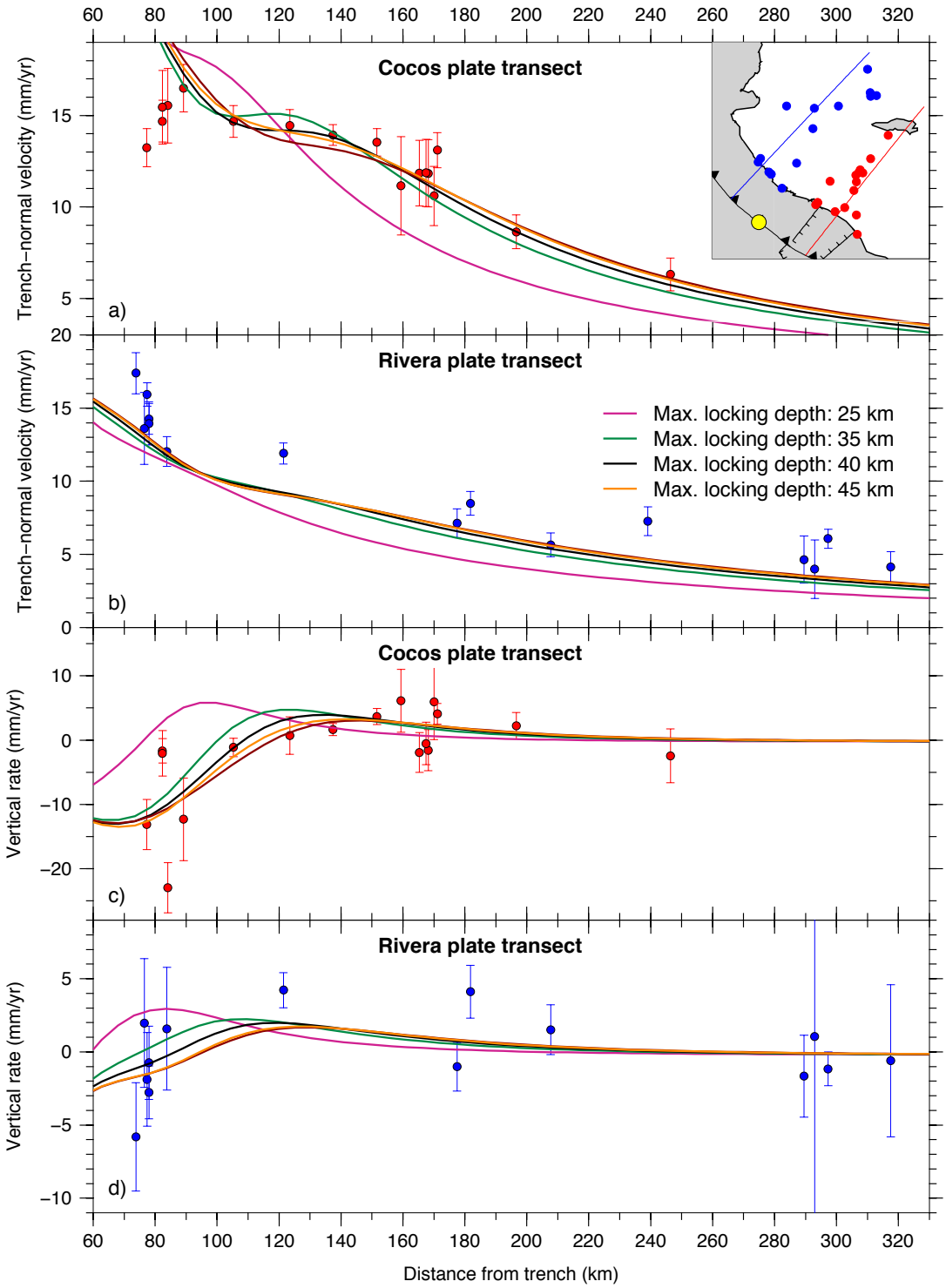

Figure 2.10. Variation in fits to trench–normal horizontal (panels a and b) and vertical (panels c and d) GPS site velocity components for velocity transects above the Rivera and Cocos plates as a function of maximum permitted subduction locking depths from 25 km to 45 km. The observed GPS site velocities (red and blue circles) are corrected for viscoelastic effects of the 1995 and 2003 earthquakes assuming τ_m = 15 yr. The predicted velocities (continuous lines) are from the best–fitting TDEFNODE inversions described in the text. The velocity error bars show the estimated 2–D, 1–sigma uncertainties. Yellow circle shows the location of the RI/CO plate boundary.

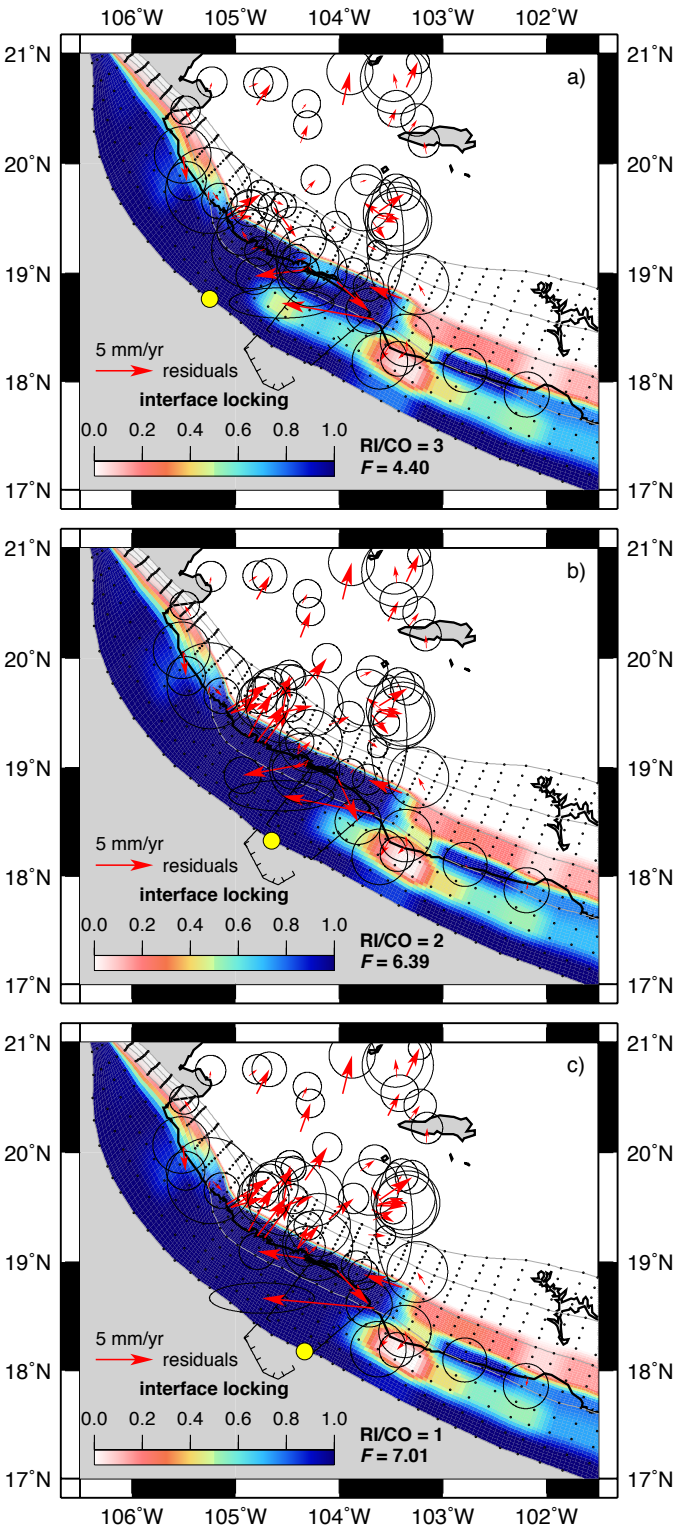

Figure 2.11. Effect of different assumed RI/CO boundary locations on subduction interface locking solutions for a maximum permitted locking depth of 40 km and GPS site velocities calibrated assuming a mantle τ_m = 15 yr. The yellow circles identify the intersection of the RI/CO boundary with the trench. The residual velocities in each panel are the observed minus the velocities predicted by the TDEFNODE inversions that are described in the text. The velocity ellipses show the estimated 2–D, 1–σ uncertainties.

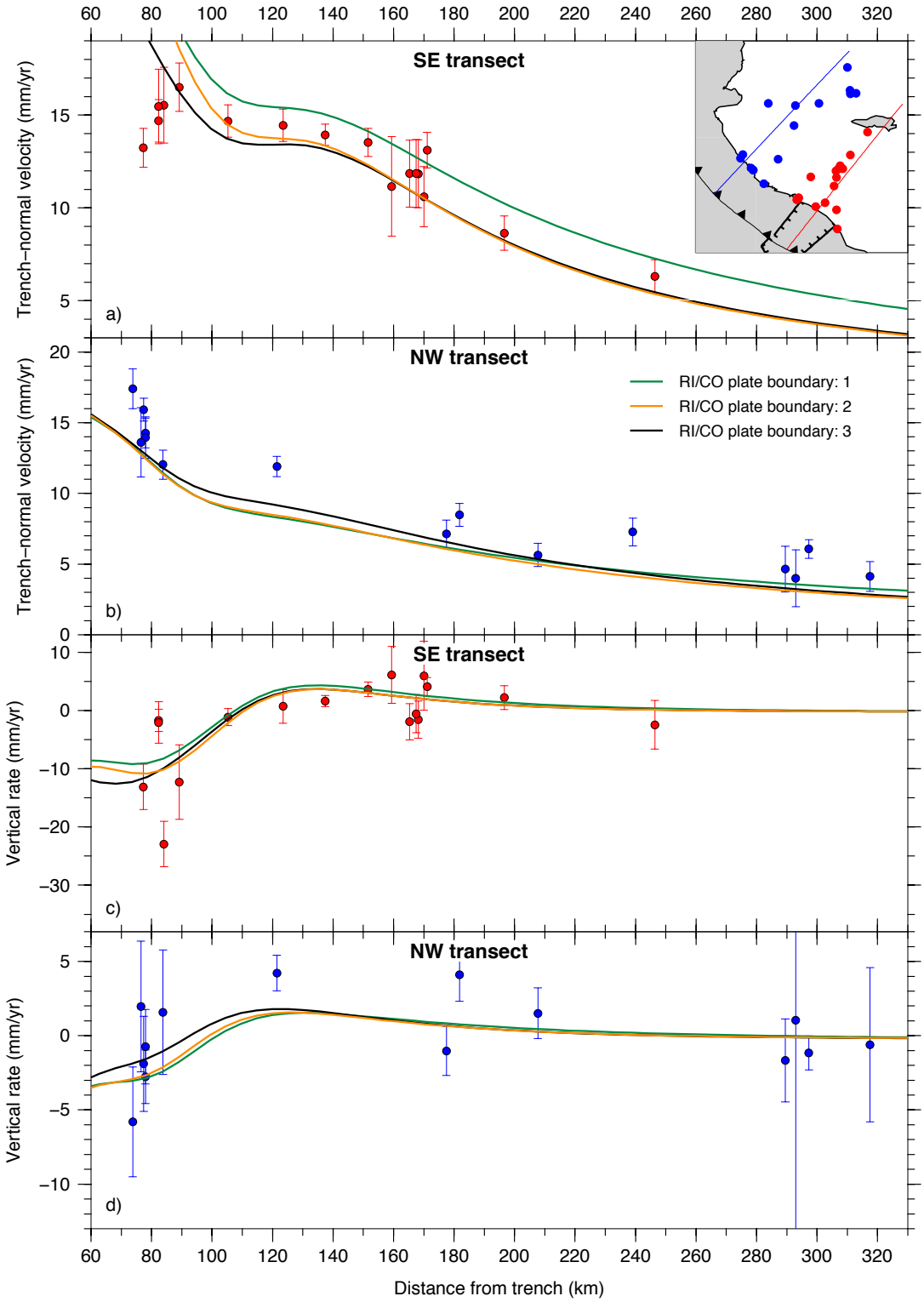

Figure 2.12. Variation in fits to trench–normal horizontal (panels a and b) and vertical (panels c and d) GPS site velocity components for transectis above the RI and CO plates as a function of the location of the RI/CO plate boundary. GPS site velocities are corrected for viscoelastic effects of the 1995 and 2003 earthquakes assuming τ_m = 15 years. The predicted velocities are from the best–fitting TDEFNODE inversions described in the text. The velocity error bars show the estimated 2–D, 1–σ uncertainties.

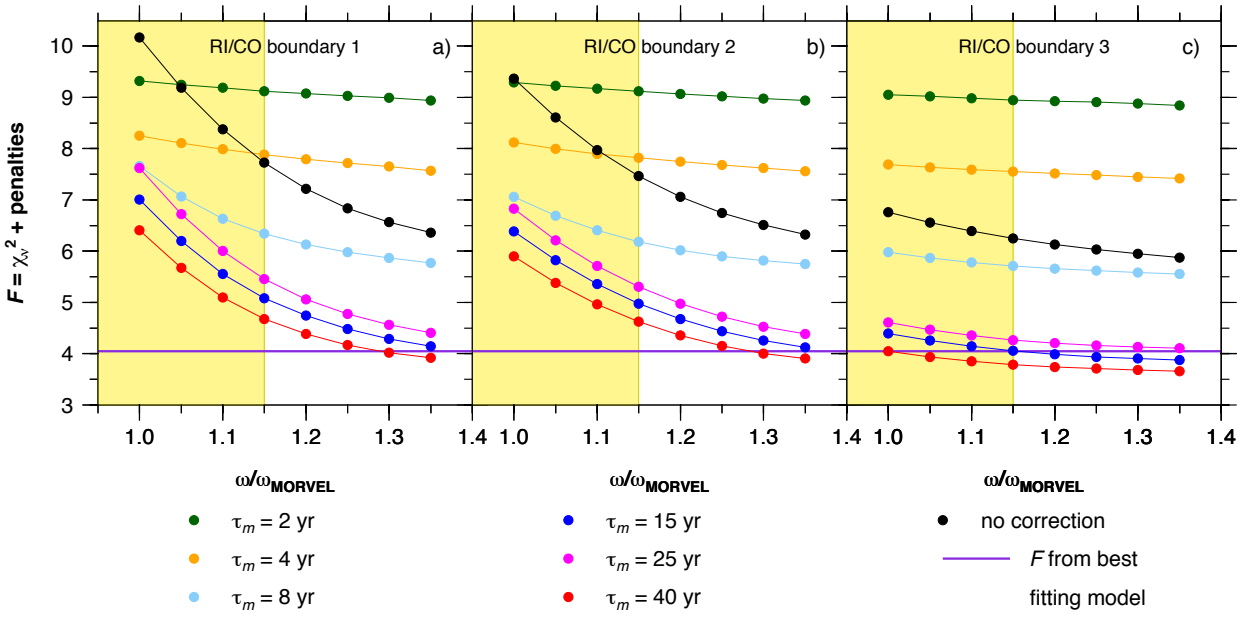

Figure 2.13. Influence of the RI–NA plate angular rotation rate on the misfit *F* for TDEFNODE inversions of GPS velocities in our study area. The RI–NA angular rotation rates ω are expressed as a fraction of the 4.37°/Myr RI–NA angular rate (ω_{MORVEL}) from the global plate motion model MORVEL (DeMets *et al*. 2010). GPS velocities are inverted while imposing a 40 km maximum interface locking depth and for three alternative locations for the RI/CO plate boundary that are defined in Fig. 2.4a. Misfits are shown for inversions of GPS velocities that are calibrated for all six mantle Maxwell times τ_m specified in the legend and for velocities without any viscoelastic calibration. The yellow region in each figure encompasses the 95% uncertainty interval for the MORVEL RI–NA angular rotation rate. The violet line denotes the χ_ν^2 value of our preferred model, i.e. the model with a 40–km maximum interface locking depth, mantle Maxwell time of 15 years, and RI/CO boundary location ~50 km NW of the Manzanillo Trough (see text).

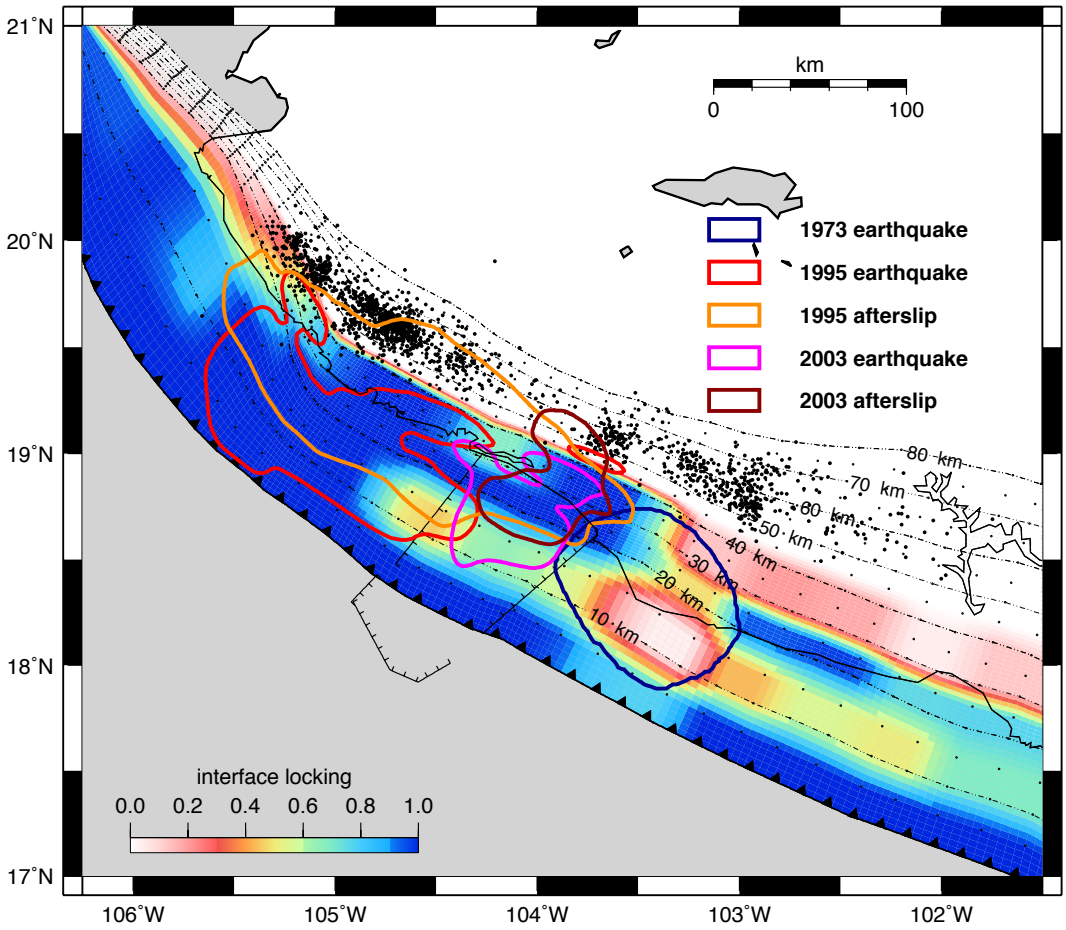

Figure 2.14. Locations of recent large thrust earthquakes (1973: blue, 1995: red, 2003: magenta), afterslip (1995: orange, 2003: dark red), and non volcanic tremor (black dots) along the Jalisco–Colima subduction interface. superposed to our preferred locking solution. The 1973 rupture is from Reyes *et al*. (1979). The 1995 and 2003 coseismic ruptures and afterslip correspond to the 0.5 m contour of the coseismic slip and afterslip solutions from our model with viscoelastic rebound corrections using τ_m = 15 years (Section 1.5). Tremor locations are from Brudzinski *et al*. (2016).

SUPPLEMENTARY INFORMATION

S2.1 SUPPLEMENTARY FIGURES

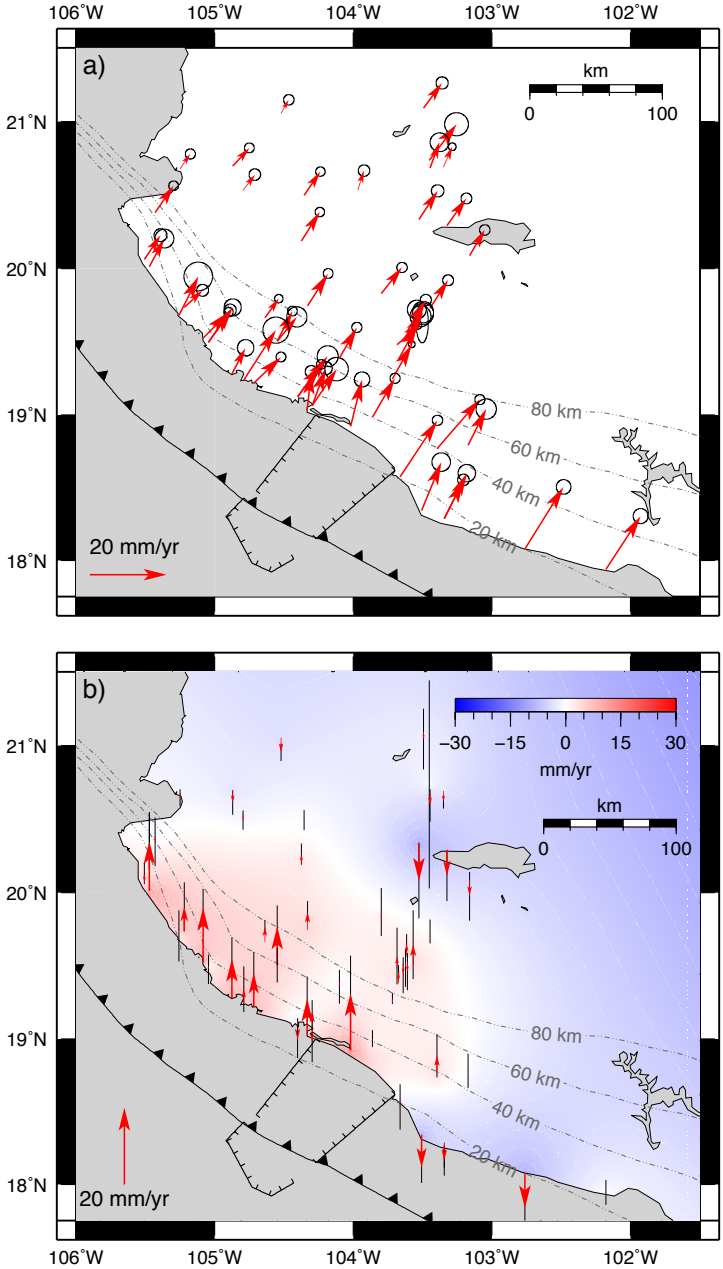

Figure S2.1. Best fitting GPS site velocities from the time–dependent inversion of GPS position time series that were corrected for viscoelastic effects of the 1995 Colima–Jalisco and 2003 Tecomán earthquakes using a mantle Maxwell time of 2.5 years. a) Horizontal velocities relative to a fixed North America plate frame of reference. Ellipses represent 2D, 1–σ uncertainties. b) Vertical velocites. Thin black lines represent 1–σ uncertainties. Color shows the interpolated surface vertical velocities over the region.

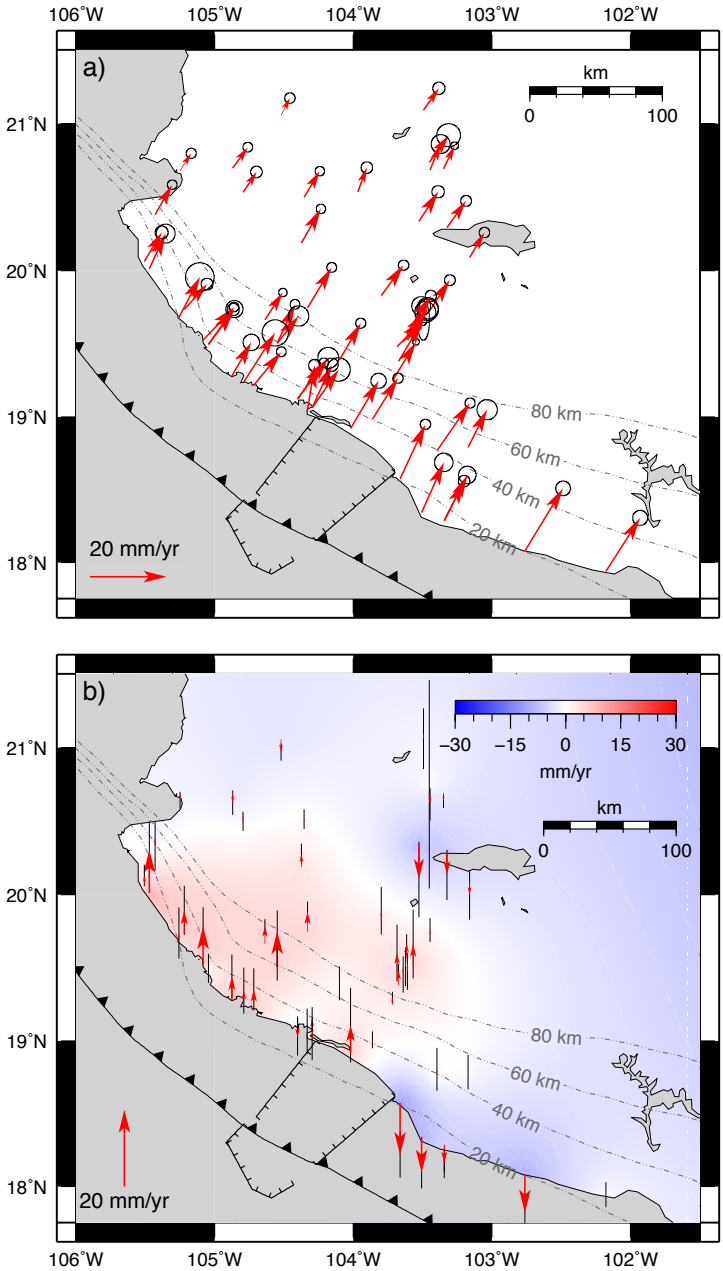

Figure S2.2. Best fitting GPS site velocities from the time–dependent inversion of GPS position time series that were corrected for viscoelastic effects of the 1995 Colima–Jalisco and 2003 Tecomán earthquakes using a mantle Maxwell time of 4 years. a) Horizontal velocities relative to a fixed North America plate frame of reference. Ellipses represent 2D, 1–σ uncertainties. b) Vertical velocites. Thin black lines represent 1–σ uncertainties. Color shows the interpolated surface vertical velocities over the region.

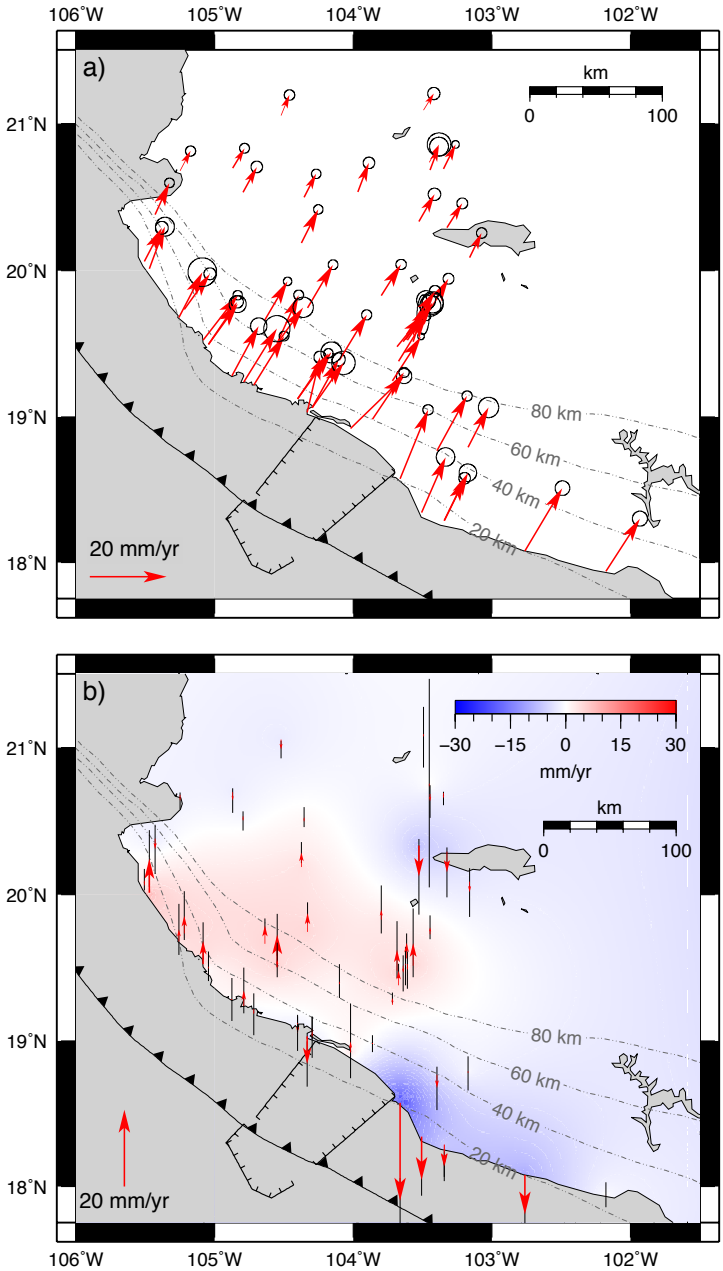

Figure S2.3. Best fitting GPS site velocities from the time–dependent inversion of GPS position time series that were corrected for viscoelastic effects of the 1995 Colima–Jalisco and 2003 Tecomán earthquakes using a mantle Maxwell time of 8 years. a) Horizontal velocities relative to a fixed North America plate frame of reference. Ellipses represent 2D, 1–σ uncertainties. b) Vertical velocites. Thin black lines represent 1–σ uncertainties. Color shows the interpolated surface vertical velocities over the region.

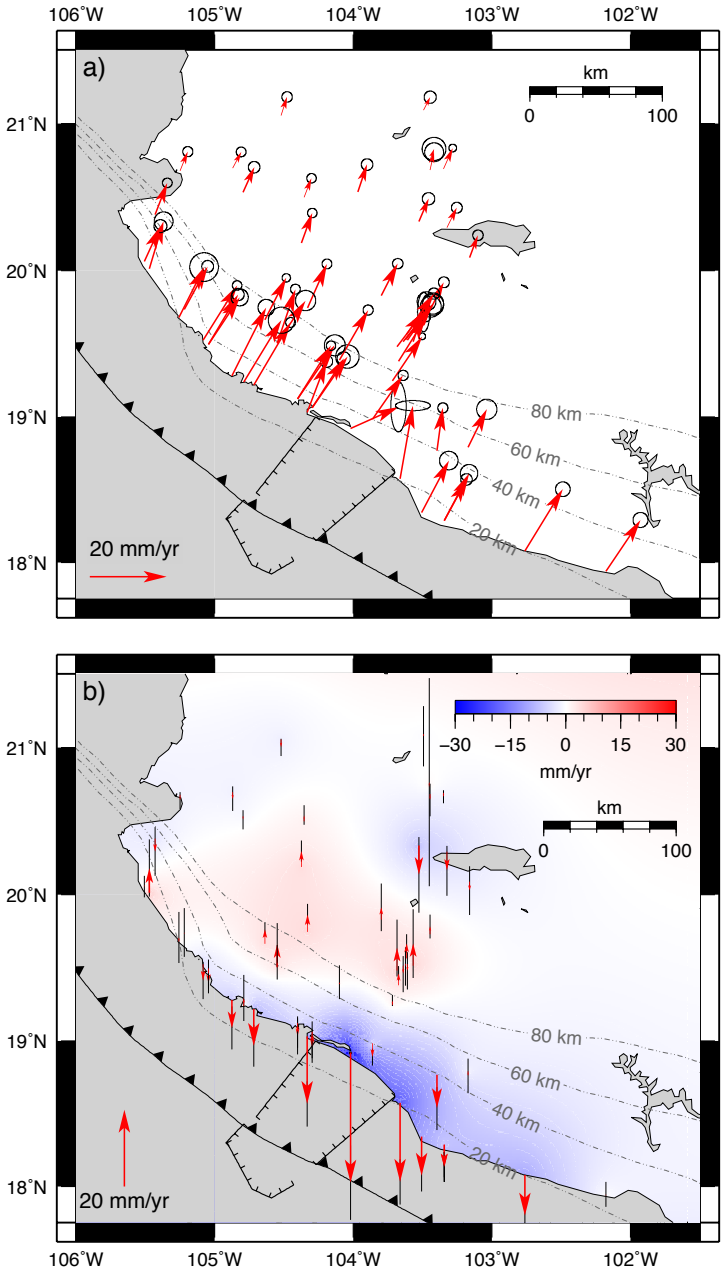

Figure S2.4. Best fitting GPS site velocities from the time–dependent inversion of GPS position time series that were corrected for viscoelastic effects of the 1995 Colima–Jalisco and 2003 Tecomán earthquakes using a mantle Maxwell time of 25 years. a) Horizontal velocities relative to a fixed North America plate frame of reference. Ellipses represent 2D, 1–σ uncertainties. b) Vertical velocites. Thin black lines represent 1–σ uncertainties. Color shows the interpolated surface vertical velocities over the region.

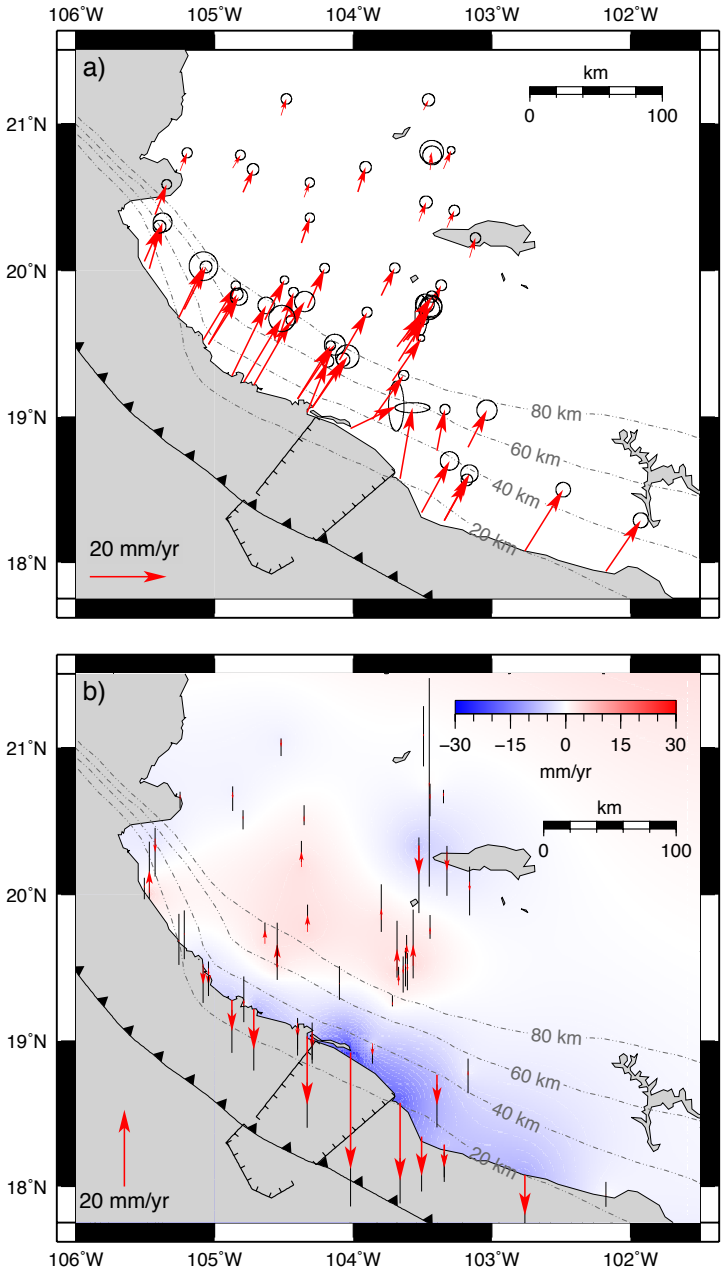

Figure S2.5. Best fitting GPS site velocities from the time–dependent inversion of GPS position time series that were corrected for viscoelastic effects of the 1995 Colima–Jalisco and 2003 Tecomán earthquakes using a mantle Maxwell time of 40 years. a) Horizontal velocities relative to a fixed North America plate frame of reference. Ellipses represent 2D, 1–σ uncertainties. b) Vertical velocites. Thin black lines represent 1–σ uncertainties. Color shows the interpolated surface vertical velocities over the region.

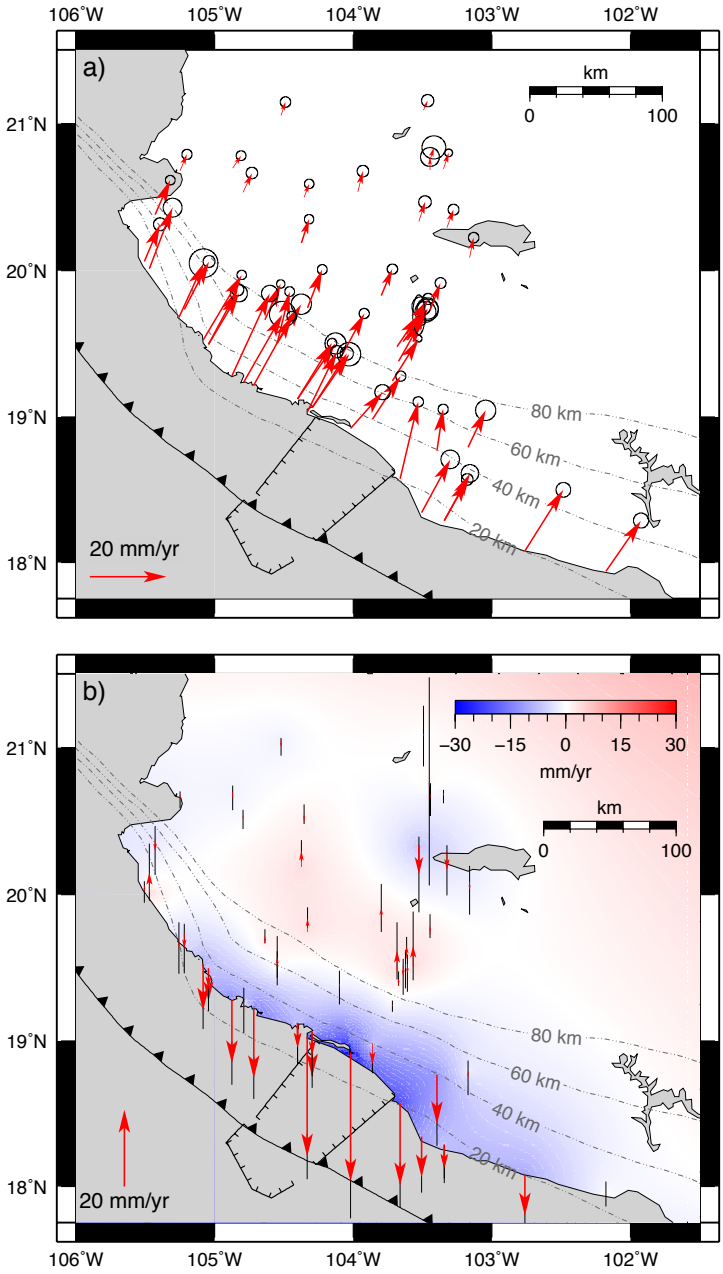

Figure S2.6. Best fitting GPS site velocities from the time–dependent inversion of GPS position time series with no viscoelastic effects corrections. a) Horizontal velocities relative to a fixed North America plate frame of reference. Ellipses represent 2D, 1–σ uncertainties. b) Vertical velocites. Thin black lines represent 1–σ uncertainties. Color shows the interpolated surface vertical velocities over the region.

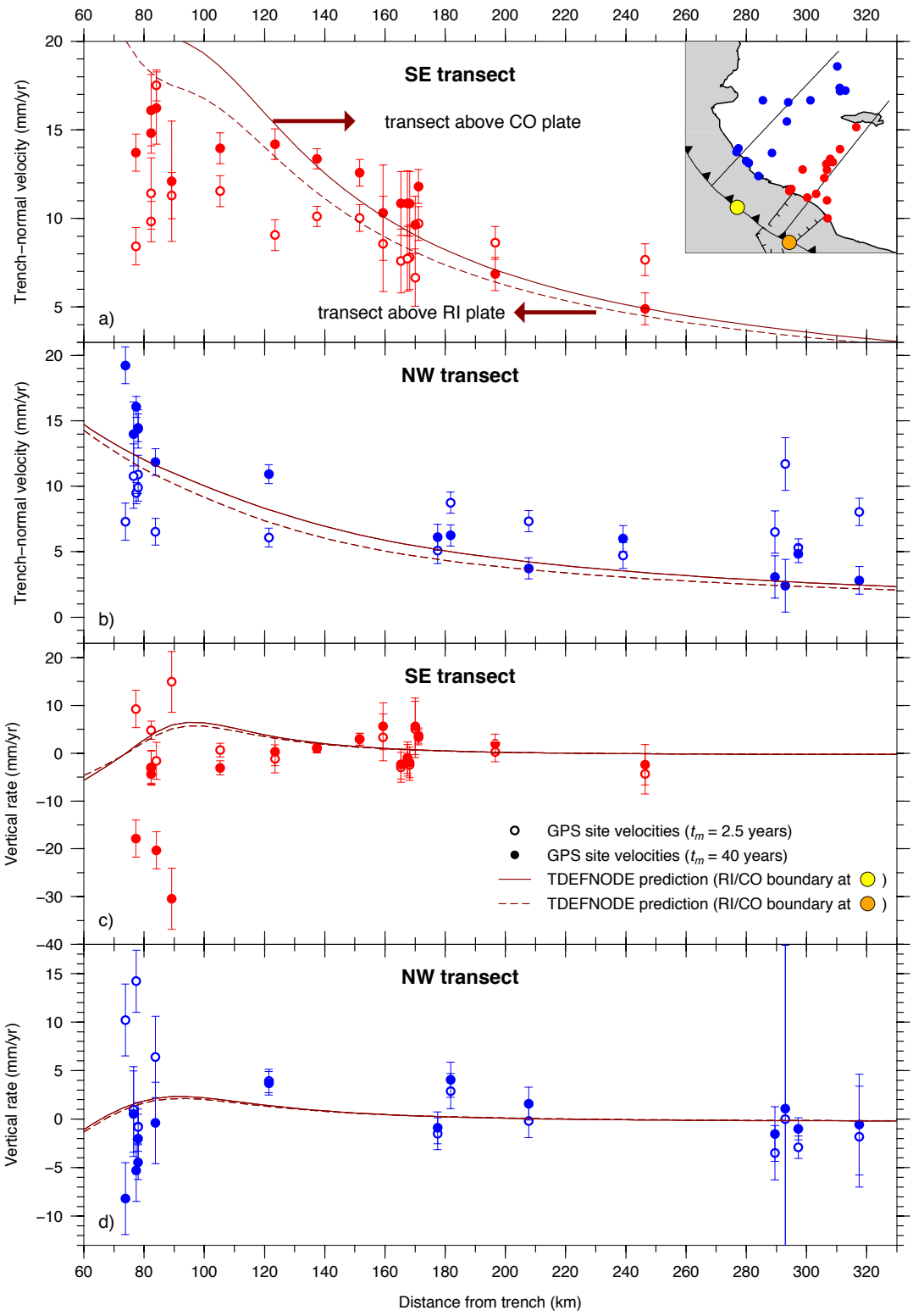

Figure S2.7. Trench–normal (a and b) and vertical (b and d) velocity components with 1–σ errors, corrected for viscoelastic efects from a mantle with τ_m = 2.5 (open circles) and 40 (filled circles) years, along the northwestern (N45°E, blue) and southeastern (N40°E, red) transects in inset map. Dashed and continuous lines show TDEFNODE predictions for an interface fully locked between depths of 0–25 km, using RI/CO boundary locations 1 (orange circle) and 3 (yellow circle), respectively.

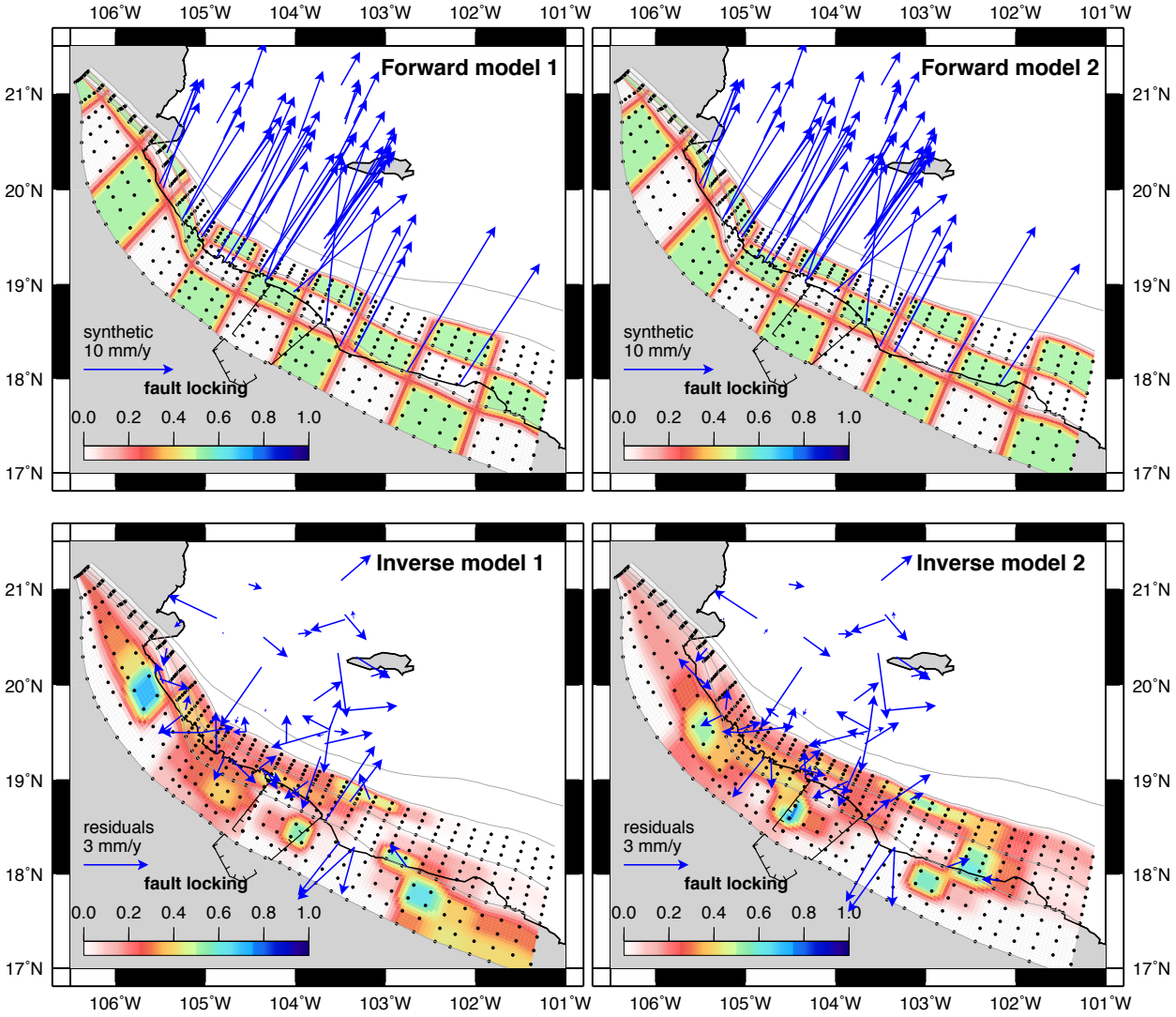

Figure S2.8. Checkerboard tests for the Jalisco Colima subduction zone. Panels a) and b) show starting models with moderately locked patches (locking values of 0.5) and their predicted (synthetic) horizontal GPS velocities. Panels c) and d) show locking solutions recovered from inversions of the synthetic GPS velocities with 1σ noise added (σ = 1 mm for the north and east components, and σ = 2 mm for the vertical component) and the residuals of the horizontal site velocities from the best fitting solutions.